Developing an Efficient FEM Structural Simulation of a Fan Blade Off test in a Turbofan jet engine.

A Thesis Submitted to the College of

Graduate Studies and Research

In Partial Fulfillment of the Requirements for the

Degree of Doctor of Philosophy

in the Department of Mechanical Engineering at the

University of Saskatchewan

Saskatoon, Saskatchewan, Canada

by

Jason Burkley Husband

Keywords: finite element method, jet engine fan blade containment, LS-Dyna

Permission to Use

In presenting this thesis in partial fulfilment of the requirements for a Postgraduate degree from the University of Saskatchewan, I agree that the Libraries of this University may make it freely available for inspection. I further agree that permission for copying of this thesis in any manner, in whole or in part, for scholarly purposes may be granted by the professor or professors who supervised my thesis work or, in their absence, by the Head of the Department or the Dean of the College in which my thesis work was done. It is understood that any copying or publication or use of this thesis or parts thereof for financial gain shall not be allowed without my written permission. It is also understood that due recognition shall be given to me and to the University of Saskatchewan in any scholarly use which may be made of any material in my thesis.

Requests for permission to copy or to make other use of material in this thesis in whole or part should be addressed to:

Head of the Department of Mechanical Engineering

University of Saskatchewan

57 Campus Drive

Saskatoon, Saskatchewan, Canada

S7N 5A9

ACKNOWLEDGMENTS

The author would particularly like to thank his wife Pamela for her patience, support and encouragement during this work. The author would also like to thank his parents, Carol and John, for their encouragement as well. Walerian Szyszkowski, as a professor and mentor, is responsible for providing much of the author's foundations in both engineering mechanics and finite element analysis; his patience and encouragement when research progress was slow is also appreciated. The aircraft engine industry must also be thanked for providing enough public domain information, through their websites and publications, to accomplish this task.

ABSTRACT

This work develops a methodology for full engine FEA simulation of the fan blade off containment test for a jet engine using LS-Dyna. The fan blade off containment test is a safety requirement involving the intentional release of a fan blade when the engine is running at full power. The released blade must not pierce or fracture the engine cases during the impact or rotating unbalance. The novel feature of the LS-Dyna simulation is the extensive full engine geometry as well as the widespread use of nonlinearities (mainly plasticity and friction) to absorb the large kinetic energies of the engine rotors. The methodology is simple to use, runs quickly and is being recognized by industry as a contender for widespread implementation. Future applications look promising enough that the methodology warrants further development and refinement.

Table of Contents

List of Figures

List of Symbols

and

Nomenclature Used

FBO	Fan Blade Out or Fan Blade Off
Aft	Direction of the engine exhaust
Forward	Direction of the engine inlet
Fan Blade	Largest, most forward Blades in engine
FEM	Finite element method
DOF	Degree of freedom
CPU	Central processing unit of computer
N-R	Newton-Raphson Equilibrium iterations
t_{int}	Total Integration time of simulation
Δt_{int}	Time step size for integrating equation of motion
apples-to-apples	a consistent comparison where model differences are clearly stated

1 Introduction to Fan Blade Off (FBO)

This chapter introduces fan blade off, how it is modeled and its importance to the aerospace industry.

1.1 Background for Turbine Engine Fan Blade Off

In aviation reducing weight is critical to developing competitive products. Airframes are typically built around the engines (airframe + engine = airplane). Engine weight has a cascading effect whereby heavier engines require large engine mounts, bigger pins, which require thicker wing segments, which requires heavier fuselage, heavier landing gear, etc. Weight savings on the engine is a major player to reducing overall airplane weight.

According to aircraft engine development experts [5,6] from the aircraft engine industry, it was understood that many engine components are sized (e.g. increased component thickness), not by operating conditions, but by the threat of a rare but potentially catastrophic event called Fan Blade Off (described further below). Said differently, most engine components are designed heavier (conservatively adding extra wall thickness to a particular component, for example) than they need to be because of the remote possibility of a Fan Blade Off. On the other hand, relatively little is known (or published) about the FBO event due the high cost of experimental testing, and there are significant difficulties with computer simulation because of the physical complexity. Plus, the business risk of failing the FBO test (described in later section) warrants a conservative approach. It is hoped that improved FEA simulation methods of Fan Blade Off can lead better understanding of it and a more efficient design methodology, which in turn should allow for a lower overall engine weight.

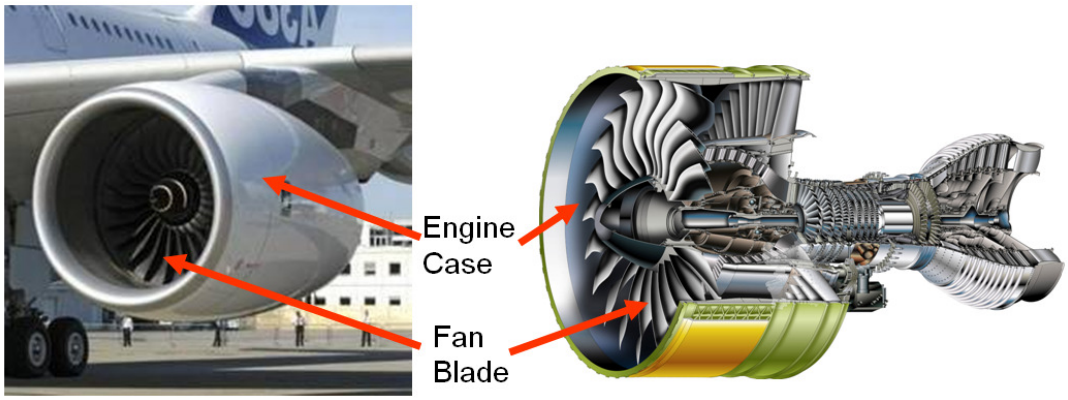

Figure 1.1 Aircraft Engine Schematic and Location of Fan Blade. [30,23]

Passing the Fan Blade Off containment test is a major milestone in the aero engine development cycle. The fan blades (not rotating) are visible in Figure 1.1. When an engine is running there is a risk that the fan blade may break off. This event is known in the turbine industry as *fan blade out* or *fan blade off* (or FBO for short).

If a fan blade does release during operation the engine cases must contain the fan blade's kinetic energy from impact and also absorb the rotating unbalanced force from the missing fan blade as indicated in Figure 1.2.

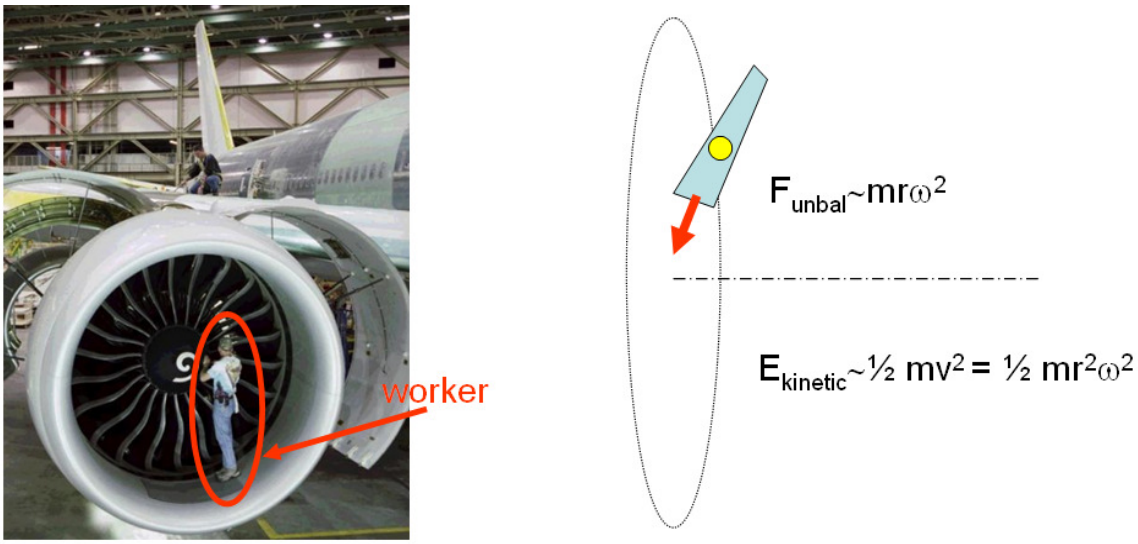

Figure 1.2 Kinetic Energy and Rotating Unbalanced Force on Fan Blade [29]

Some simple calculations demonstrate the severity of fan blade off. For demonstration, assume a fan blade mass of m = 10kg, a center of mass radius of r = 1.5m and a fan speed of 5000rpm (or ω = 523 radians/s). Note that these are typical values for a large turbo fan engine. For this typical data, the kinetic energy of a released blade is about:

$$E_{kinetic} = \tfrac{1}{2}\, mv^2 = 3.1 \cdot 10^6\ \text{Nm} \qquad (1.1)$$

which has the equivalent energy of a 2000kg vehicle falling from about 150m height. This is a huge amount of energy to be absorbed by the blades impacting the case. Further, after impact, the missing blade shifts the center of gravity of the rotor with an unbalanced rotating force of:

$$F_{unbal} = mr\omega^2 = 4.1 \cdot 10^6 \text{N (approx } 1 \cdot 10^6 \text{lb)} \qquad (1.2)$$

This unbalanced force is huge considering that a large fully assembled turbo fan engine weighs only about $7 \cdot 10^4$ N (7000kg mass) (or 15,000 lb). The engine cases must be able to withstand both the initial impact energy as well as the subsequent rotating imbalanced force from the fan blade off event. This structural absorption capacity is known as containment.

An example of structural failure due to an uncontained engine is shown below in Figure 1.3. This plane was able to land but the consequences could have been much more severe.

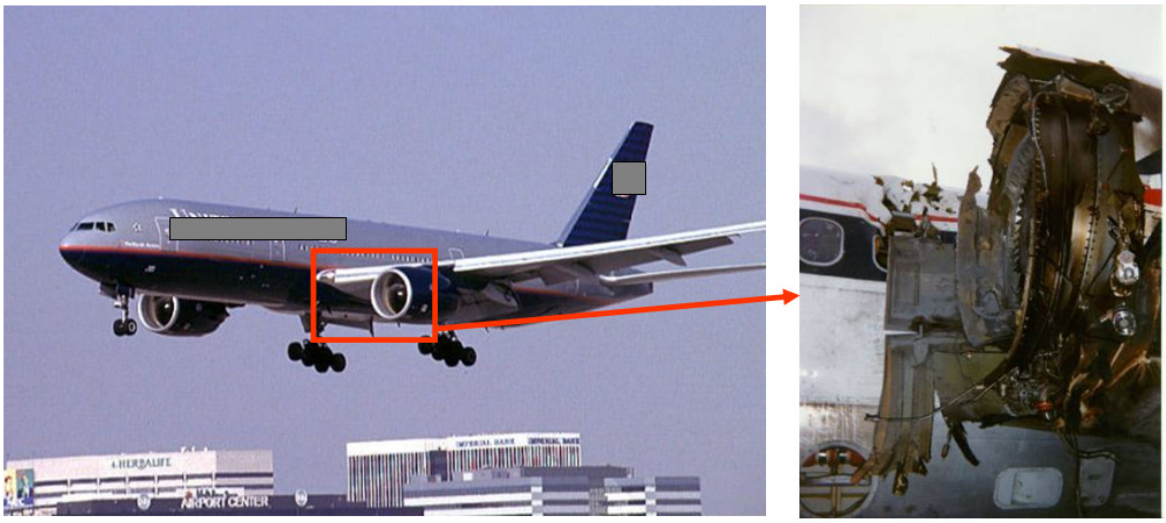

Figure 1.3 Consequences due to lack of Containment Capability [26]

1.2 FAA Regulations Governing Blade Containment

To fly, an engine must be certified by the Federal Aviation Administration (FAA). One milestone of the certification process is the fan blade off test. The regulations [7] governing blade containment are shown below. The basic idea is that the blade release should:

1. not cause an engine fire (usually from cut fuel/oil supply lines)
2. not fracture the cases/mounts.

These are more thoroughly described below. There are also other requirements stating there should be minimal debris ejected from the engine; but this is beyond the scope of the current discussion.

Sec. 33.94 - Blade containment and rotor unbalance tests.

(a) Except as provided in paragraph (b) of this section, it must be demonstrated by engine tests that the engine is capable of containing damage without catching fire and without failure of its mounting attachments when operated for at least 15 seconds, unless the resulting engine damage induces a self shutdown, after each of the following events:

(1) Failure of the most critical compressor or fan blade while operating at maximum permissible r.p.m. The blade failure must occur at the outermost retention groove or, for integrally-bladed rotor discs, at least 80 percent of the blade must fail.

(2) Failure of the most critical turbine blade while operating at maximum permissible r.p.m. The blade failure must occur at the outermost retention groove or, for integrally-bladed rotor discs, at least 80 percent of the blade must fail. The most critical turbine blade must be determined by considering turbine blade weight and the strength of the adjacent turbine case at case temperatures and pressures associated with operation at maximum permissible r.p.m.

(b) Analysis based on rig testing, component testing, or service experience may be substitute for one of the engine tests prescribed in paragraphs (a)(1) and (a)(2) of this section if --

(1) That test, of the two prescribed, produces the least rotor unbalance; and

(2) The analysis is shown to be equivalent to the test. Secs. 313(a), 601, and 603, Federal Aviation Act of 1958 (49 U.S.C. 1354(a), 1421, and 1423); and 49 U.S.C. 106(g) Revised, Pub. L. 97-449, Jan. 12, 1983)

Of particular interest is the FAA recognition of using analytical techniques which are equivalent to a rig test. The focus of this paper is to study and develop an efficient finite element simulation of the fan blade off event using finite element methods.

Although there are many shapes and sizes of jet engines, one common feature is spinning bladed rotors. Several blade sets are shown below in Figure 1.4. FAA Regulations require that all

blades must be contained but the fan blades are typically found to generate the highest impact energy and unbalanced forces. To limit scope, this project will focus on simulating fan blade off for a turbofan engine; however, the methods developed could be used to simulate blade releases in other turbofan engines as well.

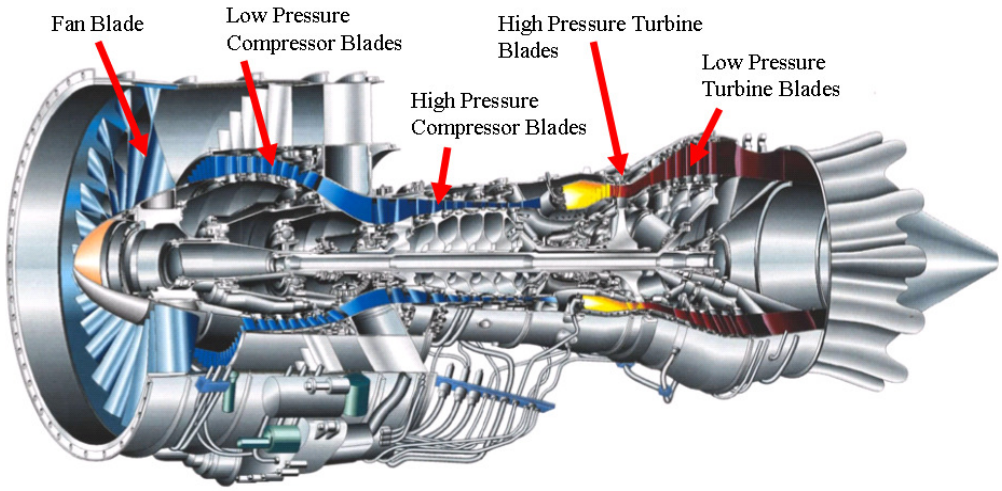

Figure 1.4 Various Rotating Blades inside a turbofan engine [23]

1.3 FBO Rig Testing

Three representative rig test stands for FBO certification are shown in Figure 1.5. To conduct this test the:

1. the engine is running at full power
2. the base of the fan blade is fractured by an explosive charge inducing the fan blade off event.

The engine cases must contain the released fan blade and handle the out of balance force without failing.

Figure 1.5 Several FBO Rig Test stands [26,27]

A movie clip of an experimental test demonstrating successful containment of the Rolls Royce Trent engine during FBO is shown in Figure 1.6. The animation can be downloaded from http://www.engr.usask.ca/classes/ME/990/thesis/ . The mpeg file is named Rolls Royce Fan_Blade Containment with a file-size of about 40Mb. Right click and "Save Target As".

Note the giant fireball shooting out of the front of engine after the blade is released. This is [5,6] due to a combination of expanding combustion gases as well as ablative oxidation of blade tips and casings rub strip material due to the enormous friction (this may be better understood using Figure 4.7). Further, accounts [5,6] of noticeable plastic yielding in post-FBO engine components give clues that blade tip friction rubbing and material plasticity/yielding are very important physics to be included in the modeling of FBO.

Figure 1.6 Rolls-Royce Movie of Successful Fan Blade Off rig test. [25]

The video sharing website YouTube also had these posted. These can also be found at http://www.engr.usask.ca/classes/ME/990/thesis/ . Right click and 'Save Target As'.

Figure 1.7 A380 Airbus engine (A380_Blade_Off_Test.wmv)


Figure 1.8 Pratt and Whitney PW4098 Engine (PW4098_Blade_out_test.wmv)

Note the large rotations, multi-body contact, sliding friction as well as inelastic deformations that occur during the FO event.

1.4 Time and Cost of FBO test to Industry

These FBO tests are very time consuming and costly. It takes in the order [5,6] of five years and $1 billion to develop and certify an engine. The FBO test is one of the major phases in this certification process.

The engines are mounted to the airframe as shown below in Figure 1.9. Clearly, massive engines cases could withstand the blade off energy and unbalanced rotor force. However, the challenge is to determine how much weight can be removed and still fly safely. Finite element simulation plays a large role in this weight reduction and can reduce the time and cost to industry.

Figure 1.9 Engines mounted on commercial (left) and military (right) aircraft. [29,31]

1.5 Simulation Tools for FBO under Development by Industry

The portion of an annual report from the NASA website is repeated (almost verbatim) directly below and summarizes the Fan Blade Off simulation methods currently being used and developed by industry.

New Tools Being Developed for Engine-Airframe Blade-Out Simulations
Structural Mechanics and Dynamics Branch 2002 Annual Report,
NASA TM-2003-212296
George Stefko, August 2003, Washington, DC 20546-0001

One of the primary concerns of aircraft structure designers is the accurate simulation of the blade-out event. This is required for the aircraft to pass Federal Aviation Administration (FAA) certification and to ensure that the aircraft is safe for operation. Typically, the most severe blade-out occurs when a first stage fan blade in a high-bypass gas turbine engine is released. Structural loading results from both the impact of the blade onto the containment ring and the subsequent instantaneous unbalance of the rotating components. Reliable simulations of blade-out are required to ensure structural integrity during flight as well as to guarantee successful blade-out certification testing. The loads generated by these analyses are critical to the design teams for several components of the airplane structures including the engine, nacelle, strut, and wing, as well as the aircraft fuselage.

Currently, a collection of simulation tools is used for aircraft structural design. Detailed high-fidelity simulation tools are used to capture the structural loads resulting from blade loss, and then these loads are used as input into an overall system model that includes complete structural models of both the engines and the airframe. The detailed simulation (shown in the figure) includes the time-dependent trajectory of the lost blade and its interactions with the containment structure, and the system simulation includes the lost blade loadings and the interactions between the rotating turbomachinery and the remaining aircraft structural components.

General-purpose finite element structural analysis codes are typically used, and special provisions are made to include transient effects from the blade loss and rotational effects resulting from the engine's turbomachinery. To develop and validate these new tools with test data, the NASA Glenn Research Center has teamed with GE Aircraft Engines, Pratt & Whitney, Boeing Commercial Aircraft, Rolls-Royce, and MSC.Software. Progress to date on this project includes expanding the general purpose finite element code, NASTRAN, to perform rotordynamic analysis of complete engine-airframe systems. Capabilities that have been implemented into the code are frequency response (windmilling), complex modes (damped critical and whirl speeds), and static analysis (maneuver loads). Future plans include a nonlinear enhancement for blade-out simulation and construction of a test rig to determine blade case interaction characteristics.

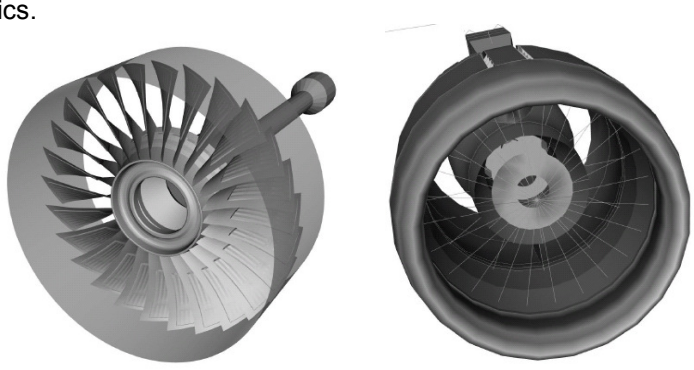

High Fidelity Model (left) and Overall System Model (right)

1.6 Industry Challenges for FEA Modeling of FBO

Currently there are two published methods being developed to predict FBO loads in components. The author believes the current (based on published data) analysis methodologies (both LS-Dyna modeling of fan blade impact and NASTRAN modeling of engine rotor imbalance) leave some gaps in the analysis requirements of industry. The focus of this work is to fill that gap.

Understanding the typical engine development cycle is important for understanding the engineering tool requirements. Figure 1.10 below shows the typical engineering staffing requirements to produce a final design.

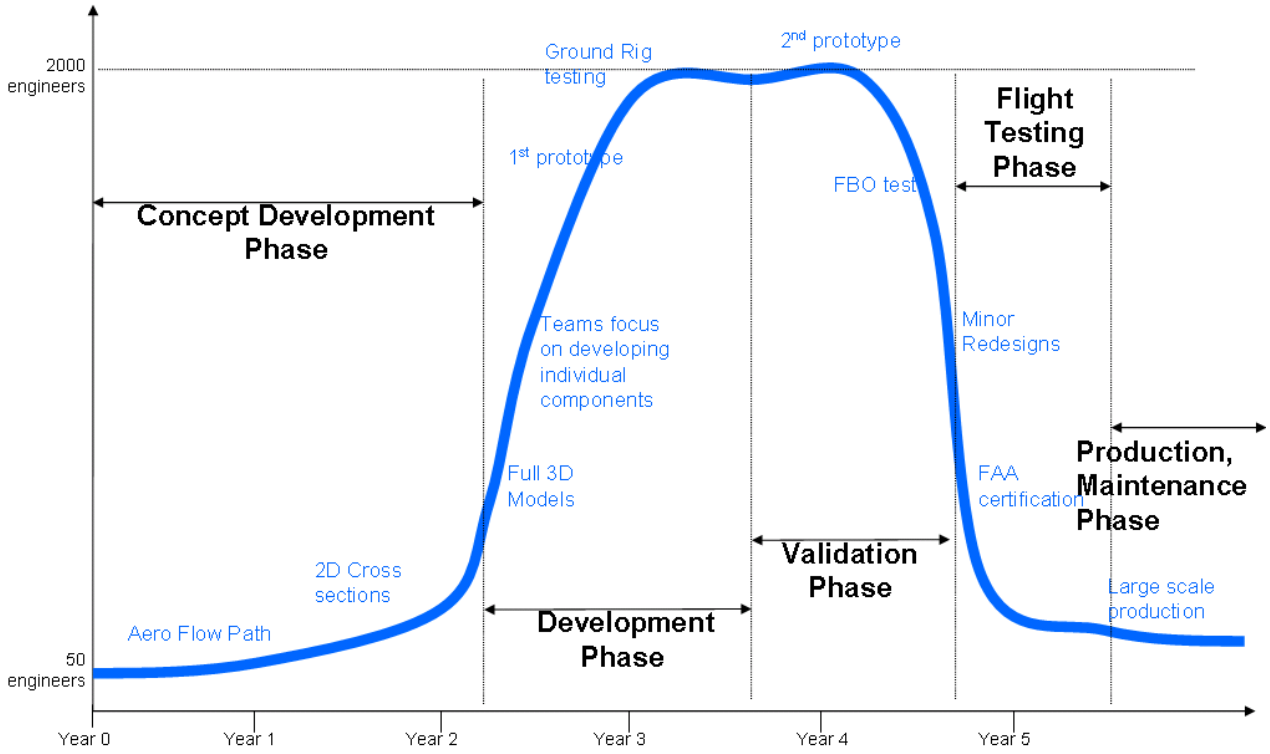

Figure 1.10 Assigned engineering staff versus engine development time.

During engine development several key phases that occur are:

1. Conceptual development - establish engine size, power, new technologies implemented. In general, fewer people are required.
2. Development phase- create 3D parts to get a working design (not optimal but works). Initial testing to prove concept. This phase is manpower intensive.

3. Validation Phase - use available test data and prior engine experience to improve working design and ensure reliability. This phase is also manpower intensive.
4. Flight testing - self explanatory. FAA certification.
5. Production and maintenance. Assembly lines produce engines.

Note how the manpower can peak to the order of 2000 engineers.

1.6.1 Design of Individual Components

In practice, this workforce is broken down into representative teams (each manufacturer organizes this differently, but the principle is the same) as shown in Figure 1.11 below with an engine cross section shown to remind the reader of the sheer number of components and assemblies inside a typical engine.

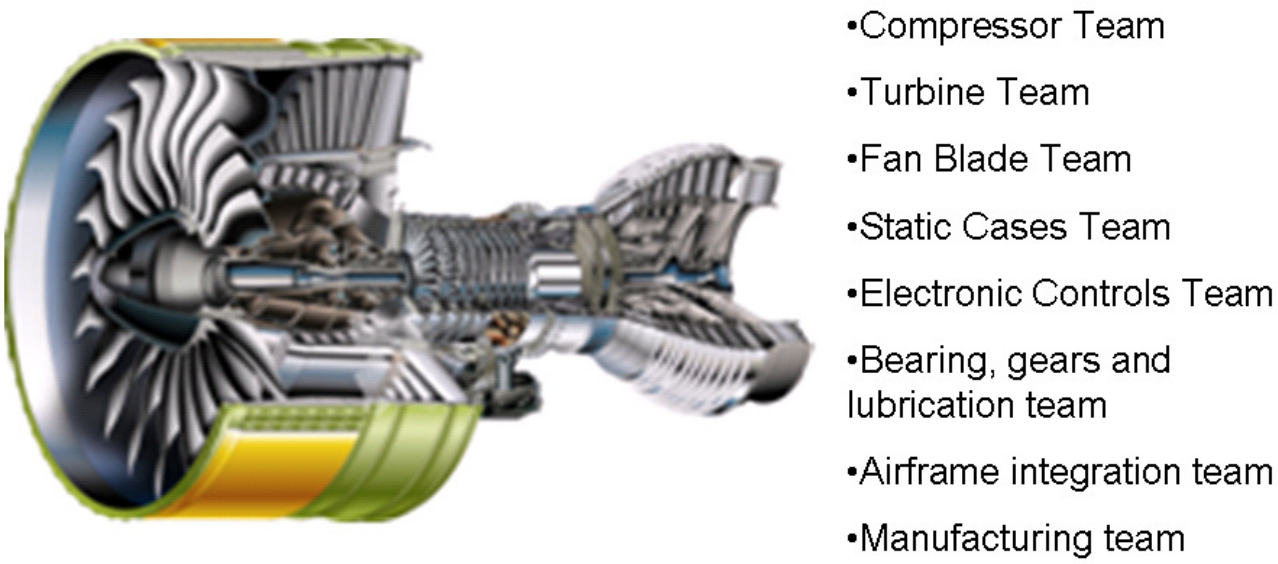

Figure 1.11 Teamwork is used to tackle the development and validation phases. [23]

Each team is in turn split into sub-teams. The amount of interaction between teams to meet all design constraints is simply mind boggling. From a structural mechanics point of view each component has major design constraints such as high cycle fatigue, resonance, low cycle fatigue (due to thermal transient stresses), static case stiffness, and thermal distortion. An example component is shown in Figure 1.12.

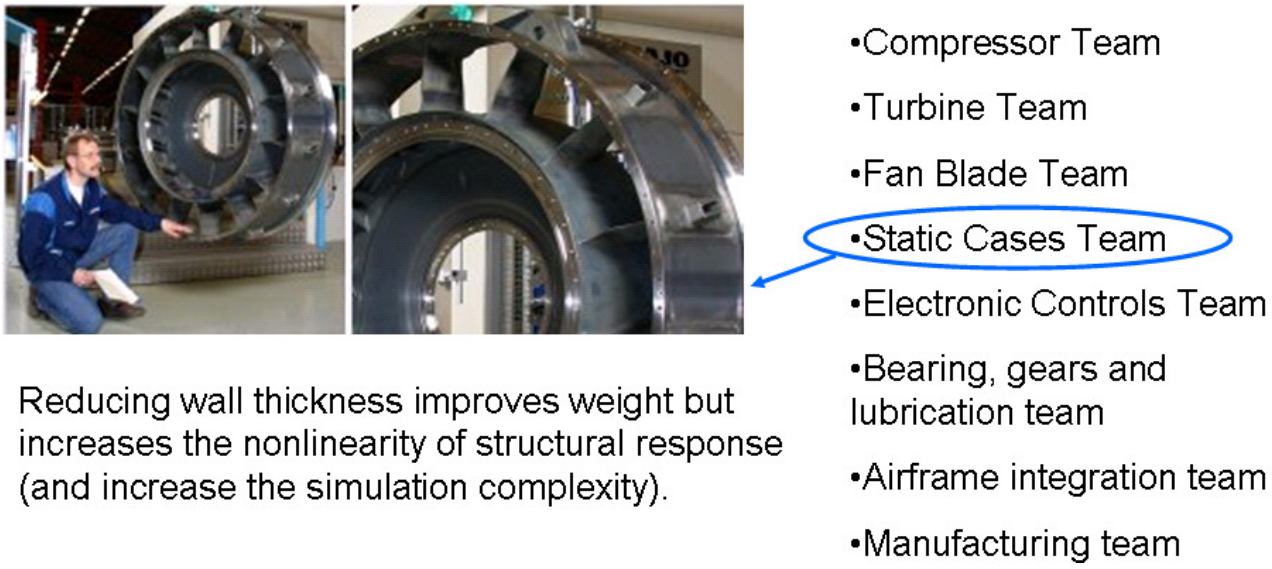

Figure 1.12 Designing a lightweight component with many constraints. [32]

1.6.2 Prediction of Ultimate Loads used to design a Component

An important design constraint is the ultimate load for any particular part. The ultimate loads are often derived from the Fan Blade Off loading condition. Further, these loads are predicted using FEA simulation. Example ultimate loads on an individual component are shown in Figure 1.13.

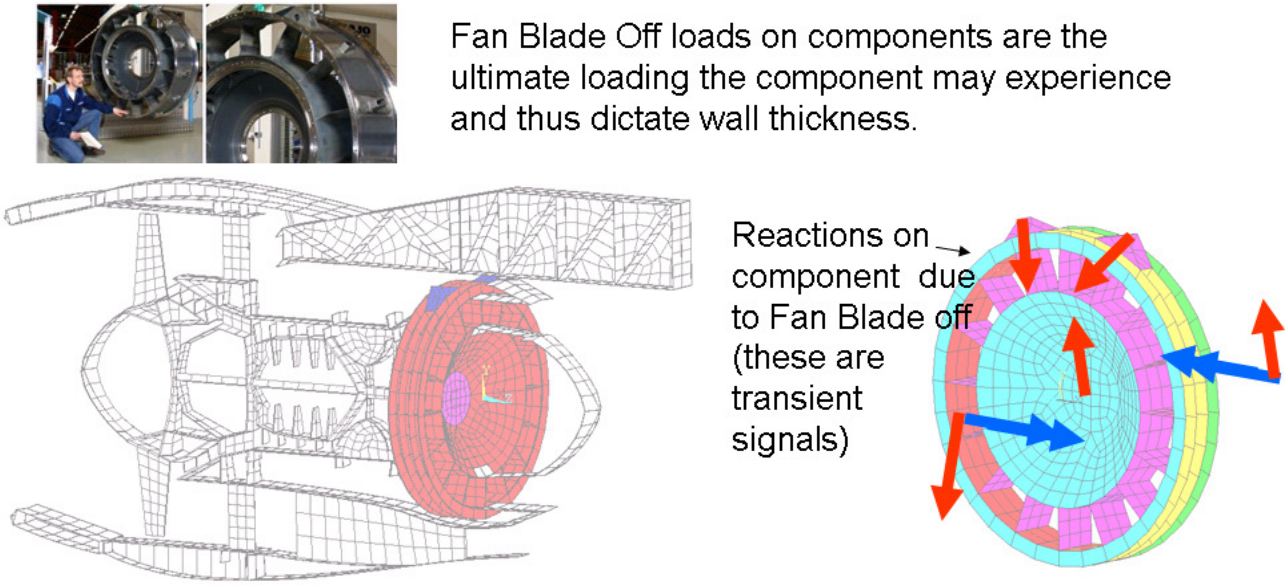

Figure 1.13 Component thicknesses are usually determined by ultimate loads. [32]

In most instances, removing weight from engines is accomplished by decreasing wall thickness of components; however, as a consequence, this wall thickness reduction leads to a higher degree of nonlinearity in the response (elastic-plastic yielding, wrinkling, etc.).

Since the ultimate load is often dictated by the fan blade out loading condition, the fan blade out loads ultimately controls the size (usually by adding extra thickness) of many large diameter cases throughout the engine (and thus has a big impact on the total weight). Improving FBO prediction is the primary modeling focus of this work.

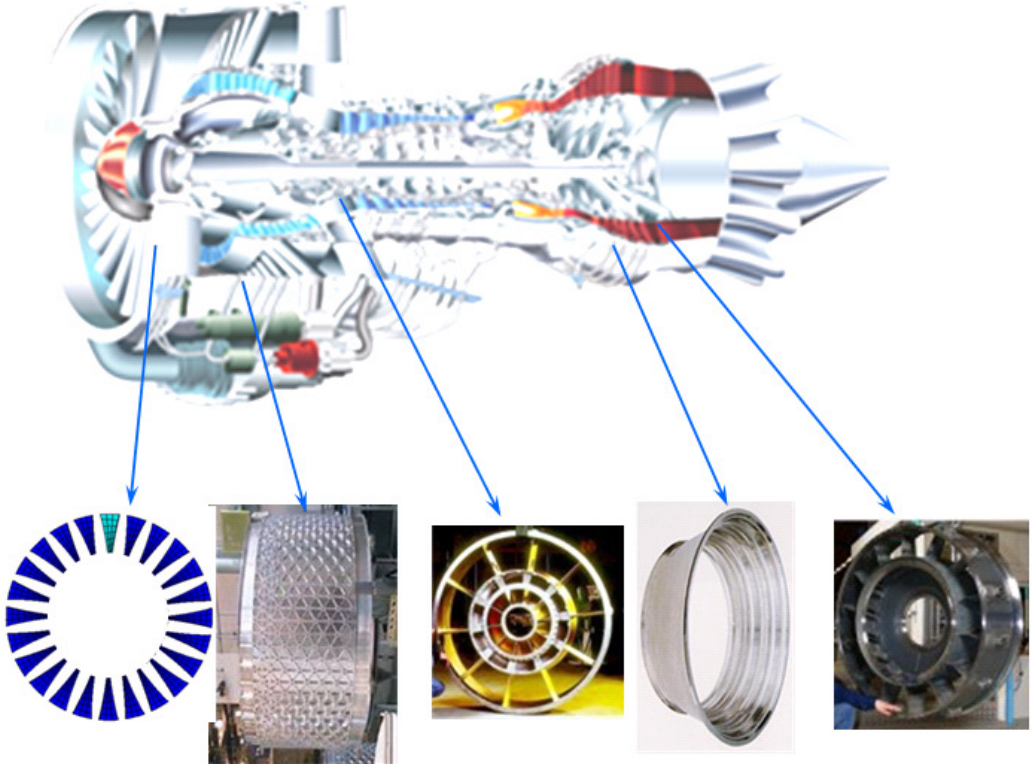

Figure 1.14 Example of large diameter, long manufacturing lead time parts. [32]

FBO loading controls the design of large diameter, long manufacturing lead time parts. These parts tend to be expensive and their designs must be 'locked in' early (not easily changeable) in the engine design cycle in order to be manufactured on time. Passing the FBO test then requires either fast and accurate FBO simulation or a very conservative design approach. Currently there are two methods (both LS-Dyna modeling of fan blade impact and NASTRAN modeling of engine rotor imbalance) being developed to predict FBO loads in components. The range of applicability of these methods is summarized in Figure 1.15.

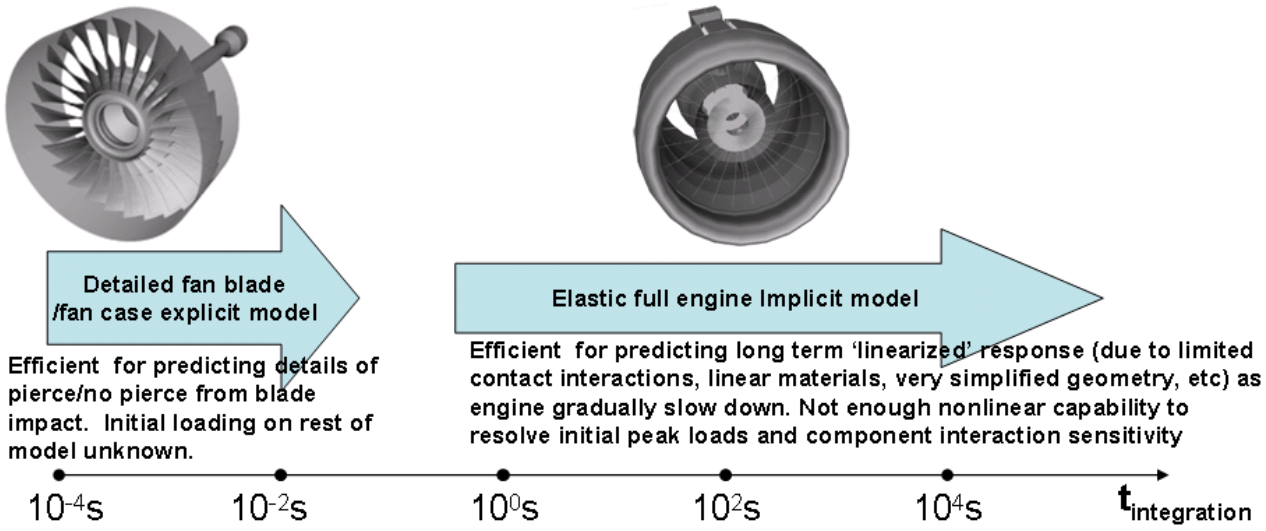

Figure 1.15 Explicit impact model and implicit unbalance model. [27]

The explicit fan case/fan blade model works very well for developing a short duration pierce or no-pierce prediction during impact. However, the impact loads are not transferred to the rest of the engine (because it is not modeled) and this important interaction is indeterminate. The reason for the short duration of applicability on Figure 1.15 for explicit is the high fidelity mesh (bricks instead of shells) and small timestep size required to track the contact and sliding with potential for material ablation and piercing.

On the other hand, the simplified implicit full engine model, solved for long durations, can predict important responses like resonance (the unbalanced shaft rotational speed is slowing and may eventually excite a resonant response, for example). The Newmark integration scheme allows for larger timesteps but implicit contact/impact technology limits the resolution of the FEA mesh (note, for example, how the fan blades are modeled coarsely as beam elements). Because of these simplifications this implicit model may not be best suited to predict peak FBO loadings where, for example, localized yielding in some components may occur or nonlinear component interactions during the critical revolutions following impact. The reduced meshing and contact fidelity for implicit on Figure 1.15 resulted in a 1-second-and-above range of applicability.

1.6.3 Example of Structural coupling during FBO

An example of component interaction (or coupled structural response) is developed from Figure 1.16. Suppose the turbine case designers wish to predict the severity of turbine blade tip rubbing during FBO. Will FBO loading distort the cases, inducing fracture of ALL the rotating turbine blades, causing a fire and engine debris to be ejected? This example is not contrived and is a typical question in design of engines.

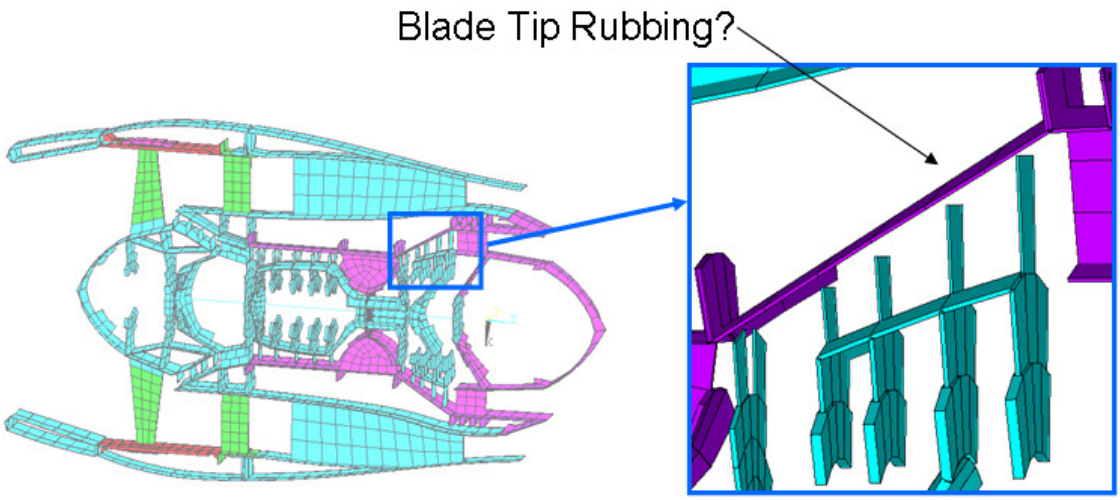

Figure 1.16 Severe blade tip rubbing of the low pressure turbine? Yes or No?

Analytically predicting blade tip rubbing is not trivial; however, it seems reasonable to assume that maintaining roundness (primarily elastic distortions rather than elastic plastic collapse) in the two adjacent cases in Figure 1.17 would be a good start to prevent tip rubbing. Unfortunately, cases with small distortions tend to be thick walled and heavy. The case teams then try to reduce thickness (weight) of a particular component based on the ultimate load predicted for that particular component. When designing within the elastic range the adjacent component interaction is often small and follows a linear trend. However, as the components become thin, their response (due to localized elastic-plastic behavior with elastic wrinkling of panels, for example) can create abrupt structural nonlinearities, which makes analyzing the two cases independently inefficient due to the strong coupling of structural response. It is more efficient to optimize the components together as a system.

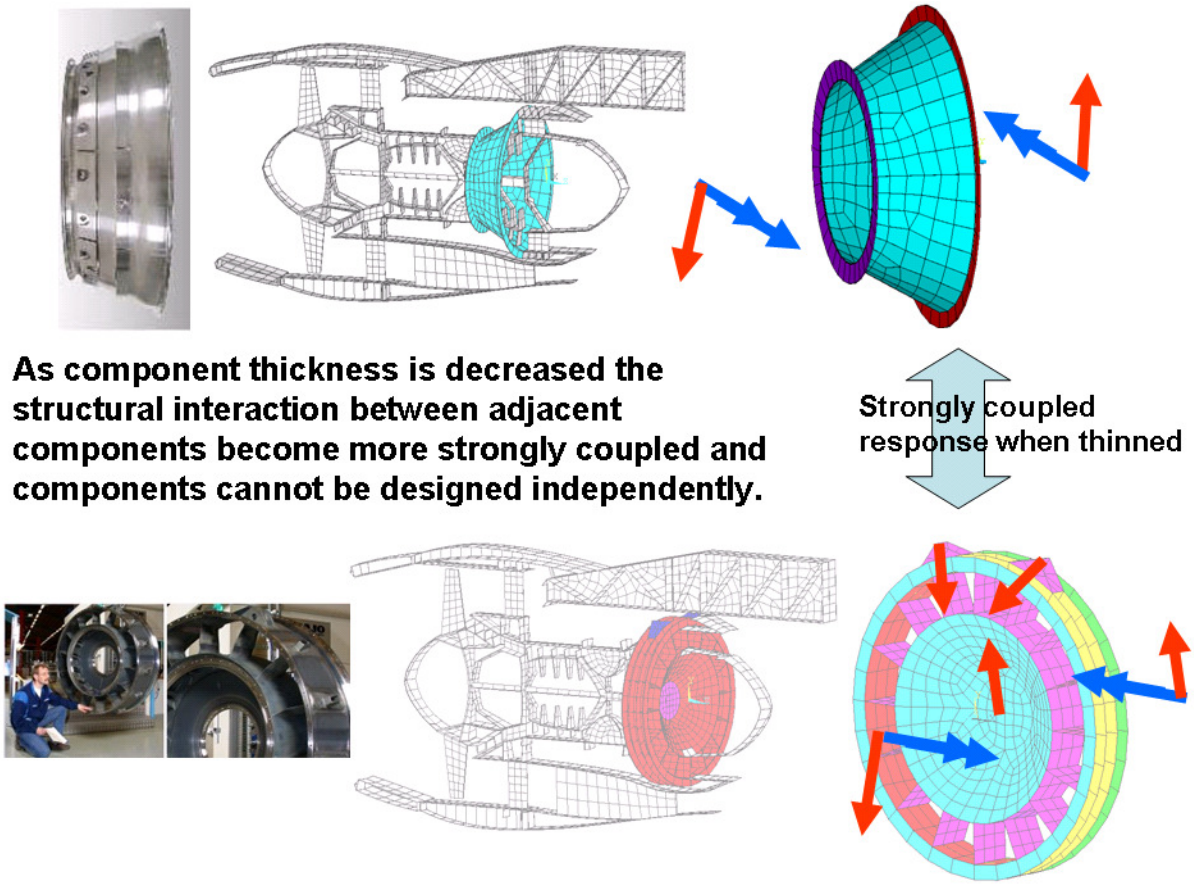

Figure 1.17 Structural coupling when components are thinned [32]

1.6.4 Development of a Baseline Model

The baseline model (the focus of this thesis) will be developed to provide a robust nonlinear methodology that can predict changes of FBO response (globally) as part teams update and optimize individual components throughout the engine. The baseline model complements the current methodologies by filling capability gaps as shown in Figure 1.18.

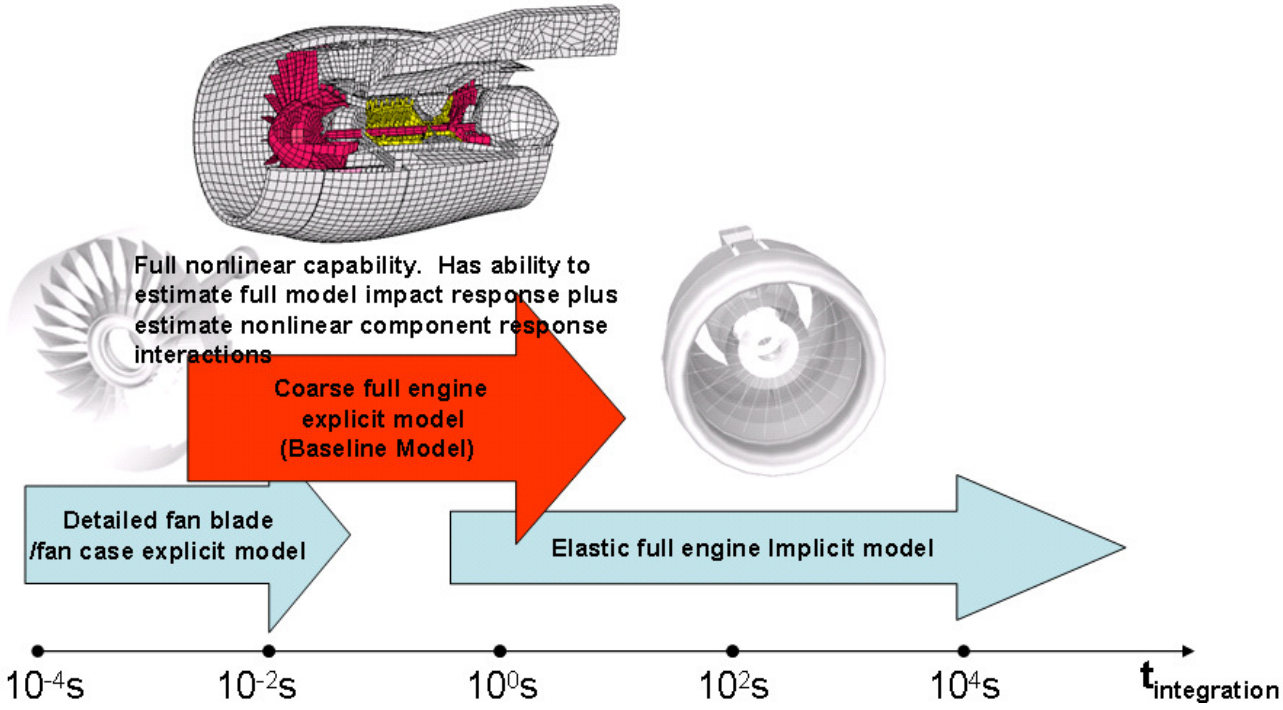

Figure 1.18 Filling the gap in analytical methodology [27]

It is clear that baseline model cannot predict long duration response, nor does it have the mesh resolution to predict detailed fan blade impact calculations. However, the baseline model is designed to obtain a unified FBO response (interacting/coupled) across all engine components for both impact and imbalance modeling; this makes it particularly useful for in the concept development, development and validation phases of Figure 1.10. Earlier and/or more accurate FBO predictions at these stages can result in lower engine weights.

1.7 Scope of Research

The focus of this work is to develop an efficient finite element simulation of the fan blade off event using explicit finite element methods. The scope includes:

1. Developing an entire system model to study rig test Fan blade off of a high bypass turbofan engine. Note that a system model contains all parts and is used to overall study model interaction. This is opposed to component level modeling, such as a more detailed fan-blade/fan-casing model (basically ignoring the rest of the engine) used, for example, to optimize the impact absorption of a particular isogrid pattern.
2. Developing a realistic generic model (baseline model) in LS-Dyna to simulate the basic physics of the FBO rig test. This will include simplified geometry of all major components, typical rotor speeds and thicknesses calibrated such that materials are loaded close to yield strength. LS-Dyna default setting will be used unless specifically changed.
3. Optimizing the model and solution procedures for fast execution.
4. Validating the model to by performing appropriate benchmark tests and examining the sensitivity of the model to various parameters.
5. Optimizing the LS-Dyna default settings (contact, constitutive models, time step size, etc.) to improve default speed or accuracy of the simulation.
6. Examine the baseline model sensitivity to understand the effect of ignoring important physics such as friction, plasticity, and etcetera.

1.8 Using Public Domain Data to build a Generic Model

Unlike academia, major aero engine manufacturers such as Rolls-Royce, General Electric and Pratt & Whitney, as well as airframe manufacturers such as Goodrich, Boeing and Airbus, restrict almost all engine test data and keep analysis methodologies proprietary and confidential i.e. it is not published. However, public domain sources (internet and the literature) provide enough bits and pieces to get 'ballpark' or typical estimates of geometry, materials, temperatures, and rotor speeds. The generic baseline model built in this thesis uses these typical values.

The author is appreciative of the above companies for graciously providing images and data on their websites, published papers or public domain data. Without these sources, this academic work would not be possible. Also is should be emphasized that none of the results or conclusions of this academic modeling study have any correlation or connection to the safety or airworthiness of any of the above mentioned companies.

Images from the following organizations were used.

- Boeing
- General Electric
- Airbus
- Goodrich
- Pratt and Whitney
- Rolls-Royce
- Federal Aviation Administration
- NASA
- United State Air Force
- Lawrence Livermore National Laboratories
- Honeywell
- Volvo

2 Modeling Issues and Requirements

This chapter gives the reader further background into jet engine operation and explores some of the physics involved with the fan blade off event. The current literature is surveyed to give an understanding of how researchers are approaching this problem. This is followed by a comparison of the pros and cons of using implicit versus explicit finite element procedures to solve the FBO event.

2.1 Jet Engine Operation

Many aero engine configurations exist; for brevity two familiar types of jet engines are shown in Figure 2.1. In all turbines engines air is compressed by a rotary compressor, fuel is added to the compressed air and combusted, and the expanding hot gases drive the turbines. In turbojets (primarily military engines) the majority of intake air passes through the engine core. In the turbofan (primarily commercial) the intake flow splits between fan bypass and the engine core.

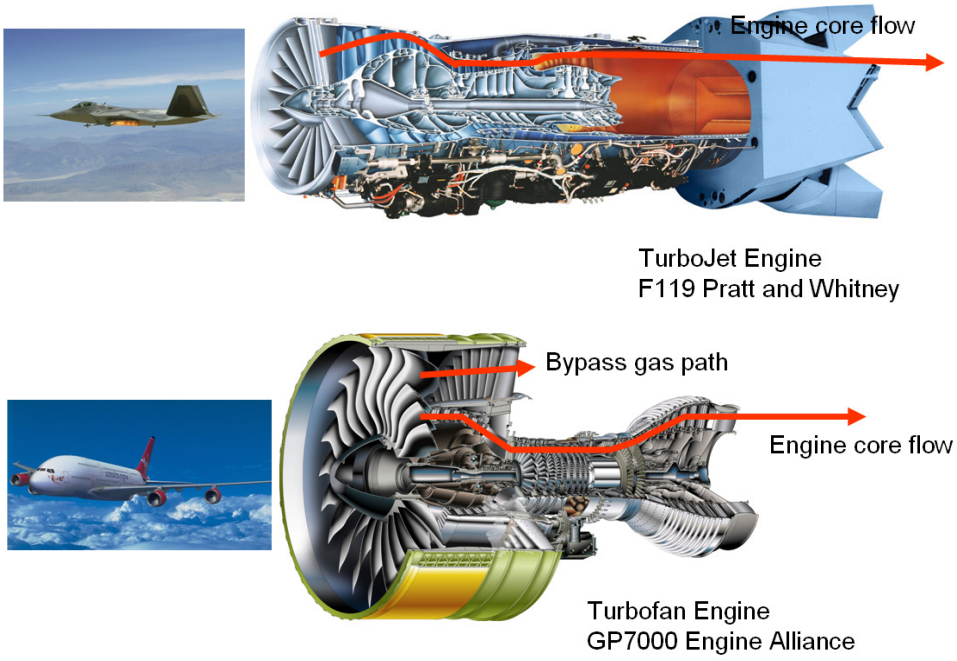

Figure 2.1 Gas flow through a military (turbojet) and commercial (turbofan) engine. [23,29,31]

For this research, the analytical methods developed to model blade out will be applicable to various engine configurations: however, in order to limit the scope, a high bypass turbofan engine configuration was chosen for modeling. Selected physics are discussed to gain insight into appropriate mathematical modeling of the fan blade off event.

2.1.1 Flowpath though High Bypass Turbofan Engine

A high bypass turbofan engine was shown in Figure 2.1. Complicating things further, some auxiliary aero control surfaces (often called a nacelle) are added to the engine to greatly increase its efficiency. The nacelle components surrounding the engine are shown in Figure 2.2.

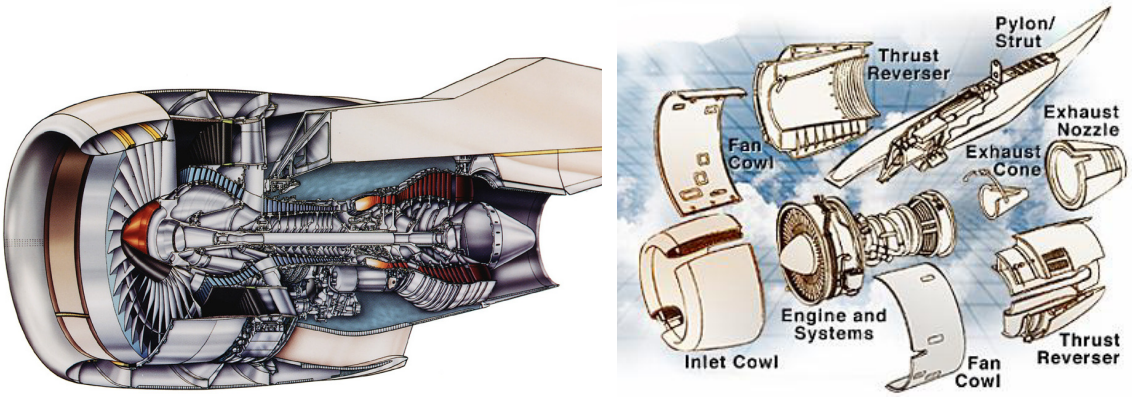

Figure 2.2 Nacelle components surrounding engine. [23,28]

The bypass and core flowpaths are explained through the Figure 2.3. The turbofan drives the cooler bypass flow moving a large volume of air with a small change of momentum; the remainder of the flow passes through the much hotter core. Note that these flowpaths are provided to convey a basic understanding of high bypass turbofan operation and no CFD was attempted.

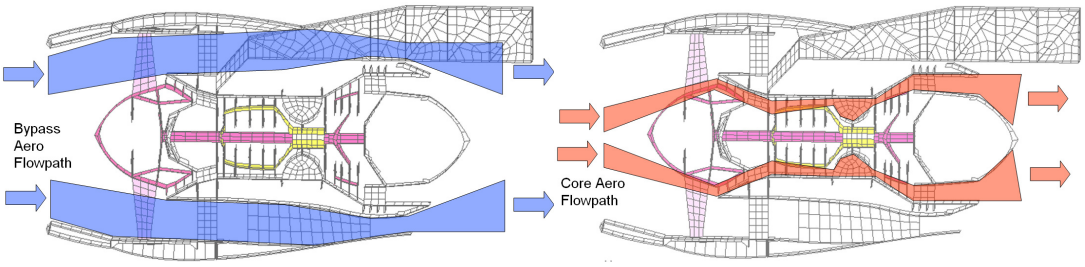

Figure 2.3 Bypass and core aero flows though high bypass turbofan.

2.1.2 Turbofan Temperatures and Pressures

Figure 2.4 below shows typical temperatures and pressures in the core gas path. Note that 1 ATM is about 14.7 psi. For simplicity it was decided to ignore pressure distributions in the baseline model. The baseline model material properties were selected to correspond to expected metal temperatures during operation.

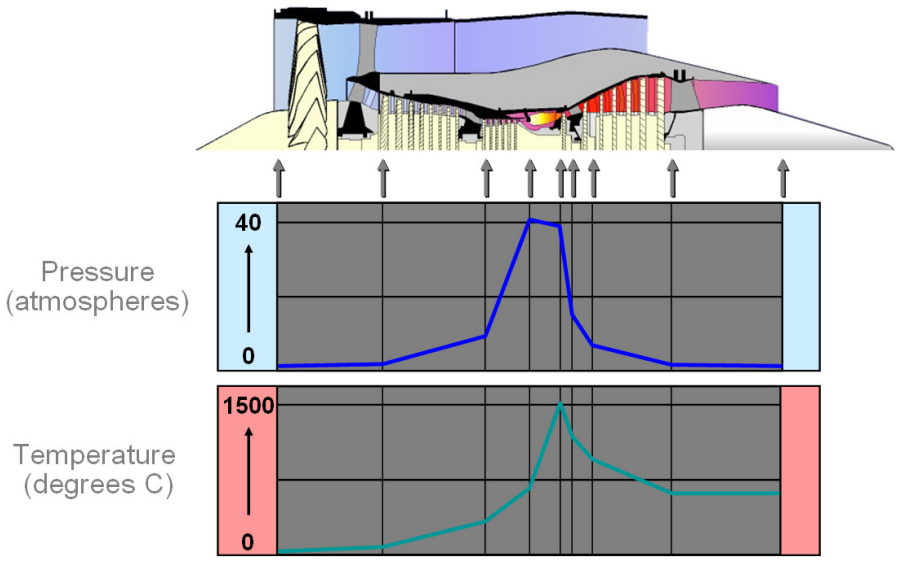

Figure 2.4 Temperatures and pressure along core flow-path. [25]

2.1.3 Turbofan Kinematics

Figure 2.5 below demonstrates the basic kinematics of a high bypass turbofan engine.

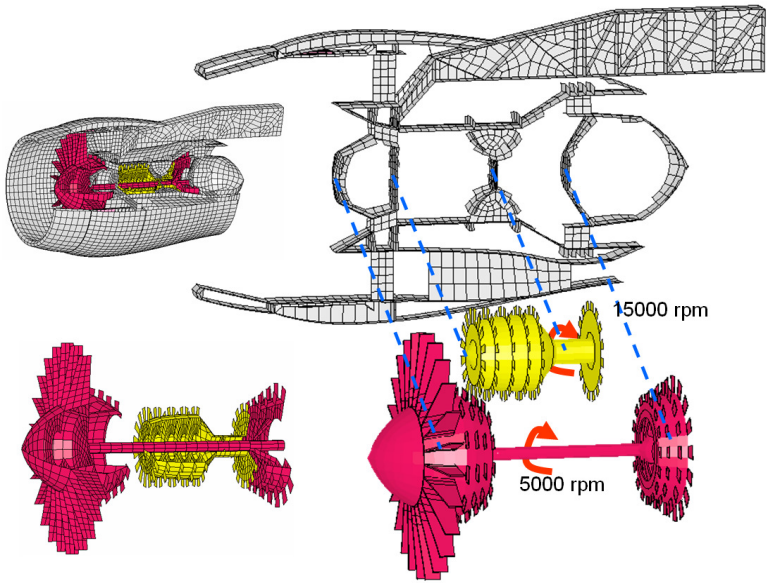

Figure 2.5 Turbofan Kinematics. Cases (grey), low rotor (red) and high rotor (yellow)

The low speed rotor (red) is mounted to the cases via bearings as shown. The high speed rotor (also called the core)(yellow) is mounted to the cases via bearings as shown. Note that the shaft of the high speed fan straddles the low speed rotor and that they run at different speeds. The mesh will be discussed thoroughly in the next chapter.

A core typically has a maximum speed in the order of 15,000 rpm; this value will be used. The low speed rotor (also called the fan rotor or fan shaft) also is mounted to the cases via bearings as shown. A fan shaft typically has a maximum speed in the order of 5,000 rpm; this value will be used.

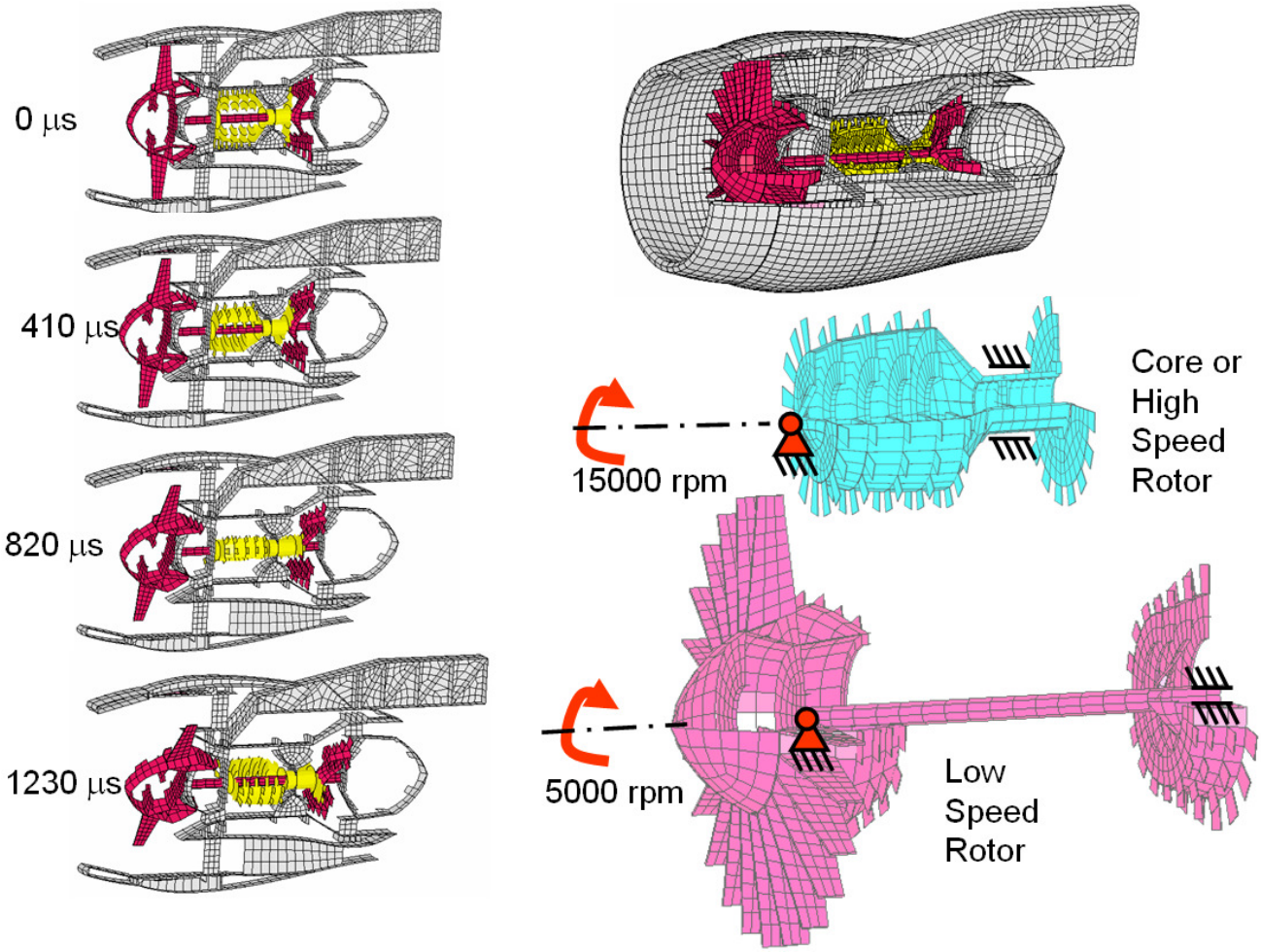

Figure 2.6 Turbofan Kinematics. Rotors rotate at different speeds

2.2 Current Literature: Analytical Approach to Fan Blade Off

As mentioned before in Chapter 1, a released fan blade contains a huge amount of kinetic energy plus it creates a large unbalanced transient force. Current analytical modeling (summarized in Chapter 1) of the fan blade off treats these two effects separately and focuses on either:

1. LS-Dyna fan blade/case models to simulate the blade impact energy absorptions i.e. an explicit approach
2. full engine rotor/case models to study the unbalanced interaction transient response i.e. an implicit approach using NASTRAN. A summary was described in Section 1.5.

These two types of FEA models are shown in Figure 2.7.

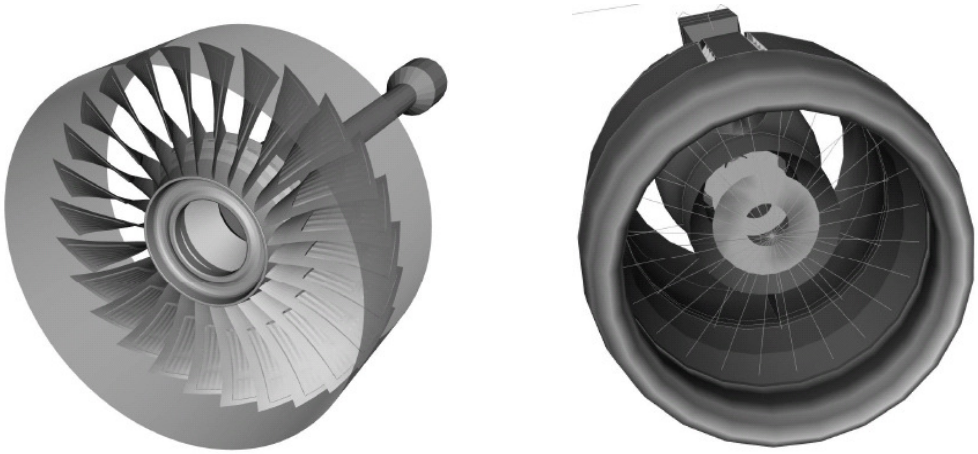

Figure 2.7 Explicit Model (left) and Implicit System Model (right). [26]

An overview of the current literature will be surveyed in the following sections.

2.2.1 Modeling Fan Case Response to Blade Impact

For blade impact, industry appears to currently favor an aluminum isogrid wrapped with composites. An example of the aluminum isogrid is shown below in Figure 2.8; the composite wrap (yellow band around fan case) or belt is also shown.

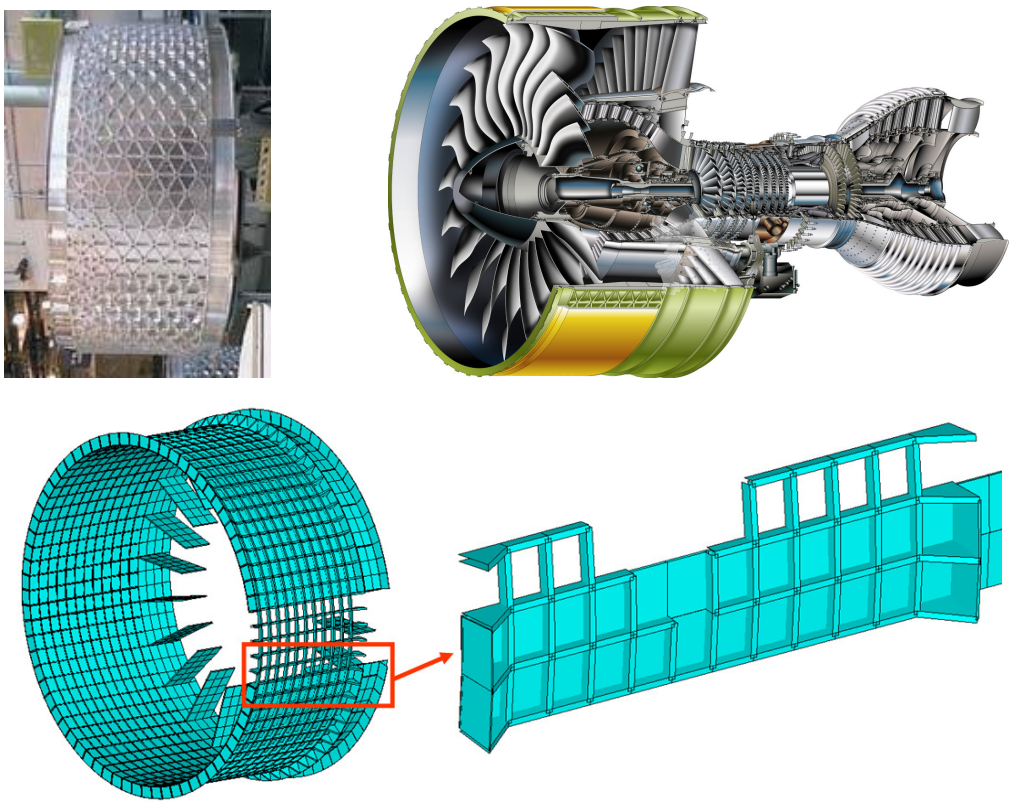

Figure 2.8 Fan case made of Aluminum Isogrid. [23]

There are variety of recent papers on high speed fabric impact tests versus simulation to calibrate fabric material models and fiber wrap modeling methodologies. Some image excerpts from these papers are shown. Explicit integration FEA codes (LS-Dyna is very popular) are used almost exclusively and the modeling domain focuses on the fan blades / fan case. This is typically a very short duration simulation to predict containment of the blade's energy.

Note that these papers are cited as references for the purpose of familiarizing the reader with current blade containment publications and research. The images in Figure 2.9 through Figure 2.14 are from papers [10,11,12,13,14,15].

Figure 5. Ballistic Test Set-up for Halfcase.

Figure 6. Titanium Blade Projectile and Sabot.

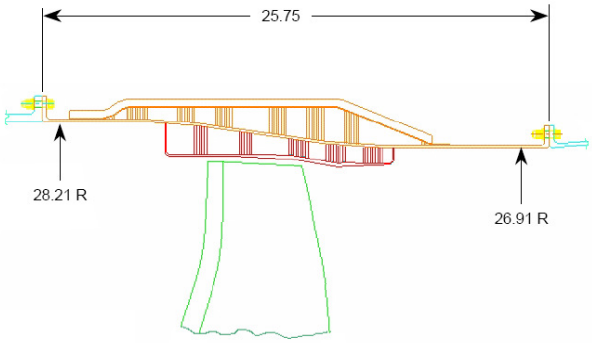

Figure 3. Prototype "Softwall" Fan Case.

Figure 2.9 Testing and Simulation Calibration for Blade Strike on Fabric [10]

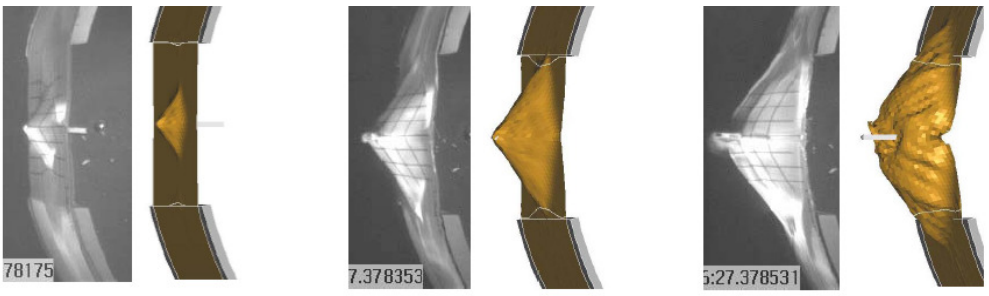

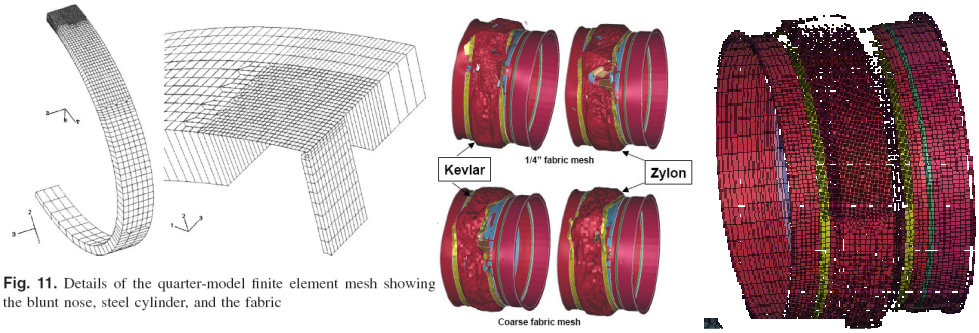

Fig. 11. Details of the quarter-model finite element mesh showing the blunt nose, steel cylinder, and the fabric

Figure 2.10 Testing and Simulation Calibration for Blade Strike on Fabric [11]

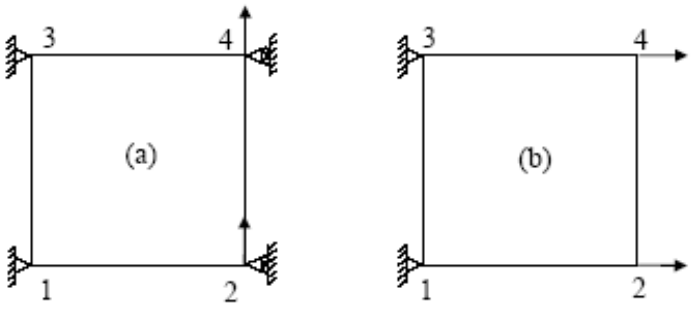

Figure 3.—Boundary and loading conditions for single element (a) shear and (b) tension finite element analyses

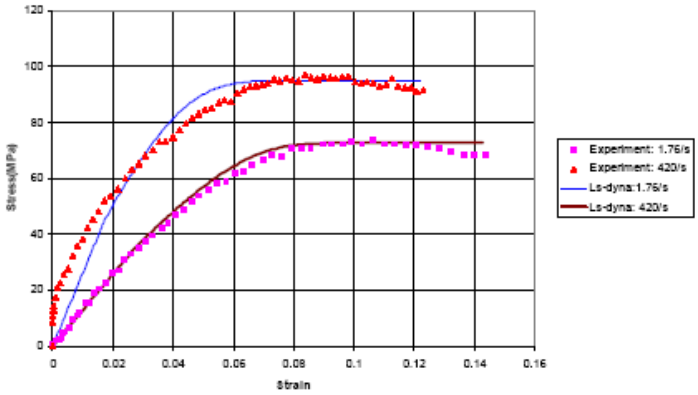

Figure 4.—Experimental and LS-DYNA simulated shear stress-shear strain curves for PR520 resin at strain rates of 1.76 /sec and 420 /sec

Figure 2.11 Development of constitutive models of fabrics [12]

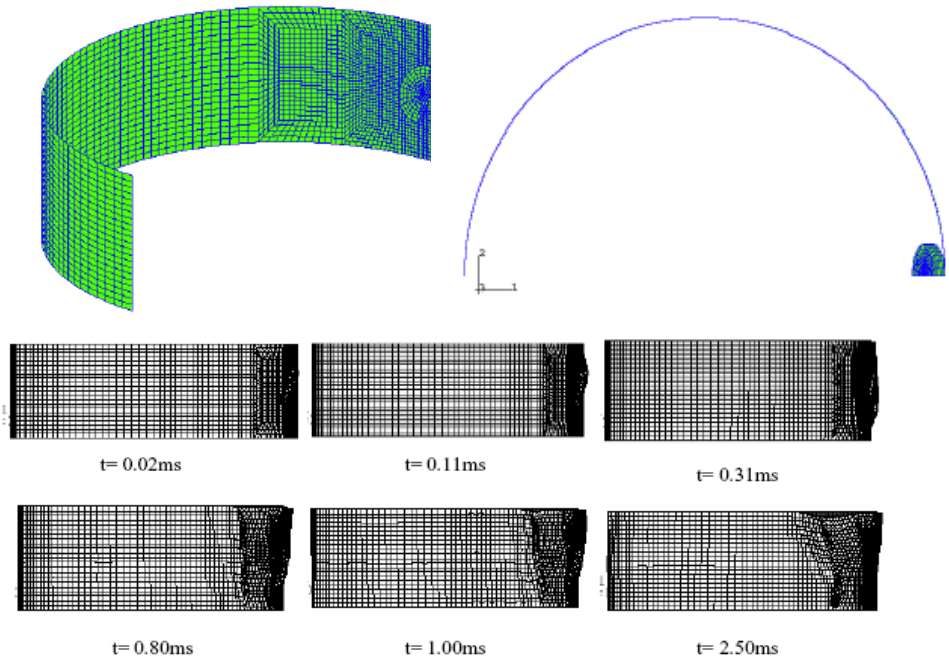

Figure 7. Deformation of 36" full-ring subcomponent at various times after impact.

Figure 2.12 Testing and Simulation Calibration for Blade Strike on Fabric [14]

NASA's website showcases computational models being developed to study of fan-blade/case interactions.

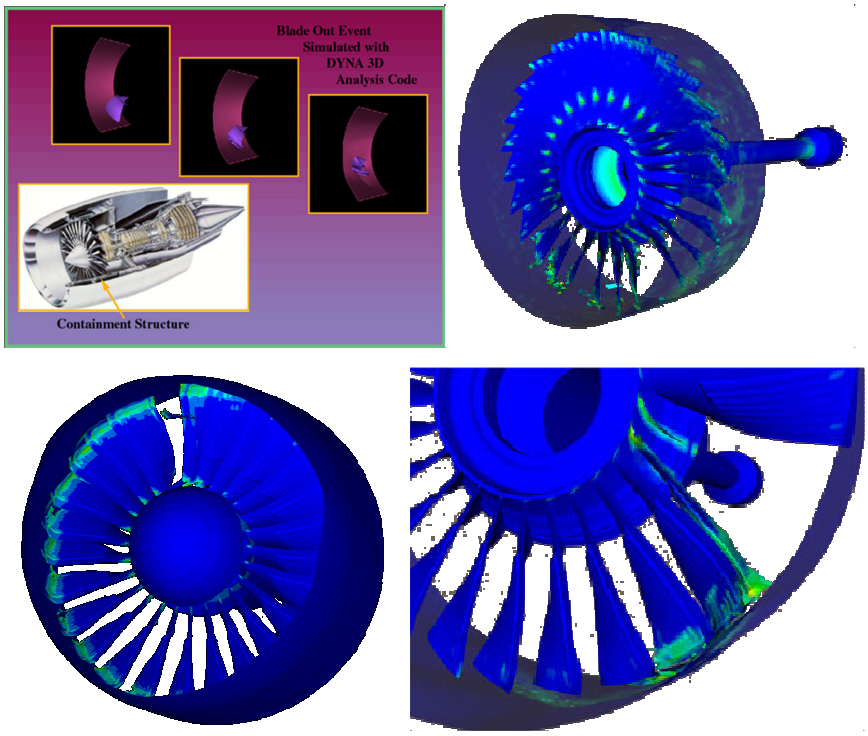

Figure 2.13 Fan Blade/Fan Case interaction Models [13]

Figure 2.14 shows a fan blade/case model to optimize energy absorption of fan blade impact. Note the limited domain of the finite element model i.e. only the front end of the engine is modeled.

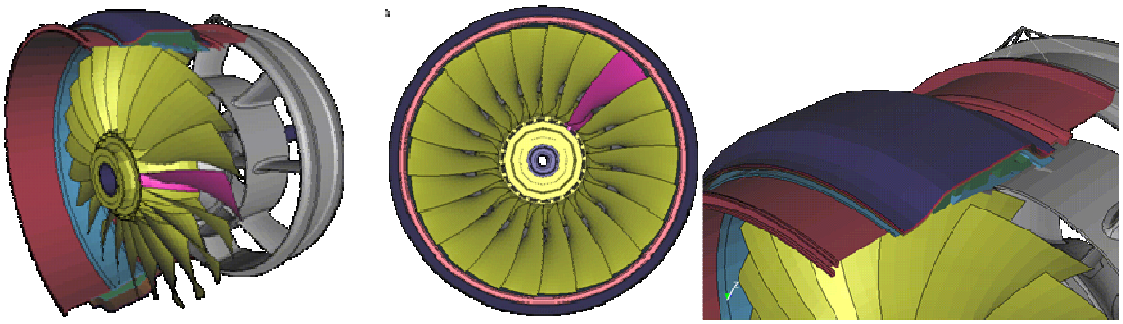

Figure 2.14 Fan Blade/Fan Case interaction Models [15]

2.2.2 Modeling Rotating Imbalance

It should be expected by the reader that solving the fan blade containment problem with an implicit code is very difficult due the highly nonlinear behavior of the system. As predicted, a review of the current state of implicit-based full engine FBO modeling shows a host of difficulties.

Some NASTRAN-based (implicit) full engine models are shown below [16,17]. As summarized in Section 1.5 the full engine FBO models are built in NASTRAN along with FBO methodologies implemented by an industry/government team led by NASA scientists Carney and Lawrence. Representative FEA meshes used for this type of full engine modeling are shown in Figure 2.15.

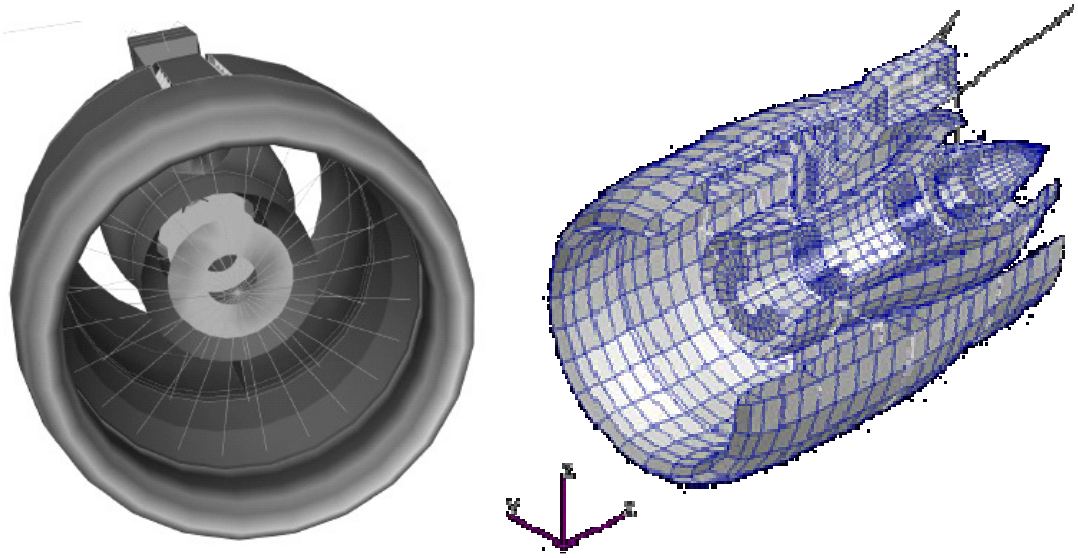

Figure 2.15 Finite element mesh in full engine model. [26]

Note the overall coarseness of the mesh; in particular note the beam elements used to represent fan blades and rotors.

Figure 2.16 shows some current techniques in NASTRAN for including rotating blade tip rubs (contact modeling). The models are beam/spring models and are very, very coarse (<50 element model). The reader should note that even with an almost trivial model, the fan case flexibility was not included in this contact study due to limitations on contact modeling capability; this indicates just how difficult this class of problem really is for an implicit FE code.

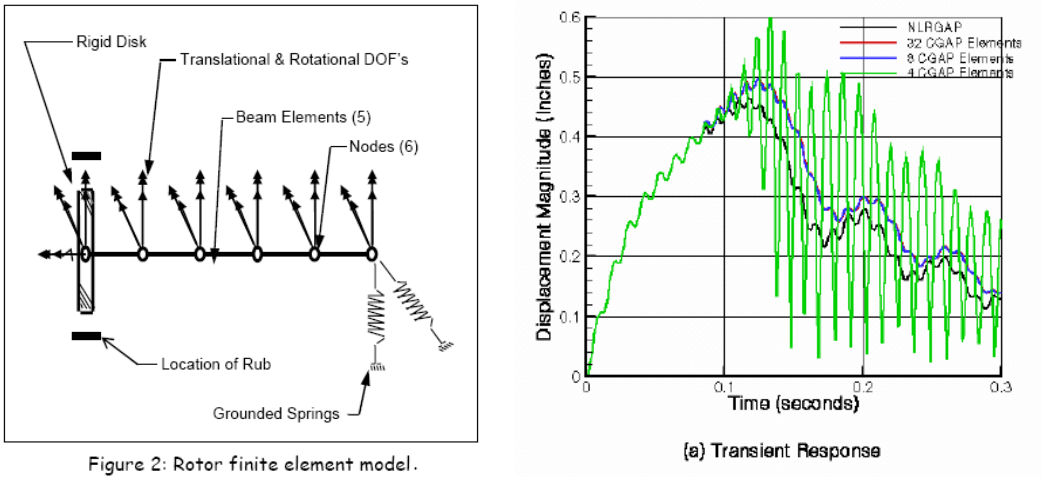

Figure 2.16 Five element NASTRAN Fan Blade/Fan Case interaction model [16]

Figure 2.17 highlights the final result of involved matrix derivations to include the effects of an unbalanced rotor and gyroscopic effects due to a released blade. The details are not useful to this work but the giant equation (implemented by modifying system matrices) are included to give the reader a flavor of the enormous complications involved with using implicit solution. Conversely, these effects are included in a very natural, straight forward method[1] in the LS-Dyna based explicit method proposed in this thesis.

$$\begin{bmatrix} \frac{I_p+\varepsilon^2 m}{2}+\frac{\varepsilon^2 m}{2}\cos 2\bar{\psi} & 0 \\ 0 & \frac{I_p+\varepsilon^2 m}{2}-\frac{\varepsilon^2 m}{2}\cos 2\bar{\psi} \end{bmatrix} \begin{Bmatrix} \ddot{\alpha} \\ \ddot{\theta} \end{Bmatrix}$$
$$+\left\{ \begin{bmatrix} 0 & -2\left(\frac{I_p+\varepsilon^2 m}{2}+\frac{\varepsilon^2 m}{2}\cos 2\bar{\psi}\right)\dot{\bar{\psi}} \\ 2\left(\frac{I_p+\varepsilon^2 m}{2}+\frac{\varepsilon^2 m}{2}\cos 2\bar{\psi}\right)\dot{\bar{\psi}} & 0 \end{bmatrix} + \begin{bmatrix} C_{\alpha\alpha} & C_{\alpha\theta} \\ C_{\theta\alpha} & C_{\theta\theta} \end{bmatrix} \right\} \begin{Bmatrix} \dot{\alpha} \\ \dot{\theta} \end{Bmatrix} \quad (5)$$
$$+\left\{ \begin{bmatrix} 0 & -I_\varepsilon \ddot{\bar{\psi}} \\ I_\varepsilon \ddot{\bar{\psi}} & 0 \end{bmatrix} + \begin{bmatrix} K_{\alpha\alpha} & K_{\alpha\theta} \\ K_{\theta\alpha} & K_{\theta\theta} \end{bmatrix} \right\} \begin{Bmatrix} \alpha \\ \theta \end{Bmatrix} = \begin{Bmatrix} F_\alpha \\ F_\theta \end{Bmatrix}$$

Figure 2.17 First order gyroscopic effects for an unbalanced rotor[17]

[1] This is done by using a bonded contact definition to constrain the fan blade to the rotor at the root. This definition is then deleted at time t, which effectively creates an impact along with an unbalanced rotor.

A full engine model (with beam elements for the fan blades) is shown in Figure 2.18. This full engine model is being used to develop FBO loads for the design of all engine components.

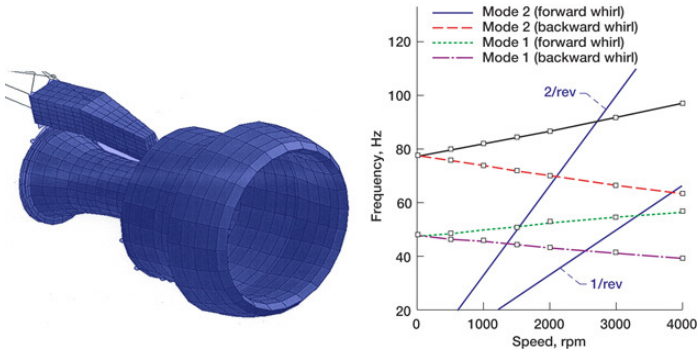

Figure 2.18 Full engine model for NASTRAN [8]

The timestep size for the FBO containment problem and the integration method used in NASTRAN are important and will be discussed in later sections.

Some notable highlights extracted[2] from these NASTRAN [16,17] papers are summarized in Table 2.1 below. These highlights give the reader some ideas of the methods and difficulties faced by researchers attempting to solve this class of problem (full engine FBO) using implicit methods. This table will be revisited after the explicit approach has been further outlined.

Table 2.1 Some notable highlights from implicit-based FBO papers

1	5% damping at 60 Hz
2	the rotor speed is prescribed i.e. rotor speed is a problem input
3	4 μs integration timestep size
4	Reported radial displacement amplitudes (due to resonance) in the order of 35" (~1000mm)
5	beam model rotors, with lumped mass approximations to mimic unbalance, are implemented
6	Derivation of skew symmetric 'plowing' forces (applied to the end of a beam element) to artificially induce an axial force component during tip rubbing. (due to blade 3D geometry with chord angle)
7	case flexibility ignored or difficult to include
8	tip rubbing study highly influenced by damping coefficient as well as large displacement
9	Complicated gyroscopic derivations with a host of assumptions

Overall, these teams are providing well written, well documented, innovative solutions in attempting to solve this class of problem (full engine model FBO) with implicit tools; however, the author believes, based on years of industry experience with both implicit and explicit tools, that the required integration timestep size and the computational cost per timestep for this class of problem are not compatible/amenable to an implicit strategy. The author's belief is that implicit-based FEA tools cannot include the physics required to tackle full engine FBO modeling with a target of obtaining fast and accurate component-by-component loads for design teams. This table will be revisited in later sections.

[2] The papers were not studied in detail due to the large strategic differences between implicit and explicit integration approach. However, a good faith effort was used to extract some of the basic ideas of the difficulties researchers using implicit codes are facing.

2.3 Computational Challenges for FEA Modeling

During a turbofan blade out there are many physical phenomena that are nonlinear from a computational mechanics viewpoint. These phenomena may affect significantly the simulation of either the blade impact or the rotating unbalance or both. Some of these are listed below.

Blade impact/energy absorption FEA modeling might consider:

1. steady state pre-stresses in rotors
2. aerodynamic forces
3. finite rotations and translations (versus infinitesimal)
4. impact/contact of fan blades to case
5. impact/contact of fan blade to fan blade
6. elasto-plastic response of metals
7. failure criteria for metals
8. strain rate effects on yield strength for metals
9. fiber wrap/isogrid casing interaction
10. elastic/inelastic orthotropic/anisotropic material response of fabric wrap
11. contact/impact interaction of case with adjacent components
12. friction/rubbing interaction of rotor blade tips with case
13. gyroscopic effects from spinning rotors
14. model grid size and mesh connectivity for multiple components

Rotating Imbalance modeling might consider:

1. residual transient shock/vibrations from the blade impact in the fan case
2. transient dynamics of rotors with finite rotations and translations (versus infinitesimal)
3. transient dynamics in cases
4. case/rotor interactions at bearings
5. gyroscopic effects from spinning rotors attached to deformable cases
6. case/rotor interactions through friction/rubbing
7. nonlinear response of rotors/cases to large magnitude cyclic loads (buckling, elastic-plastic yielding or large deformations)
8. aerodynamic drag on rotors
9. model grid size and mesh connectivity for multiple components

Each of the above problems poses certain, usually different, simulation challenges. In particular, some of them may be better suited to implicit finite element strategies and some by explicit finite element strategies. In order to better understand the simulation challenges and to help in selecting an efficient method for a particular problem (in this case the FBO containment problem) the main differences between implicit and explicit will be compared.

2.4 An Overview of Implicit and Explicit Integration in FEA

For the FBO problem, a choice must be made between either explicit or implicit based integration. Thorough discussion of both implicit and explicit integration finite element solution methods can be found in the literature [4] [19]. For FBO modeling purposes, a brief review of the mathematical differences between implicit and explicit is provided in the following sections. In particular, it is intended to show the important role the integration timestep size (or integration time increment), Δt, plays and how it determines efficient solution of the blade containment problem.

The purpose of numerical integration in computational mechanics of solids[3] in all finite element solutions is to track a particle's position X_1 (X at time t_1) to position X_2 (X at time t_2) as shown below.

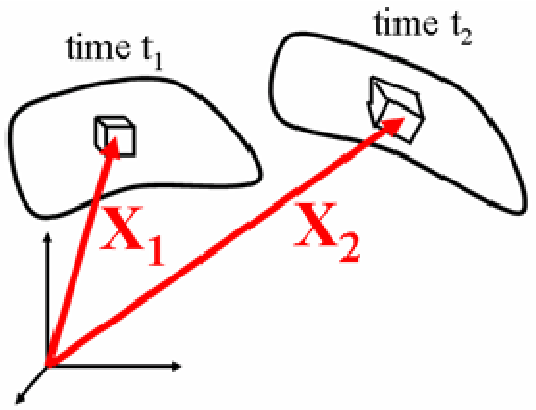

Figure 2.19 Tracking the position of a deformable particle

At all times the dynamic equilibrium equation (or the kinetics) for an infinitesimal portion of the body indicated in Figure 2.19 must be satisfied. The typical form of this equation is:

$$\frac{d\sigma_{ij}}{dx_j} + f_i = \rho \ddot{d}_i \qquad (2.1)$$

The three equations (i=1,2,3) in (2.1) involve the spatial derivatives of six components of the stress tensor $\boldsymbol{\sigma}_{ij}$, three components of acceleration $\ddot{d}_i$ (or the time derivatives of the displacement vector usually defined as $d_i=X_i-X_0$) and three components of the body force vector

[3] A Lagrangian frame of reference is described here as it is found to be efficient for FBO containment; however, more generally, an Eulerian or hybrid reference could also be used.

f_i. Then, making use of the materials constitutive law and the kinematics of deformation to 'eliminate' the stress components, the equations of motion are derived in a mathematically 'complete' form in terms of only three components of displacement. In the finite element formulation, the continuum body is discretized and shape functions are used to approximate the solution in the spatial domain. This allows for direct calculation of all the spatial derivatives. The equation of motion is derived to the familiar force-displacement relation as:

$$M(d)\cdot\ddot{d} + C(d)\cdot\dot{d} + K(d)\cdot d = F(t) \qquad (2.2)$$

Where d and F(t) are the vectors of nodal displacement and applied forces, respectively. This equation also provides a generalized time varying force-displacement relationship governing the body's behavior. The M, C & K terms represent inertia, damping and restoring forces, respectively. These can be dependent on displacement which makes the problem nonlinear (this will be the case for the physical phenomena during FBO as mentioned before). This equation indicates that the external (applied) forces must be balanced by the inertia, damping and internal forces (which are both dependent on the displacements). It should be noted that vector ***d***, which represents the displacement of the body at the nodal points only (or the number of DOF's for the FE model), may be large.

The above equations contain time derivatives of the nodal displacements and are to be solved for a given set of initial conditions (i.e. $d(0)=d_0$ and $\dot{d}(0) = \dot{d}_o$). Therefore the selection of a proper strategy to integrate these equations efficiently is of paramount importance. The integration schemes are generally divided into explicit or implicit depending on whether current information only at time t_1 (explicit strategy) or information at both time t_1 and t_2 (implicit strategy) is used (see Figure 2.19 for t_1 and t_2). The next two sections highlight strategic features in the so-called implicit and explicit integration schemes usually employed by commercially available finite element codes to solve the equations of motion. The most popular implicit method is often known as Newmark's method. The most popular explicit method is often known as the central difference method.

2.4.1 Newmark's Method (Implicit)

Consider Figure 2.20 showing the generalized load displacement response of a particle, governed by the equation of motion, moving from known position d_1 to unknown position d_2.

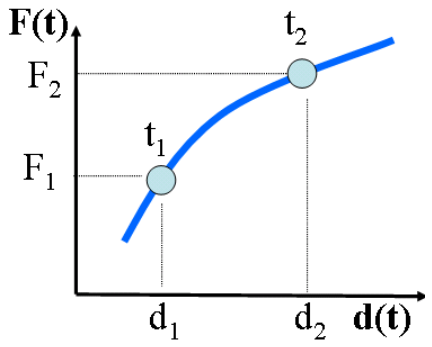

Figure 2.20 Nodal Load-Displacement response governed by equations of motion.

Forces F_1 and F_2 (at t_1 and t_2 respectively) are known. Time t_2 is based on $t_1 + \Delta t$ (the integration time step size). The reader should note that the equation of motion will met be exactly (or iterated almost exactly to within a numerical tolerance) at times t_1 and t_2.

Forces F_1 and F_2 (at t_1 and t_2 respectively) are known. The solution at t_1 satisfies:

$$M_1\ddot{d}_1 + C_1\dot{d}_1 + K_1 d_1 = F_1 \qquad (2.3)$$

The challenge is to find $d_2 = d(t_2)$ that satisfies:

$$M_2\ddot{d}_2 + C_2\dot{d}_2 + K_2 d_2 = F_2 \qquad (2.4)$$

In general:

$$\begin{aligned} d_2 &= d_1 + \Delta d \\ \dot{d}_2 &= \dot{d}_1 + \Delta\dot{d} \\ \ddot{d}_2 &= \ddot{d}_1 + \Delta\ddot{d} \end{aligned} \qquad (2.5)$$

Assume that the increments (2.5) are such that the equation of motion is met also at time t_2 (in addition to being met at time t_1). Substituting (2.6) into (2.5) gives:

$$M_2\Delta\ddot{d} + C_2\Delta\dot{d} + K_2\Delta d + \underbrace{M_2\ddot{d}_1 + C_2\dot{d}_1 + K_2 d_1}_{\widetilde{F}_1} = F_2 \qquad (2.6)$$

Note that if M, C, and K are constant (a linear problem) then $\widetilde{F}_1 = F_1$, otherwise $\widetilde{F}_1 = \widetilde{F}_1(d_1, \dot{d}_1, \ddot{d}_1, d_2)$ is referred to as the restoring force (where d_2 is an unknown). Eq. (2.6) can be written re-written as:

$$M_2\Delta\ddot{d} + C_2\Delta\dot{d} + K_2\Delta d = F_2 - \widetilde{F}_1 \qquad (2.7)$$

Newmark's method [19] approximates the unknowns d_2 and $\dot{d}_2$ in terms of unknown $\ddot{d}_2$ as:

$$\begin{aligned} d_2 &= d_1 + \Delta t\dot{d}_1 + (\Delta t)^2\left[\left(\tfrac{1}{2} - \beta\right)\ddot{d}_1 + \beta\ddot{d}_2\right] && 0 \le \beta \le \tfrac{1}{4} \qquad (2.8) \\ \dot{d}_2 &= \dot{d}_1 + \Delta t\left[(1-\gamma)\ddot{d}_1 + \gamma\ddot{d}_2\right] && \gamma \le \tfrac{1}{2} \end{aligned}$$

Using (2.8) the increments of velocity and acceleration can be obtained in terms of known quantities d_1, $\dot{d}_1$ and $\ddot{d}_1$ along with the unknown $\Delta d = d_2 - d_1$ and can be rewritten as:

$$\begin{aligned} \Delta\dot{d} = \dot{d}_2 - \dot{d}_1 &= \tfrac{\gamma}{\beta}\tfrac{\Delta d}{\Delta t} - \tfrac{\gamma}{\beta}\dot{d}_1 + \ddot{d}_1\left(1 - \tfrac{1}{2}\tfrac{\gamma}{\beta}\right)\Delta t \qquad (2.9) \\ \Delta\ddot{d} = \ddot{d}_2 - \ddot{d}_1 &= \tfrac{1}{\beta}\left(\tfrac{\Delta d}{(\Delta t)^2} - \tfrac{\dot{d}_1}{\Delta t} - \tfrac{1}{2}\ddot{d}_1\right) \end{aligned}$$

Substituting (2.9) into (2.7) to obtain (while recalling that $\Delta d = d_2 - d_1$):

$$\underbrace{\left(\frac{M_2}{\beta(\Delta t)^2} + \frac{\gamma}{\beta}\frac{C_2}{\Delta t} + K_2\right)}_{\hat{K} = \hat{K}(d_2, \Delta t)}\Delta d = F_2 - \widetilde{F}_1 \qquad (2.10)$$

For linear problems M, C, and K are constant the so-called equivalent tangent stiffness matrix $\hat{K}$ can always be determined for any t_2 (recall $t_2 = t_1 + \Delta t$). However, for nonlinear (where M, C, and K are not constant) problems $\hat{K} = \hat{K}(d_2, \Delta t)$ and the vector $\widetilde{F}_1$ depend on the unknown displacement d_2 and computational iterations are required for solution.

Symbolically this iterative procedure is written as:

$$d_2^{\,i+1} = d_1 + \hat{K}^{-1}(d_2^{\,i}, \Delta t) \cdot \left(F_2 - \widetilde{F}(d_2^{\,i})\right) \qquad (2.11)$$

Where the current approximation $d_2^{\,i}$ is substituted into the RHS of (2.11) to obtain the next approximation of $\mathbf{d}_2^{\,i+1}$ until a prescribed tolerance of $\left\| d_2^{\,i+1} - d_2^{\,i} \right\| \le \varepsilon$ is met. In fact such iterations are more complicated and are known as Newton-Raphson (N-R) equilibrium iteration procedure. Two key features should be noted for the FBO containment problems. First, the stiffness matrix, $\hat{K}$, must be reformulated and inverted, $\hat{K}^{-1}$, during each iteration; this is relatively expensive operation computationally. Second, the procedure is very sensitive to the chosen integration timestep size, Δt, as the problem becomes nonlinear.

Some advantages of implicit integration are:

1. The equation of motion is satisfied exactly (or at least to within a numerical tolerance) at time t_2.
2. The time step size Δt is, in principle at least, arbitrary and can be adjusted at strategic times to maximize increase overall computational efficiency.

Some disadvantages of implicit integration are:

1. As already mentioned, the stiffness matrix formulation, $\hat{K}$, and inversion, $\hat{K}^{-1}$ operations are numerically expensive.
2. If the M, C or K matrices vary significantly (for example- an abrupt change of interface stiffness due to contact/impact between bodies) then the equivalent tangent stiffness matrices $\hat{K} = \hat{K}(d_2, \Delta t)$ become highly sensitive to small displacement increments thus forcing either a very small timestep size or a lot of iterations to achieve convergence.
3. The effect in point 2 is further exacerbated if large displacements and rotations create extensive contact topology (for example, blade tip #1 must contact an entire annulus, blade tip #2 must contact an entire annulus, blade tip #3 must contact an entire annulus, and so on). This results in enormous computational hardware requirements (RAM and I/O speed) to avoid page file creation. Alternately, the model must be greatly

simplified to enable generous contact treatment up to the point where the modeling accuracy becomes questionable.

4. Also, the path dependence of large interface sliding with friction (rotating blade tip to static case, for example) between bodies forces very small timestep size.
5. Implicit based constitutive evaluations (for nonlinear materials in particular) tend to be computationally expensive as the Total Lagrangian formulations with exact and expensive matrix inversion are required (as opposed to approximate Updated Lagrangian constitutive formulations). Also, the constitutive path dependence in inelastic materials usually requires smaller time steps anyway (placing expensive evaluations at a disadvantage).
6. Structural instability becomes a major issue. Formulating and inverting large, nearly singular (that is if $\hat{K} \to 0$ and $\hat{K}^{-1} \to \infty$) is very difficult to overcome (or impossible) for problems with large degrees of freedom.

2.4.2 Central Difference Method (Explicit)

The explicit solution takes a fundamentally different strategy from the implicit approach presented above. The central difference [4] method of solution is used. The equations of motion are met only at time t_1. It allows separating the inertia forces from equation (2.3) to obtain:

$$M_1\ddot{d}_1 = F_1 - \underbrace{\left(C_1\dot{d}_1 + K_1 d_1\right)}_{\tilde{F}_{in}} = F_1 - \tilde{F}_{in} \qquad (2.12)$$

Where F_1 is the external force applied to nodes and $\tilde{F}_{in}$ represents the damping and restoring forces at t_1 (which are the internal forces produced by stresses at this instant). The acceleration can be calculated at t_1 as:

$$\ddot{d}_1 = M_1^{-1}\left(F_1 - \tilde{F}_{in}\right) \qquad (2.13)$$

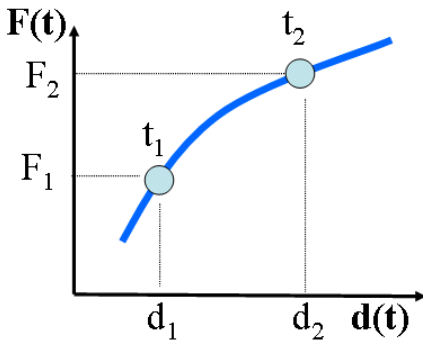

Figure 2.21 Explicit Load-Displacement response.

Inverting the mass matrix, $M_1 \rightarrow M_1^{-1}$, is generally much less computationally expensive and becomes almost trivial when the so-called lumped mass finite element formulation is used. Next, the velocities and positions are evaluated (LS-Dyna staggers the velocity evaluations by a ½ Δt factor) as:

$$\dot{d}_{2-\Delta t/2} = \dot{d}_{1-\Delta t/2} + \ddot{d}_1 \Delta t$$
$$d_2 = d_1 + \dot{d}_{2-\Delta t/2} \Delta t \qquad (2.14)$$

The explicit methods are very effective at handling various nonlinearities. Recall that in the implicit approach nonlinearities generally cause some residual imbalance between the external and internal forces that is iterated to equilibrium (the Newton-Raphson procedure). Explicit methods handle this differently. Note in (2.14) how d_2 is calculated directly from d_1; there are no equilibrium iterations. This feature greatly improves speed and robustness when solving certain types of nonlinearities.

For example, consider multi-body contact (with sliding and friction) between components which are highly nonlinear due to the interface stiffness discontinuity. This class of problem is generally very difficult for implicit methods. Conversely, explicit methods handle enforcing the impenetrability condition or compatibility condition in a direct manner. After the displacement $\mathbf{d}_2$ is calculated a contact penetration check flags all nodes which are penetrating a surface. The normal velocities of these nodes (recalling velocities are staggered by ½ Δt) at the contacting interfaces are then adjusted [4] to momentum conserving values as:

$$\dot{d}^{i\_penetrating}{}_{2-\Delta t/2} = \dot{d}^{i\_surface}{}_{2-\Delta t/2} \quad \text{i=all penetrating nodes} \qquad (2.15)$$

The penalty method [4] is used to generate the contact interface forces and a small penetration is usually tolerated in exchange for the methods' simplicity. Explicit integrations treatment of directly solving for d_2 (as opposed to iterating for d_2) has a very profound effect on overall computational efficiency. The majority computational effort in such methods lies in constitutive evaluations to obtain $\widetilde{F}_{in}$, the internal force. Explicit integration contact evaluations in complex multi-body assemblies are significant but are usually secondary (compared to element stress evaluations) in terms of computational cost.

The simplicity and directness of the explicit method have a major drawback- for stability and accuracy the required timestep size Δt is very small. Unlike implicit integration which is stable and where the timestep size, Δt, may be somewhat large (as large as the system's vibrational

response and the applied loading variation allows), in an explicit solution the maximum time step size (to ensure integration scheme stability) is governed by the Courant condition and is approximately:

$$t_{cr} \cong l_{edge} / c \cong l_{edge} \sqrt{\rho / E} \qquad (2.16)$$

Where t_{cr} is the largest allowable time step size, l_{edge} is the shortest element edge length (in the entire grid) and $\boldsymbol{c}$ is the speed of sound (approx. $\sqrt{E/\rho}$ in the element). For example, a meshed steel structure with 25.4mm (1 inch) element edge lengths must be integrated using time step increments of about $5 \cdot 10^{-6}$ s or 5 μs. This equation also indicates the importance of meshing carefully to control element edge length.

Some advantages of explicit integration are:

1. Robust and efficient sliding and contact interfaces
2. More sophisticated material models are possible
3. Readily handles instability.

Some disadvantages of explicit integration are:

1. Small timestep size limits integration time
2. Solution scheme can diverge
3. Local stress resolution sacrificed for computational speed.

The last point results from minimizing the number of Gauss points (usually reduced to a single point) when evaluating the element stresses that are needed for the calculation of $\widetilde{F}_{in}$.

2.5 Baseline Model Requirements

According to industry sources [5,6], peak FBO loadings (based on gauged rig tests) on many engine case components typically occur very quickly after the blade release or shortly thereafter. The components either:

1. Fail very quickly (often leading to other failures), or

2. They survive the initial fury and often withstand the progressively smaller cyclic loading.

As the recent literature demonstrates [8-17] current analytical modeling of fan blade off typically treats the impact and imbalance effects separately and focuses on either:

1. Explicit integration for fan blade/case models to simulate the blade impact energy absorptions (often using LS-Dyna [9]), or
2. Implicit integration based rotor/case models to study the unbalanced interaction transient response (often done using NASTRAN [9]).

The approach used in this study is different and focuses on providing a more physically based FBO system model to provide loads to design teams focusing on optimizing individual components. This involves a coarser full engine model in LS-Dyna (with full nonlinear interaction) which will study the response interaction of **both** the blade impact and short term rotating imbalance force. The baseline model (the focus of this thesis) will be developed to provide a robust nonlinear methodology that can predict changes of FBO response (globally) as part teams update and optimize individual components throughout the engine. Figure 1.18 is repeated below.

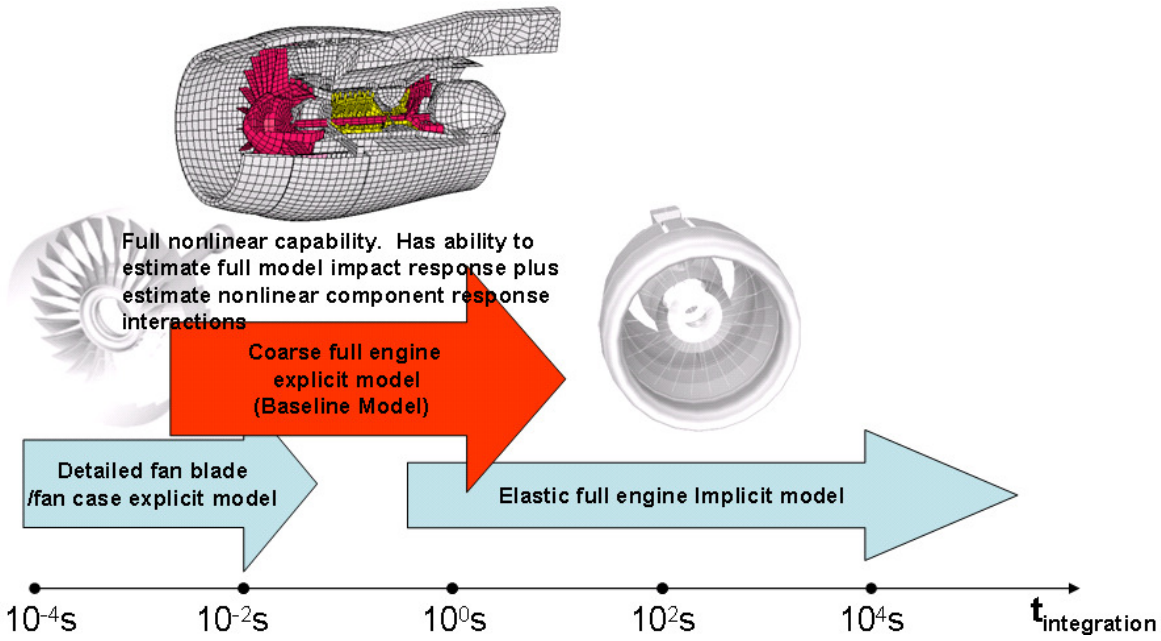

Figure 2.22 Filling the gap in analytical methodology

This model is designed to obtain a unified FBO response (interacting/coupled) across all engine components for both impact and imbalance modeling; this makes it particularly useful for in the concept development, development and validation phases of Figure 1.10. Faster and/or more accurate FBO loading predictions at these stages can result in lower engine weights and faster development of the long lead time FBO controlled cases.

For the steady state prior to the FBO event, the low fan and high rotor speeds of ω=523.6 radians/s and ω=1571 radians/s, respectively, were chosen. Then a 0.15second event duration, also known as the total integration time, t_{int}, was chosen. A blade release time, $t_{release}$, of approximately 0.03 seconds was also chosen. The exact $t_{release}$ can be varied slightly to accommodate different blade release angles.

To give the reader an idea of the large displacements and rotations involved note that after t_{int}=0.15 s the low rotor will have made approximately 12.5 complete revolutions and the high speed rotor will have made approximately 37.5 complete revolutions.

2.6 Estimating Solution Time

Solving a 0.15 second event duration (about 12½ full revolutions of the fan shaft) requires the equations of motion to be solved at least in the order of 10^4 times. This is not computationally trivial and solution method selection (implicit versus explicit) requires careful consideration.

A model of 16974 nodes and 19925 elements was tested in both ANSYS (implicit) and LS-Dyna (explicit) to obtain time estimates for solving a 0.15s FBO event.

2.6.1 Explicit Solution Time for Integration Methods

LS-Dyna took 5721 seconds to solve 33,334 substeps, with a timestep size of 4.5 μs (minimum element edge length constrained by the Courant condition), to a final integration time of 0.15s. This indicates a computational cost of 0.171s per sub-step. This model included full contact, friction and well as material nonlinearities.

2.6.2 Implicit Solution Time

With integration time and fan speeds prescribed, an estimate of the integration timestep size required for implicit solution of the equation of motion can be found. The speed of the spinning blade tips (relative to the static case) is very important for calculating an appropriate time-step increment size for numerical integration.

The fan blade tip velocity, V_{spin}, is determined directly from Figure 2.23 as about 653m/s (25,700 inches per second). Note that this is close to the speed of sound.

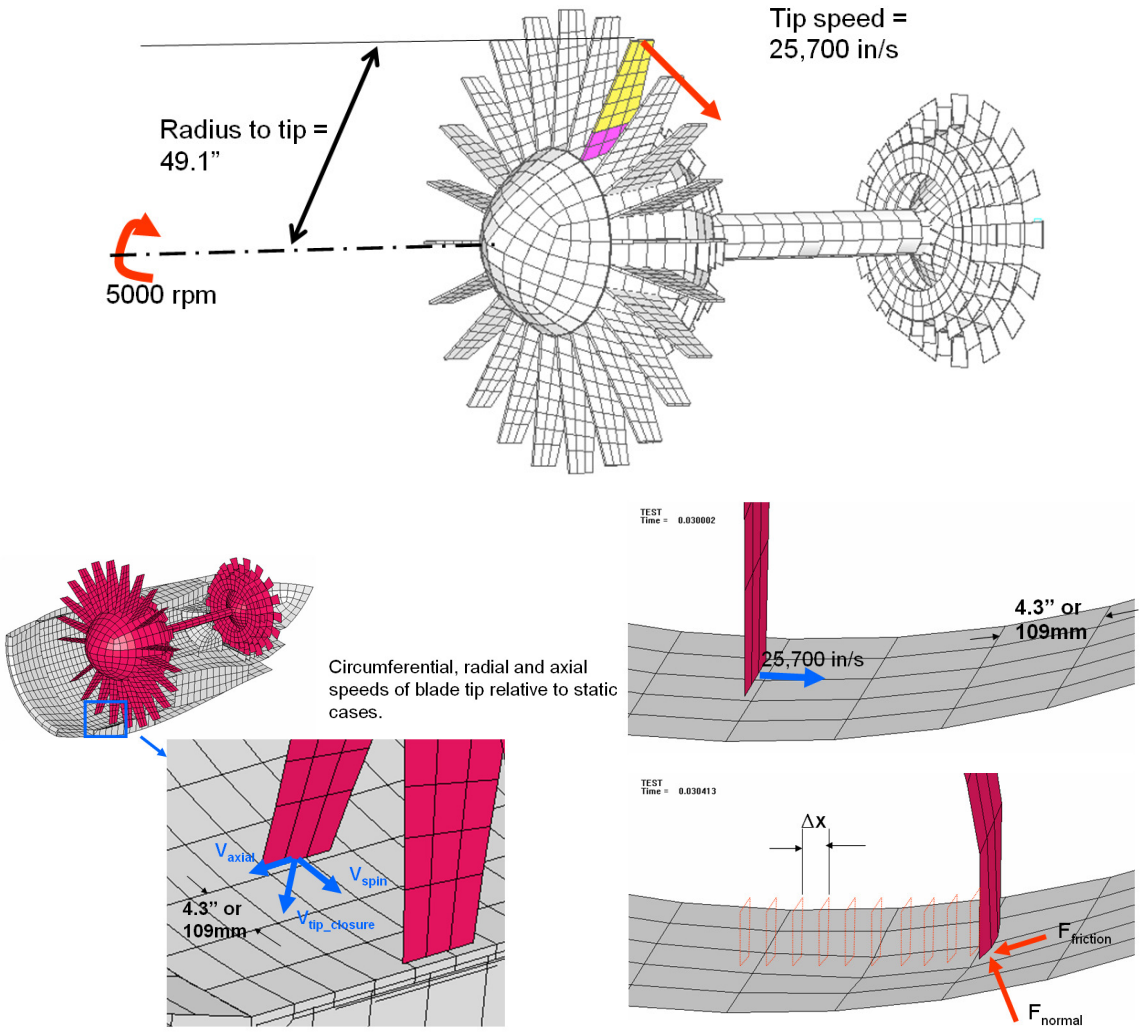

Figure 2.23 Blade tip speed of Low Rotor relative to shell element on static case

To adequately compute path dependent plasticity, contact and sliding friction, it is assumed, based on experience, that at least ten Δx blade tip displacement increments are required to traverse a single case element. For the example shown, the case elements are 4.3inch or 109mm long. The ten increment traverse assumption gives a displacement increment of Δx equals about 11mm (or 0.43inch). Using $v = \Delta x / \Delta t$ reveals an integration timestep increment of Δt=17 μs.

The high speed rotor tip speed has a similar velocity to the low speed rotor as demonstrated in the Figure 2.24. This high rotor tip speed is about 798 m/s.

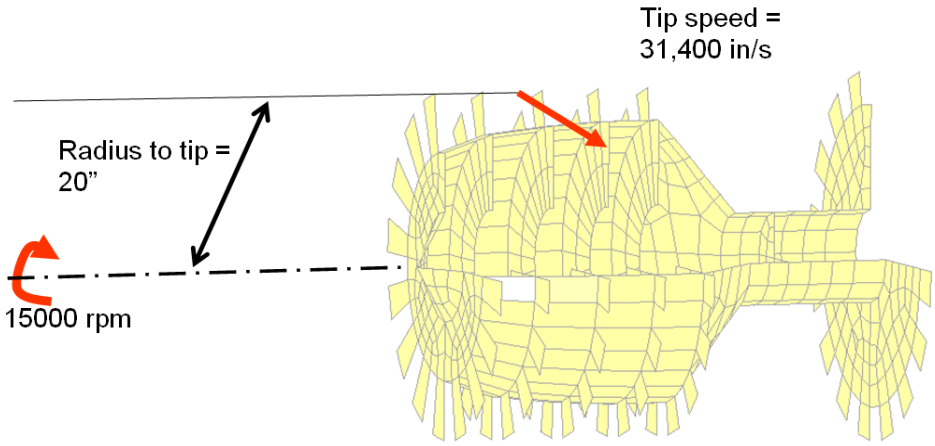

Figure 2.24 Blade Tip speed of high rotor

A multi-step ANSYS linear static solution (for the exact same mesh which includes the full stiffness matrix formulation and inversion) was averaged at 7.43s per iteration (NASTRAN would be expected to perform similarly). Typically, even for small timesteps, several N-R equilibrium iterations (perhaps 3-4) are required to converge forces/displacements for a particular timestep. With contact, sliding friction and material nonlinearity this is very likely to increase even more; however, for this estimation, a conservative 3.5 iterations per timestep will be assumed. A 17 μs timestep (based on blade tip to case speed estimates) will be assumed for Newmark solution. Integrating to 0.15 seconds then requires about 8965 substeps. With these assumptions, the CPU time estimate to integrate to 0.15 seconds is about 233,000s (or about 65 hours).

This time-per-step estimate is optimistic[4]. Real world computations using implicit codes that contain extensive contact surface definitions require more complicated system matrix operations to handle contact and friction. Large meshes quickly become computationally intractable. Note, for example, the fan blades modeled with simple beam elements as shown in Figure 2.18; this was done to reduce DOF (not because beams are great representations of the complex geometry).

Further, solving elastic or elasto-plastic structural instability is another major issue- even by including the mass matrix (which tends to maintain positive definiteness in the system matrices), achieving convergence around system instability points can still be very challenging.

2.6.3 Choosing a Solution Method

It is estimated (with optimistic assumptions based on industry experience solving this class and size of problems) that the baseline model for the FBO problem solved explicitly is about 40 times faster than would be achievable by implicit methods. The explicit solver performed robustly and included material nonlinearity as well as extensive contact and sliding interfaces. The contact and sliding features will almost surely create issues (known a priori from industry experience) for implicit based integration further increasing the above estimate.

Considering that interface sliding and friction, as well as nonlinear constitutive capability is required to accurately and robustly predict FBO, an explicit solver is the clear choice for simulating fan blade off. The chosen explicit solver was LS-Dyna 970 Revision: 5434 - A Program for Nonlinear Dynamic Analysis of Structures in Three Dimensions. LS-Dyna default values, except as noted were used.

[4] Wildly optimistic in the author's experience.

3 Constructing the Baseline Model: Geometry, Materials, and Kinematics

This chapter outlines the nomenclature, geometry, meshing, materials, constraints, connections and kinematics for a typical turbofan engine along with the corresponding finite element modeling approximations. This baseline model will then be the basis for further academic study of turbofan engine FBO.

3.1 Nomenclature of Baseline Model

Turbofan engines consist of many assemblies of components. Figure 3.1 is intended to familiarize the reader with some of the industry specific nomenclature used.

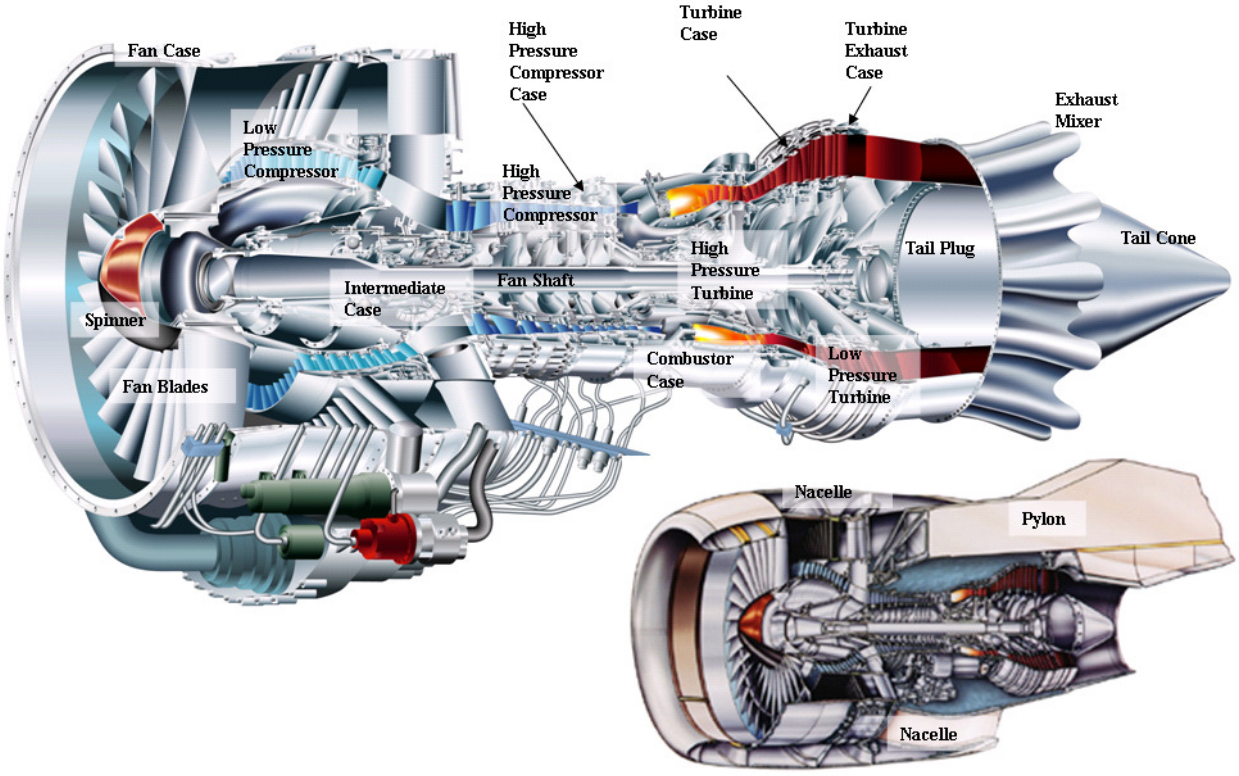

Figure 3.1 Outline of major components inside turbofan engine. [23]

The baseline FEA model in Figure 3.2 is shown to provide the reader with a high level overview of the modeling detail. This model will be fully described in later sections.

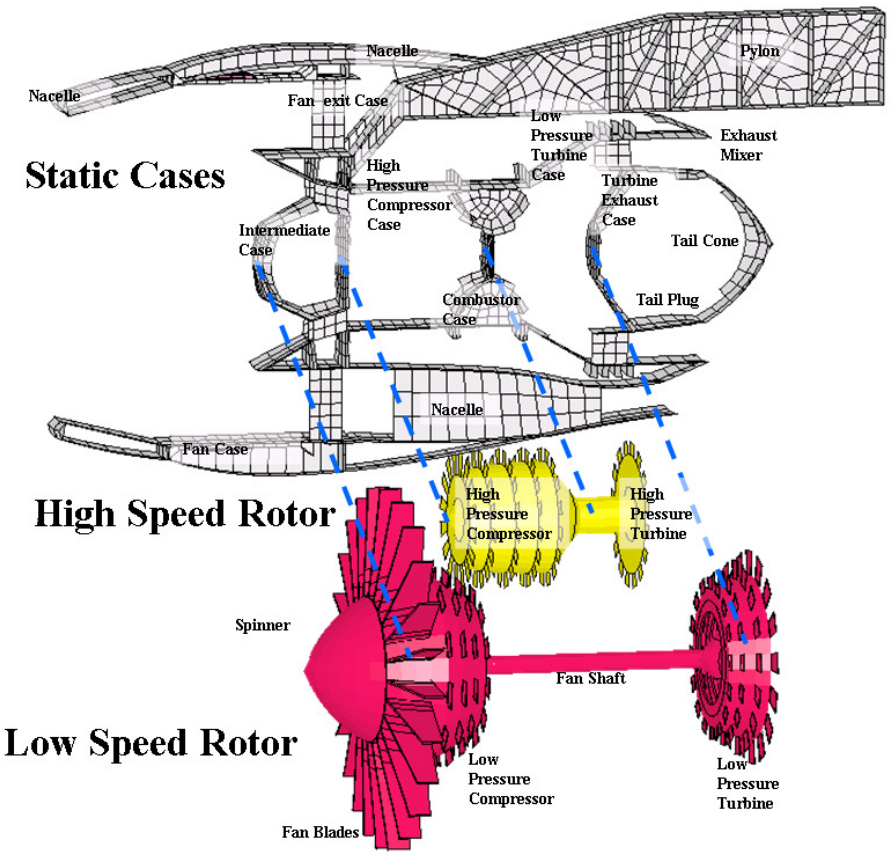

fan case must absorb and sustain kinetic energy of released fan blade
fan exit case joins the fan case and intermediate case.
intermediate case is the heart of the engine. This case is connected to pylon (essentially grounded). This reacts out both the fan/core bearing loads (FBO imbalance). The IMC also holds the fan case during impact.
high compressor case contains the rotating compressor core
combustor case core gas flow entering the combustor reduces speed and pressure soars. This case holds the aft core bearing.
turbine case contains the spinning turbines
turbine exhaust case This case holds the aft fan shaft bearing. This case is also connected to pylon (essentially grounded).
mixer blends bypass gas flow with core gas flow.
tail plug and tail cone provide aerodynamic surface to control exiting gases
high pressure compressor **HPC** disks with attached fan blades.
high pressure turbine driven by hot exit gases which in turn drives the compressor
HPT and HPC are joined together.
spinner entry aero surface.

Figure 3.2 Overview of Baseline Model.

The baseline FEA model in Figure 3.3 is shown to provide the reader further detail of the engine overview.

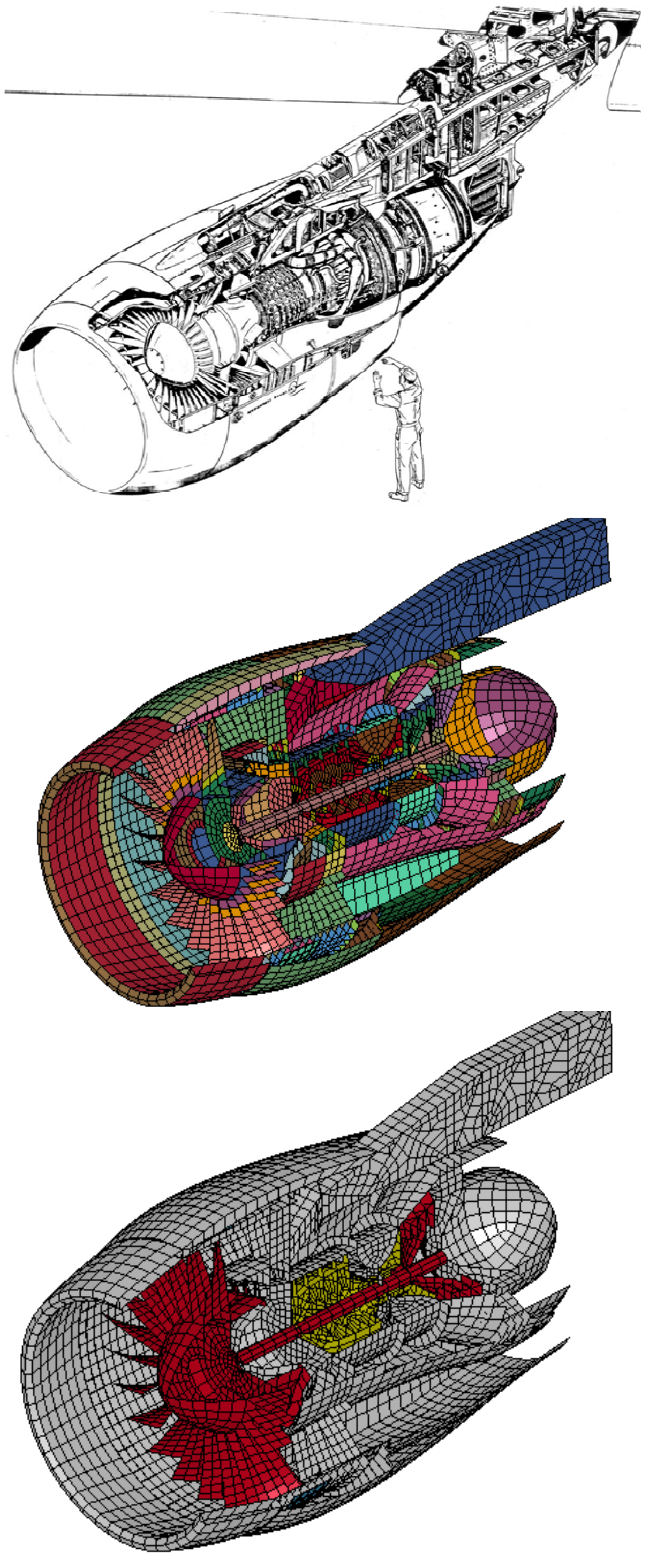

Figure 3.3 More Overviews of Baseline Engine Model [26]

3.2 Constructing the Baseline Model

The goal was to build an efficient explicit finite element model of the FBO test; more specifically, a blade containment rig test for a high bypass turbofan will be constructed. An overview of the primary components is shown below.

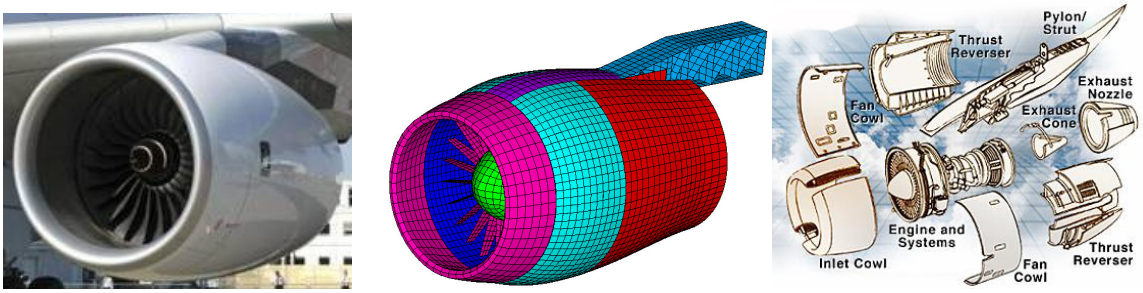

Figure 3.4 Building the Baseline Model of a high bypass turbofan engine. [28]

A cross section of this engine model is shown in Figure 3.5. Component features were scaled and modeled from public domain images found on the internet.

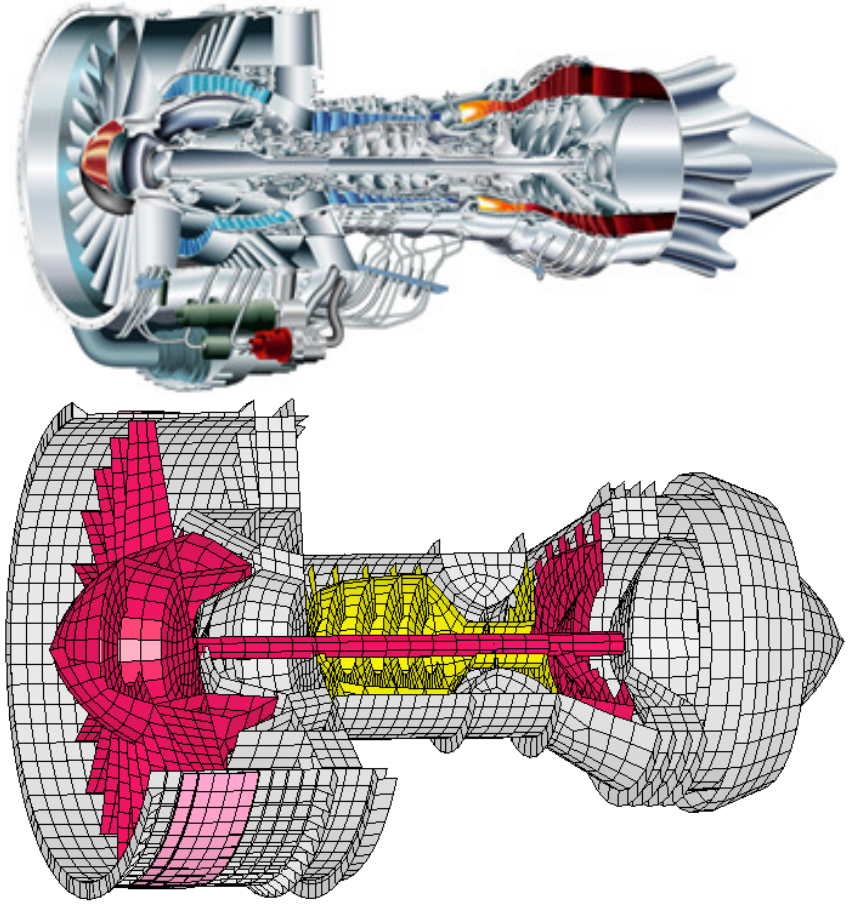

Figure 3.5 High bypass turbofan engine and baseline FEA model [23]

A cross section of the mounted engine model is shown in Figure 3.6. Component features were scaled and modeled from public domain images found on the internet.

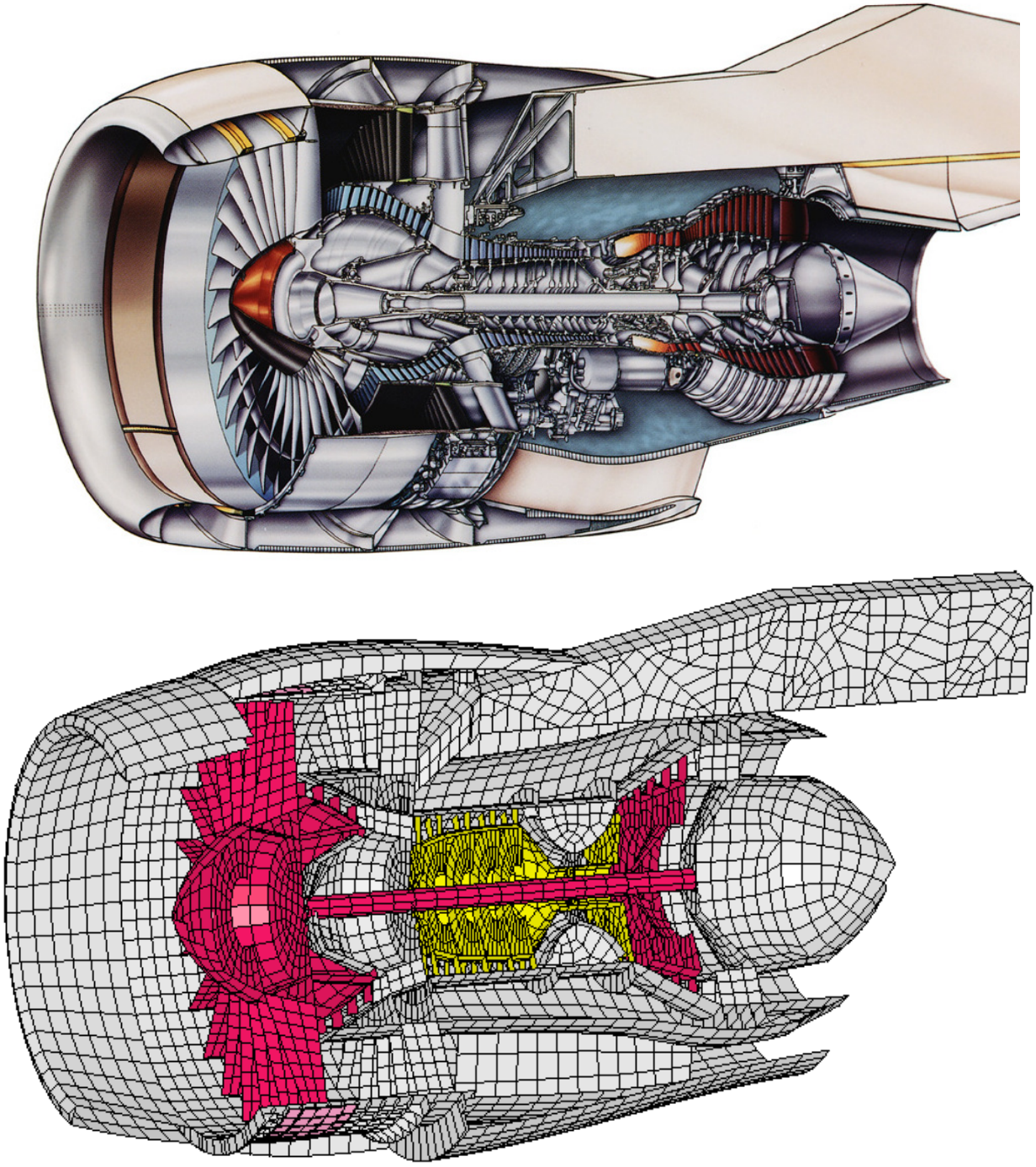

Figure 3.6 Engine mounted inside nacelle. [23]

A cross section of the bypass and core flowpaths are repeated below.

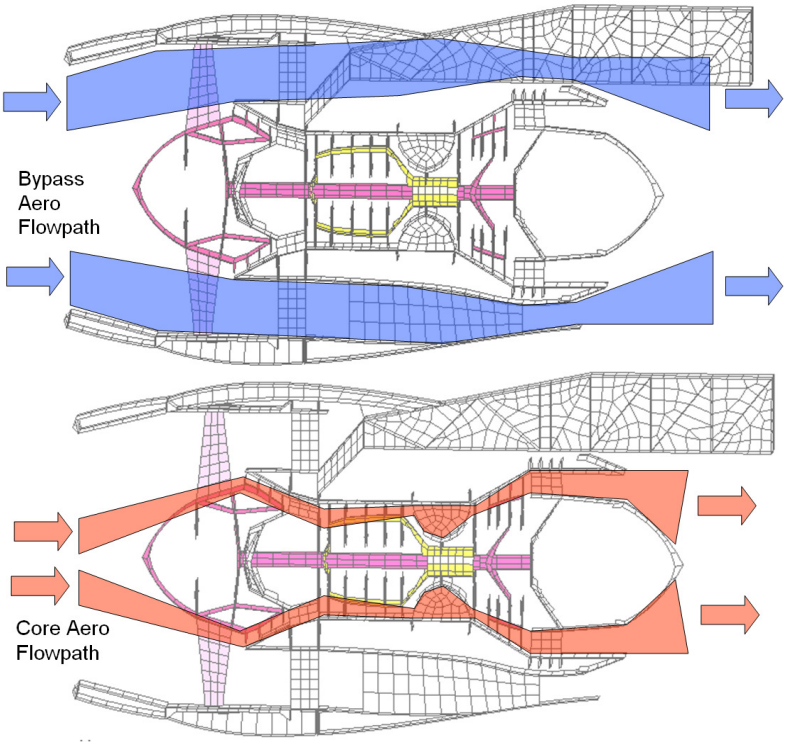

Figure 3.7 Bypass and core aero flows though high bypass turbofan.

The horizontal and vertical cross section is compared in Figure 3.8.

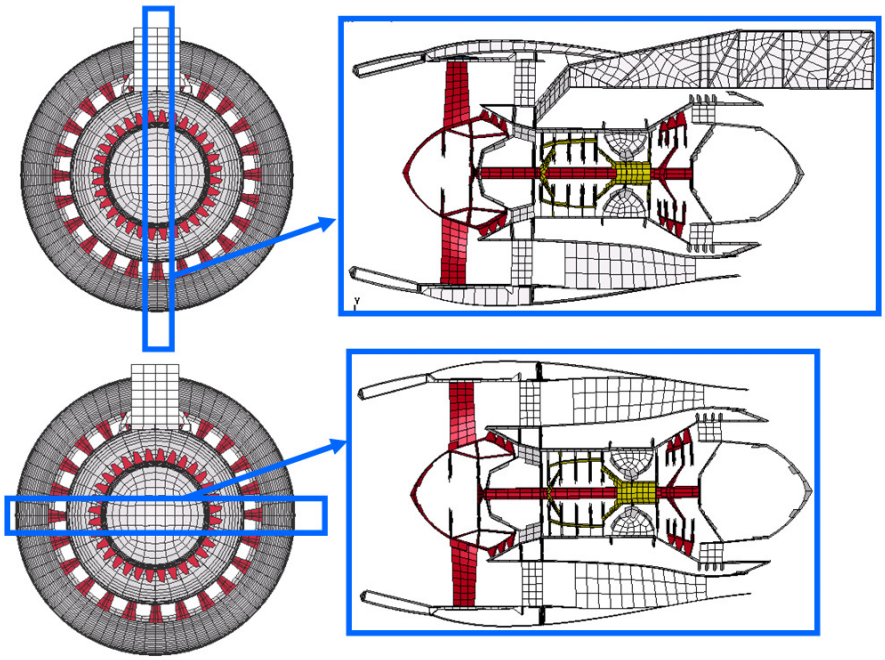

Figure 3.8 Horizontal and vertical cross section comparison.

3.2.1 Meshing Requirements for Explicit Integration

When meshing for explicit calculations the Courant condition (Equation 2.3) indicates that when meshing for explicit calculations the minimum integration time step size in the model is dictated primarily by the minimum element edge length (searching through the whole grid). As a consequence, uniform element edge lengths (a uniform grid) are often used as to get extra computational speed; unfortunately this comes at the cost of stress accuracy at high stress gradients. This compromise is demonstrated with Figure 3.9. For example, making the element edge lengths about 3 times shorter (to more accurately capture the expected stress gradient at the hole) increases the solution time by about 3 times. On the other hand, when using an implicit solution strategy, adding extra elements around the hole to improve stress accuracy would have a minimal penalty on solution time (perhaps 10% for the mesh shown).

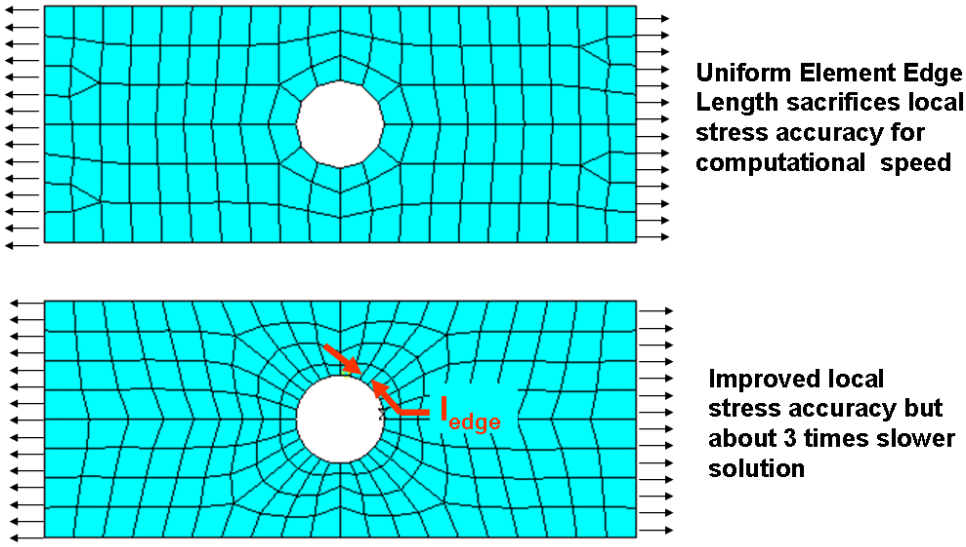

Figure 3.9 The compromise between local stress accuracy and speed.

It should also be understood that this work is primarily a methodology development and will involve a huge amount of debugging. Uniform edge length and overall model coarseness for the meshing was chosen so it would run quickly.

For purposes of baseline model construction each individual engine component was modeled with a simple grid to capture the mass and stiffness of the part. Detailed stress values, which become very important to jet engine modeling, are not resolved with the relatively coarse mesh. It is a simple matter to develop a more refined grid once a validated methodology is developed.

3.2.2 Selecting LS-Dyna Elements: Element Formulation

Figure 3.10 shows in-plane integration locations for both reduced and fully integrated shell elements. Reduced integration elements are recommended for explicit calculations but are subject to hourglassing (spurious strain energy modes). Fully integrated shells avoid potential hourglassing difficulties but are four times slower.

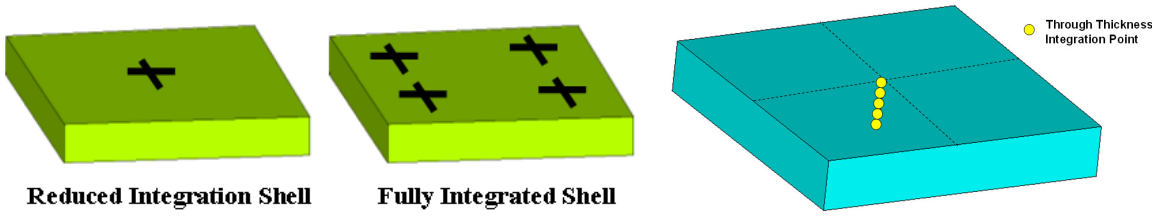

Figure 3.10 In-plane integration points and through-thickness integration.

There are multiple reduced and fully integrated element formulations available [1,2] in LS-Dyna. ELFORM 2 was chosen for reduced and ELFORM 16 was chosen for fully integrated formulations. An exception was the fabric belt model (to be discussed later) which had a membrane formula with ELFORM 9.

Through thickness integration is very important for shell calculations. Two integration points through thickness are adequate for elastic material shells; however, five integration points through thickness is recommended for elasto-plastic material shells and was used for the baseline model. Examples[5] of the LS-Dyna shell section definitions are shown in the deck below:

```
*SECTION_SHELL
      22       2  0.8330      5.0      0.0      0.0        0
 0.100    0.100    0.100    0.100     0.00
*SECTION_SHELL
      23      16  0.8330      5.0      0.0      0.0        0
 0.150    0.150    0.150    0.150     0.00
```

Including this code allows LS-Dyna users to understand precisely which defaults were used; other readers may not be interested in the LS-Dyna syntax and can ignore this.

[5] Syntax is included for interested LS-Dyna users; non-users can ignore can ignore these specifics.

3.3 Individual Components in Baseline Model

3.3.1 Inlet Cowl

The simplified mesh below represents the inlet cowl.

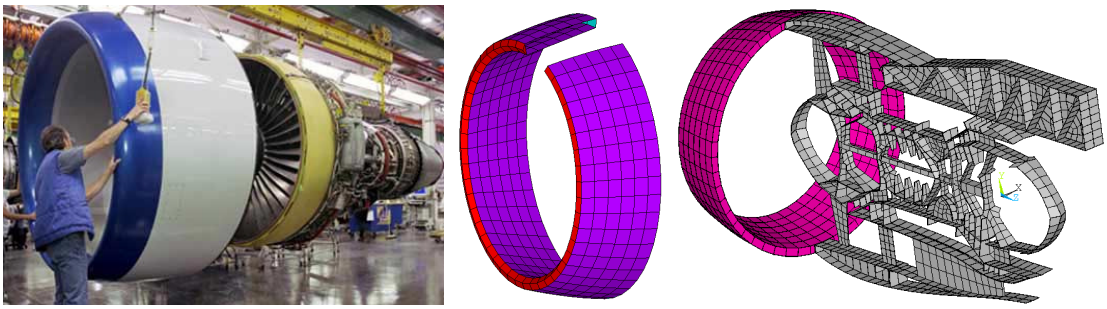

Figure 3.11 Inlet Cowl Shell Mesh [27]

3.3.2 Intermediate Case

The simplified mesh below represents the intermediate case. This case houses two bearings and constrains both the low and high speed rotor.

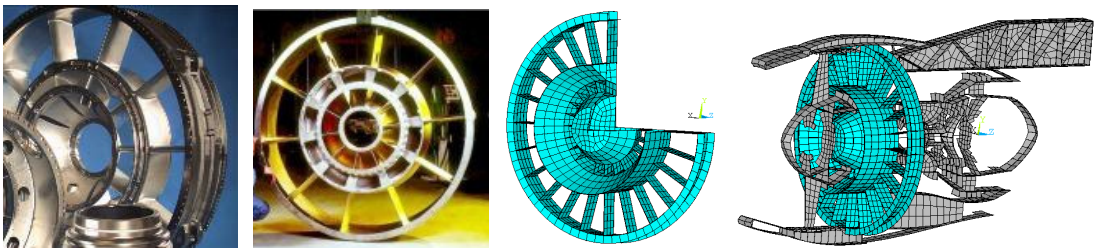

Figure 3.12 Intermediate case Shell Mesh [32]

3.3.3 Combustor Case

The simplified mesh below represents the combustor case. This case has a bearing providing radial support to the high speed rotor.

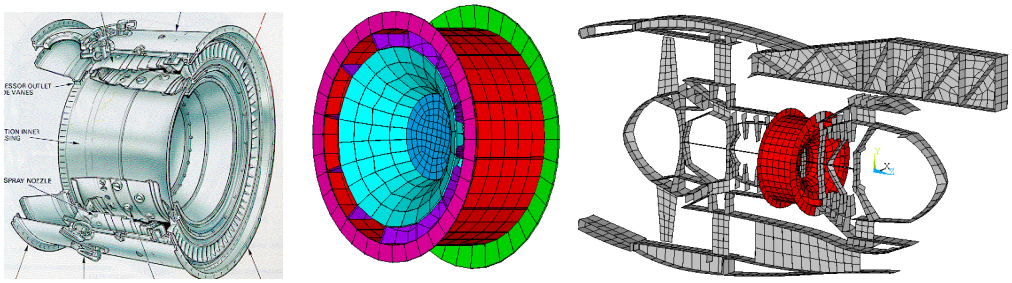

Figure 3.13 Combustor Case Shell Mesh [24]

3.3.4 Compressor Case

The simplified mesh below represents the compressor case.

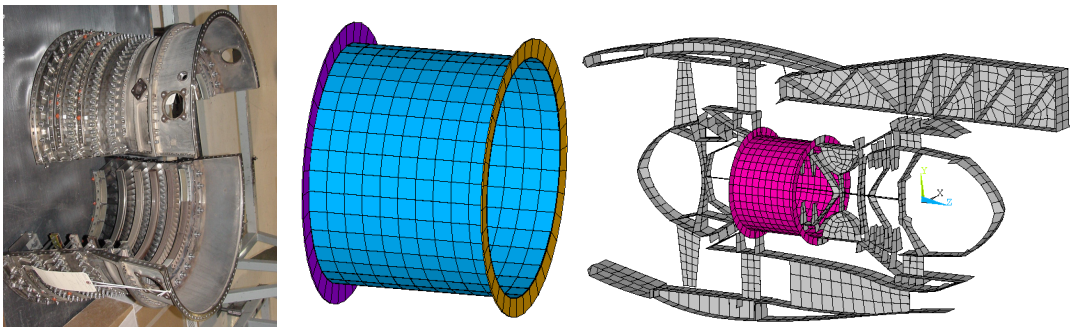

Figure 3.14 Compressor Case Shell Mesh [24]

3.3.5 Turbine Case

The simplified mesh below represents the turbine case

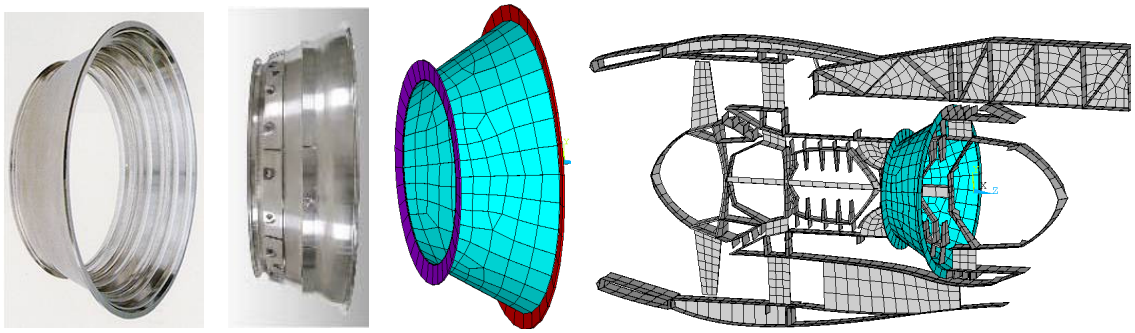

Figure 3.15 Turbine Case Shell Mesh [32]

3.3.6 Tail Cone

The pictures below explain tail cone.

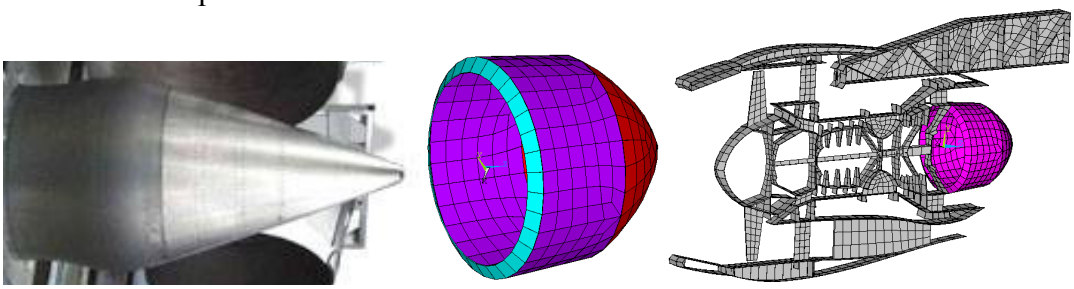

Figure 3.16 Tail Plug and Tail cone Shell Mesh [26]

3.3.7 Fan Cowl

The simplified mesh below represents the fan cowl doors.

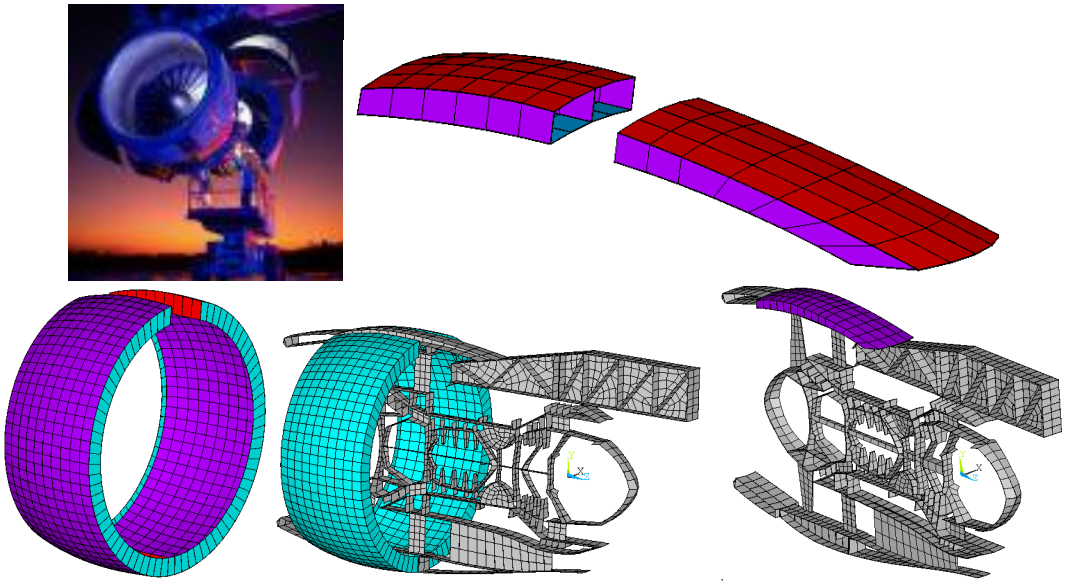

Figure 3.17 Fan Cowl Shell Mesh

The fan cowl doors are coupled (all translation DOF) to the fan cowl support as shown below. The bottom of the fan doors are bonded together. The fan cowl doors also contact the fan case. This sliding contact interface is shown below with the red dotted line.

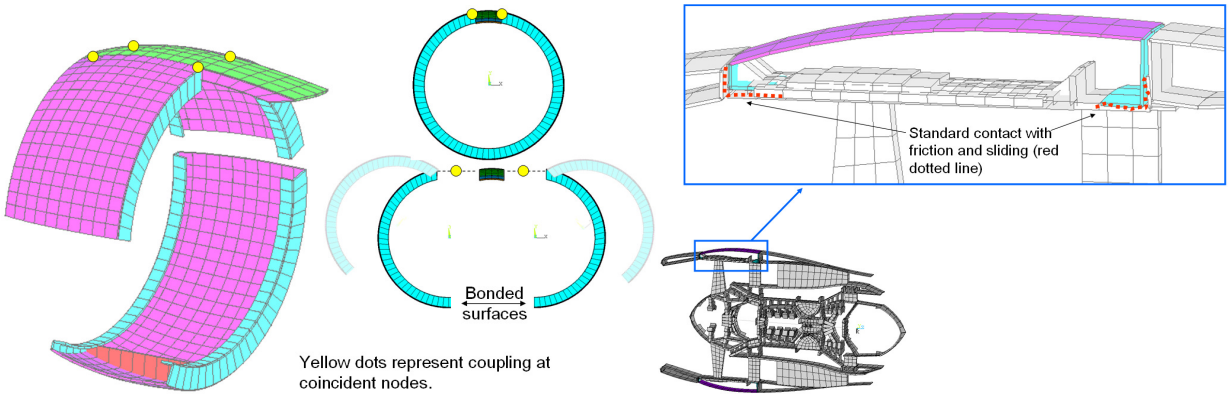

Figure 3.18 Kinematics and Contact interfaces on Fan cowl.

3.3.8 Fan ByPass Doors

The simplified mesh below represents the fan bypass doors.

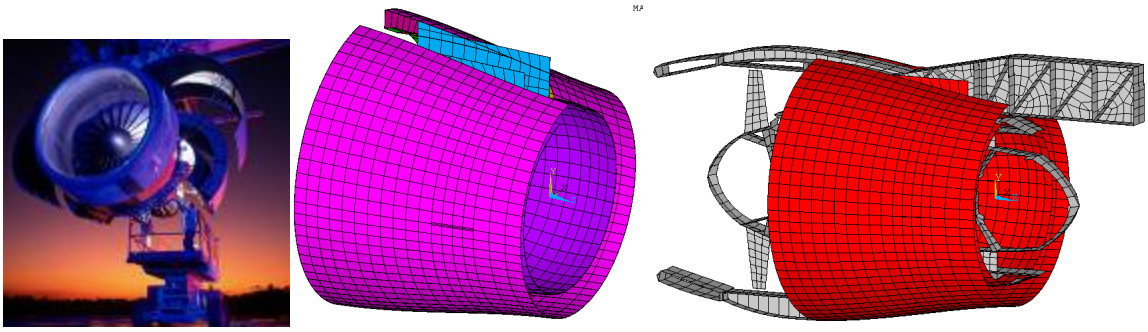

Figure 3.19 Fan Bypass doors Shell Mesh

The yellow dots below show the locations of coincident nodes on the pylon and fan bypass doors. These coincident nodes are coupled in translation DOF to simulate a hinge. Two contact interfaces with sliding and friction are represented by the red dotted lines.

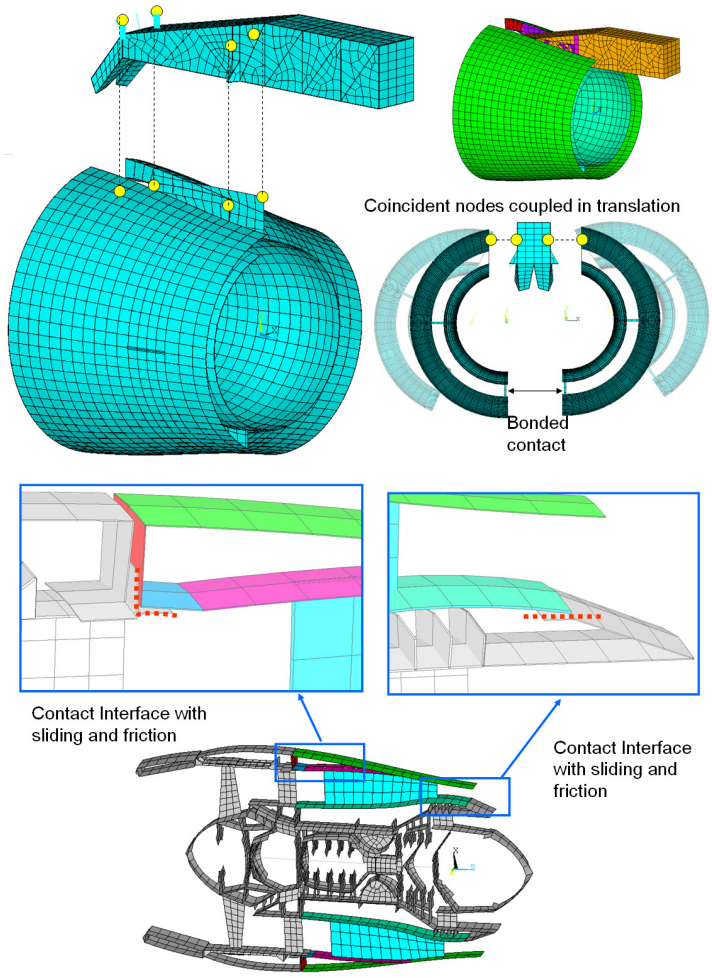

Figure 3.20 Fan Bypass Kinematics and Contact interfaces

3.3.9 Fan Case: Isogrid and Kevlar Belts

The fan case is constructed of aluminum isogrid as shown below.

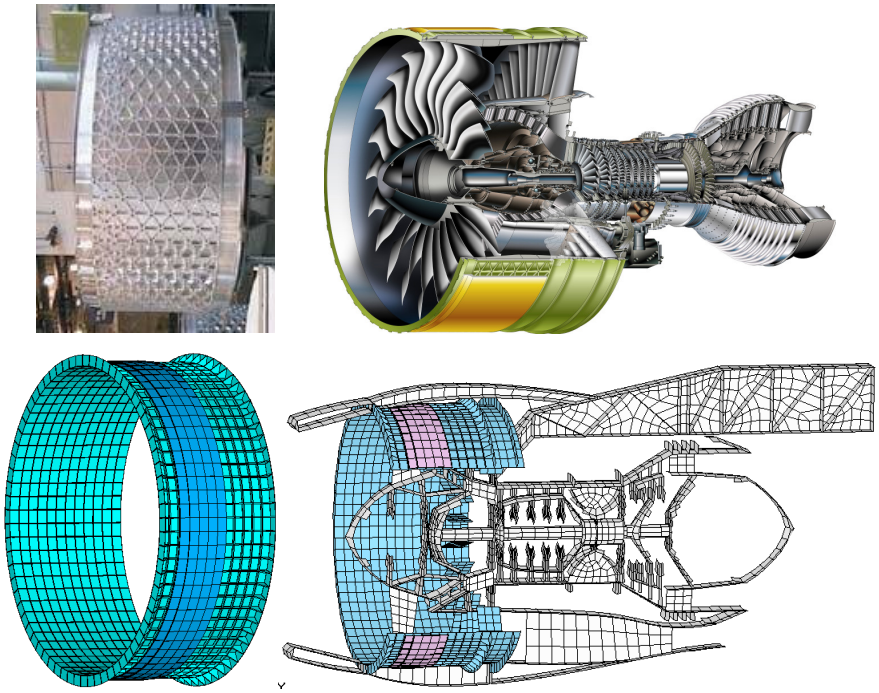

Figure 3.21 Shell Mesh of Fan Case and Kevlar belt

Two Kevlar belts circumscribe the isogrid fan case as shown below. The belts are in contact that can slide against each other or slide against the isogrid aluminum cases. Static or sticking as well as sliding friction is included. The before and after deformation plot below shows the relative sliding between belt-to-belt as well as belt-to-isogrid.

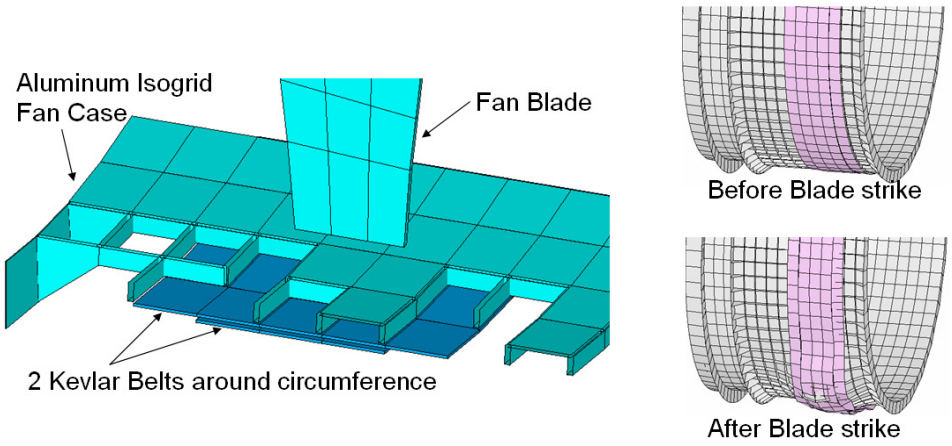

Figure 3.22 Detail of blade / fan case / belt shell mesh

3.3.10 Turbine Exhaust Case (TEC)

The simplified mesh below represents the turbine exhaust case. As discussed previously this case provided a secondary load path to the pylon for reacting out unbalanced fan blade loads. The TEC is attached to the pylon via link elements. The TEC also has a bearing that provides radial constraint to the low speed shaft.

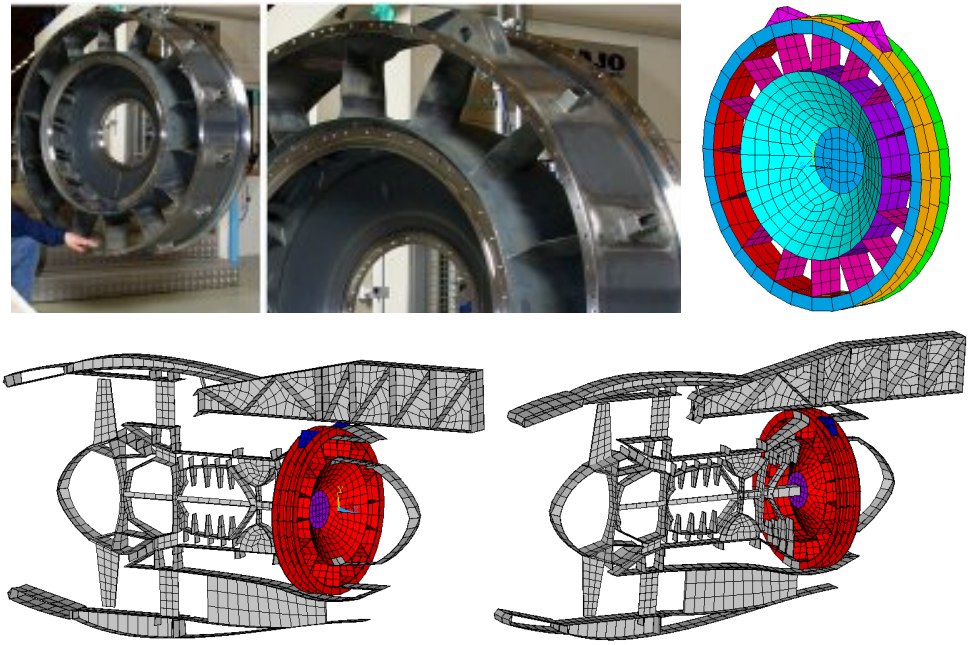

Figure 3.23 Turbine Exhaust Case Shell Mesh [32]

3.3.11 Exhaust Mixer

The pictures below explain the exhaust mixer. The red dotted line shows the contact with sliding friction interface with the fan bypass doors.

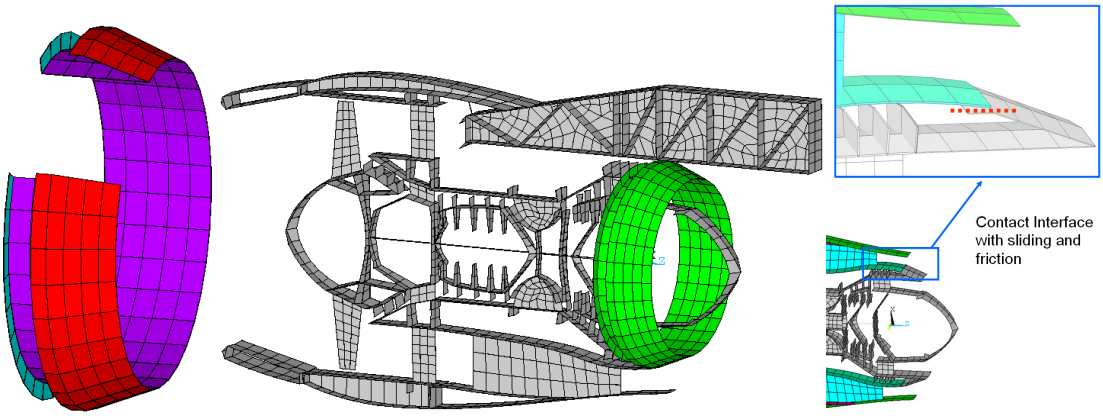

Figure 3.24 Exhaust Mixer Shell Mesh

The part is called the exhaust mixer because the high speed and low speed exhaust flows mix together here. Interestingly, some seemingly crazy looking shapes (below-red background) have been very effective at mixing the high&low speed gas flows and reducing overall engine noise levels. This detail was not modeled but the picture helps give the reader an idea of what minimum size mesh would be required for a fully detailed engine model.

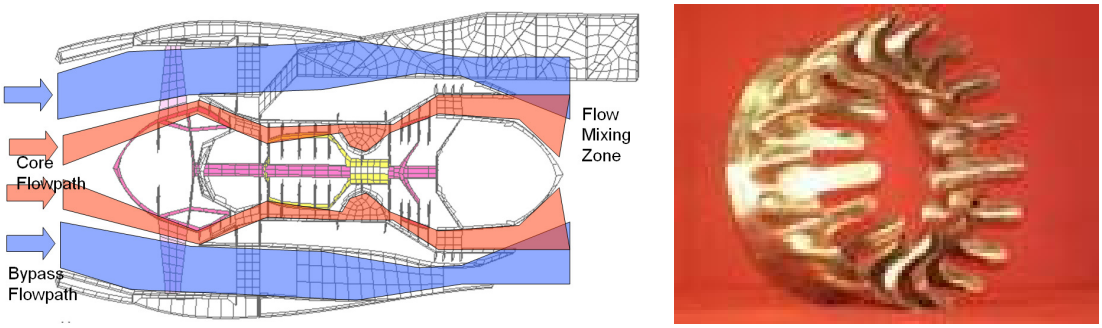

Figure 3.25 Complex geometry of Exhaust mixer [26]

3.3.12 High Speed Rotor

The pictures below show the high speed rotor. The bearing is simulated by coupling coincident nodes to the static structure and has already been fully described. There is a contact interface (with sliding and friction) between the blade tips and the case.

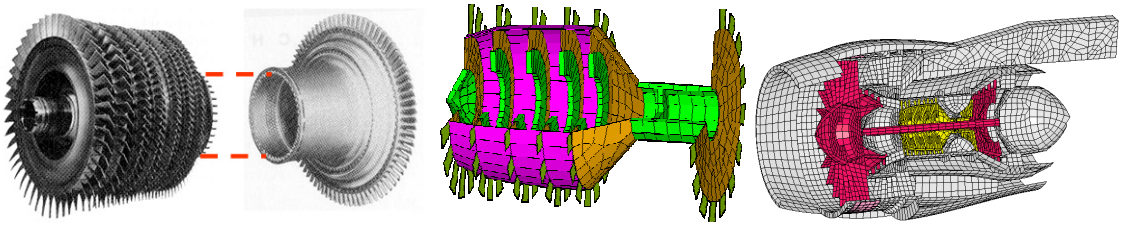

Figure 3.26 High Speed Rotor: High pressure compressor plus high pressure turbine.

Prior to fan blade off, the steady state centrifugal stresses in the spinning rotor will be significant. An example of the stress state in the high rotor is shown below.

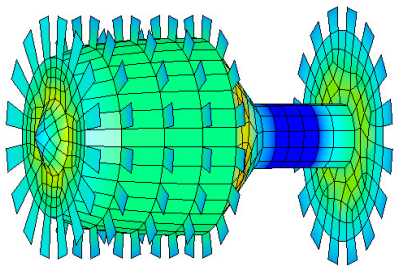

Figure 3.27 Steady state stresses in spinning rotor

3.3.13 Low Speed Rotor

The pictures below show the low speed rotor. The bearing is simulated by coupling coincident nodes to the static structure and has already been fully described. There is a contact interface (with sliding and friction) between the blade tips and the case. Recall that the low speed rotor passes through the high speed rotor.

Figure 3.28 Low Speed Rotor Mesh (red) [26]

Prior to fan blade off, the steady state centrifugal stresses in the spinning rotor will be significant. An example of the stress state (the yellow/red regions are set to be near yield strength while the blue regions are relatively unstressed) in the low rotor is shown in Figure 3.29.

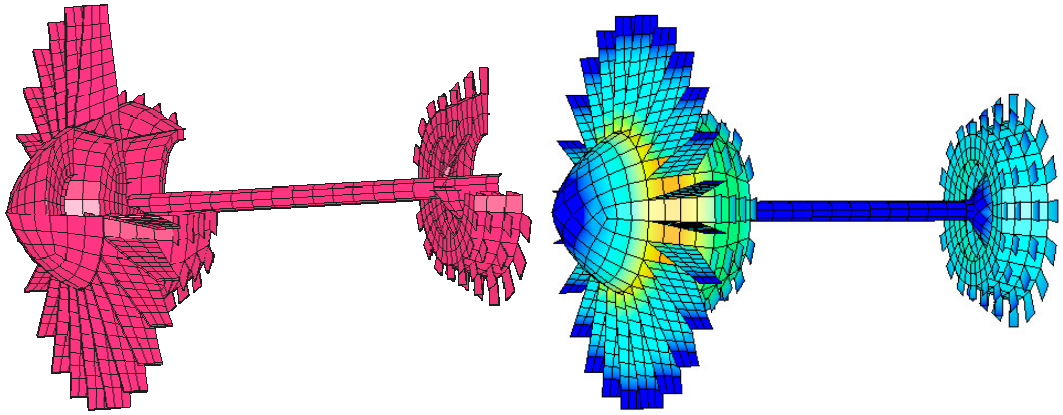

Figure 3.29 Low Speed Shaft beam elements. Steady state stresses in spinning rotor

The fan blade off event will be initiated by releasing a single blade (yellow and pink blade below) at the root of the blade. The nodes at the root of the blade are tied to the rotor surface with a bonded contact definition; at time $t_{release}$ this contact definition is deleted, and with no centripetal force to constrain the blade, the fan blade off event is triggered.

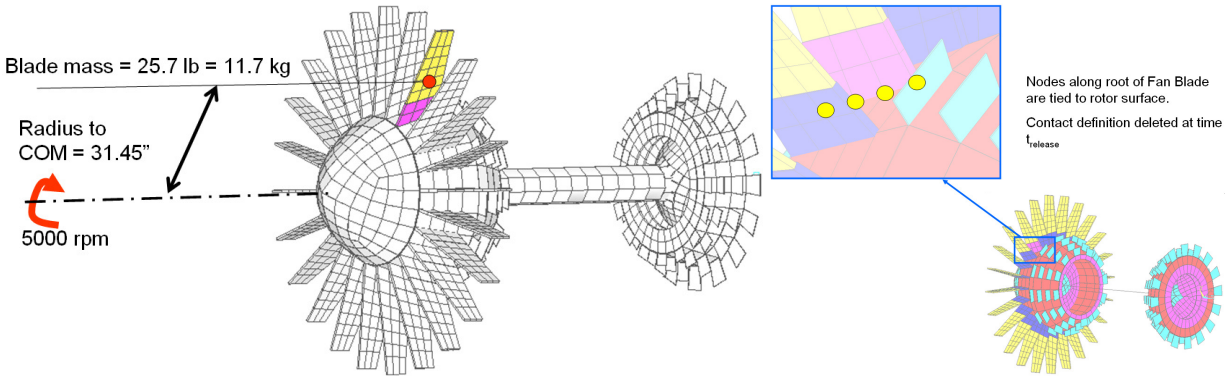

Figure 3.30 Low Speed Shaft beam elements. Steady state stresses in spinning rotor

The specific LS-Dyna script used to tie the blade root to the rotor and 'fail' at $t_{release}$ was:

```
*CONTACT_TIED_SHELL_EDGE_TO_SURFACE
      44       2       4       0       0       0       0       0
 0.000   0.000   0.000   0.000   0.000          0 0.000  0.3000E-01
 1.000   1.000   0.000   0.000   1.000   1.000   1.000   1.000
```

It is also important to note that the fan blade-to-fan blade contact is also defined. How adjacent blades may strike each other after the FBO release is illustrated in Figure 3.31.

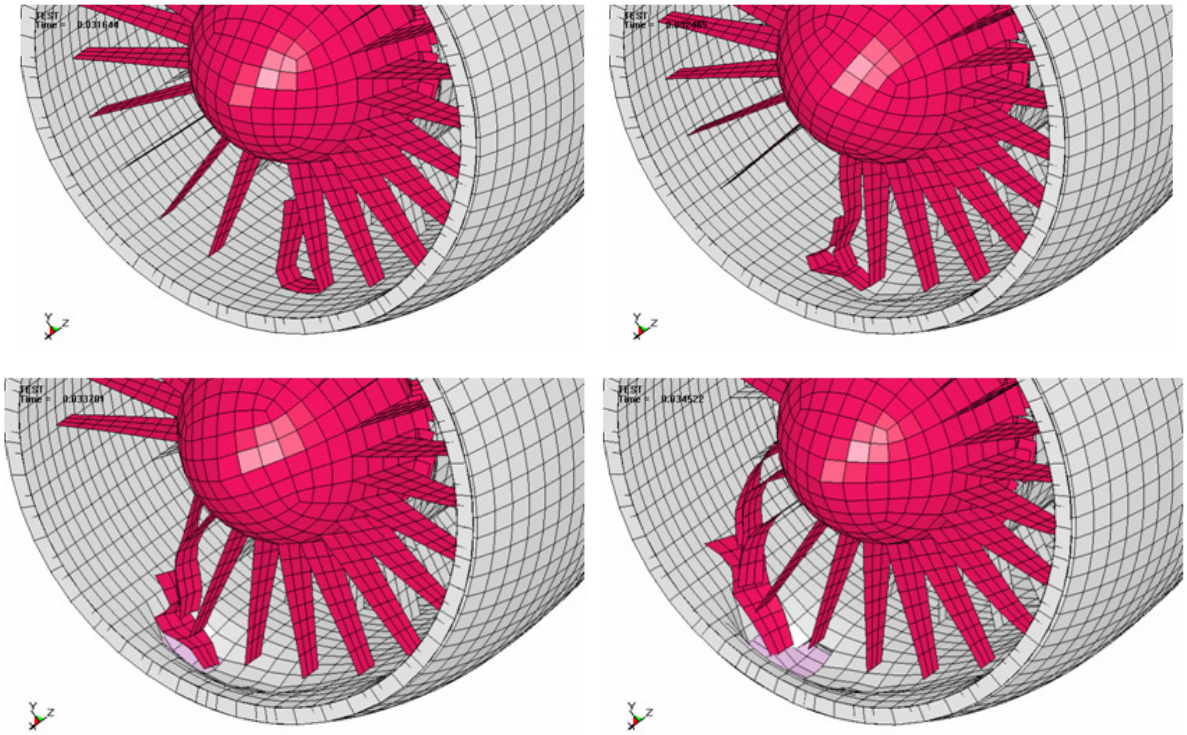

Figure 3.31 Blade to blade and blade to case interactions.

3.4 Geometry and Weight of Baseline Model

Some basic geometry and weights for the baseline model is provided in Figure 3.32.

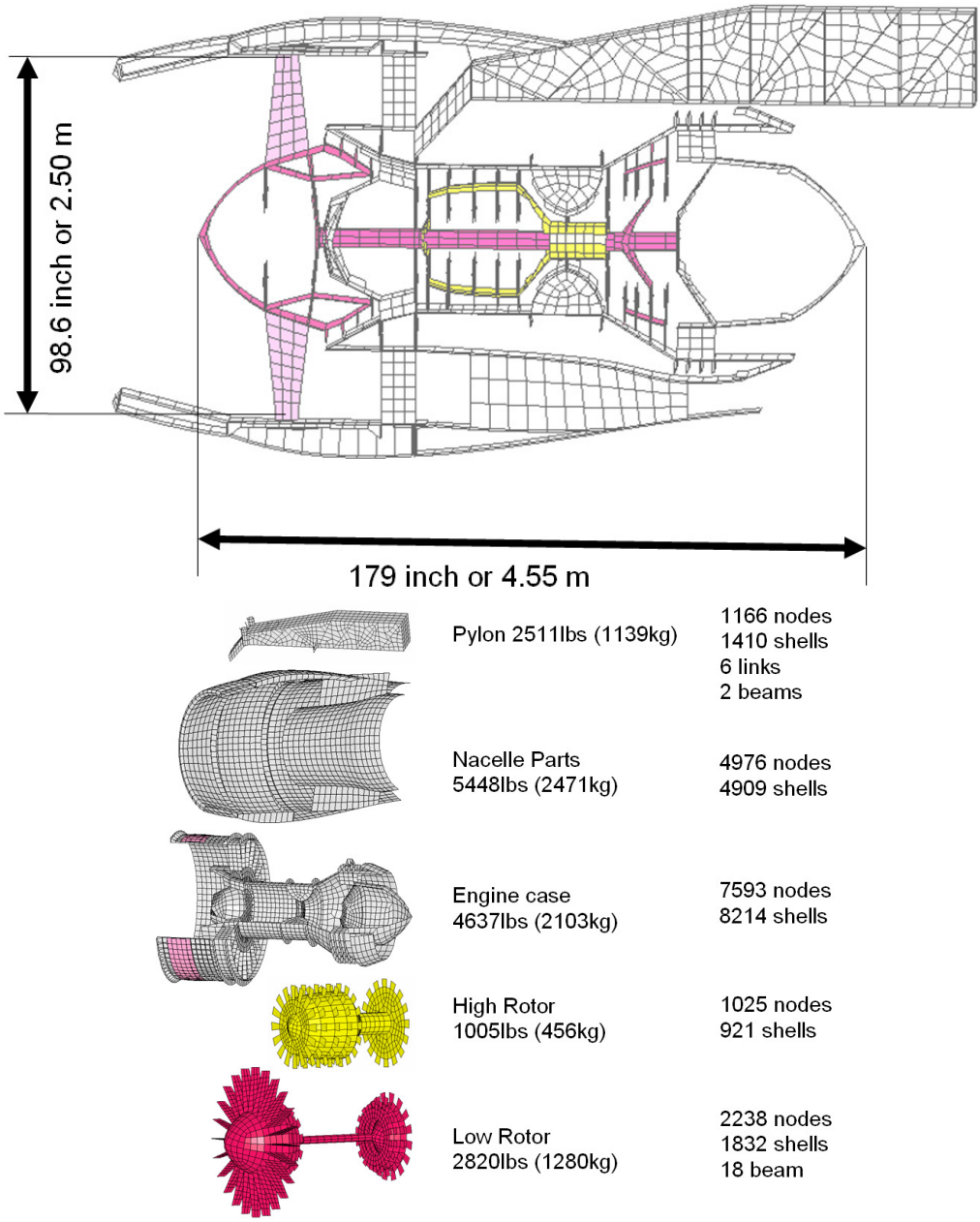

Figure 3.32 Dimensions and weights of baseline model

The basic system masses of the baseline model also provided. The baseline model is primarily constructed of 4 node shell elements. Some spar elements are used for pins and a beam element is used for the low rotor shaft. The total node count is about 17,000. The total element count is about 17,000.

3.5 Rotor to Static Case Connection

Modeling the bearings in detail is beyond the scope of this work for two main reasons. Firstly, high speed bearing are enormously complicated and we are only interested in their kinematics; secondly, these are often manufacturer rated to sustain particular loads and the stress analysis by engine builders is not required (although the bearing manufacturers will generally perform stress analysis on their parts).

For simplicity, bearings will be simulated by coupling coincident nodal DOF (degrees of freedom) between cases and rotors. It is important to understand that the front (or forward) bearing is a thrust bearing (ran react both radial and axial loads). Conversely, the rear (or aft) bearing can take only radial loads.

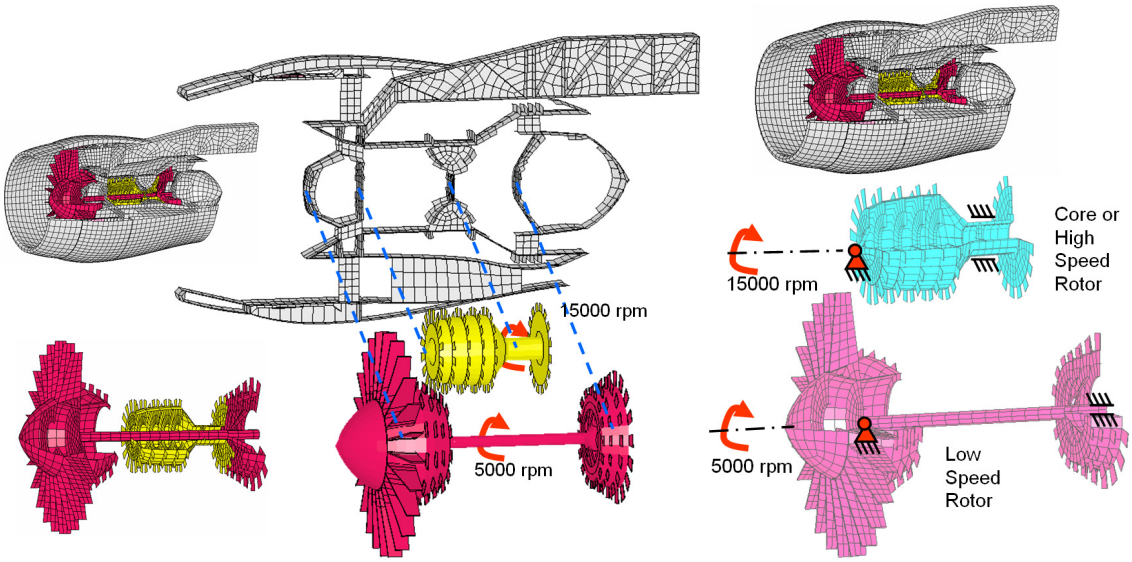

Figure 3.33 Coupling used to simulate bearing connections.

3.6 Engine Mounting to Pylon

The pictures below explain the pylon. This structure suspends the engine as well as the fan bypass doors and a portion of the fan cowl. The nodes along the aft (far right) edge are fixed in all translation DOF.

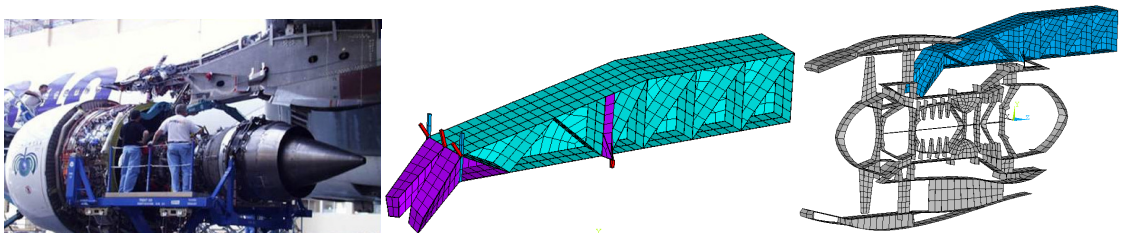

Figure 3.34 Pylon Shell Mesh

The jet engine is mounted to a pylon as shown below. The primary pylon-to-engine connection occurs by bolting at the intermediate case. This connection is simulated using bonded surface-to-surface contact. The engine is further connected at the turbine exhaust case by link elements.

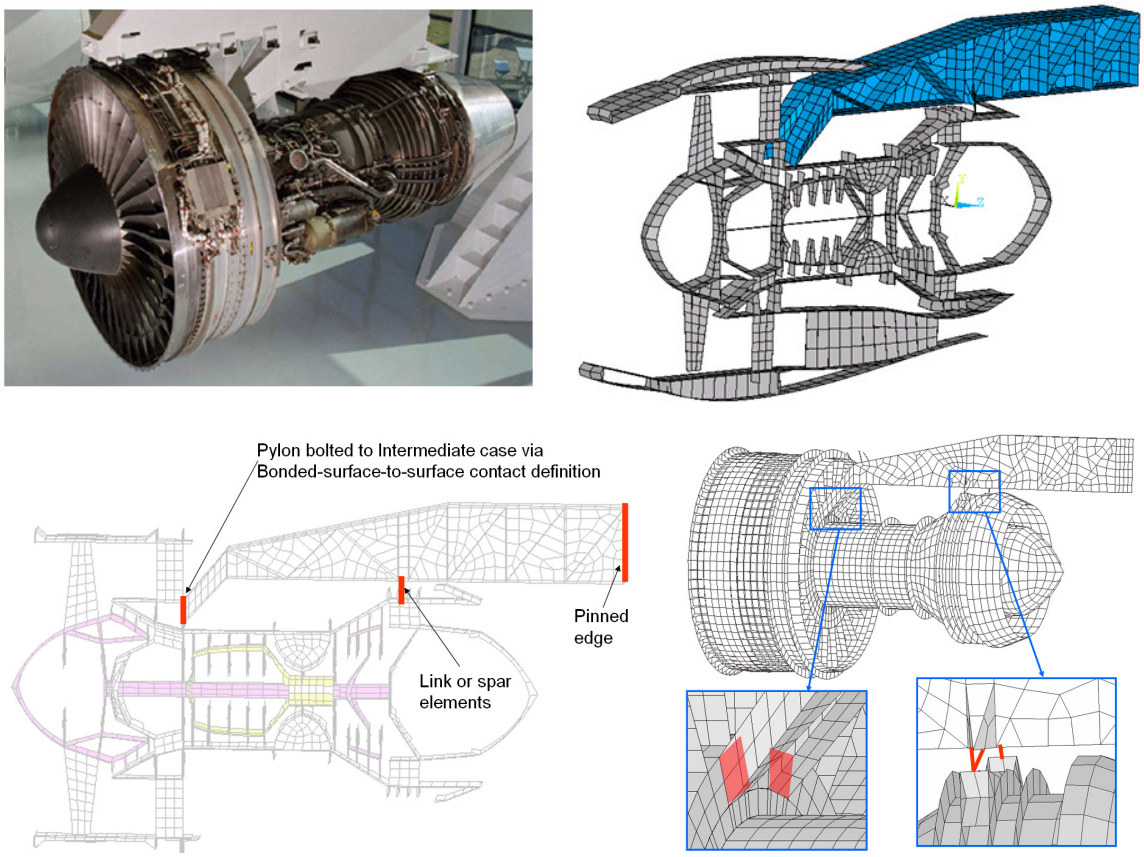

Figure 3.35 Pylon to Engine Connection [27]

The pinned DOF along the aft edge of the pylon was done to simplify the baseline model. For better accuracy, the airframe compliance (or frequency dependent impedance) could be included but this was outside the scope of this work.

3.7 Connecting the Cases: Bolted Connections

Many of the components are bolted together along flanges as shown below.

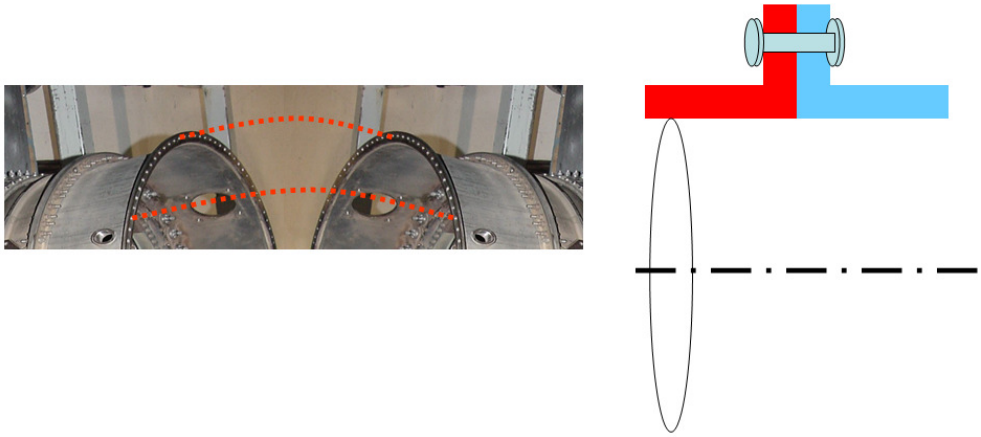

Figure 3.36 Schematic of bolted flange connecting two cases.

Surface-to-surface bonding was used to simplify these bolted flanges. The tail cone to turbine exhaust case bonding is illustrated in Figure 3.37.

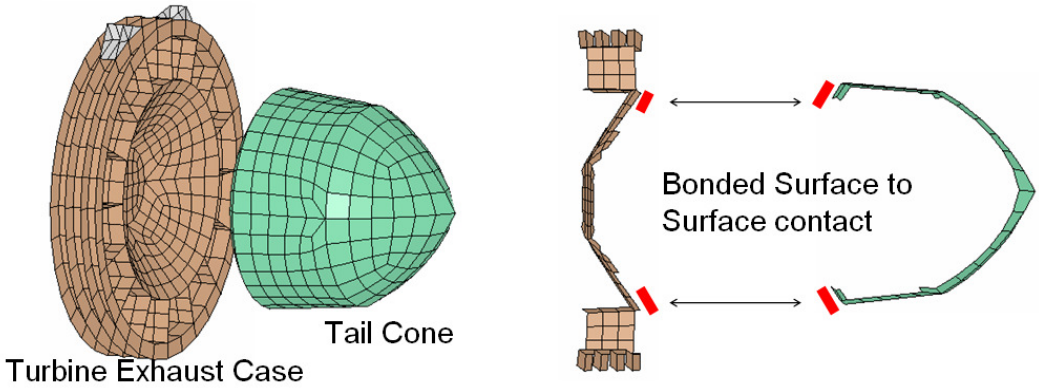

Figure 3.37 Example of surface-to-surface bonding used to simulate bolted joints.

Figure 3.38 highlights the primary surface-to-surface bonding used throughout the baseline model.

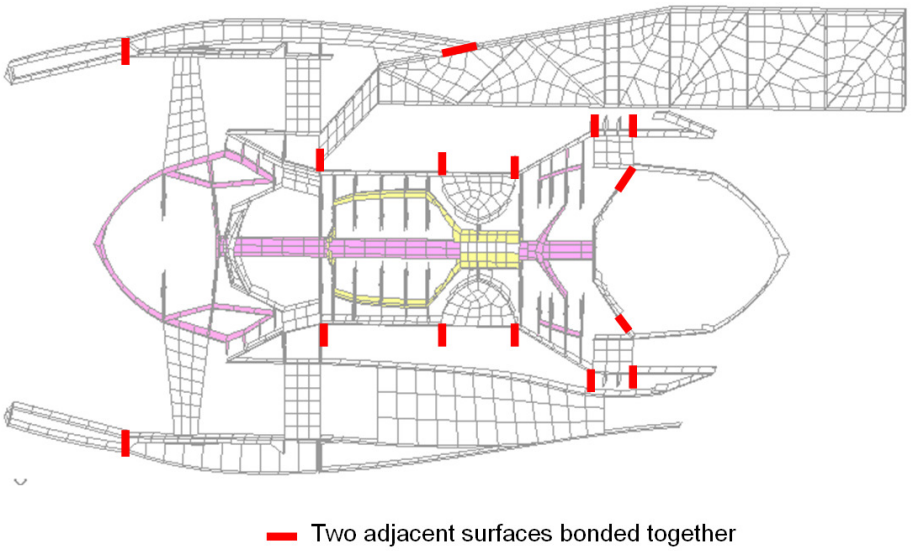

Figure 3.38 bonded surface to surface joints in baseline model

The bonding work well. Examples of both the initial and deformed shapes of several tied flanges are shown below.

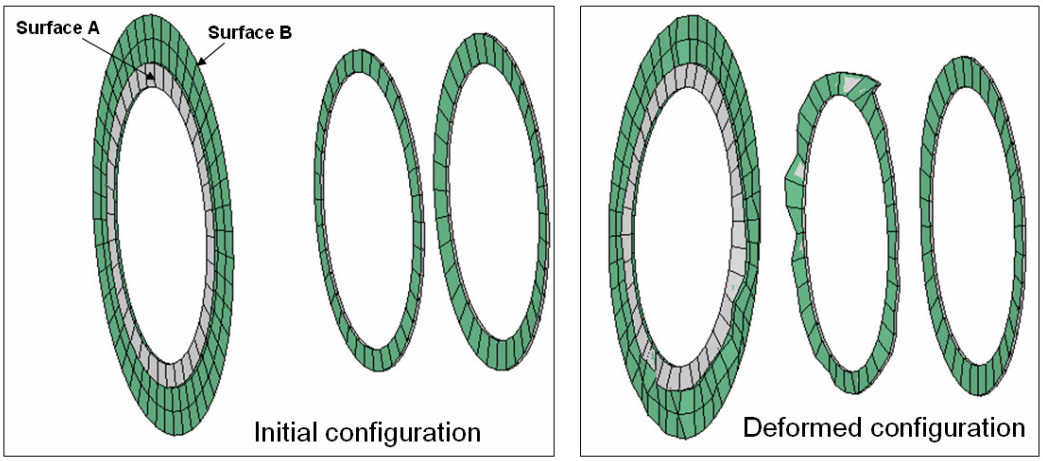

Figure 3.39 Validation of surface to surface bonding

The LS-Dyna code used to create these bonded connections was:

```
*CONTACT_TIED_SURFACE_TO_SURFACE
         6       7       0       0       0       0       0       0
 0.000   0.000   0.000   0.000   0.000           0 0.000   0.1000E+21
 1.000   1.000   0.000   0.000   1.000   1.000   1.000   1.000
```

3.8 Contact Interfaces with Sliding and friction

Other cases are assembled together without being bolted. The rotor blade tips (with a tight clearance) are also running inside the flexing cases. These contact interfaces can withstand compressive only force normal to the surface. When compressed, the surfaces develop friction and can slide tangentially.

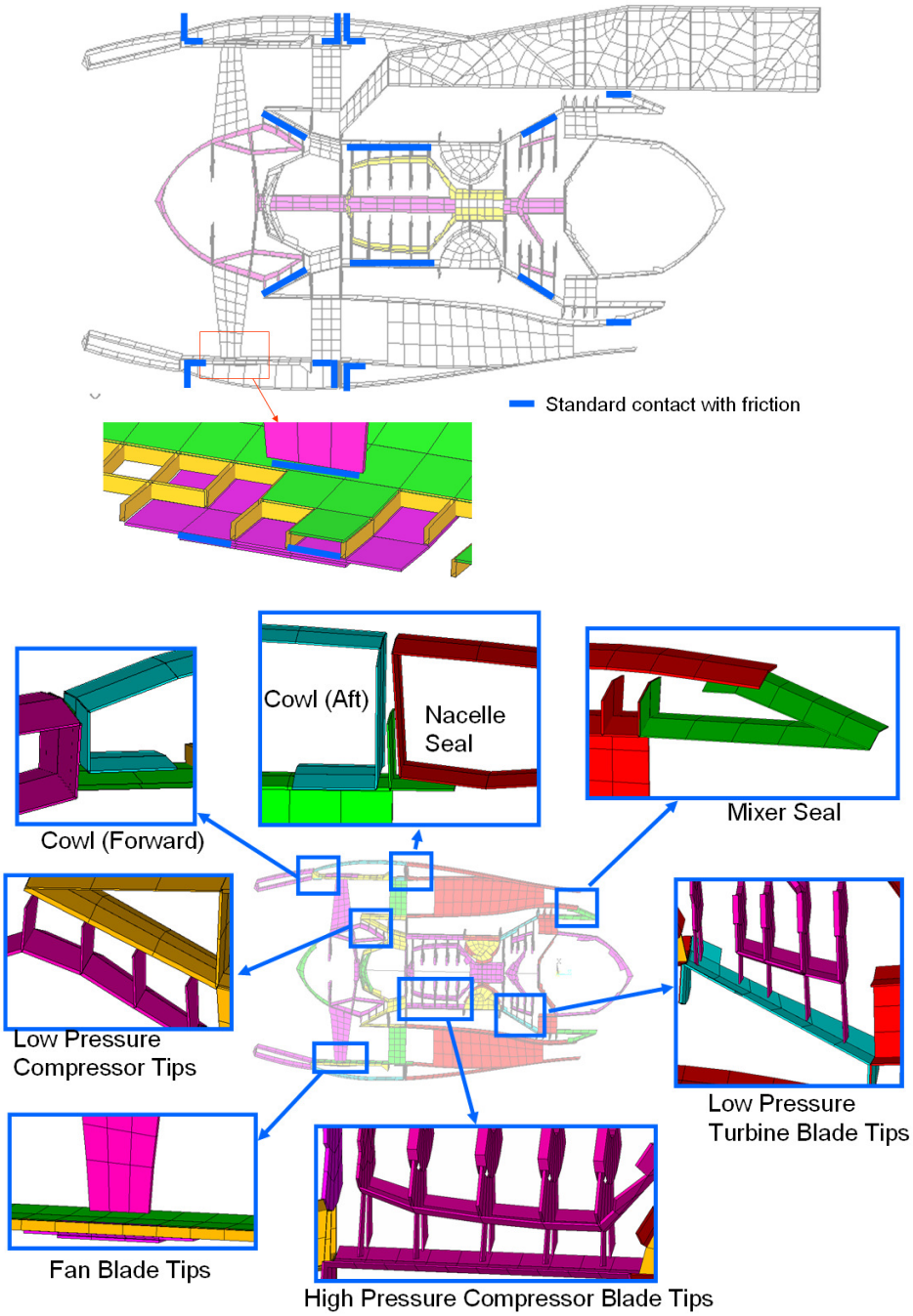

Figure 3.40 Sliding interfaces with contact and friction in baseline model.

Blade tip rubbing against the cases is important. Several blade sets are allowed to rub against the cases. Tip rubbing can occur at the fan blade, low pressure compressor, high pressure compressor and low pressure turbine (shown).

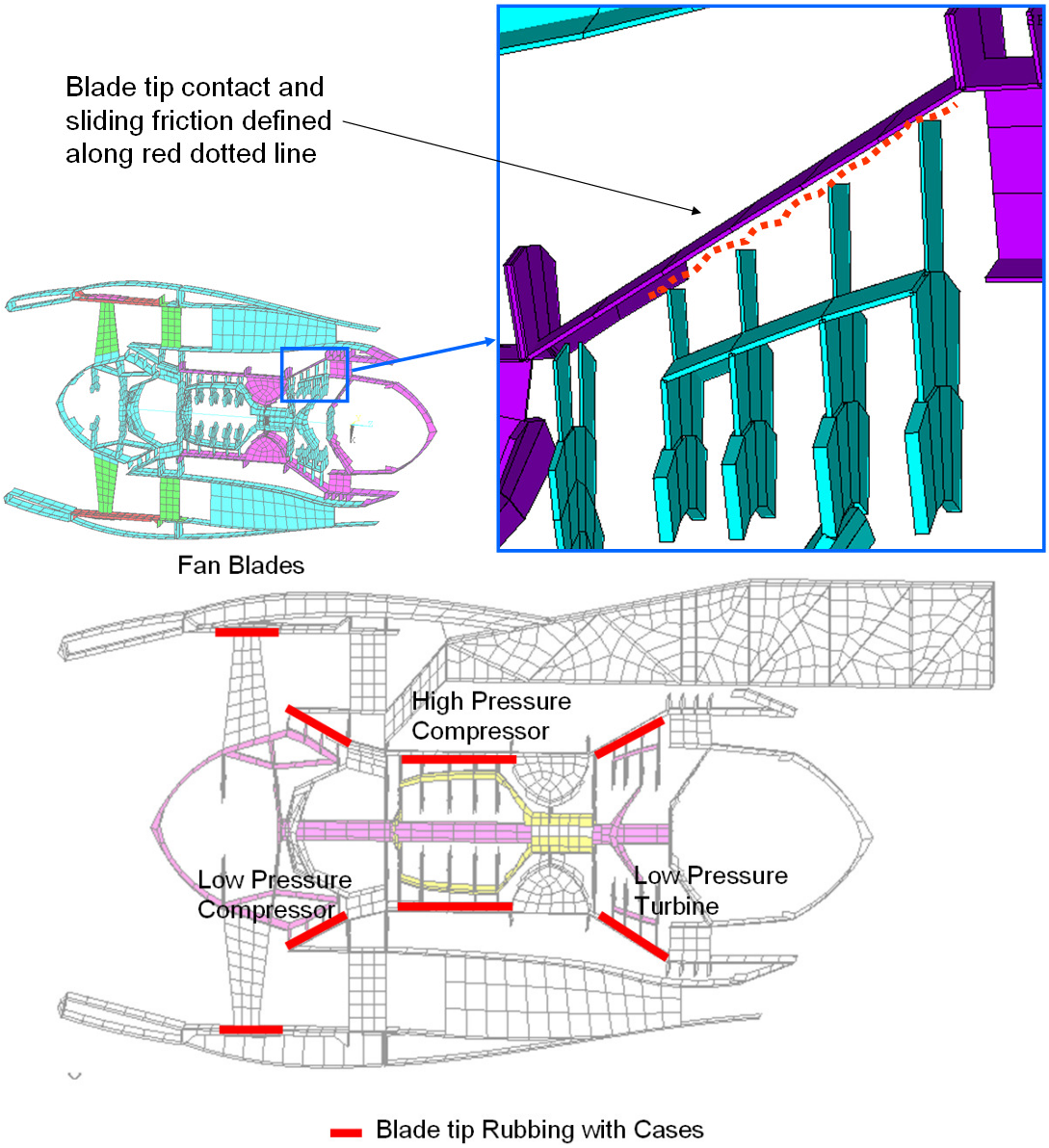

Figure 3.41 Blade Tip Rubbing Locations

Developing and defining robust and efficient contact parameters for large complex finite element models is not trivial; implementation details will be discussed fully in the next chapter.

3.9 Turbofan Materials

Materials typically used in a turbofan engine are shown below in Figure 3.42.

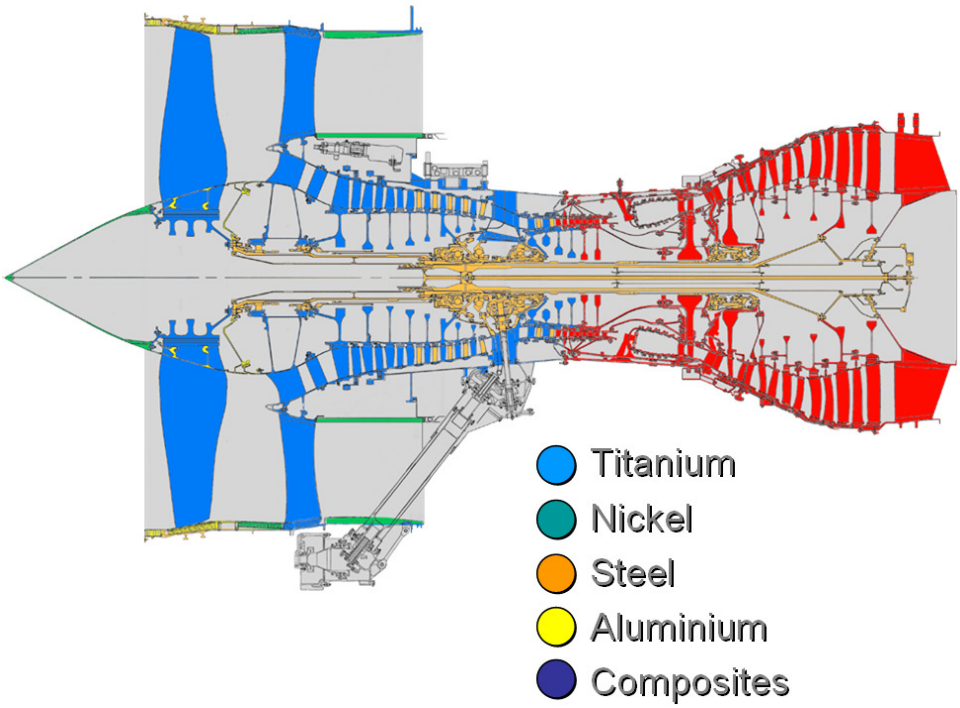

Figure 3.42 Typical Materials in a Modern High Bypass Turbofan [25]

For simplicity, the material distribution shown in Figure 3.43 will be assigned to the baseline high bypass turbofan engine as follows.

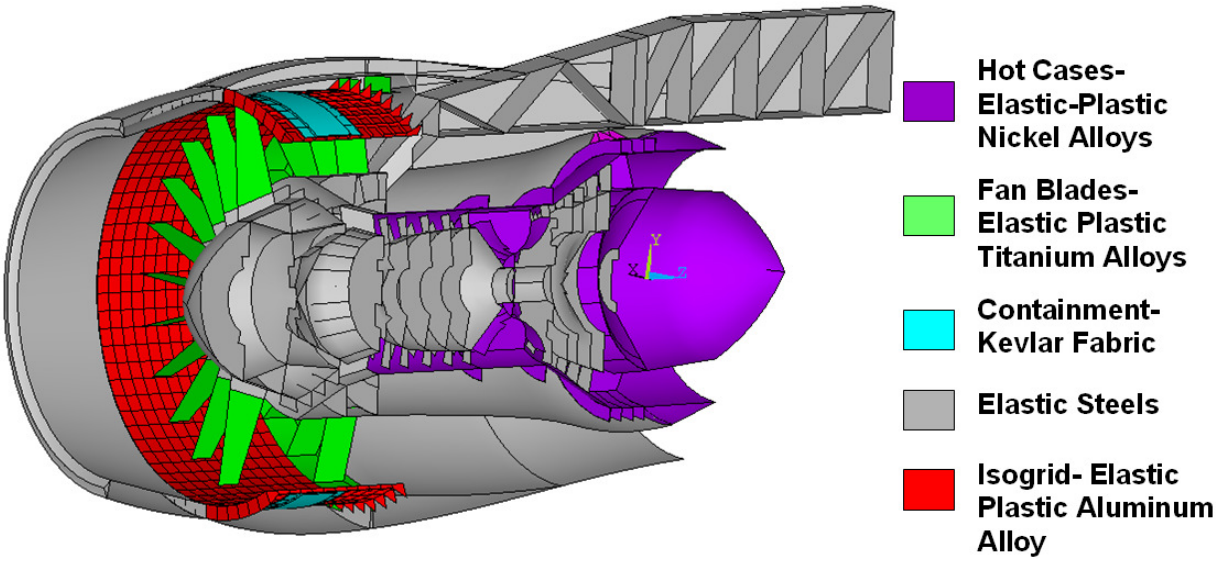

Figure 3.43 Materials Selected for Baseline Model

3.9.1 Developing Large Strain Elastic-Plastic Constants for LS-Dyna

The proposed method was developed for use in full engine modeling of FBO systems due to its large strain capability, simplicity as well as the ability to use existing engineering stress-strain data (which relate to both cost and time). The intent was to provide a starting point for modeling the first order[6] behavior of large strain behavior of complex multi-material structures. Further accuracy studies, calibrations and more advanced constitutive modeling are beyond the scope of this work but are encouraged for the reader.

Most tensile test data are recorded as engineering stress and engineering strain. LS-Dyna constitutive models require input of true stress-true strain constants. Also, since large strain plasticity is expected during fan blade out the proper (true stresses and true strain) data becomes important.

Ultimate tensile strength (UTS), 0.2% offset yield point and reduction of area are readily available mechanical strength data extracted from engineering stress-engineering strain tensile test. This test is demonstrated in Figure 3.44.

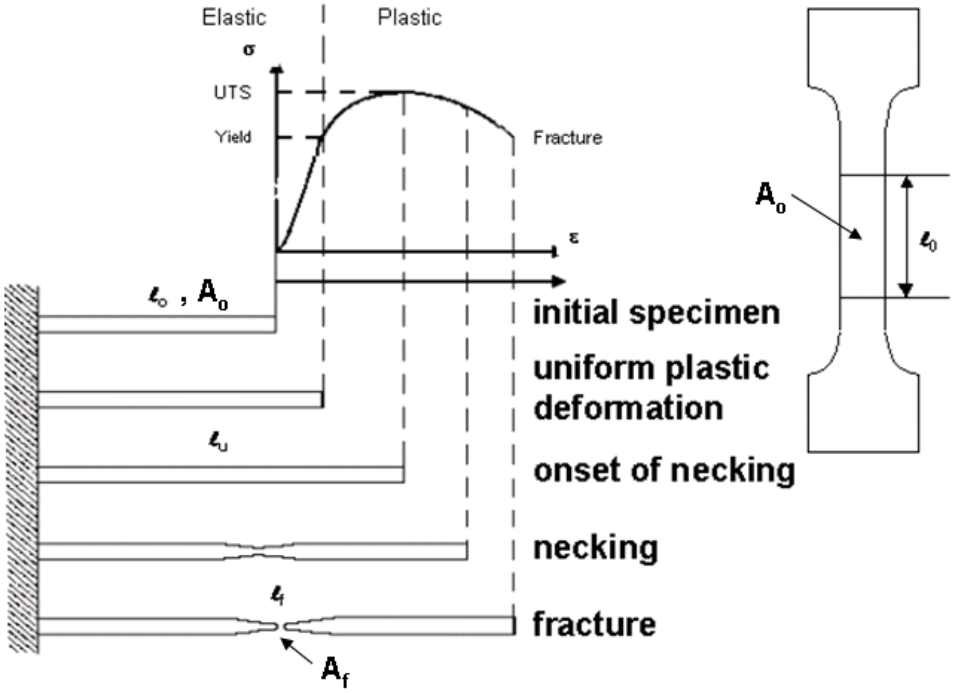

Figure 3.44 Experimental tensile test data

[6] The words 'first order' implies the basic or primary behavior.

For simplicity in LS-Dyna, a bilinear elastic-plastic constitutive model is chosen as shown in Figure 3.45. A typical experimental true stress-strain curve[7] is overlaid on the bilinear curve. This simple constitutive model requires Young's Modulus, E, a yield strength, σ_{yield}, plastic tangent modulus, E_{tan}, as well as a failure strain, ε_{fail}. All constants are based on true stresses and true strains. The material is linear up to the yield point. After yielding a simple isotropic hardening modulus, E_{tan}, governs the plastic strain increments. When the strain in any particular element reaches the failure strain, fail, that specific element is deleted (along with its strength and stiffness) during the LS-Dyna calculation. Note that this element failure criterion occurs dynamically allowing for complete structural failure.

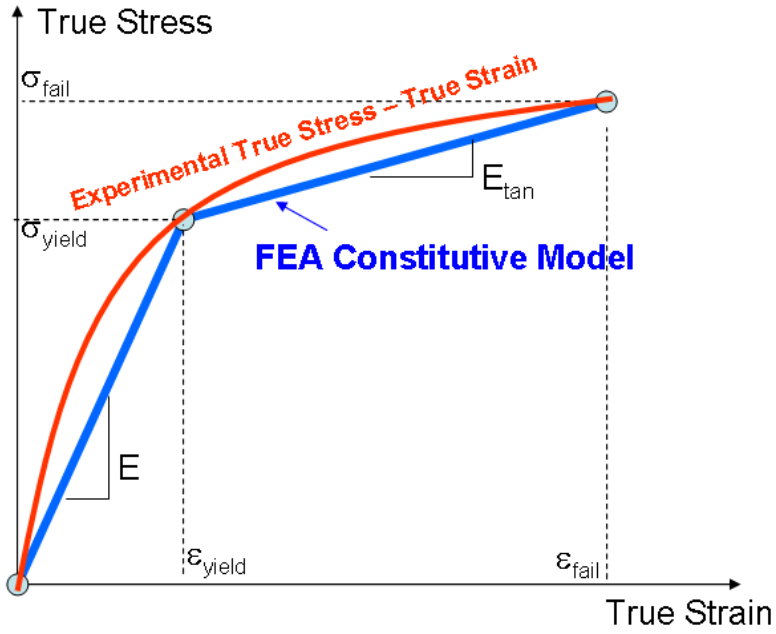

Figure 3.45 Bilinear stress strain curve to approximate yield behavior

The true strain and true stress at failure is approximately:

$$\varepsilon_{fail} = \ln\left(A_o / A_f\right) = \ln\left(1 / 1 - ROA\right) \qquad (3.1)$$

Where ROA=1-A_f/A_o. Note that the final engineering stress, σ^{eng}_{final} is generally not recorded during the typical tensile test; instead this value is approximated as UTS to obtain:

[7] Recall that this is a different shape than the more familiar engineering stress-strain curve.

$$\sigma_{fail} = \sigma_{final}^{eng} \, A_0 \big/ A_{fail} \approx UTS\left(1 \big/ 1 - ROA\right) \qquad (3.2)$$

The plastic tangent modulus, E_{tan}, was approximated as:

$$E_{\tan} \cong \Delta\sigma \big/ \Delta\varepsilon = \sigma_{fail} - \sigma_{yeild} \Big/ \varepsilon_{fail} - \varepsilon_{yeild} \cong \sigma_{fail} - \sigma_{yeild} \Big/ \varepsilon_{fail} \qquad (3.3)$$

Typically, that the elastic component of strain, ε_{yeild}, in the tangent modulus calculation is insignificant (compared to the magnitude of the plastic component and experimental test scatter) and can therefore be ignored. Engineering stress-strain curves for metals are well documented and implementing these elastic-plastic materials into LS-Dyna will be discussed after a short explanation of the effect of strain rate on yielding.

3.9.2 Including Strain Rate Effects: Cowper-Symonds Parameters:

Experiments show that yield strength is affected by the speed of loading. This is an important factor to consider for fan blade out impact simulations. Typically, for many metals, the yield strength increases as the strain rate increases. The Cowper-Symonds parameters, available in LS-Dyna, scale the yield strength to have strain rate dependency according to:

$$YS = YS^{static}\left[1 + \left(\frac{\dot{\varepsilon}}{C}\right)^{1/P}\right] \qquad (3.4)$$

where C and P are experimentally determined particular for a particular alloy, and $\dot{\varepsilon}$ is the Euclidian norm of the deviatoric strain rate tensor. For simplicity in the baseline model only the aluminum isogrid constitutive model will include strain rate effects. The values C=6500 s^{-1} and P=4 were assumed [20]. A typical blade tip strain rate could be determined using the approximation:

$$\dot{\varepsilon} = \Delta\varepsilon/\Delta t \qquad (3.5)$$

where $\Delta\varepsilon$ is the change in strain and Δt is the change in time of the simplified blade strike model. These changes were determined numerically and are shown in Figure 3.46.

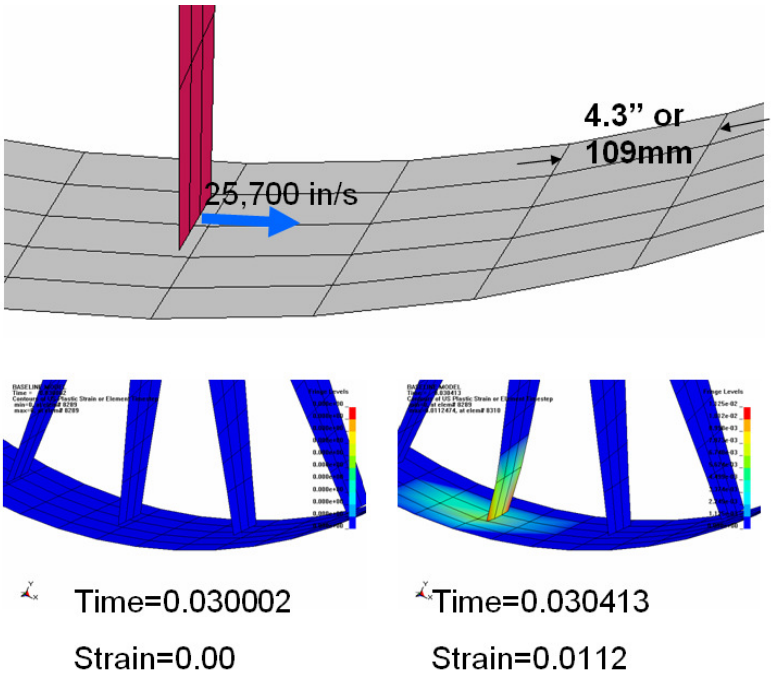

Figure 3.46 Numerical Determination of Strain Rate.

From the figure above we get a typical strain rate of $\dot{\varepsilon} = \Delta\varepsilon/\Delta t = 27\ s^{-1}$. This strain rate was checked in conjunction with the published Cowper-Symonds parameter for aluminum. Figure 3.47 demonstrates a 20% increase in yield strength during high strain rate experienced during initial impact.

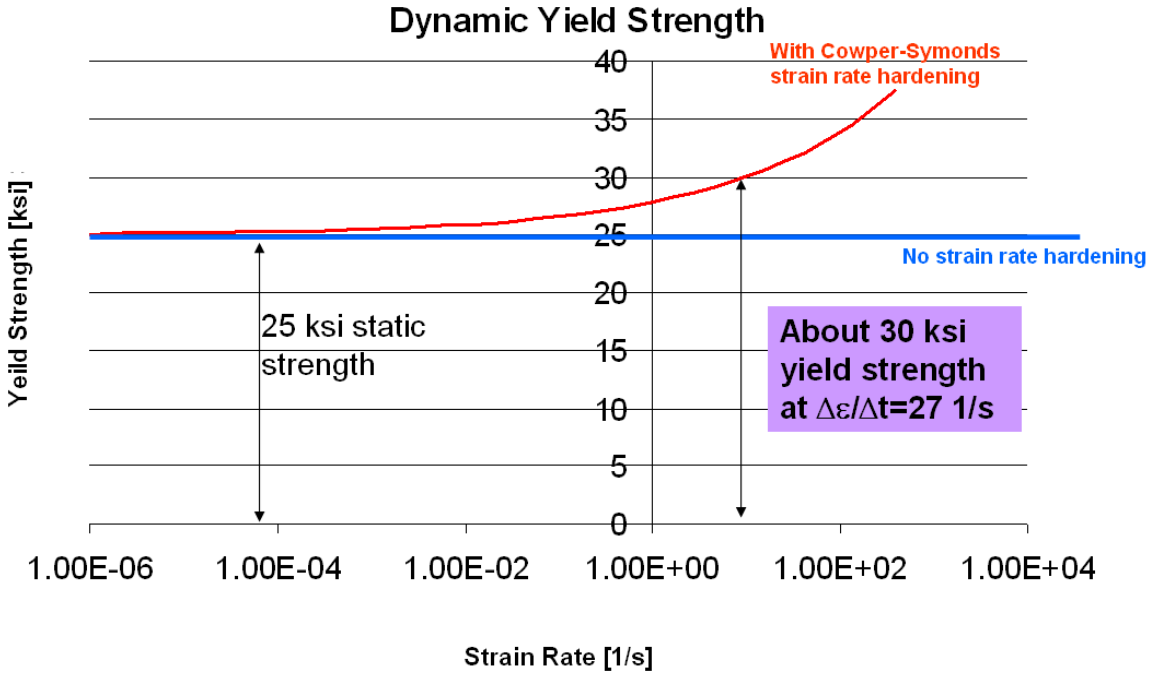

Figure 3.47 Dynamic yield strength predicted by Cowper-Symonds parameters

3.9.3 Zylon Fabric Containment Band Data

Zylon is a fabric similar to Kevlar currently being studied for blade containment. The FAA has contracted investigating the use of high-strength polymeric fabrics as ballistic barriers to protect critical aircraft components against fragments resulting from uncontained failure of a turbine engine [18]. For the reader's convenience, this data is repeated below in Figure 3.48.

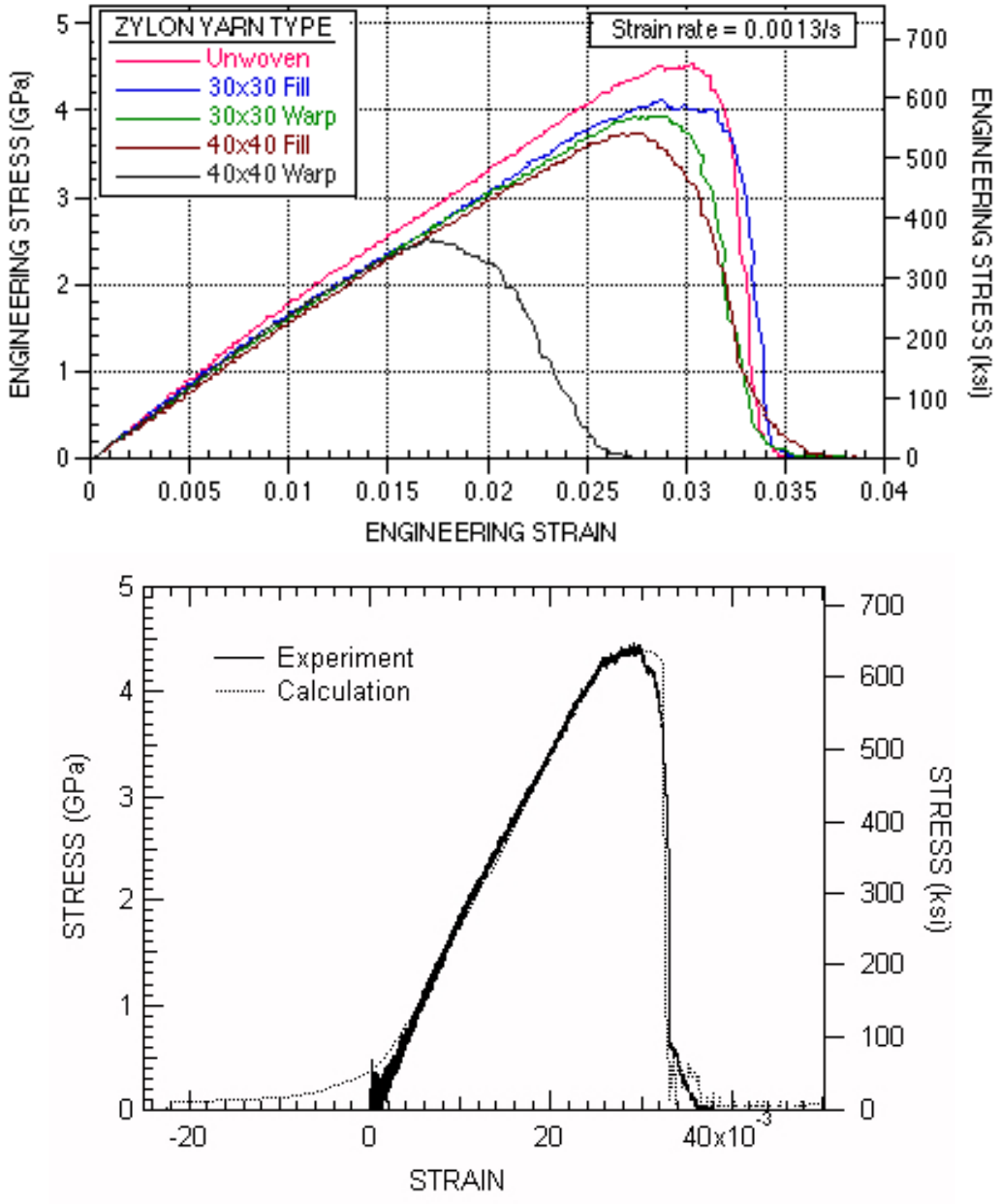

Figure 3.48 Zylon Stress Strain Curves

3.10 Material Summary

Using these equations, the following typical data was used as input for the LS-Dyna constitutive models. A choice was made to use US standard units (inch-pound-second) for the LS-Dyna model. Based on this, providing both SI and US units was not deemed practical and SI was dropped.

Elastic Steel

$E=30\cdot10^6$ lb/in^2	$\nu=0.3$	$\rho=0.3$ lb/in^3

Hot Cases- Nickel Alloy

$E=25\cdot10^6$ lb/in^2	$\nu=0.3$	$\rho=0.3$ lb/in^3
$\sigma_{yeild}=155\cdot10^3$ lb/in^2	UTS$=185\cdot10^3$ lb/in^2	ROA=36%
$\sigma_{fail}=289\cdot10^3$ lb/in^2	$\varepsilon_{fail}=0.45$	$E_{tan}= 300\cdot10^3$ lb/in^2

Isogrid Fan Case- Aluminum Alloy

$E=10.5\cdot10^6$ lb/in^2	$\nu=0.3$	$\rho=0.1$ lb/in^3
$\sigma_{yeild}=25\cdot10^3$ lb/in^2	UTS$=55\cdot10^3$ lb/in^2	ROA=60%
$\sigma_{fail}=137\cdot10^3$ lb/in^2	$\varepsilon_{fail}=0.92$	$E_{tan}= 123\cdot10^3$ lb/in^2
C=6500 s^{-1}	P=4	

Fan Blades/Fan Case - Titanium Alloy

$E=15\cdot10^6$ lb/in^2	$\nu=0.35$	$\rho=0.15$ lb/in^3
$\sigma_{yeild}=140\cdot10^3$ lb/in^2	UTS$=171\cdot10^3$ lb/in^2	ROA=45%
$\sigma_{fail}=311\cdot10^3$ lb/in^2	$\varepsilon_{fail}=0.60$	$E_{tan}= 286\cdot10^3$ lb/in^2

Zylon Fabric Containment Band

$E=0.63\cdot10^6$ lb/in^2	$\nu=0.35$	$\rho=0.05$ lb/in^3
$\sigma_{yeild}=188\cdot10^3$ lb/in^2	UTS$=196\cdot10^3$ lb/in^2	ROA=8%
$\sigma_{fail}=213\cdot10^3$ lb/in^2	$\varepsilon_{fail}=0.08$	$E_{tan}= 291\cdot10^3$ lb/in^2

As an example, the aluminum isogrid bilinear isotropic data implemented into the baseline LS-Dyna model was as follows:

```
*MAT_PLASTIC_KINEMATIC
 3 0.259E-03 0.105E+08  0.300000 0.250E+05 0.123E+06  0.00
 0.650E+04  4.00     0.920
```

The bilinear true stress-true strain material response is summarized on Figure 3.49; the stress (ordinate) units are ksi. Note that the top plot provides small strain resolution (up to 1%) while the bottom plot shows higher plastic strain (to a resolution of about 1).

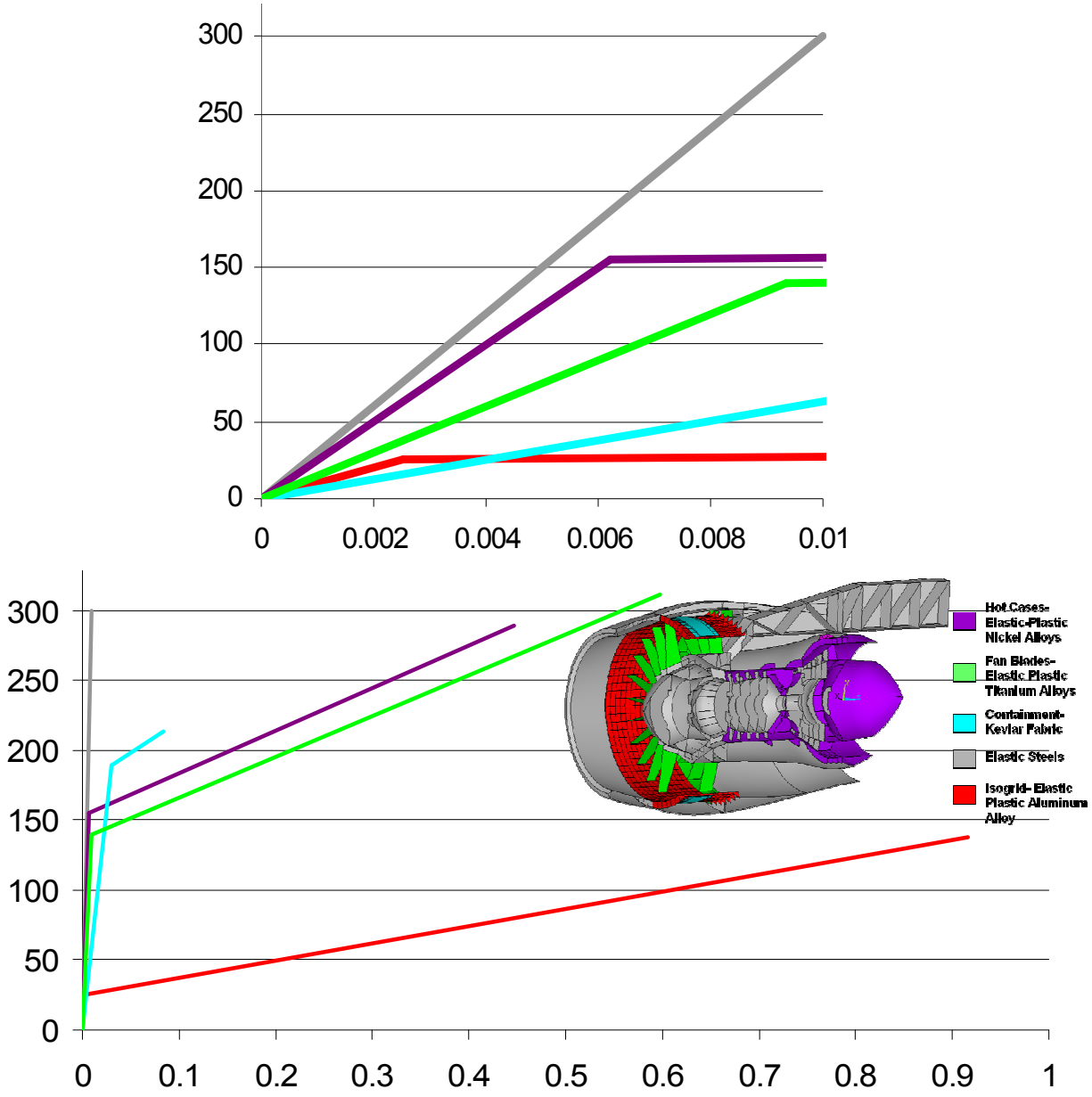

Figure 3.49 Stress-strain summary overview of baseline materials

4 Accuracy Validation of the Baseline Model

The basic geometry, materials and kinematics were outlined in Chapter 3. This Chapter focuses on checks for calibrating and developing LS-Dyna solution defaults and LS-Dyna procedures that validate the accuracy of this baseline model. A choice was made to use US standard units (inch-pound-second) for the LS-Dyna model. Based on this, providing both SI and US units was not deemed practical and was dropped for the numerical results. Also, some LS-Dyna specific syntax used in this work was provided for the LS-Dyna users; full explanations of each LS-Dyna card would overwhelm the FBO discussion.

4.1 Integration Time and Blade Release Time Definition

A 0.15 second total integration time, t_{int}, was chosen. A blade release time, $t_{release}$, of approximately 0.03 seconds was also chosen. The exact $t_{release}$ can be varied slightly to accommodate different blade release angles.

4.2 Identifying Rotor Resonance Issues

After the blade release the unbalanced rotors slow down gradually. The unbalance force provides a harmonic input that may be further amplified through resonance. A pre-stressed modal analysis was performed in ANSYS to identify potential mode shapes that may be harmonically excited to resonate by the unbalanced rotor. Said differently, the spinning speed range of the rotors in 0.15s should not overlap any system natural frequencies.

The expected input speed of the low rotor started at about 5000rpm (83Hz) and might be expected[8] to slow down to 4500 rpm (about 10%) in 0.15s. The pre-stressed (centrifugal stresses at 5000 rpm) eigenvalue solution results are shown in Figure 4.1.

[8] A reasonable spool-down value according to [5,6].

Since no major natural frequencies lie between 83 and 75Hz the low speed rotor should not be affected by resonance.

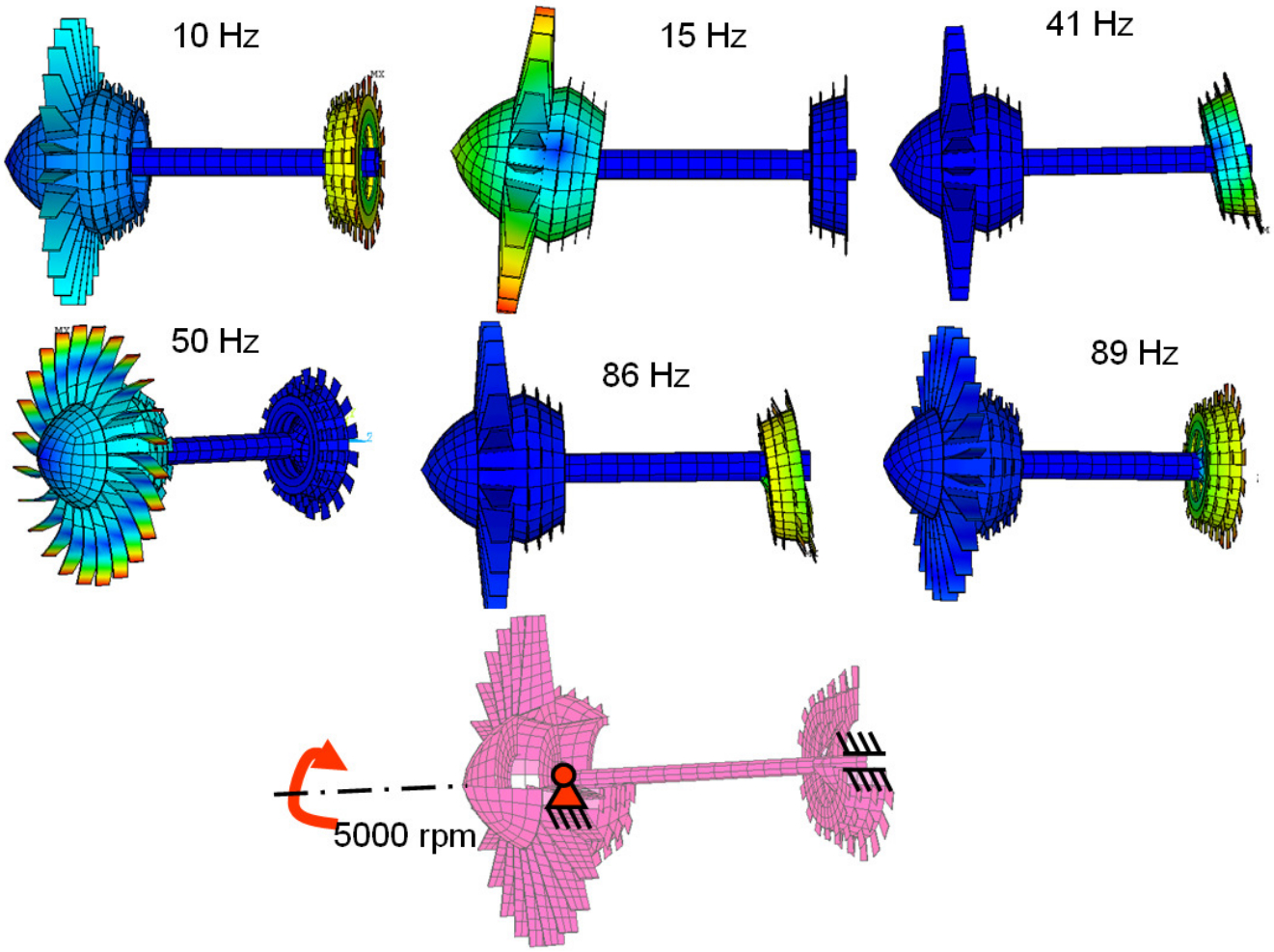

Figure 4.1 Pre-stressed eigenvalue analysis. Low spool mode shapes.

The expected input speed of the high rotor started at about 15,000rpm (250Hz) and would be expected to slow down perhaps 13,500rpm (about 10%) in 0.15s. The pre-stressed (centrifugal stresses at 15,000 rpm) eigenvalue solution results are shown in Figure 4.2.

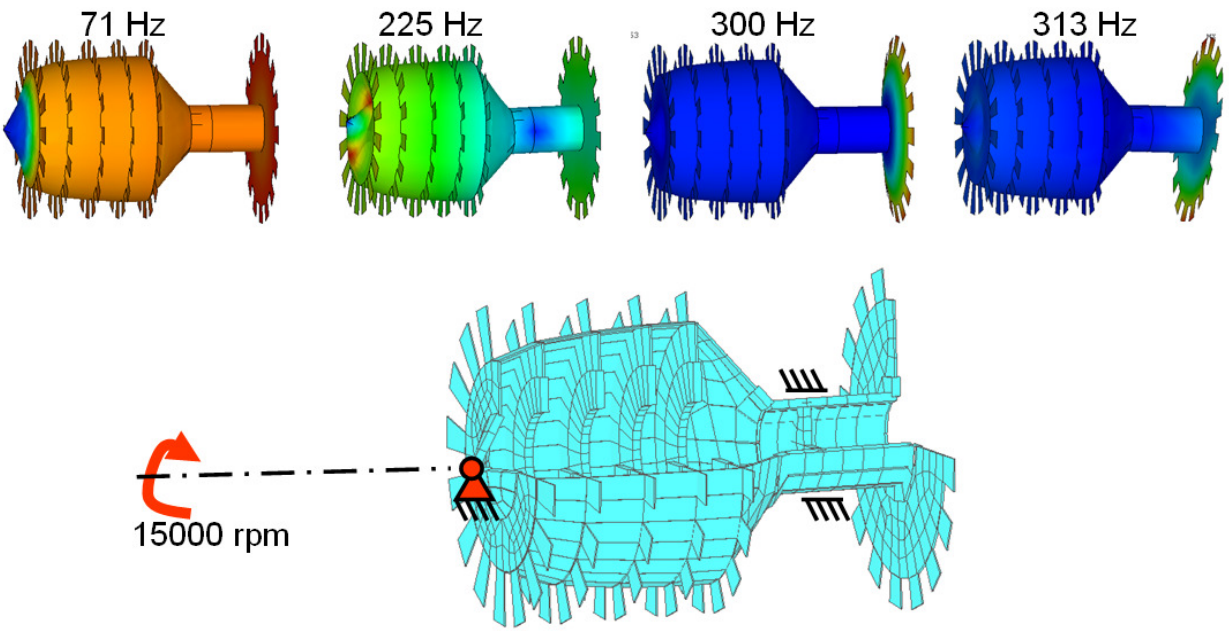

Figure 4.2 Pre-stressed eigenvalue analysis. High spool mode shapes.

There is no issue for the expected range; however, if the integration time was extended, the high speed rotor would be expected to pass through the 225Hz natural frequency and resonance (if there is any small imbalance in the rotor) may become potentially an issue.

4.3 Analytical Estimation of Blade Energy and Imbalance

The released fan blade energy can be found from Figure 4.3. Note that ω=523.6 radians/s and the center of mass velocity is v_{com}= 16,467 in/s or 418 m/s.

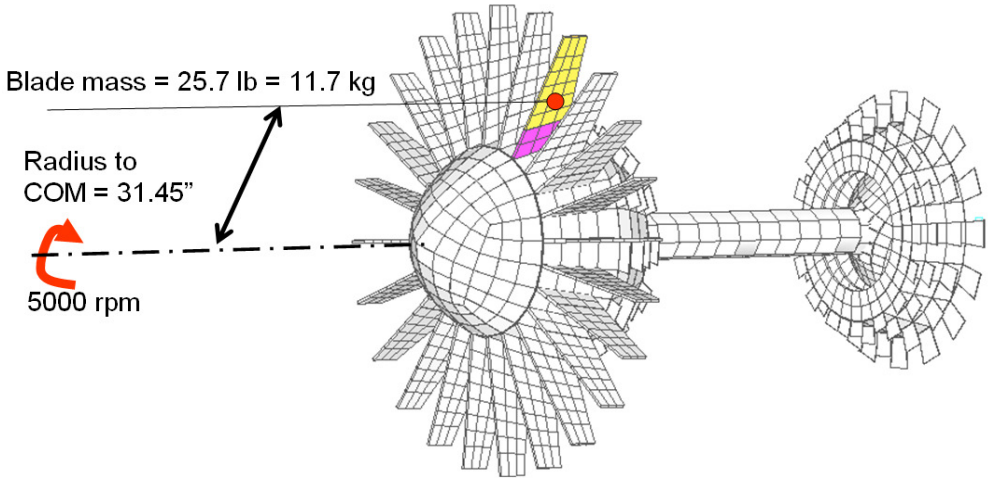

Figure 4.3 Schematic of released fan blade.

For the baseline model, the released fan blade's kinetic energy is:

$$KE = \tfrac{1}{2}mv^2 = \tfrac{1}{2}mr^2\omega^2 = 9.02\cdot10^6 in\cdot lb = 1.02\cdot10^6 N\cdot m \qquad (4.1)$$

The static cases must absorb this energy. For the baseline model, the rotating imbalance acting on the rotor is:

$$F_{unbal} = mr\omega^2 = 573{,}500lb = 2.56MN \qquad (4.2)$$

These values will be later used to compare results from the simulation.

4.4 Unbalanced Force

As stated previously, the blade release is initiated by deleting a tied contact defining at the root of the blade at $t_{release}$=0.03s. This force magnitude was estimated from (4.1) as $F_{unbal} = mr\omega^2 = 573{,}500lb$. Some contact reactions from the baseline model are extracted in Figure 4.4. The plot on the right shows the time history of the force exerted by the released blade. Note the sinusoidal component of vertical component of force. This is consistent with the expected rotating steady state amplitude. Also note that the force drops to zero after $t_{release}$=0.03s as expected. This magnitude is very close to the estimated load. The plot on left shows the force exerted by the remainder of the blades.

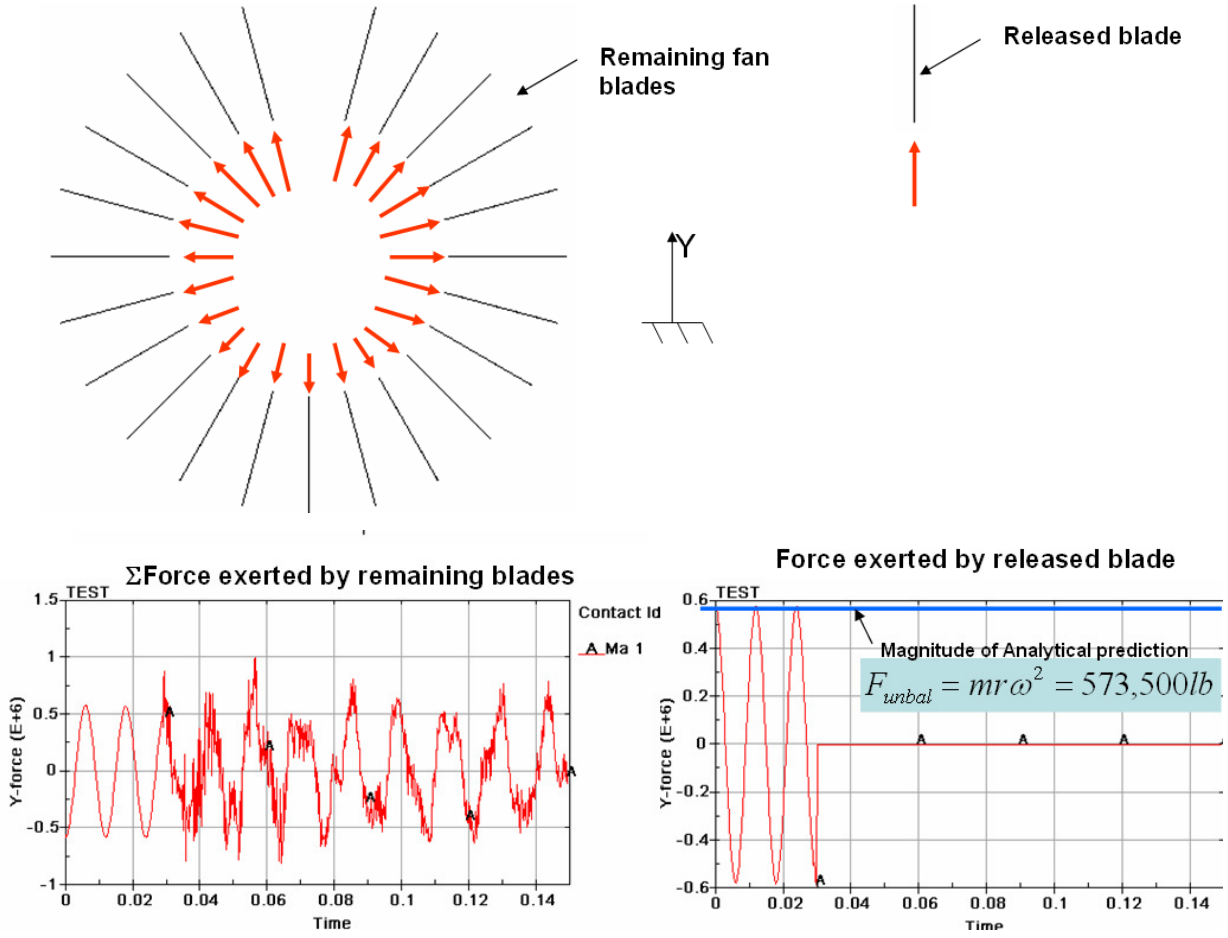

Figure 4.4 Vertical Force on remaining blades (left) and released blade (right).

Note how at time=0 through $t_{release}$ the remaining blade forces balance the released blade force demonstrating equilibrium.

4.5 Discussion of Energy Dissipation Mechanisms

The large rotor kinetic energies must be absorbed by the cases, either converted into friction work or dissipated as heat through plastic deformation. Some primary energy absorption mechanisms which were included in the baseline model are:

1. Strain energy- work done by strains
2. Sliding energy- work done by sliding friction
3. Viscous blade work- air compressed by spinning rotors

The implementation of these is important and will be further discussed later in this chapter.

Each energy dissipation mechanism is physically based and independent of one another. This distinctive approach is particularly attractive for accurate simulations/calibrations when compared current literature methods of applying 'global damping' which 'smears' all the energy dissipation mechanisms into one homogenous value.

Some energy dissipation mechanisms that were excluded from the baseline model were

1. acoustic losses
2. heat generation and thermodynamics
3. hydrodynamic bearing breakdown friction

Regardless of which energy conversion forms are included or excluded, energy conservation laws will be used to validate the LS-Dyna simulation and to understand which parameters are important for accurately simulating Fan Blade Off.

4.6 Conservation of Energy in Explicit Computations

For the baseline model, LS-Dyna tracks and stores the global system energy components over the prescribed integration time. Monitoring this information can detect problems or error accumulation in the system. By global system we mean all elements, nodes and interfaces in the model. Figure 4.5 shows, for the global system, the total energy, kinetic energy, internal energy (work done by stress and strain), damping energy, Hourglassing energy (more on this later), as

well as sliding friction energy dissipation. Energy units are in inch·pounds and time is in seconds. These energies will be broken down into components in later sections.

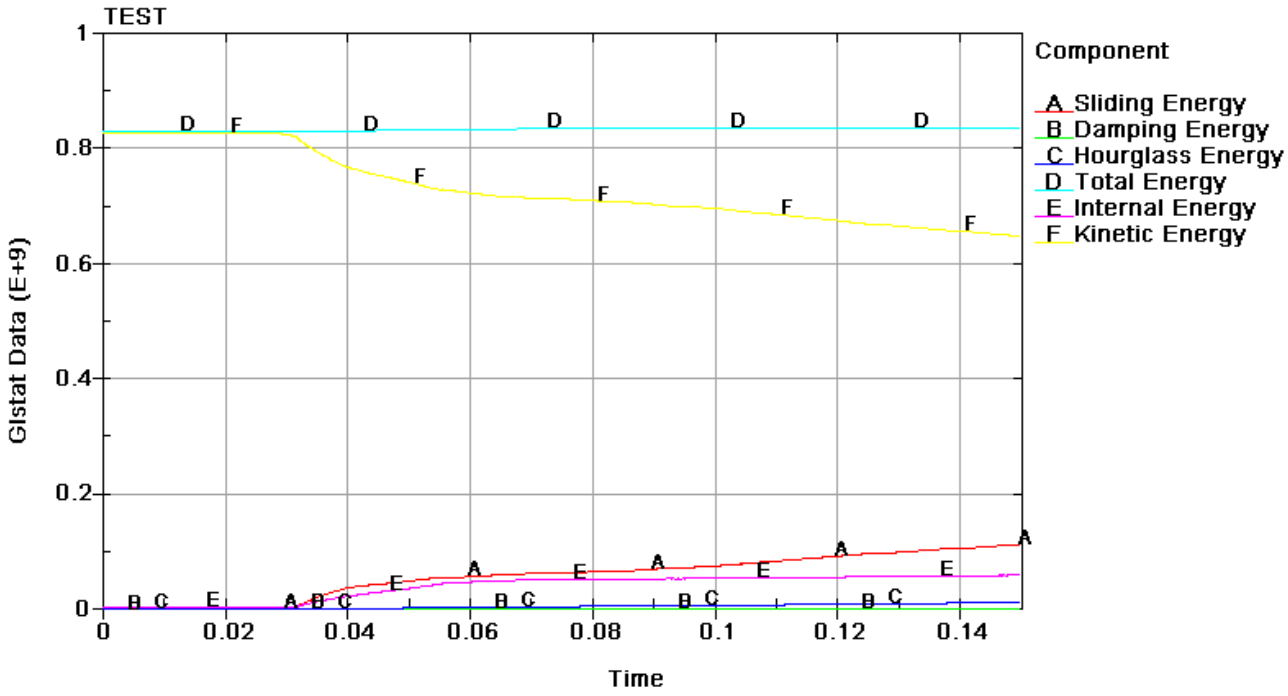

Figure 4.5 Global energy balance of entire system

Note how the kinetic energy is flat until 0.03s which corresponds to blade release; after blade release the kinetic energy drops with the expected rotor slow down.

After $t_{release}$ the strain, sliding and damping energies increase as expected. The total energy, E_{total}, is approximately constant during the integration period demonstrating that LS-Dyna is enforcing the law of conservation of energy:

$$E_{total} = E_{Kinetic} + E_{damp} + E_{sliding} + E_{Strain} = \text{constant} \qquad (4.3)$$

Hourglass energy is a non-physically based energy that forms due to difficulties in mathematical formulation of the reduced integration shell elements. Negligible hourglassing energy in a simulation is desirable. There will be further hourglassing discussion in a later section.

4.7 Strain Work

The rotor's kinetic energy can be absorbed by straining the structure. The amount of strain work, W_{int}, absorbed by the structure is:

$$W_{internal} = \oint_v \sigma : \Delta\varepsilon dv \qquad (4.4)$$

Where σ is the current stress and Δε is the work conjugate increment of total strain. Recall that total strain includes both elastic and inelastic components; however, at a practical level the plastic strains are often much larger than elastic strain therefore the strain work is approximately the plastic work. Analytically, this integral is intractable for a multi-body large deformation problem; however LS-Dyna conveniently computes and stores this data. Global strains were stored by issuing:

```
*DATABASE_GLSTAT
0.1500E-03
```

Strains energies in individual components were stored by issuing:

```
*DATABASE_MATSUM
0.1500E-03
```

LS-Dyna syntax is provided for the interested LS-Dyna user; other readers can ignore specific LS-Dyna commands.

4.8 Sliding Work at Contact Interface

Friction in contact interfaces dissipates rotor kinetic energy. This friction work, $W_{sliding}$, is computed over all sliding interface surfaces as:

$$W_{sliding} = \oint_a \mu_{slide} \vec{t} \cdot \Delta\vec{x} da \qquad (4.5)$$

where μ_{slide} is the coefficient of friction, the surface traction vector, t, is defined as the stress-normal vector product $\sigma\vec{n} = \vec{t}$, and Δx is the sliding distance increment. Note that other case-to-case sliding interfaces (i.e. hinged doors, etc.) can dissipate sliding work as well. This integral is calculated by LS-Dyna during solution. Results from this are stored by issuing:

```
*DATABASE_SLEOUT
0.1500E-03
*DATABASE_GLSTAT
0.1500E-03
```

4.8.1 Shear Slippage Assumption at Contact Interfaces

LS-Dyna easily handles standard Coulomb friction and additionally incorporates a maximum shear slippage model as shown Figure 4.6. Physically, this slippage friction is based on material yield strength in shear. For this study, a constant value of 20,000psi (approximately the shear strength of aluminum) was prescribed[9] as a starting point.

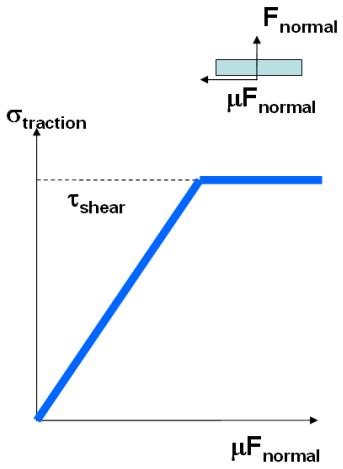

Figure 4.6 Friction Stress limited by material yield strength

More generally, the rotor blade tips are coated with an abrasive material and the cases have an ablative rub strip (see Figure 4.7) so computing a constant slippage shear would be challenging (particularly as the coatings are worn away during FBO). LS-Dyna has the capability for the user to create a more sophisticated user-programmed contact model [1,2].

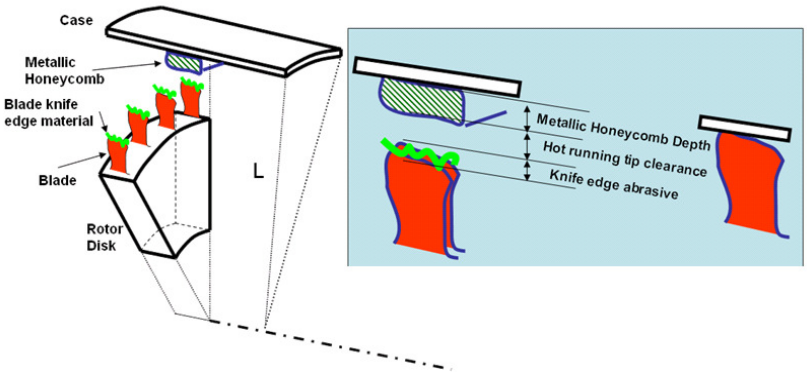

Figure 4.7 Modeling friction can become very complex.

[9] Other ablative materials and coatings may be present at the tip rub but quantifying this is well beyond the scope of this project.

4.8.2 Friction Modeling and Assumptions at Contact Interfaces

The sliding interface friction coefficient is dependent [1,2] on the relative velocity, V_{rel}, of sliding segments. This is governed by:

$$\mu = \mu_{dyn} + \left(\mu_{static} - \mu_{dyn}\right) \cdot e^{-DC \cdot Vrel} \qquad (4.6)$$

For the baseline model, the static and dynamic friction coefficients were prescribed[10] as μ_{static} =0.4 and μ_{dyn} = 0.2 where DC is a decay coefficient. The blade tip speeds (both high and low rotors) were found to be about 30,000 in/s. DC was prescribed to 1/10,000 setting $DC \cdot V_{rel}=3$ (three time constants or about 98% decayed) at the blade tip speeds.

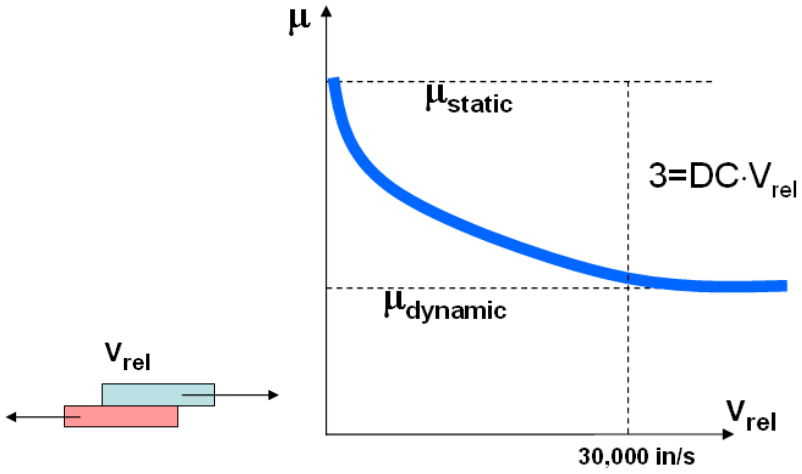

Figure 4.8 Smooth transition from Static to dynamic friction

This is illustrated in Figure 4.8. Again, LS-Dyna has the capability for the user to create a more sophisticated user-defined contact/friction sliding model; more information is available in [1]. For this model a simpler approach was taken as explained above.

[10] Friction coefficients arbitrarily prescribed for this academic study. In principle, these values would be a variable to be calibrated by some experimental testing.

4.9 Aerodynamic Damping

After the FBO occurs, the fuel is cut off and aerodynamic drag will tend to decelerate the rotors. This effect will be modeling by including part based mass damping to the blades. The viscous drag applied to the blades is expected to be proportional to the rotor speed.

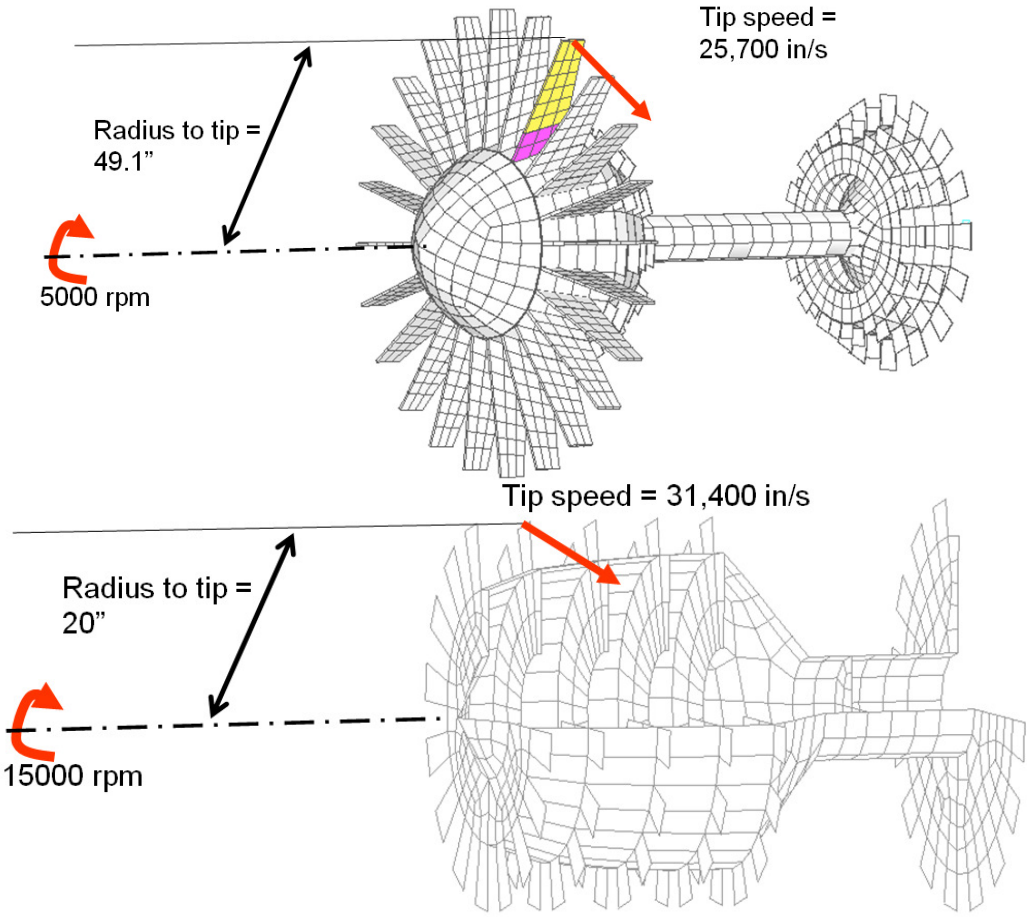

Figure 4.9 Spinning rotors

This resistive damping effect can be simulated by defining mass damping on the blade nodes. The damping force, F_{damp}, applied to each node will be:

$$\vec{F}_{damp} = -D(t)m\vec{v} \qquad (4.7)$$

where m is the mass of a node, v is the node velocity, and D(t) is a user prescribed curve as defined in Figure 4.10.

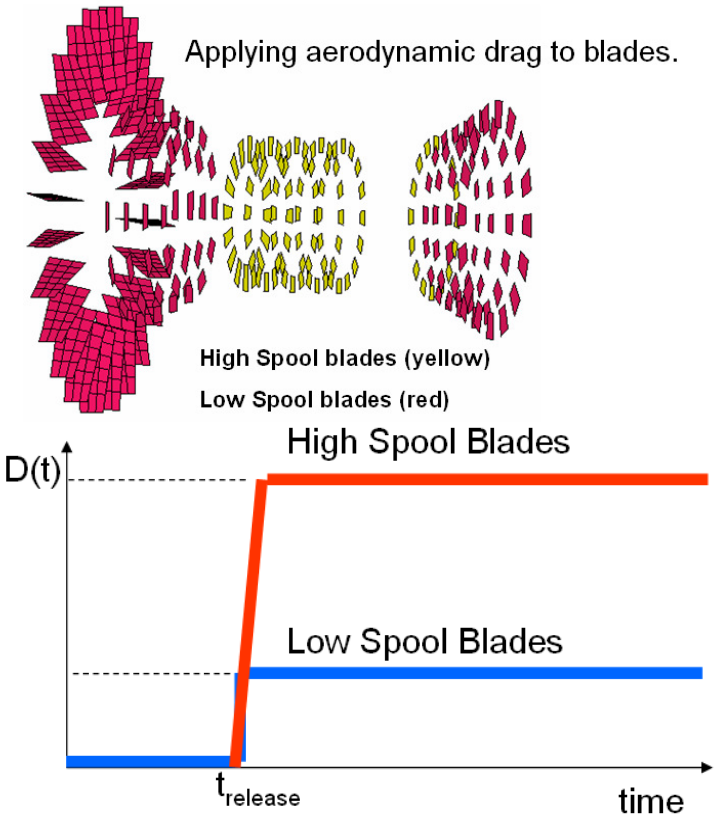

Figure 4.10 Damping applied to rotors

The following input was implemented into the LS-Dyna input; this was numerically prescribed[11] to give (no data in the literature was found on this) an approximately 0.1% reduction in speed every 0.01 second.

```
*DEFINE_CURVE
      70       0    1.000    1.000    0.000    0.000
 0.000000000000E+00 0.000000000000E-02
 0.030000000000E+00 0.000000000000E-02
 0.030100000000E+00 1.000000000000E-02
 1.000000000000E+00 1.000000000000E-02
$         HPC Blades damping
*damping_part_mass
1,70,3
$         LPC & LPT Blades damping
*damping_part_mass
9,70,1
$         FAN Blades damping
*damping_part_mass
12,70,1
*damping_part_mass
15,70,1
```

[11] Arbitrarily prescribed for this academic study. In principle this would be calibrated to engine spool down due to a fuel shut down (without a fan blade off).

Other, more sophisticated, values of damping could be prescribed and calibrated to match known engine data; however, this simple model was chosen for this study. Note that this damping could be calibrated to a non-destructive fuel shut down rig test (i.e. without losing a fan blade) and measuring the rotor spooldown rates; this strategy allows for calibrating the aerodynamic damping independently of other dissipation mechanisms.

4.10 Blade Kinetic Energy

In the baseline model, the kinetic energy history of the released blade was plotted in Figure 4.11. This compares well to the analytical estimate presented in Section 4.3.

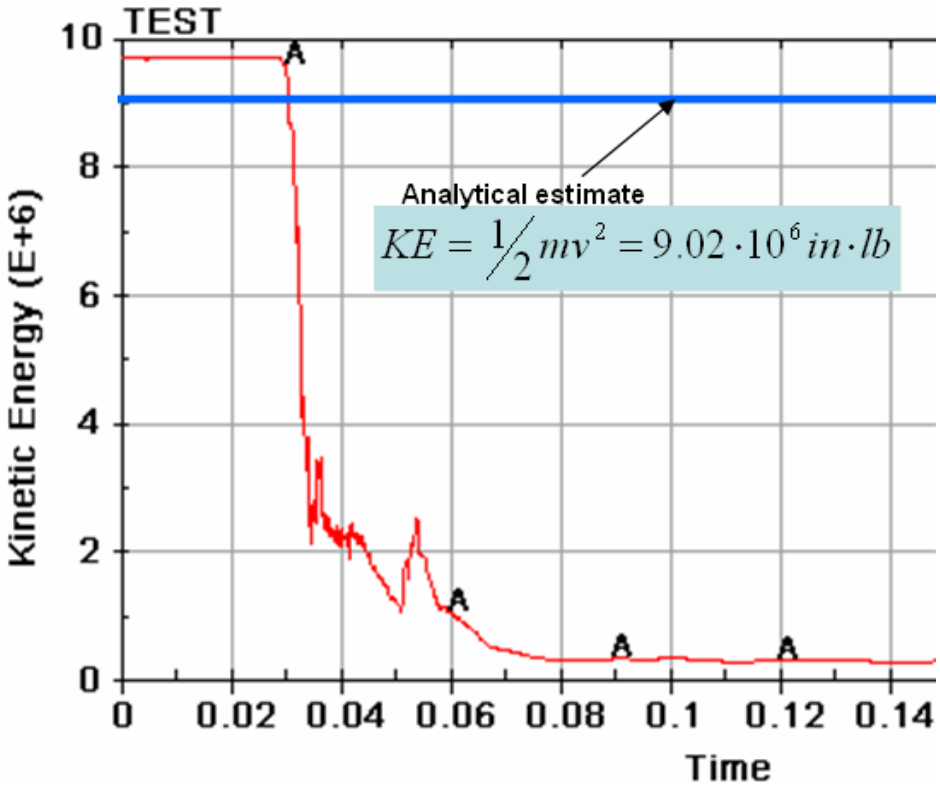

Figure 4.11 Kinetic energy history of released blade.

The estimation error is due to small errors in stress initialization as well as LS-Dyna using the deformed geometry (versus undeformed center of mass geometry for the hand calculation) which radially shifts the center of mass of the blade.

4.11 Fan Bearing Reaction

Fan bearing reaction magnitude plotted in Figure 4.12 compares well to the analytical prediction in Section 4.3.

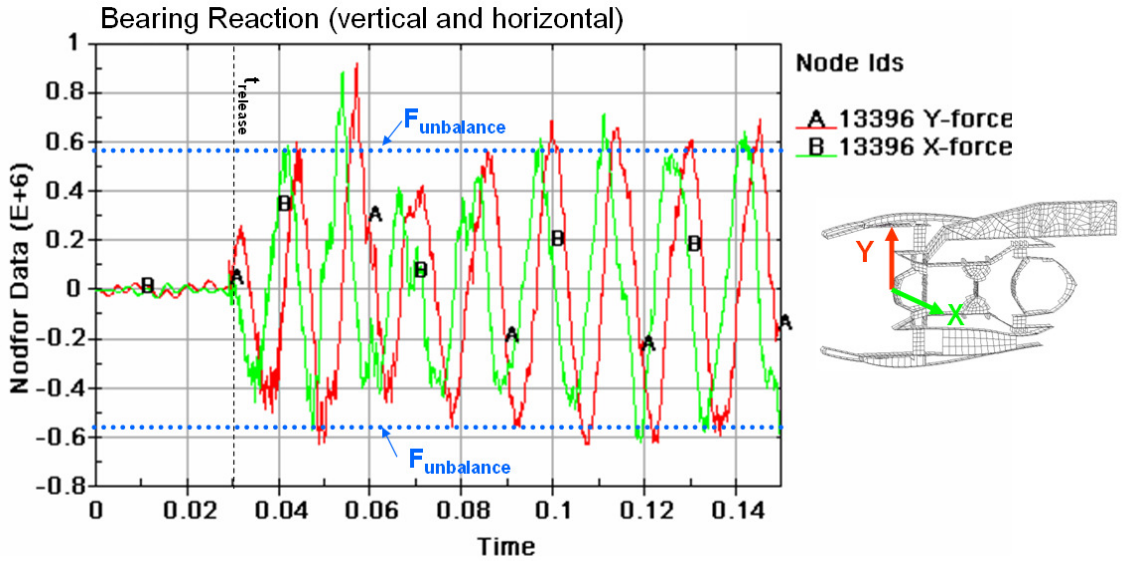

Figure 4.12 Low rotor forward bearing reactions.

4.12 Strain Energy in Isogrid

The containment isogrid's strain energy absorption history is shown in Figure 4.13. Note that the cases absorb more energy than is released by the blade. This extra work is done by the remaining rotor blades 'beating up' the case.

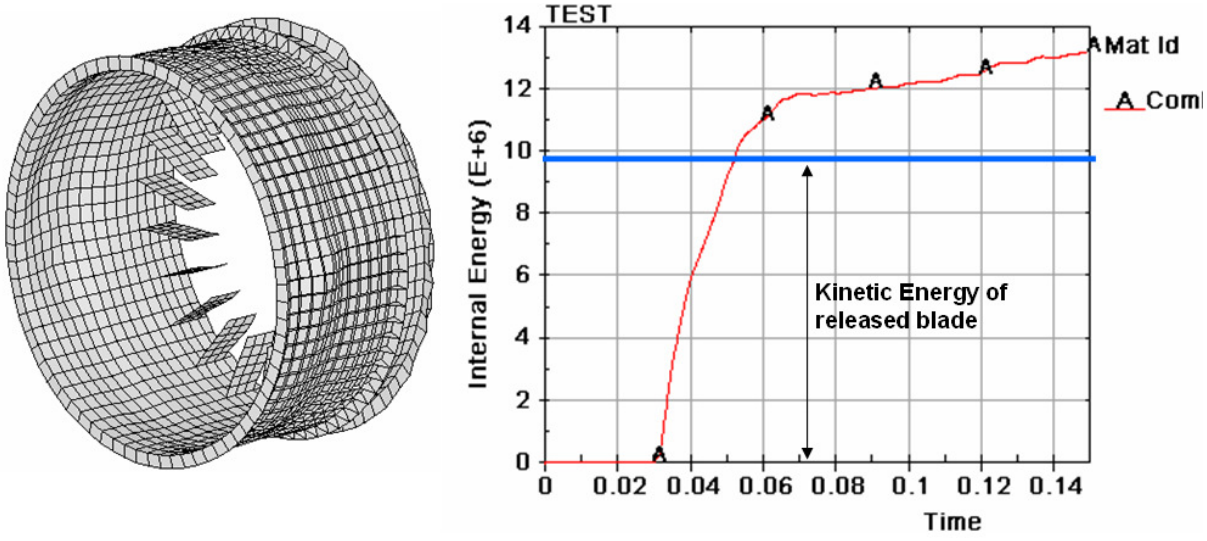

Figure 4.13 Strain energy absorbed by fan case.

4.13 Validating Gyroscopic Effects

Due to the very high rotational speeds, gyroscopic reactions at the bearings are expected to be significant during the transient. Even simplified analytical treatment of gyroscopic effects is difficult; however, the flexibility of the rotor, case flexibility as well as intermittent blade tip rubbing make all but the simplest analytical treatments impractical- perhaps even impossible. Fortunately, these effects are included automatically in LS-Dyna when the rotors are modeled realistically i.e. with 3D shell elements including blades.

To validate to a simple hand calculation, one can run a simple numerical experiment to observe the gyroscopic effects on the model. This was done by reversing the direction of the high speed rotor (yellow) as shown Figure 4.14.

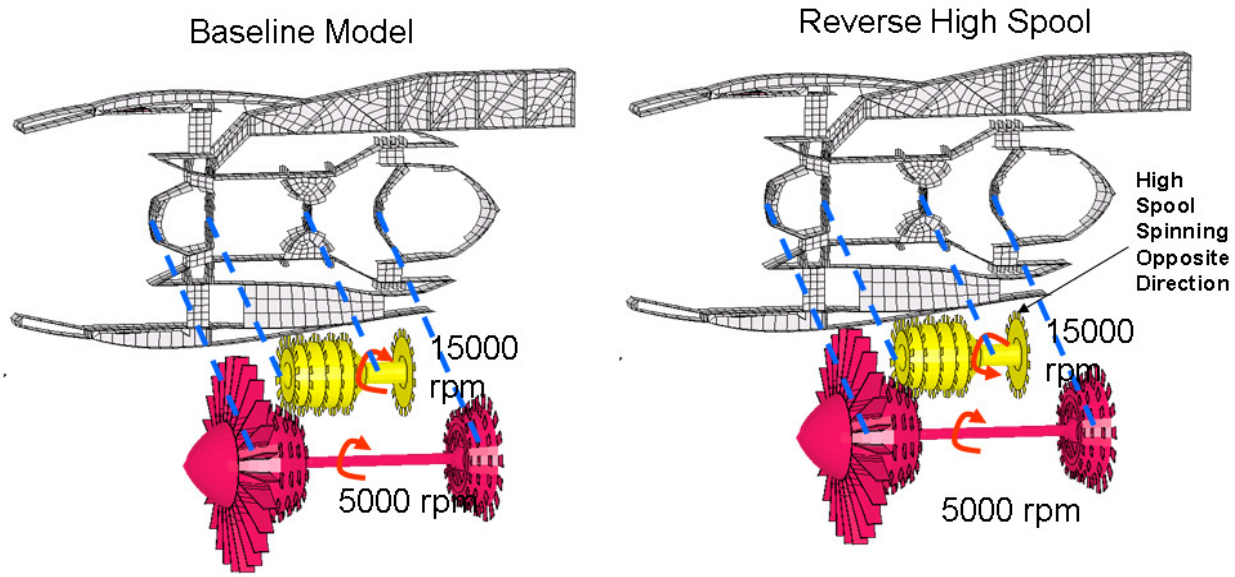

Figure 4.14 Definition of Reverse High Spool

For both the ***baseline*** and ***reverse high spool***, the forward bearing reaction (for the high speed rotor) is shown in Figure 4.15.

The bearing force differences due to full reversal of the high speed rotor rotation will approximately double[12] the gyroscopic effects. The gyroscopic forces acting on the forward high speed rotor bearing are thus approximately measured from Figure 4.15 as:

$$F_{gyro} = \tfrac{1}{2}\left|F_{ave}^{baseline} - F_{ave}^{reversehigh}\right| = \tfrac{1}{2}\left|125e3 - 175e3\right| = 25\cdot 10^{3} \text{ lb} \qquad (4.8)$$

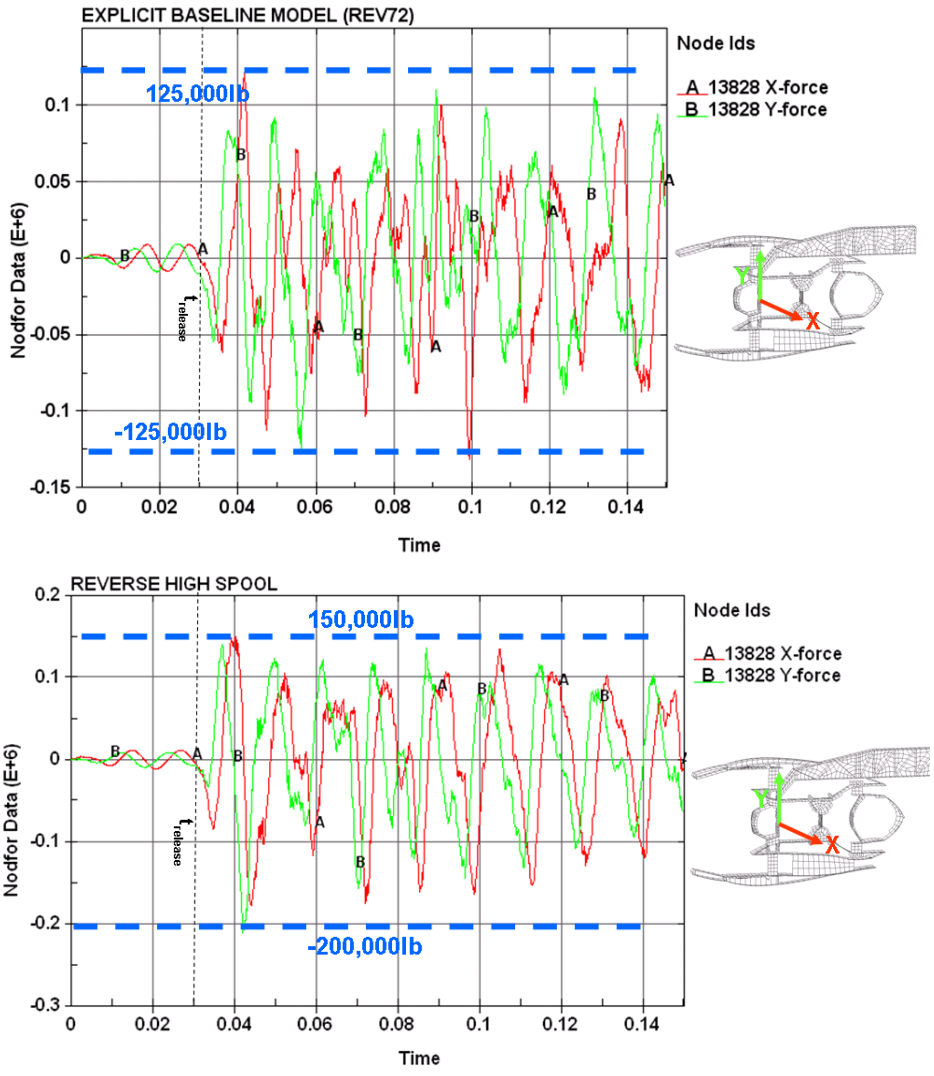

Figure 4.15 Differences in front bearing reactions due to high spool rotation.

[12] Static (translational and rotational) inertial properties of the rotor in a flexible structure complicate this. A non-spinning rotor bearing would have reaction X (due to static inertia). A positively spinning rotor bearing would see reaction X + Y (static inertia plus gyroscopic reactions due to rotor tilt). A negatively spinning rotor bearing would see reaction X - Y (translational inertia minus gyroscopic reaction from rotor tilt). Reversing the rotor direction allows isolation of the gyroscopic effects with magnitude 2Y.

The gyroscopic forces can also be predicted analytically. It is apparent that the gyroscopic forces will be proportional to the angular pitch/yaw velocity, $\Delta\theta/\Delta t$, of the bearings (which constrain the rotor). If this angular velocity (not the rotor spinning speed but rather the speed of pitch/yaw speed) can be estimated, the magnitude of the gyroscopic reaction can be calculated. The peak angular velocity, ω_p, can be estimated with Figure 4.16 and Figure 4.17 where the velocity is defined and the displacement history of the forward node is extracted numerically from LS-Dyna results:

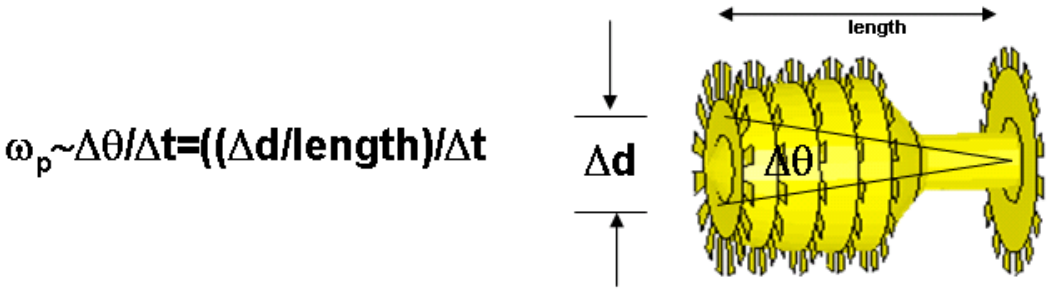

Figure 4.16 Angular velocity of high speed rotor

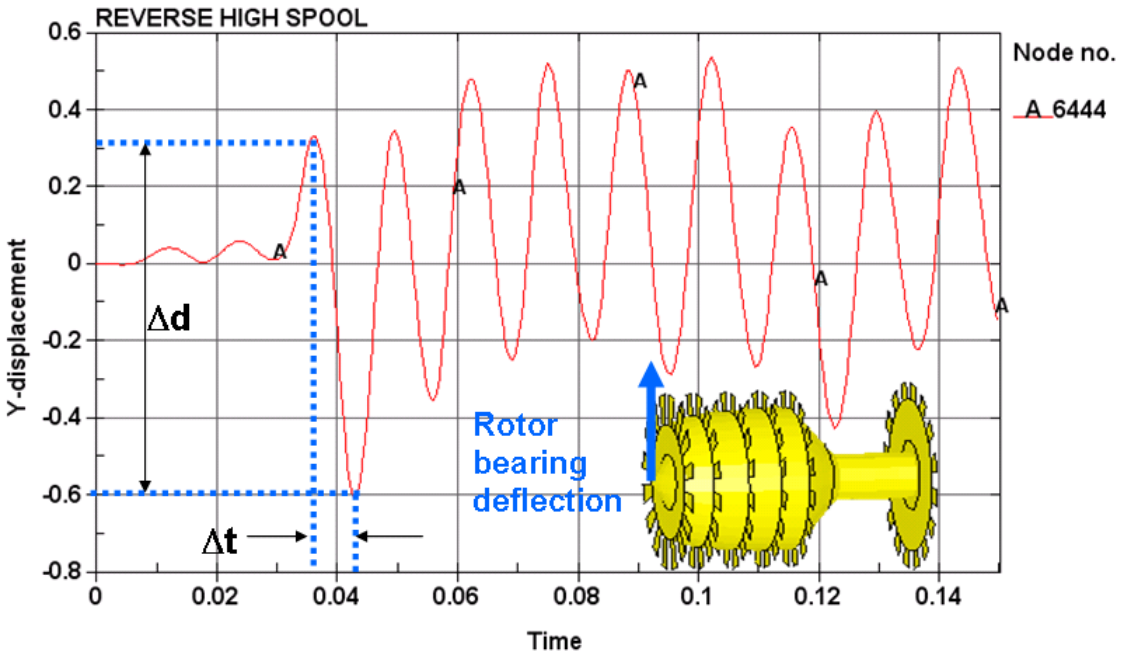

Figure 4.17 Deflection history of forward bearing node

The peak angular velocity of the high speed rotor is approximately:

$$\omega_p \sim \Delta\theta/\Delta t = ((\Delta d/\text{length})/\Delta t = 0.9"/41"/0.0075s = 2.92 \text{ rad/s} \qquad (4.9)$$

Figure 4.18 shows a body with moment of inertia I_{axial}, spinning about its axis at speed Ω where I_{axial}= 273.1 lb·s^2·in (summed for parts 1-5 using mass moment of inertia data tabulated in the LS-Dyna d3hsp file) and the high speed rotor Ω=15000 rpm= 1571 rad/s. The high speed rotor length is 41". This rotor is precessing about a fixed axis at precessional speed where ω_p is estimated as:

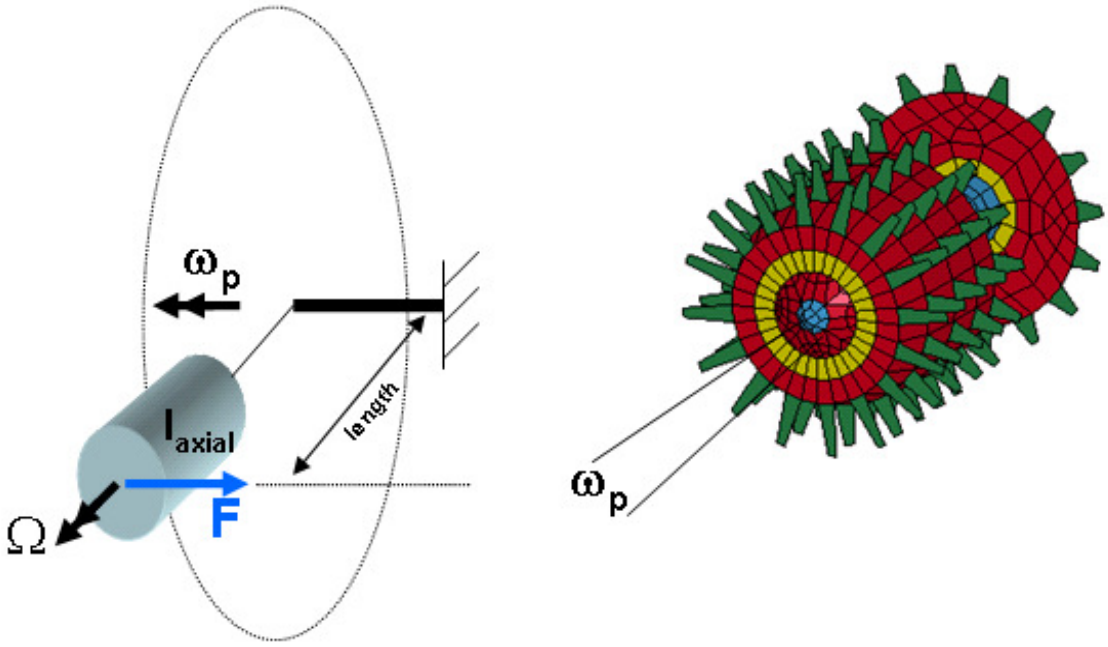

Figure 4.18 Gyroscopic Equilibrium of Precessing Rotor

The force, F, acting on the end at length L, required for countering the gyroscopic moment and establishing steady motion of the system is given by:

$$F = \omega_p I_{axial} \Omega / l = 2.92 \cdot 273.1 \cdot 1571 / 41 = 30{,}500 lb \qquad (4.10)$$

This 30,500 lb analytical estimate correlates quite well to the measured 25,000lb gyroscopic force from (4.8) measured by comparing the ***baseline*** to the ***reverse high spool*** solutions.

4.14 LS-Dyna Contact Algorithms at Sliding Interfaces

Sliding contact is vital to dissipating the kinetic energy of the rotor. The sliding contact interfaces in the baseline model are shown in Figure 4.19. Red boxes denote node-to-surface contact between the blade tips and the cases. Blue boxes denote surface-to-surface contact definitions between the engine and nacelle parts. The green box denotes eroding single surface contact with edge contact.

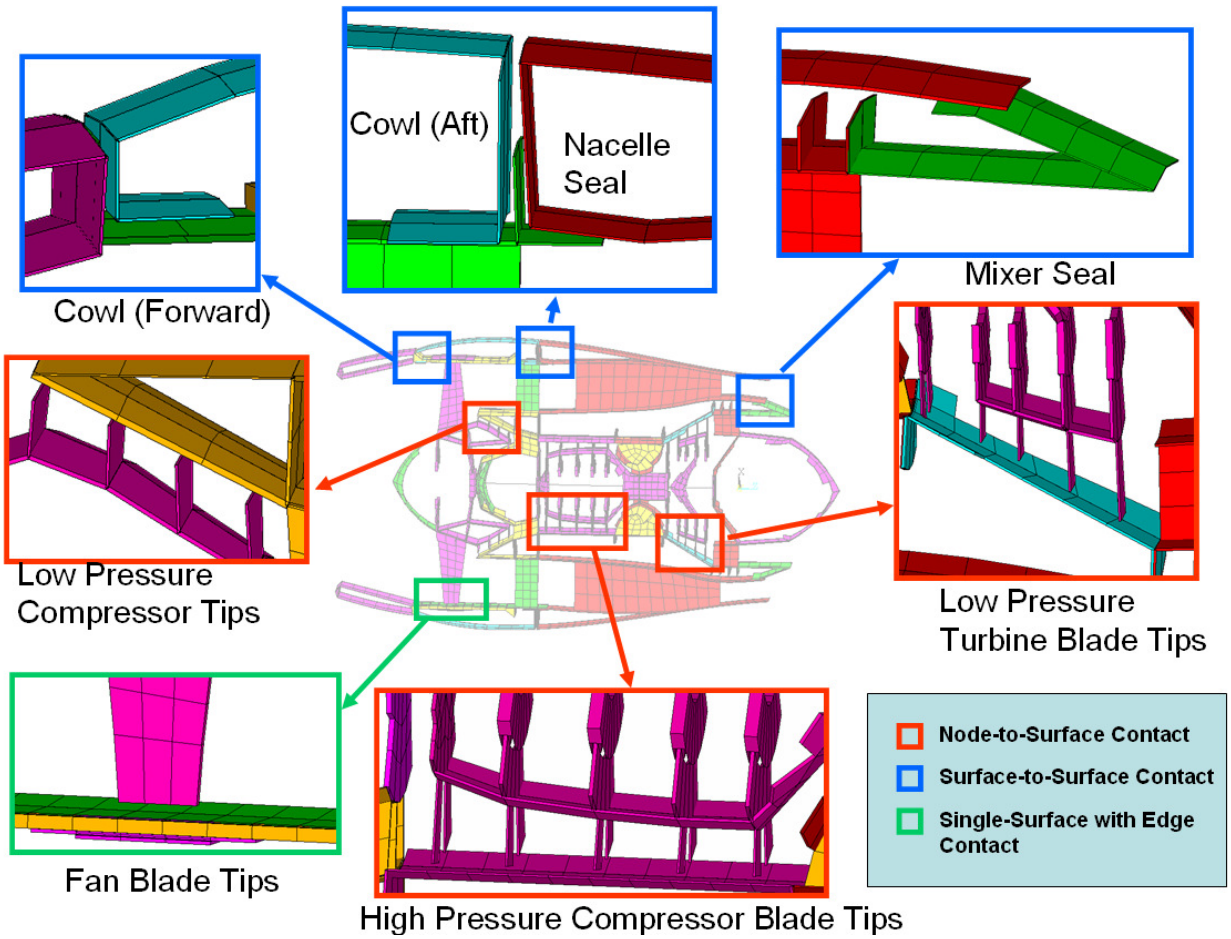

Figure 4.19 Contact interfaces with sliding friction

A careful check of the preliminary LS-Dyna contact settings revealed a 'loss' of total sliding energy[13] during the debugging phase of building the baseline model. An example is shown below. This loss of sliding energy is unphysical and cannot be permitted in the baseline model.

[13] Sliding energy is dissipative in nature and any gain must always remain constant or increase.

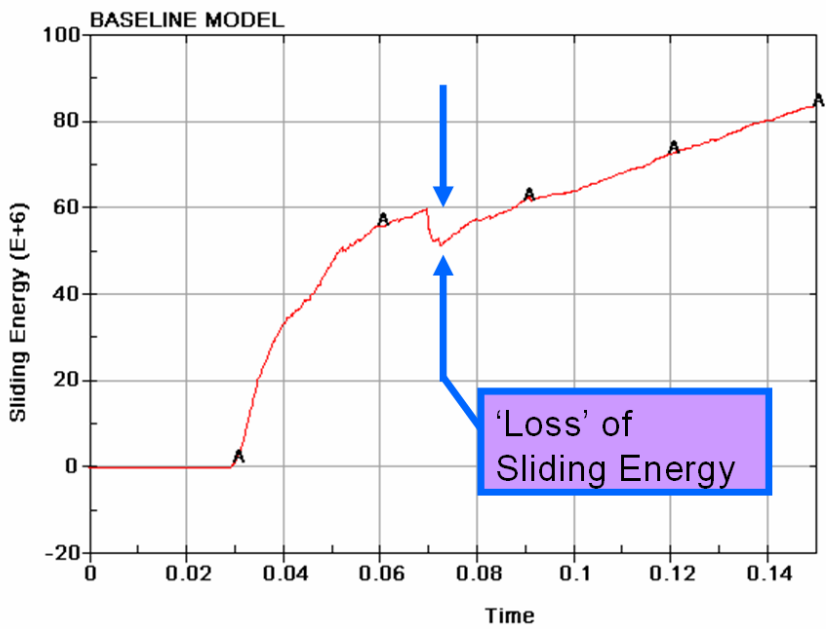

Figure 4.20 'Loss' of sliding energy discovered during debugging. This was fixed.

During model debugging, it was discovered that this negative sliding energy is a result of unrealistic contact penetration between slave and master surfaces. It was discovered that the computationally inexpensive surface-to-surface contact algorithm allowed some surfaces to 'pass through' other surfaces in an unphysical manner. The surface-to-surface contact algorithm did not recognize edges of shells contacting the edges of another shell. During the extremely large deformations during the FBO event, these non-recognized shell edge segments passed through and became 'tangled' as shown in **Figure 4.21**

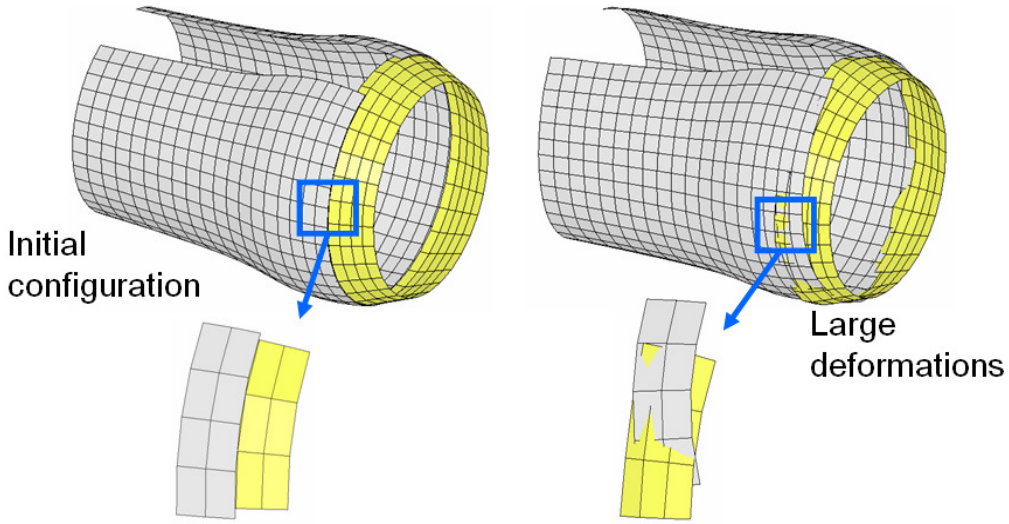

Figure 4.21 Contact Penetration causing negative sliding energy.

To alleviate this unrealistic penetration and edge-pass-through, a grid of non-structural beam elements was overlaid on the shell elements as demonstrated below. The structural shells are grey and yellow; the overlaid non-structural beams are green and purple. Edge-to edge contact can be defined between the beams prohibiting pass through and consequent negative sliding energy.

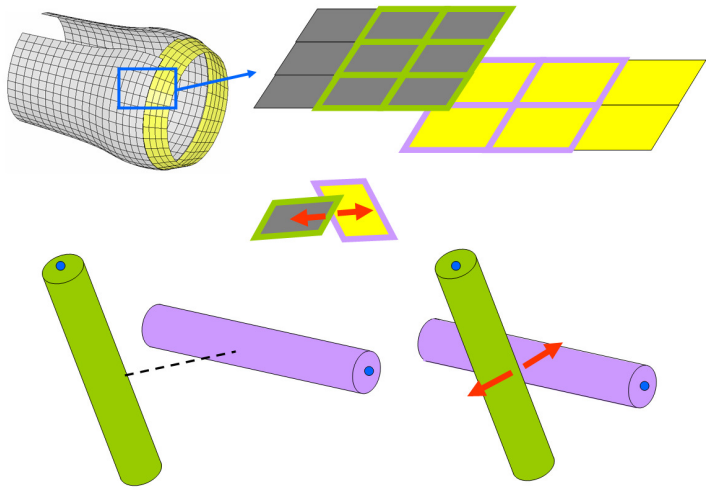

Figure 4.22 Implementing simple edge-to-edge contact via non-structural beams.

Figure 5.16 in the next chapter shows the 'loss' of total sliding energy has been alleviated by the careful choice of LS-Dyna contact definition.

4.14.1 Blade tip to Case Sliding Interface Definition

The blade tip to case for the low pressure turbine, high pressure compressor and low pressure compressor were modeled with using the LS-Dyna contact definition as shown below.

```
*CONTACT_NODES_TO_SURFACE
      45       3       4       0       0       0       0       0
0.4000  0.2000  0.1000E-030.2000E+05 10.00         0 0.000    666.0
 1.000   1.000   0.000   0.000   1.000   1.000   1.000   1.000
```

Adding a contact definition such as this is very computationally efficient and would be expected to increase CPU time by about 0.5%. A reader with implicit FEA experience may find this computational efficiency with contact almost 'magical' as a simple contact definition like this in an implicit code might be expected to double, triple or even increase by an order of magnitude the computation time.

4.14.2 Nacelle to Engine Sliding Interface Definition

All the interfaces below, which are subjected to very large deformations during the FBO, had the grid of beams applied. Surface to surface contact was defined between the shells (grey) and edge to edge between the beams (blue).

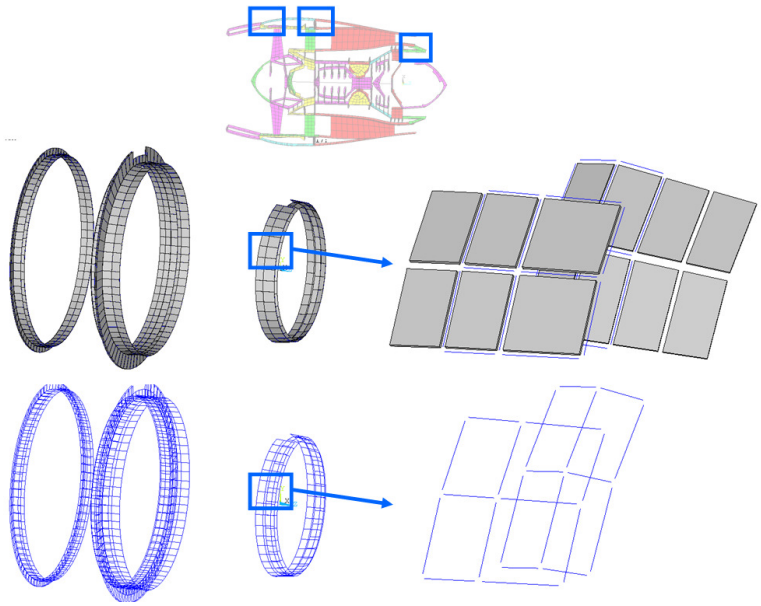

Figure 4.23 Surface-to-surface contact and Edge-to-edge contact

The surface to surface contact was defined by:

```
*CONTACT_AUTOMATIC_SURFACE_TO_SURFACE
      26      27       0       0       0       0       0       0
0.4000   0.2000   0.1000E-030.2000E+05 10.00          0 0.000    666.0    1.000
1.000    0.000    0.000    1.000    1.000    1.000    1.000
```

Adding a surface-to-surface contact definition such as this would be expected to increase CPU time by about 0.5%.

These beams can be made non-structural and edge-to-edge contact recognized by adding:

```
*mat_null
10,0.00001,,,,,3E+07,.3
*contact_automatic_general
87,,3
0.4000,0.2000,0.1000E-03,0.2000E+05,10.00,0,0.000,666.0
1,1
```

Adding a more sophisticated edge-to-edge contact definition such as this would be expected to increase CPU time by about 5%.

4.14.3 Fan Blade, Fan Case, Isogrid and Fabric Sliding Interface

Since the deformation is not known a priori a very general contact definition called **contact_automatic_general_interior* is used to allow all surfaces and edges on both the fan blades, isogrid and fabric (basically, the element set shown in Figure 4.24) to contact. Basically, since large arbitrary motions are possible, any of the surfaces/edges can contact any other surface/edge. This includes surface-to-surface, edge-to-surface as well as edge-to-edge for all element in the set.

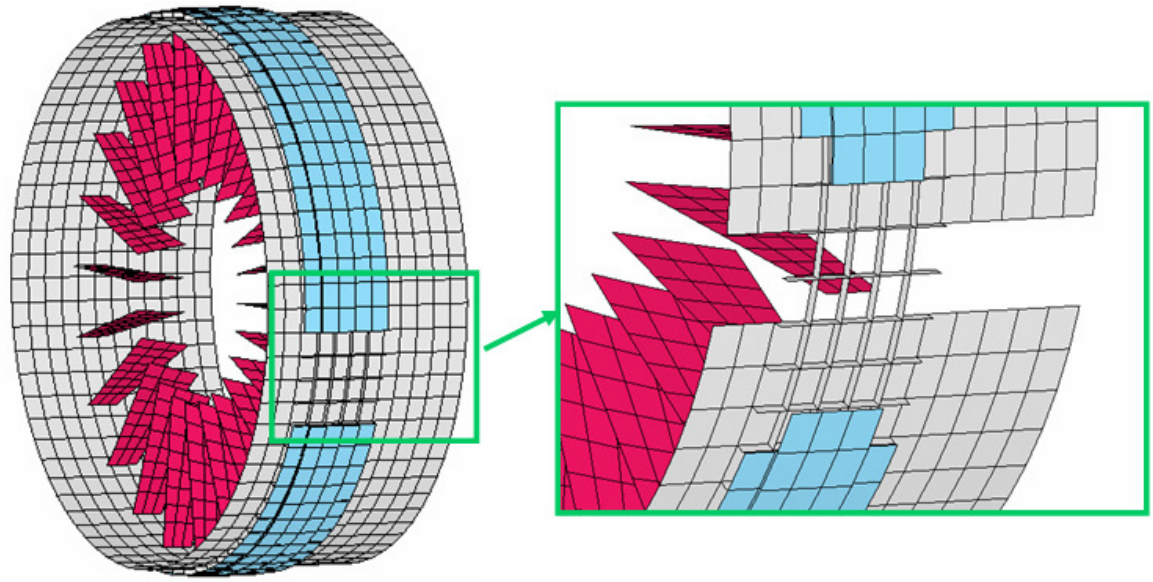

Figure 4.24 Fan Blade, Fan Case, Isogrid and Fabric Sliding Interface

.

Note the deformed in Figure 4.25 showing blade/case/isogrid/fabric interaction. Edge-to-edge contact prevents the edges of surface segments to 'entangle' as was shown in **Figure 4.21**; the more common surface-to-surface contact will not detect these types of penetrations. The *interior* card feature dynamically updates the edge/surface contact topology to account for interior contact that may be realized when elements fail due to high strains.

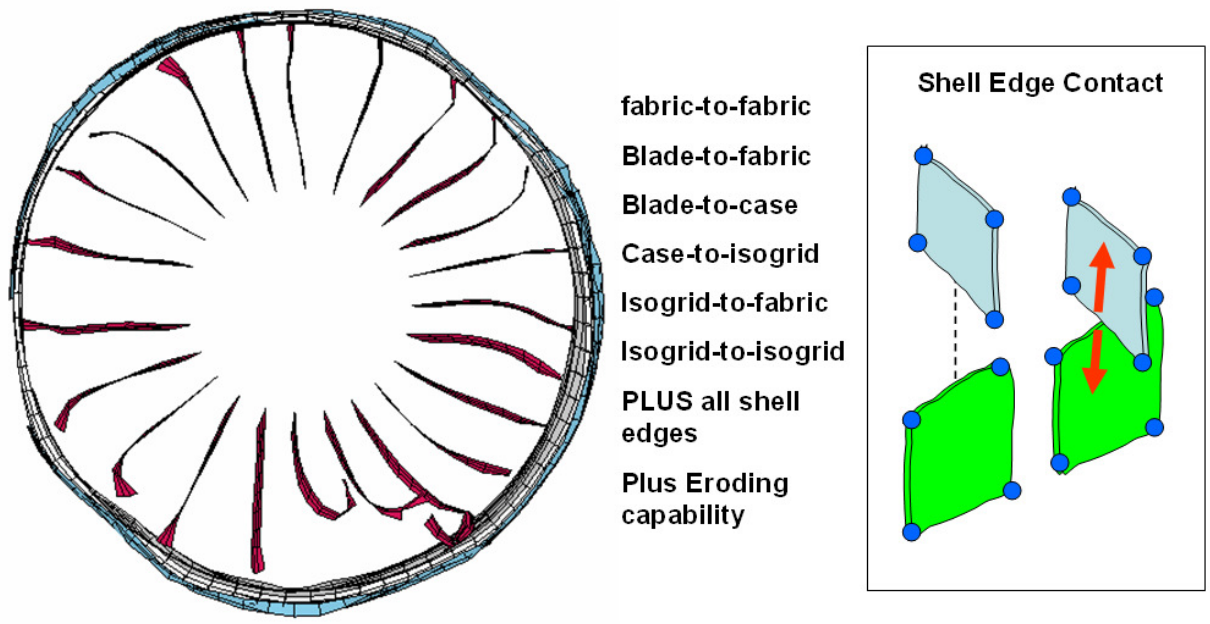

Figure 4.25 Deformed Fan Blade, Fan Case, Isogrid and Fabric

This definition is added into LS-Dyna with:

```
*contact_automatic_general_interior
777,,2
0.4000,0.2000,0.1000E-03,0.2000E+05,10.00,0,0.000,666.0
1,1
*set_part_list
777
10,11,12,13,14,15
80,81,85,86
```

Adding the more sophisticated *automatic_general_interior* contact definition to the fan blades and fan case isogrid is expected to increase CPU time by about 50%. This is a significant increase but the more sophisticated definition is necessary so that important impact calculations during FBO are not omitted. Note that this type of contact is not practical to implicit users for anything beyond academic sized problems.

4.15 Stress Initialization

At $t=0^+$ rotational velocities are prescribed to the rotors. If the rotors are not pre-stressed when spinning starts at $t=0^+$ there will be ringing (overshoot of both displacements and stresses) as explained in Figure 4.26. This shows the dynamic motion ('ringing') of an un-stressed rotor given a initial angular velocity.

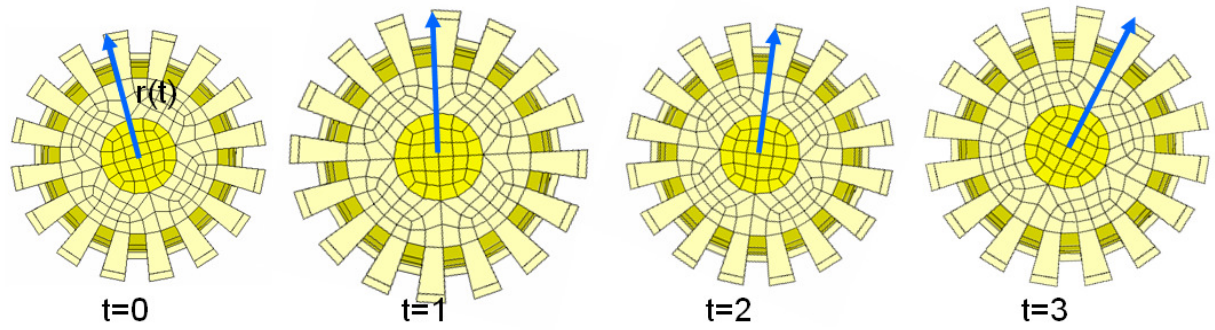

Figure 4.26 System 'rings' if not pre-stressed.

For single DOF systems, the undamped displacement subjected to a step load, the overshoot is twice the steady state as indicated in Figure 4.27. This overshoot can be damped out; however, this is both difficult to implement and is computationally inefficient. Also, aircraft engine parts are typically operate near the material's yield strength and a large overshoot might plastically yield the parts in an artificial manner before any FBO occurs.

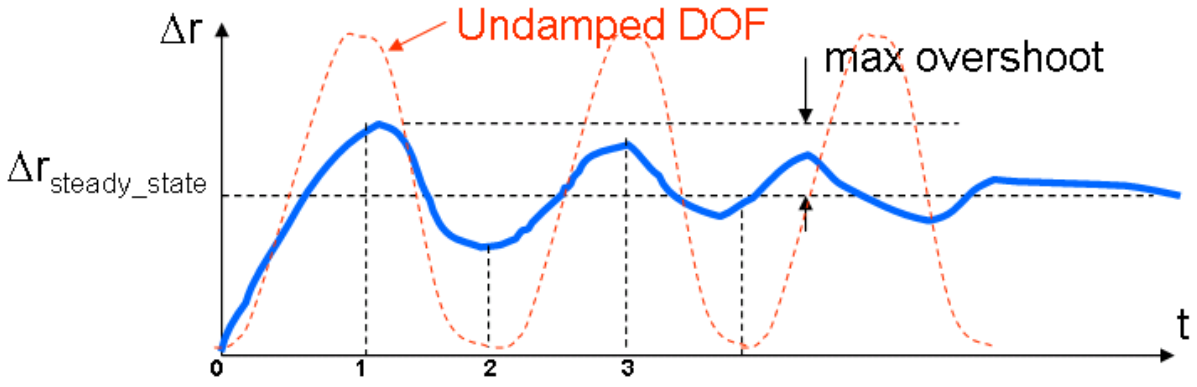

Figure 4.27 Displacement overshoot due to centrifugal body force step loading

To obtain a steady state initial stress and displacement state of the rotors at $t=0^-$ a LS-Dyna feature called dynamic relaxation was used. Dynamic relaxation is a method for finding the solution to quasi-static problems (example shown in Figure 4.28) using transient integration.

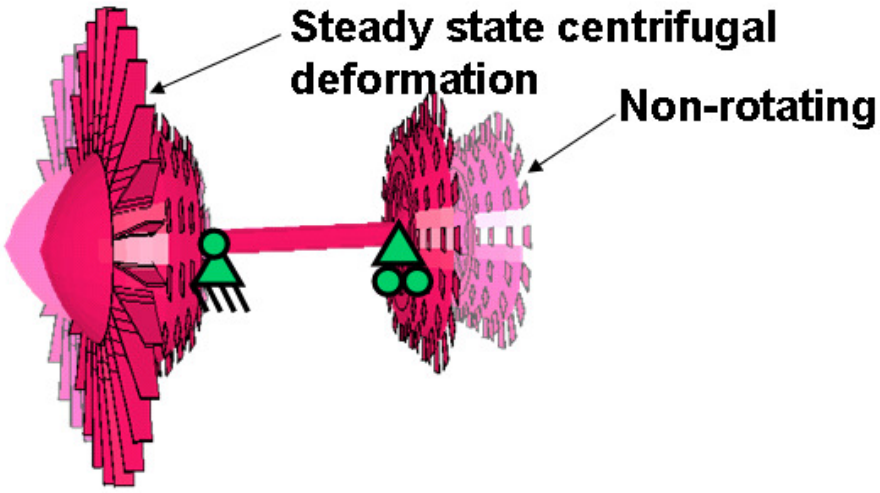

Figure 4.28 Deformed shape of spinning rotor (centrifugal loading).

To effectively use dynamic relaxation the lowest natural frequency of the system is vital. This was found from measuring the system oscillations in a partially pre-stressed (a sample unconverged solution used expressly for computing the lowest natural frequency) transient solution as shown in Figure 4.29.

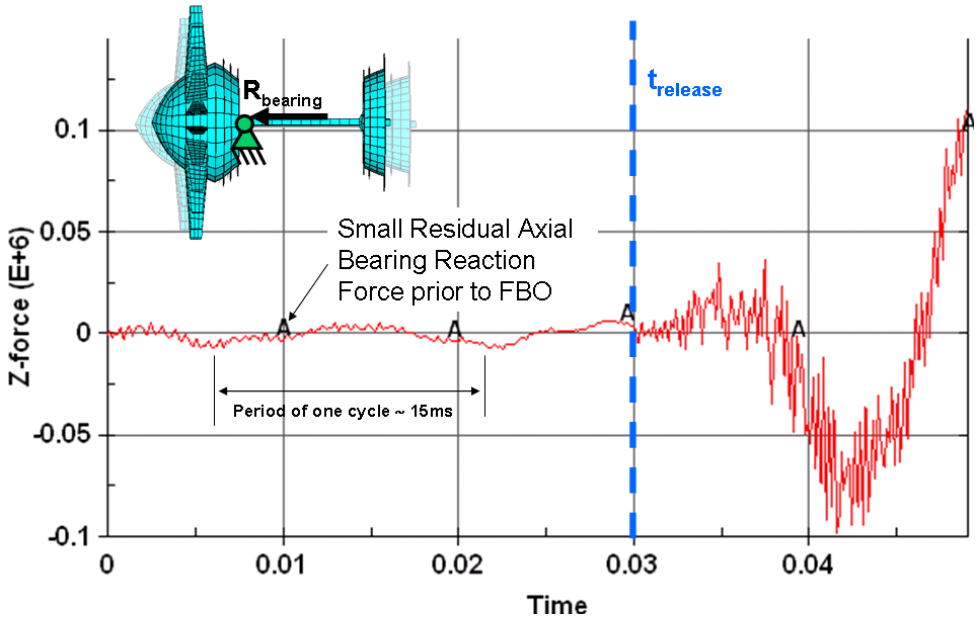

Figure 4.29 Numerically measured natural frequency from system noise.

This shows an axial rotor frequency of about 67Hz as shown in Figure 4.30.

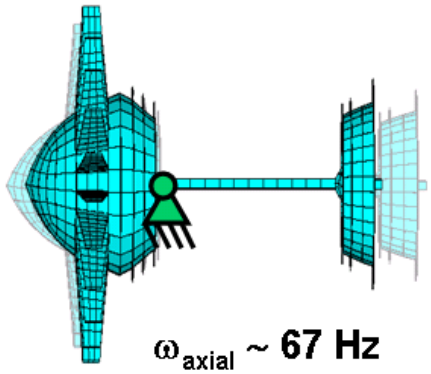

Figure 4.30 Natural frequency and mode shape of low rotor.

To avoid overshoot the initialization centrifugal loads are applied to the rotors with the ramping shown in Figure 4.31. Note how the full centrifugal load is applied in a ¼ period.

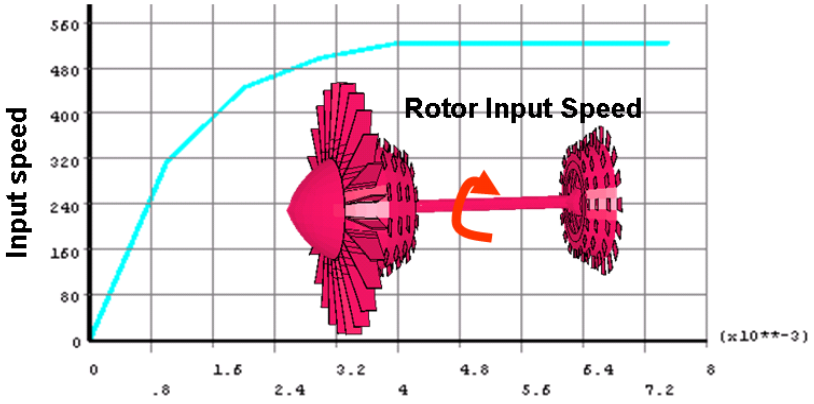

Figure 4.31 Rotor Speed ramp curve for relaxation

In dynamic relaxation, the centrifugal loads were applied to the rotors at t=0$^-$ and damping is automatically applied to remove the system's kinetic energy. The automatic damping, DRFCTR, controls the amount of pseudo-damping applied. It's simply a velocity scaling factor applied every time step. As a rule-of-thumb the automatic damping should be prescribed as:

$$DFCTR = 1 - \left(2 \cdot c_{cr} \cdot \omega_{nat\_\min} \cdot \Delta t_{\text{int}}\right) \qquad (4.11)$$

where $\boldsymbol{c_{cr}}$ is the fraction of critical damping (typically set $\boldsymbol{c_{cr}}$=1.0), $\omega_{\text{nat\_min}}$ is the minimum frequency of oscillation (rad/time), and $\boldsymbol{\Delta t_{int}}$ is the integration timestep. If DRFCTR =1 the

system is undamped. Assigning ω_{nat_min} =66Hz and Δt_{int} =$0.6 \cdot 10^{-5}$s reveals of about DRFCTR =0.995.

Some simple numerical experiments found that DRFCTR =0.980 (corresponding to c_{cr}=4) solved more quickly so this value was used. The specific dynamic relaxation (DRFCTR =0.980) inputs for LS-Dyna are below:

```
*CONTROL_DYNAMIC_RELAXATION
50,0.200E-03,0.980,.0511,.9,0,0.400E-01,1
```

The dynamic relaxation is solved until the following equation is satisfied:

$$cvtol = 0.2 \cdot 10^{-3} \geq E_{KE}^{current} / E_{KE}^{max} \qquad (4.12)$$

where *cvtol* is a user prescribed tolerance, and E_{KE} is the current and maximum system distortional kinetic energy, respectively. Note that a looser tolerance ($0.2 \cdot 10^{-3}$) was chosen for this study as the low frequency vibrations due to shell bending damp out very slowly. The input loading and convergence rate are plotted in Figure 4.32.

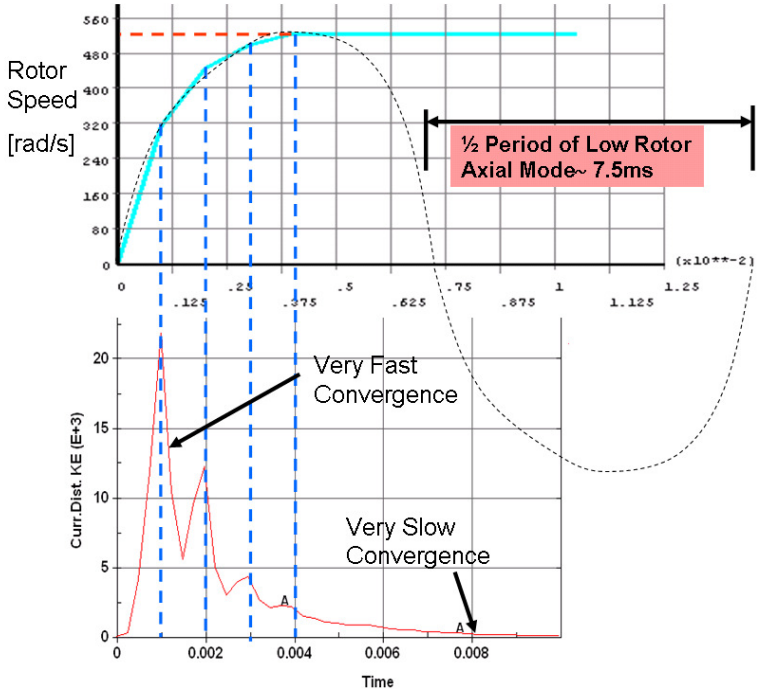

Figure 4.32 Relaxation Convergence for Baseline Model.

Note the slow convergence leaves some small residual kinetic energy in the system. Rotor stresses after the dynamic relaxation, as seen in Figure 4.33, are seen to be approximately steady state (about $100 \cdot 10^3$ psi stress) up to $t_{release}$=0.03s. This small stress oscillation prior to blade release is a small error due to early termination of dynamic relaxation.

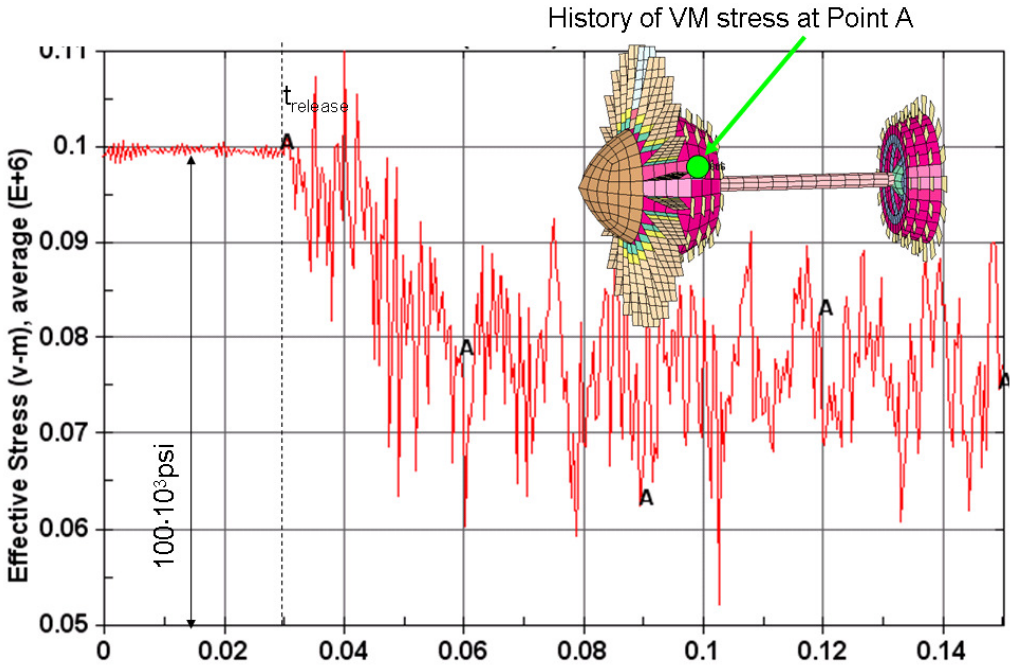

Figure 4.33 Approximately constant stresses prior to blade release.

The accuracy versus speed trade-off between slow relaxation convergence and an exact steady state requires engineering judgment.

It should also be noted that the double precision option (I8R8 format) should be specified when executing LS-Dyna. This was found to avoid round-off error which led to model divergence during stress initialization through dynamic relaxation.

4.16 Mesh Modifications

Shell thicknesses in the baseline model were iteratively assigned based on plastic strain levels and stability margins. Most components were thinned until they had slight permanent set or small observable localized buckling during fan blade off. This was done to get a reasonable starting point for studying design sensitivity (it is assumed that aircraft engine components are designed fairly close to strength limits).

Figure 4.34 shows the evolution of the high speed rotor shell mesh. The slight asymmetry of mesh in revision 2 with the short element edge length is circled. This type of asymmetry was found to create problems such as rotor imbalance as well as potential initiation of hourglassing problems.

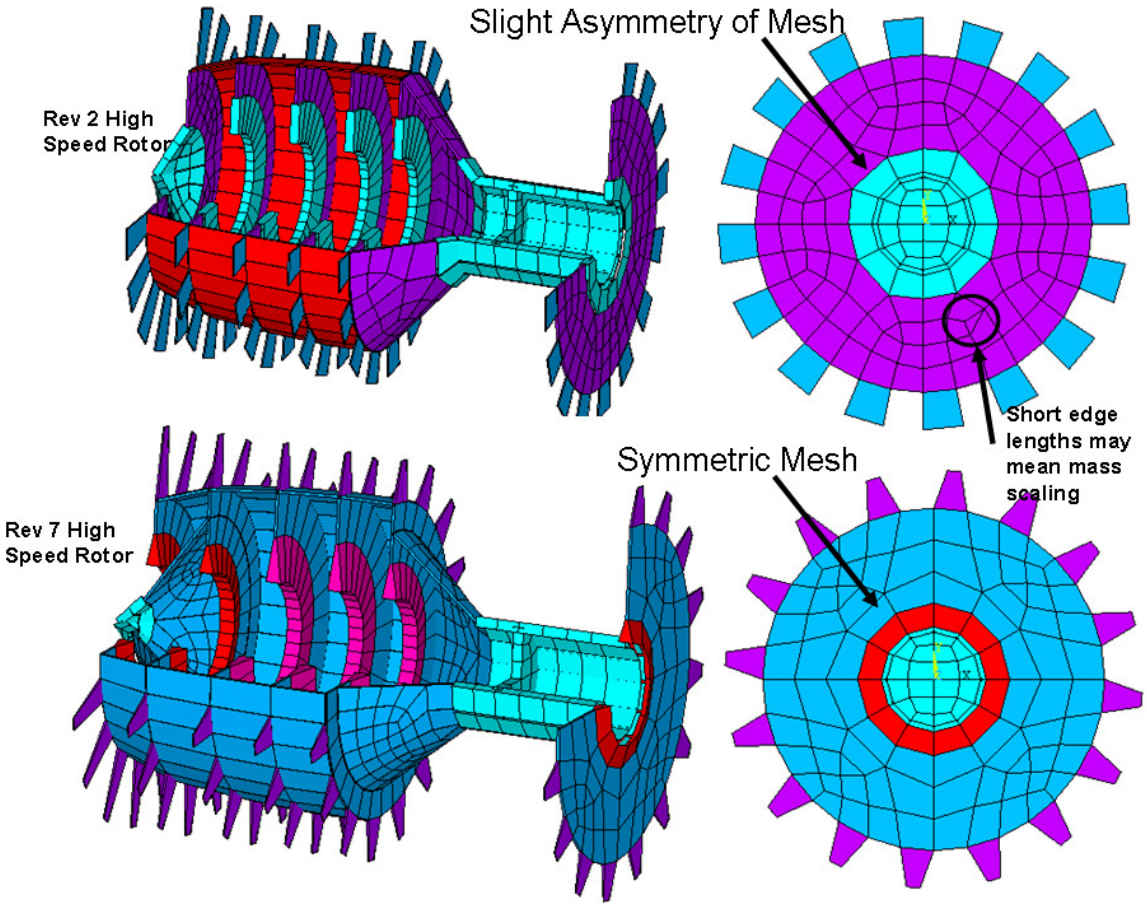

Figure 4.34 Evolution of High Rotor Mesh

The blades were also tapered from root-to-tip to prevent hourglassing problems.

Figure 4.35 shows the evolution of the low speed rotor mesh. The turbine and compressor blades were re-meshed multiple times (revision 3 and revision 16 shown) as problems with hourglassing and mass scaling were identified.

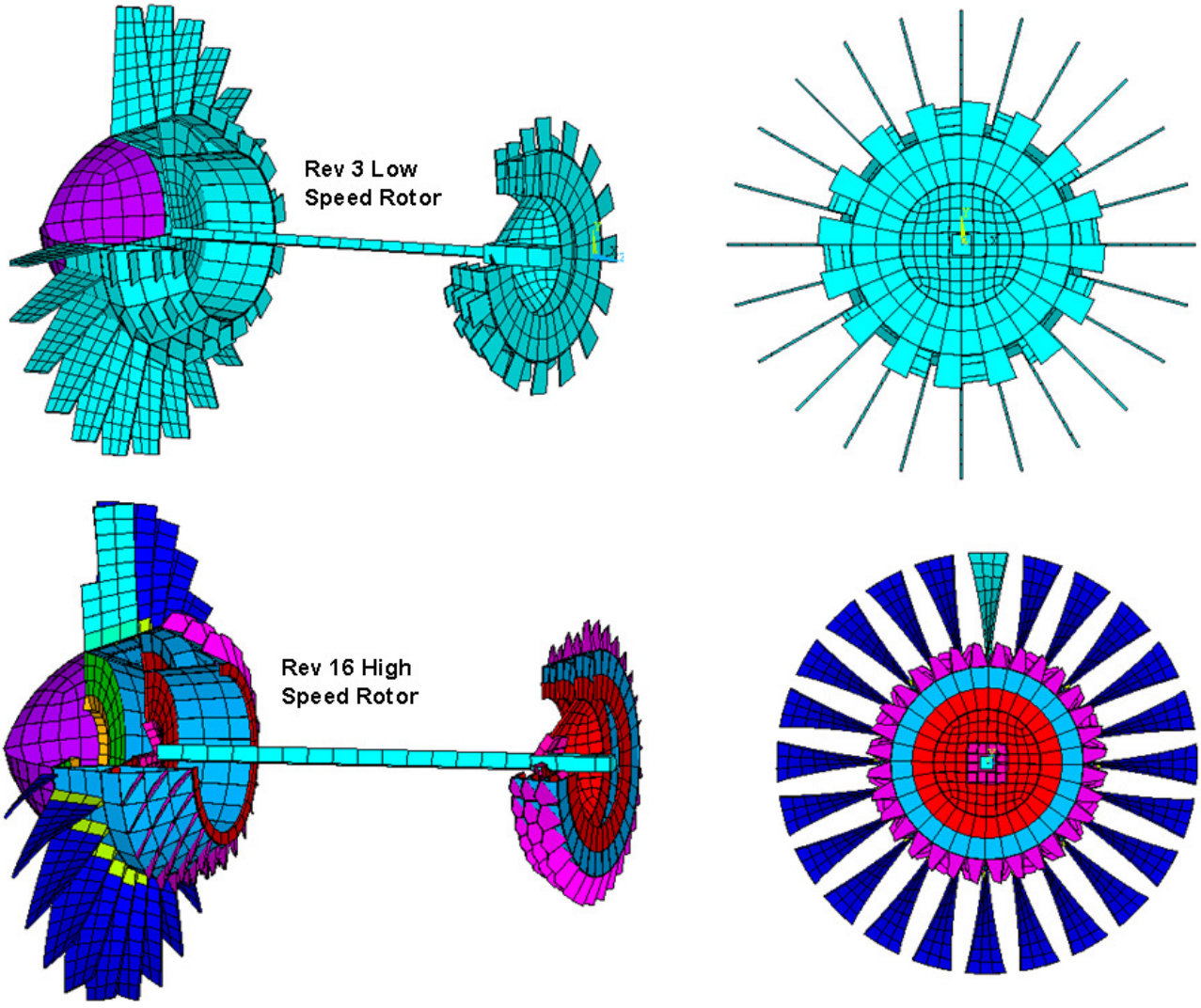

Figure 4.35 Evolution of Low Rotor Mesh

Revised meshing of the low speed rotor included a twist along the axis of the fan blades; other changes included root-to-tip tapers of the compressor and turbine blades.

4.17 Stress Rate Accuracy

The Jaumann stress rate is implemented into LS-Dyna to update stresses incrementally during each time step; this Jaumann stress rate [3,4], σ^{∇}, is written as:

$$\sigma^{\nabla} = \dot{\sigma} + \sigma\omega - \omega\sigma \qquad (4.13)$$

By default, in LS-Dyna the spin tensor,**ω**, is approximated as:

$$\omega = \dot{R}R^{T} \qquad (4.14)$$

This (objective) assumption gives good results for many LS-Dyna applications and is very computationally fast. Recall that **R** is the rotation tensor in the decomposed deformation gradient **F**=**RU**. The **U** is the stretch tensor and will be revisited several paragraphs below.

The baseline model (with default settings) was integrated for full duration without releasing a fan blade to test the capability of LS-Dyna to track the large rotations. The plot below shows an observed (spurious) energy gain. This is a result of cumulative error due to the approximate spin tensor used in the Jaumann stress rate.

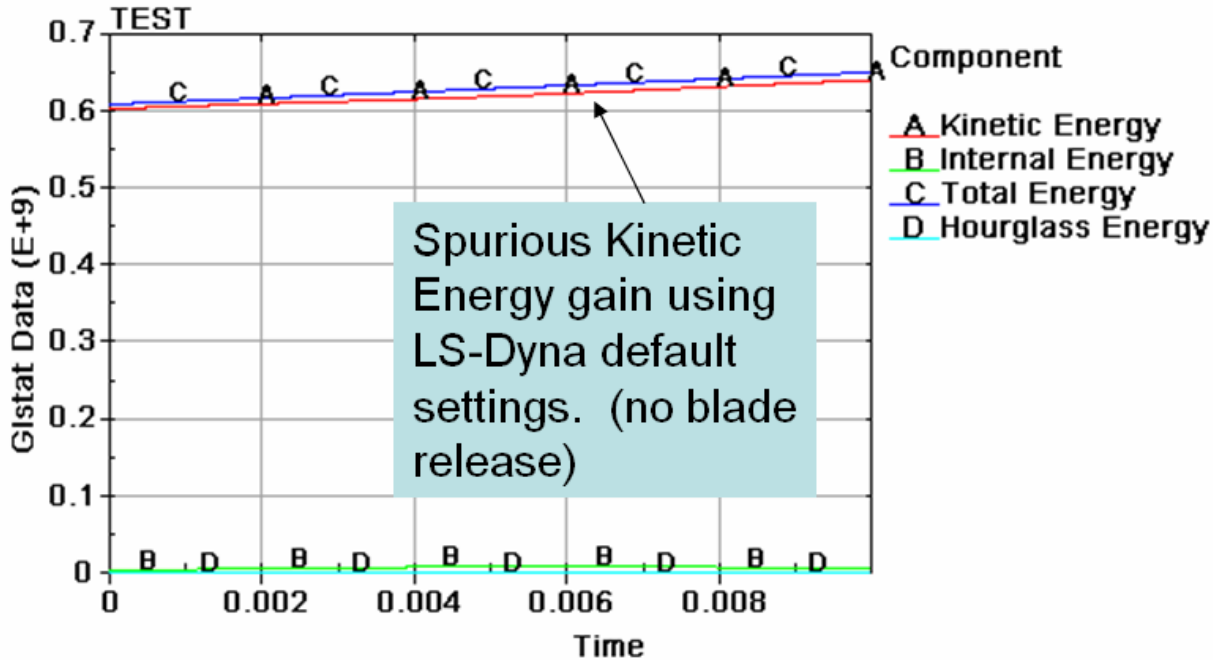

Figure 4.36 Spurious energy gain from Jaumann stress rate approximation

LS-Dyna has an option to make improve the accuracy of stress updates to selected bodies (the rotors are Parts 1-18 in this example). Augmenting the LS-Dyna defaults with the following lines improves the stress update accuracy.

```
*set_part_list_generate
555,0,0,0,0
1,18
*CONTROL_ACCURACY
1,2,555
```

When this input code is added, the spin tensor, **ω**, is more exactly computed [2] as shown below and includes the stretch, **U**, terms:

$$\omega = \dot{R}R^T + \tfrac{1}{2} R\left(\dot{U}U^{-1} - U^{-1}\dot{U}\right)R^T \qquad (4.15)$$

Adding this option was found to resolve the spurious kinetic energy gain issue.

4.18 Element Hourglassing

Typically, about 80% of the CPU time in solving the baseline model is spent computing element stresses. The user is faced with selecting fully integrated shell elements versus reduced integration elements. Fully integrated elements, with 4 Gauss integration points take about four times as much CPU time as do the reduced integration. Unfortunately, the reduced integration elements are susceptible to hourglassing [4]. A brief explanation of hourglassing is provided in Figure 4.37. Basically, reduced integration elements allow spurious deformations to occur in the element without causing any physical strain at the Gauss points (and zero strain energy for the element). These deformations lead to 'hourglass' patterns in the mesh and lead to non-physical behavior.

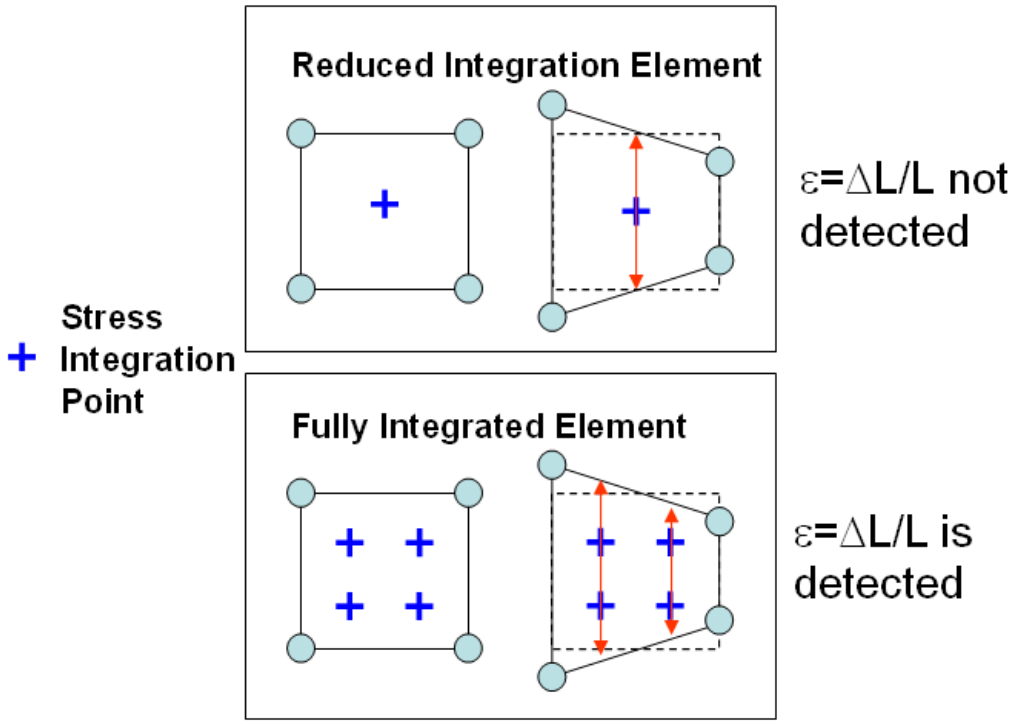

Figure 4.37 Simplified explanation of hourglassing in reduced integration elements

The first attempt at solving the baseline model, created exclusively with reduced integration elements, showed 'textbook' hourglassing as shown in the Figure 4.38. Note the deformed shape of the elements comprising the disk. A typical energy plot with 100% reduced integration elements is also provided.

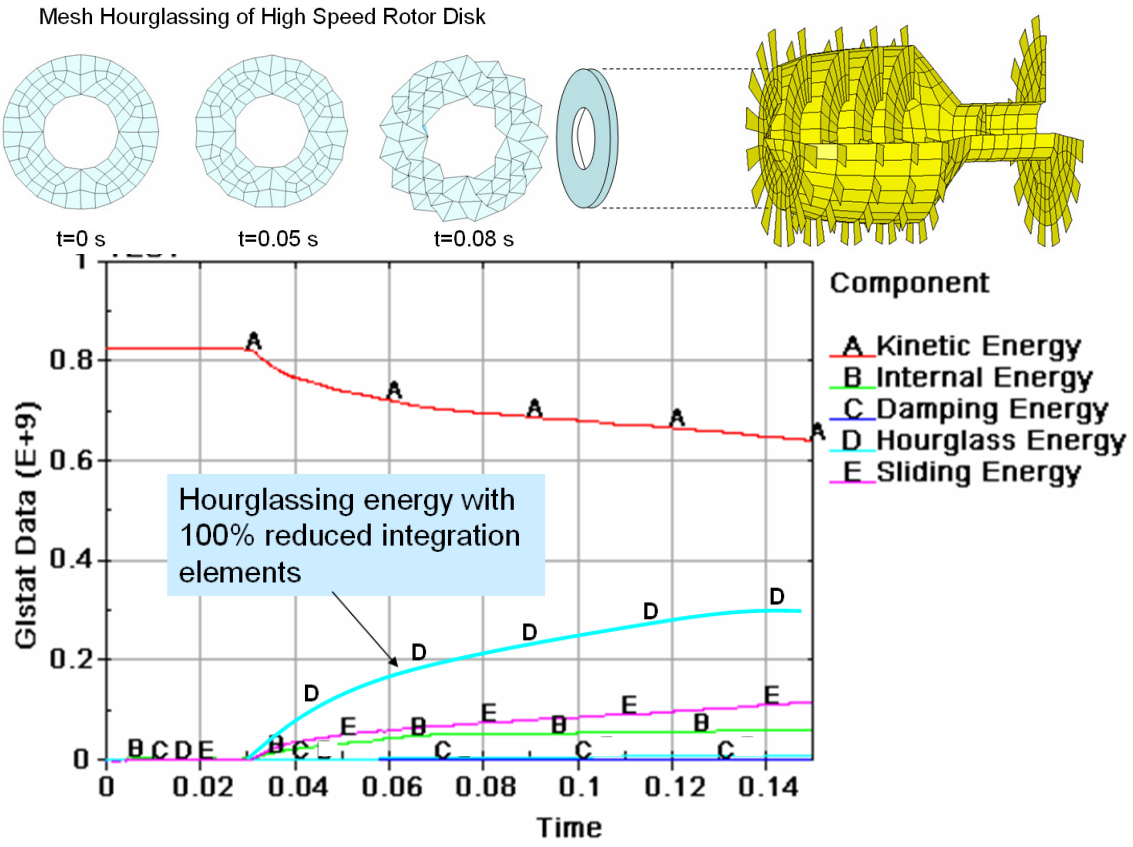

Figure 4.38 Hourglassing energy of disk and gain in global system

High hourglassing energy generally renders meaningless results. Once the Hourglassing exceeds a particular threshold the solution will usually diverge with typical result shown below. Note how the rotor disk (yellow line) is flying off into space in Figure 4.39.

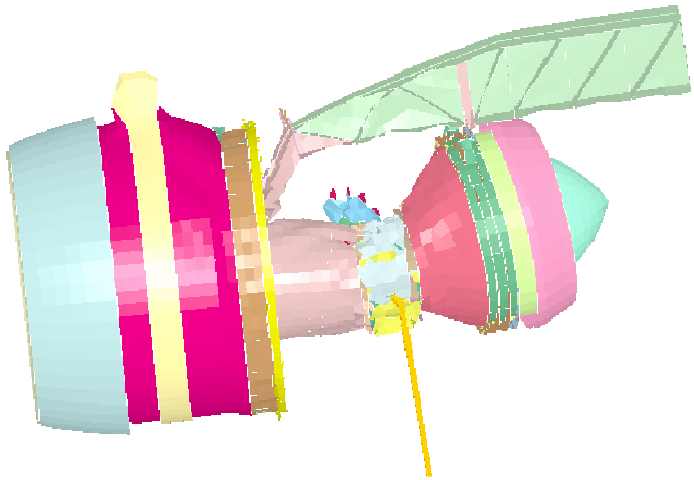

Figure 4.39 Divergence of model due to spurious hourglassing energy gain.

In industrial problems where large meshes are often employed, solution speed is very important, and hourglassing problems are typically mitigated by selecting a particular subset of elements in the model and prescribing these as fully integrated. Consider the simple 2D example below in Figure 4.40 with bottom nodes fixed and a single horizontal force applied to the top left corner. In the example below the 100% reduced integration mesh experiences severe hourglassing problems; whereas making one element (in purple) fully integrated essentially eliminates the hourglassing problem.

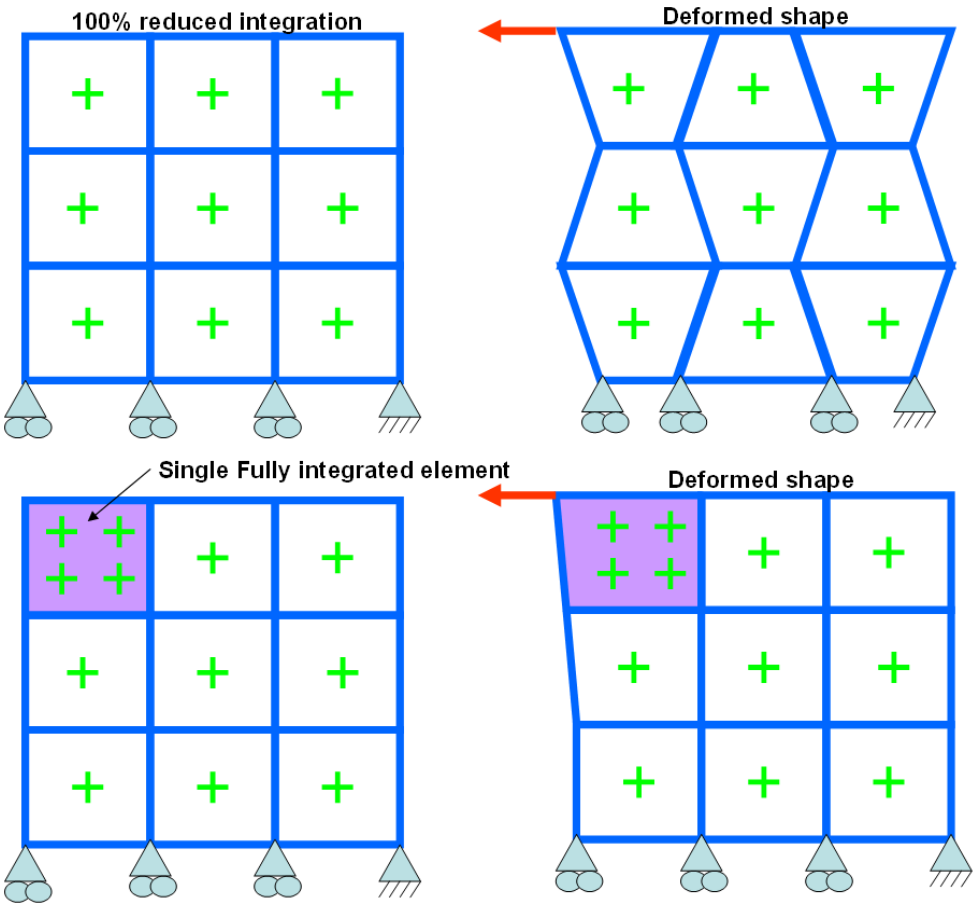

Figure 4.40 Judicious use of fully integrated element

In theory, the user could prescribe all elements as fully integrated but this makes run times about four times longer. This is the classic battle between speed and accuracy. Exactly which elements to prescribe as fully integrated requires experience running explicit finite element codes as well as a priori knowledge of the potential load paths in the problem. As shown in Figure 4.41, for example, by prescribing only the blades as fully integrated, with everything else being reduced integration, dramatically reduces the hourglassing in the rotor disk in Figure 4.42. Note how the global hourglass energy levels drop as well.

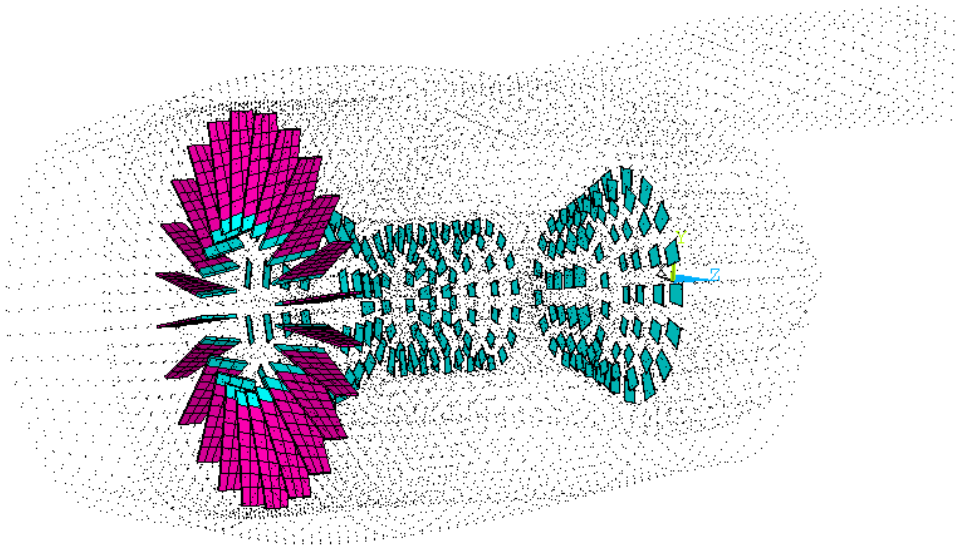

Figure 4.41 Blade shell elements were prescribed as fully integrated.

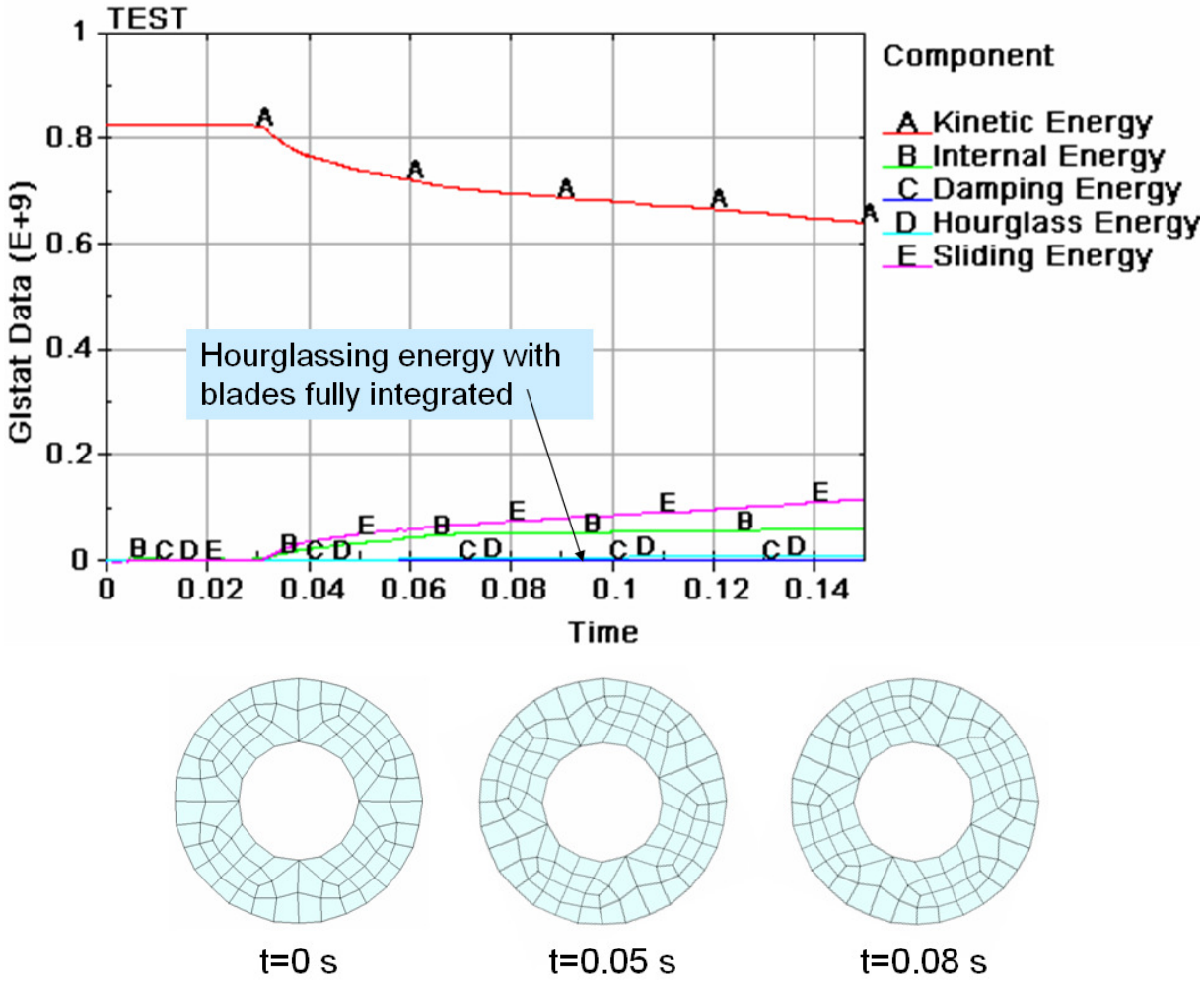

Figure 4.42 Fully integrated blades dramatically reduces hourglassing

The baseline model, as presented in this thesis, had minimal hourglassing energy and any potential deleterious effects were deemed acceptable for the speed increase gained. However, during a routine check with an extended integration time (longer than the prescribed 0.15 seconds) to ensure that the kinetic energy and bearing reaction loads were decreasing monotonically a potential issue was identified. This hourglassing issue is shown in Figure 4.43.

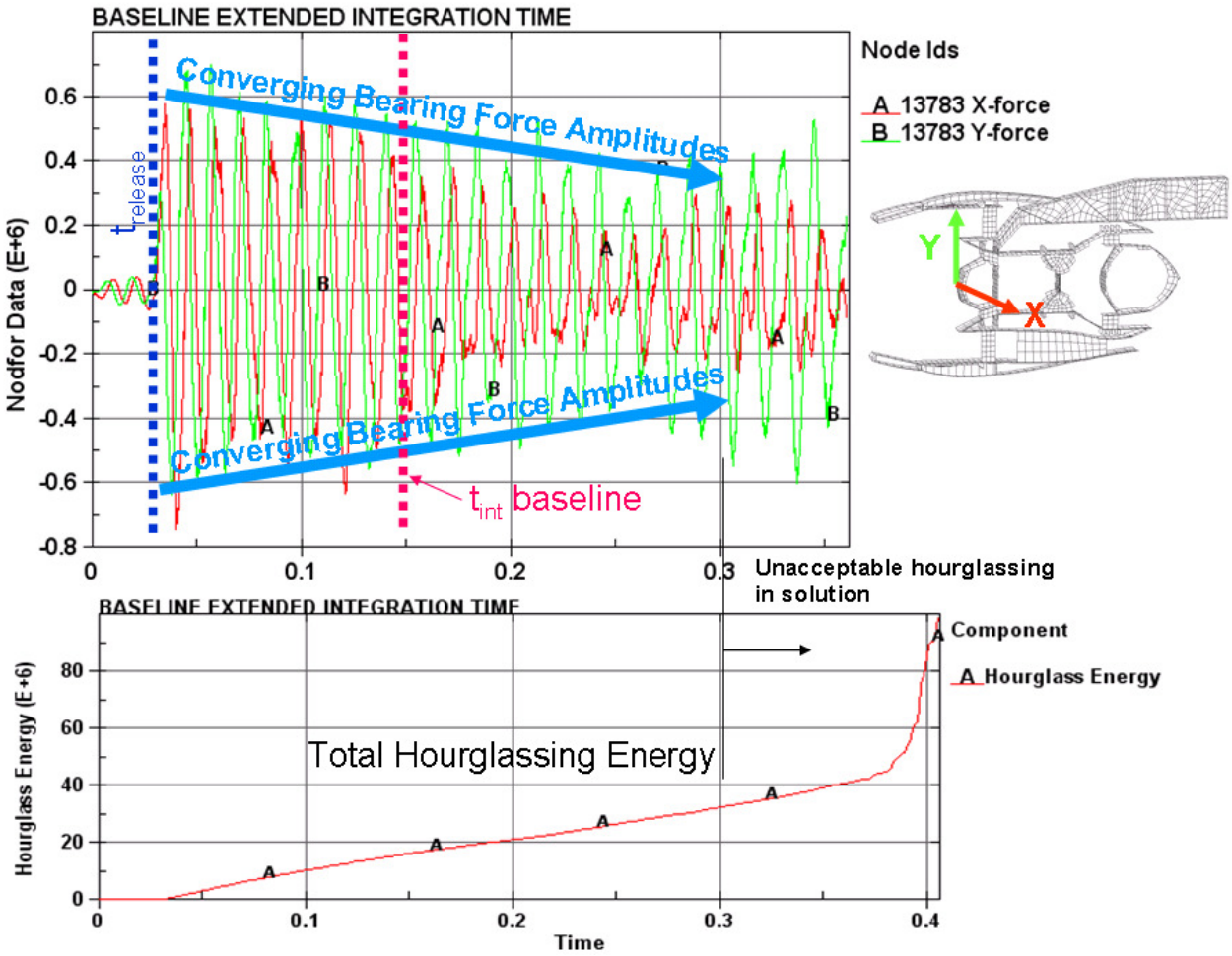

Figure 4.43 Hourglassing during extended integration

Note how the total hourglassing energy continues to rise and then 'blows up' after 0.35 seconds. The low pressure turbine rotor was identified as the culprit and is shown in Figure 4.44.

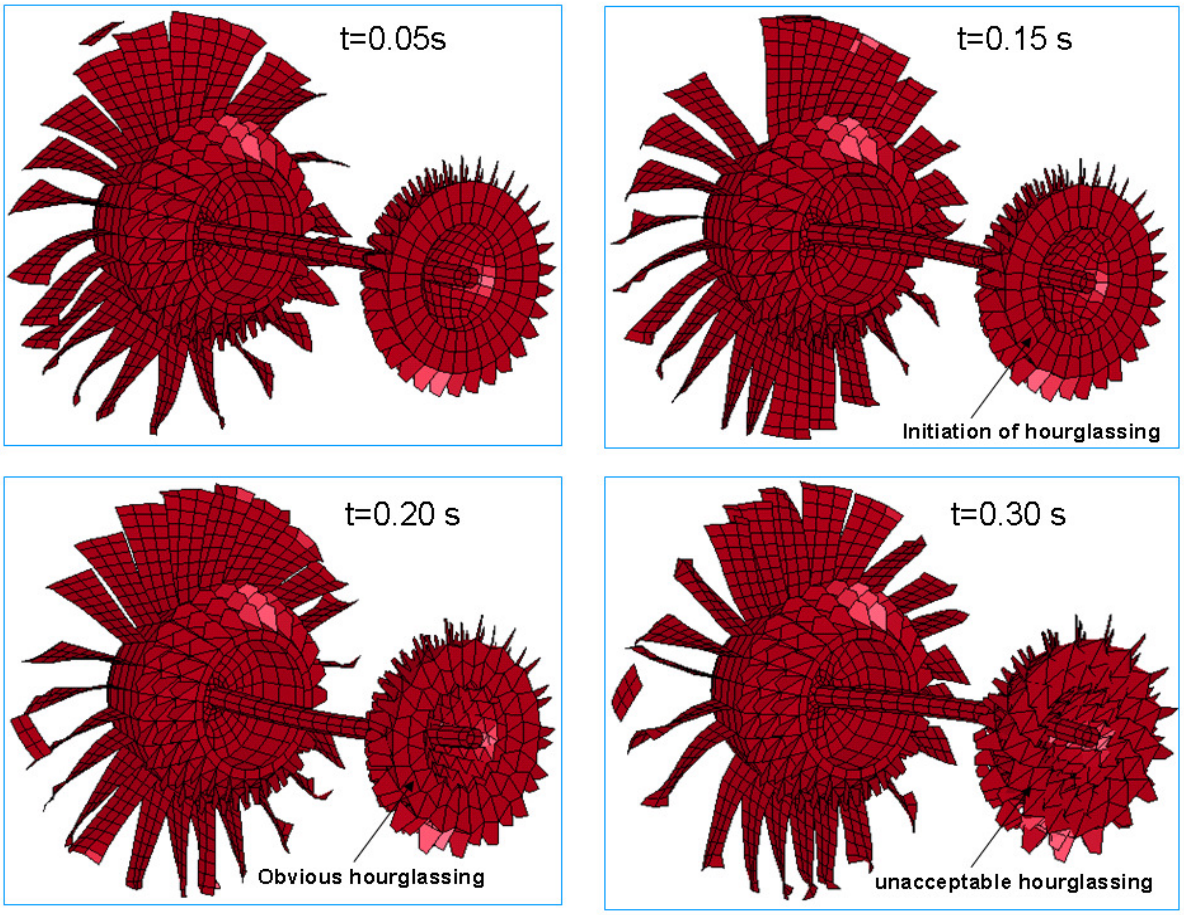

Figure 4.44 Development of Hourglassing energy in low pressure turbine

A proposed 'fix' to mitigate this hourglassing is shown below in Figure 4.45. Again, it should be stressed that this extended integration time result is not an accuracy issue for the current work but it does illustrate how hourglassing problems manifest in a real-world mesh and the methods used to repair the problem.

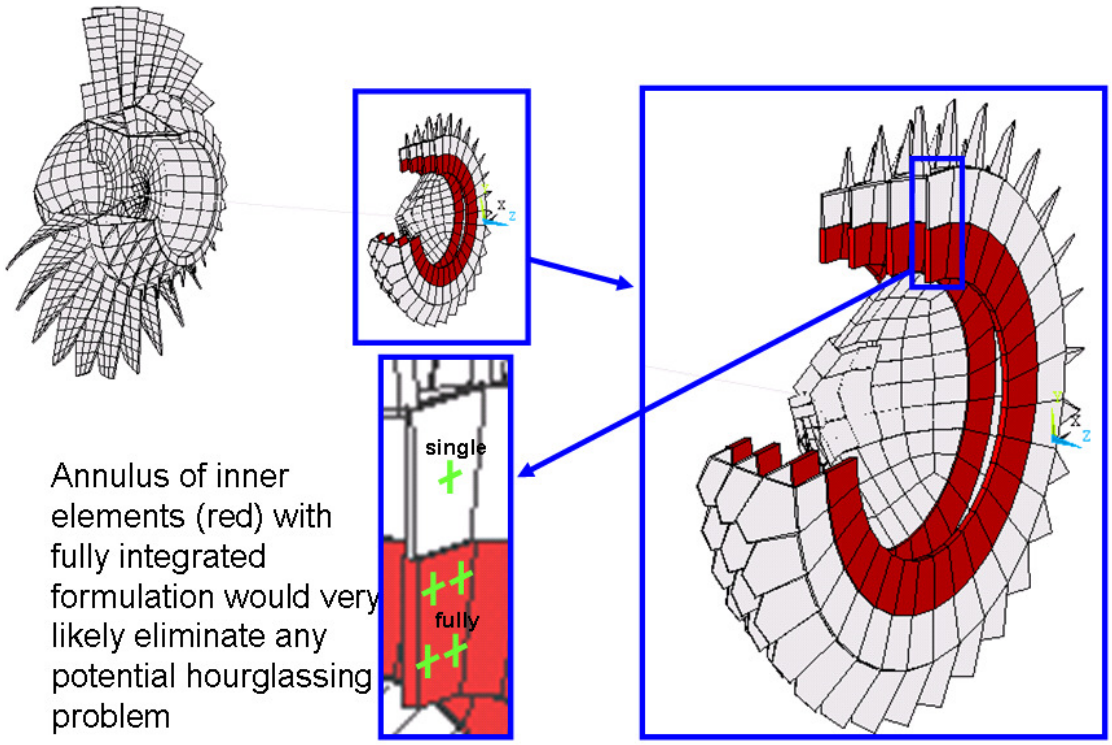

Figure 4.45 Mitigating hourglassing in low pressure turbine

The trade-off between accuracy and speed always requires engineering judgment; using reduced integration elements requires user vigilance to ensure that hourglassing energy remains insignificant during computations.

4.19 Mass Scaling: Understanding Critical Timestep Size

The critical timestep size, Δt_{crit}, is a crucial parameter for success with LS-Dyna and is approximately defined by:

$$\Delta t_{crit} = l_{edge}/c \qquad (4.16)$$

where l_{edge} is the shortest shell element edge (searched through the entire mesh) and c is the speed of sound in the metal (which is approximately constant for common metals). In LS-Dyna, to ensure stability, this Δt_{crit} is further reduced by a scalar factor k_1 as:

$$\Delta t_{\text{int}} = k_1 \cdot \Delta t_{crit} \qquad (4.17)$$

The scalar k_1 defaults to 0.9 and is numerically determined. If divergence (integration instability) problems are encountered reducing k_1 will often help in achieving integration stability. Execution time in LS-Dyna is inversely proportional to t_{int} (a larger t_{crit} is desired for fast solution). The primary control the analyst has over t_{int} (and thus solution time) is by creating a uniform mesh with no short element edge lengths. Alternately, a technique called mass scaling can be used to address a mesh with a few short element edge lengths.

Example: The two plates below both have the same number of elements, nodes and DOF (both 6x6). An implicit code (ANSYS, for example) solves these in equal times; however, in an explicit code (LS-Dyna, for example) the left mesh will take about 5 times as long to solve (the smallest edge length is about 1/5th of the uniform edge length) . This is because the shortest l_{edge} is used to calculate t_{crit}. Note how a single small element acts as a bottleneck on solution time (this is similar to the example is Section 3.2.1).

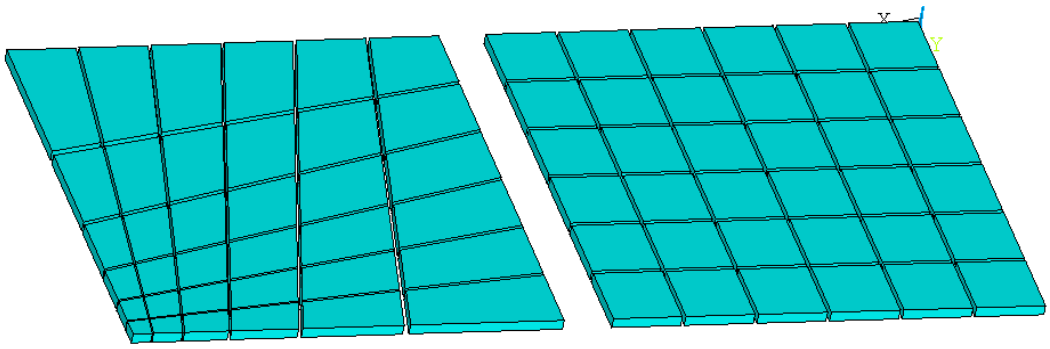

Figure 4.46 A 6x6 element plate meshed uniformly and with biasing.

4.19.1 Using mass scaling to Increase Critical Timestep Size

Sometimes short elements edge lengths in a mesh are unavoidable. LS-Dyna solution speed can be increased by using mass scaling. Mass scaling changes the speed of sound in a particular element by increasing the density in that element. The resulting slower sound speed increases t_{crit} for the particular element (which speeds up the whole run). Mass scaling should not be used for elastic wave propagation studies.

The shortfall of mass scaling is that artificial mass is added to the system. Sound speed, c, is approximately $c \cong \sqrt{E/\rho}$ where E is Young's modulus and ρ is mass density. Applying mass scaling to the mesh below, to get the left mesh CPU time to match the right mesh ($t_{crit}^{left}=t_{crit}^{right}$), would require increasing the pink element density by about 25 times, the yellow element density by about 16 times, and the green & orange element density by about 10 times and so on. Note the total mass of the left mesh would increase.

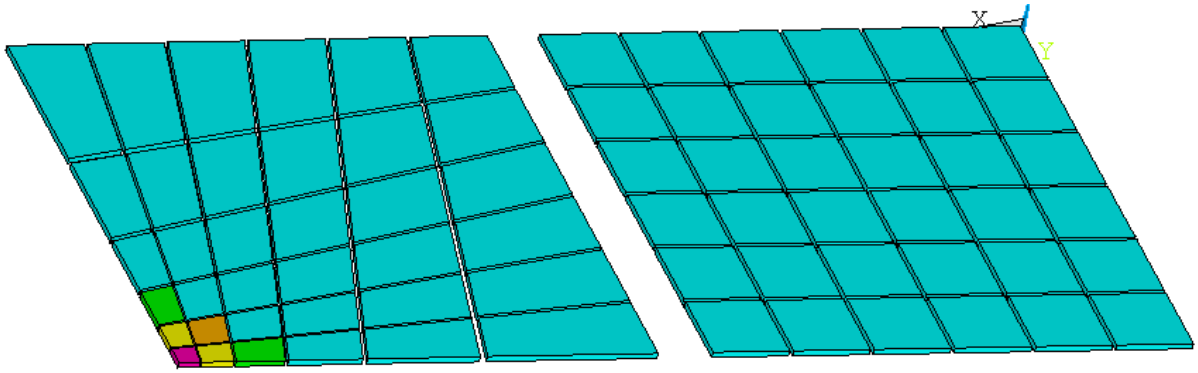

Figure 4.47 Mass scaling changes the density to locally alter wave speed.

Mass scaling is handled automatically by LS-Dyna. For the baseline model, mass scaling for elements with t_{crit}=5 μs (iteratively determined) or less was prescribed by adding the following code:

```
*CONTROL_TIMESTEP
 0.0000,0.9000,0,0.00,-0.500E-05
```

During the simulation, some elements may strain significantly and change their edge length. In this case, LS-Dyna dynamically updates the mass scaling for all elements (by computing edge lengths) during each timestep. This may cause the total mass of the system to change during the simulation. This is unphysical and the gained mass should be monitored.

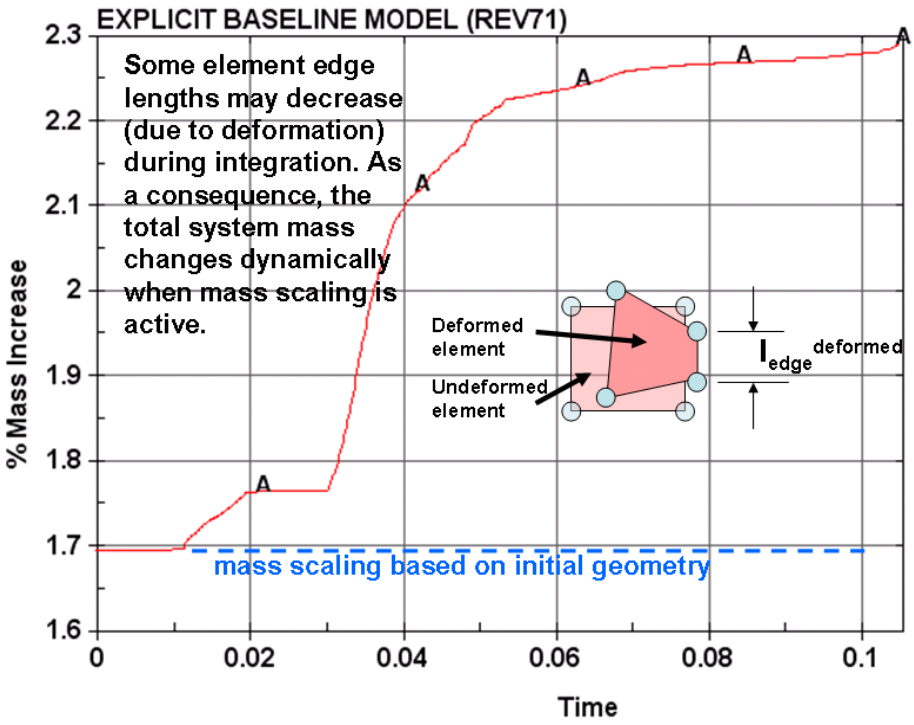

Figure 4.48 Increase of System Mass during Integration

For the Baseline model the d3hsp output file reports the smallest timestep sizes calculated.

100 smallest timesteps

type	element number	timestep
shell	1679	0.24679E-05
shell	2689	0.24679E-05
shell	7331	0.34481E-05
shell	7293	0.34481E-05
…….		
shell	2701	0.35683E-05
shell	2681	0.35683E-05
beam	5143 (axial)	0.37336E-05
beam	5141 (axial)	0.37336E-05
beam	5143 (bending)	0.37336E-05
…….		
beam	5140 (bending)	0.37336E-05
shell	7333	0.37461E-05
…….		
shell	7219	0.37461E-05
……..		
shell	6540	0.52906E-05
shell	6525	0.52908E-05

According to this, elements 1679 and 2689 have the smallest timestep size of about 2.5 μs. These two short edge length elements dictate the integration timestep size for the entire model. However, if we increase the density of these two particular elements by a factor of four, we can change the timestep size of this limiting pair to about 5.0 μs. Similarly, the element pair 7331

and 7293 have a timestep size of about 3.4 μs. Increasing the density of this pair by a factor of two increases the timestep size to about 5 μs. This 'localized' density modification is performed on all short elements until they all have a user defined target (about 5 μs in this example).

As mentioned before, this mass scaling process was handled automatically in LS-Dyna for the baseline model. There is a trade-off between accuracy (due to system mass addition) and overall simulation speed. Mass scaling was used in the baseline model as well; the elements outlined below in red in Figure 4.49 and Figure 4.50 were mass scaled. Note that this increased the total system mass of the baseline model by about 2%.

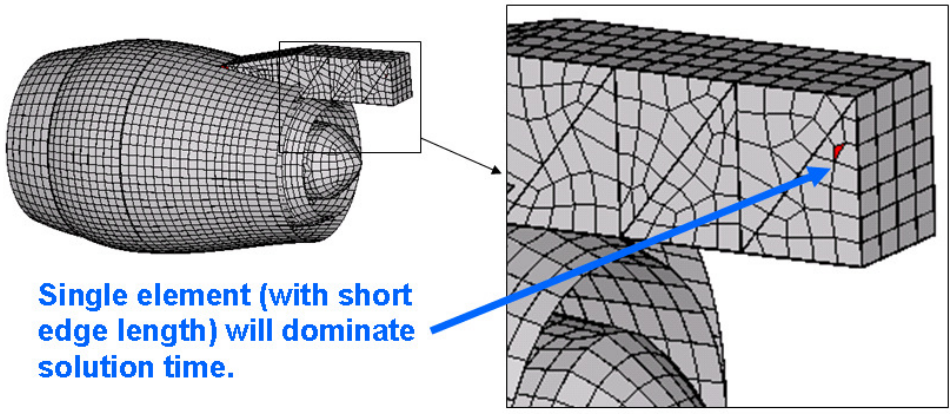

Figure 4.49 A single 'short' element can dominate solution time.

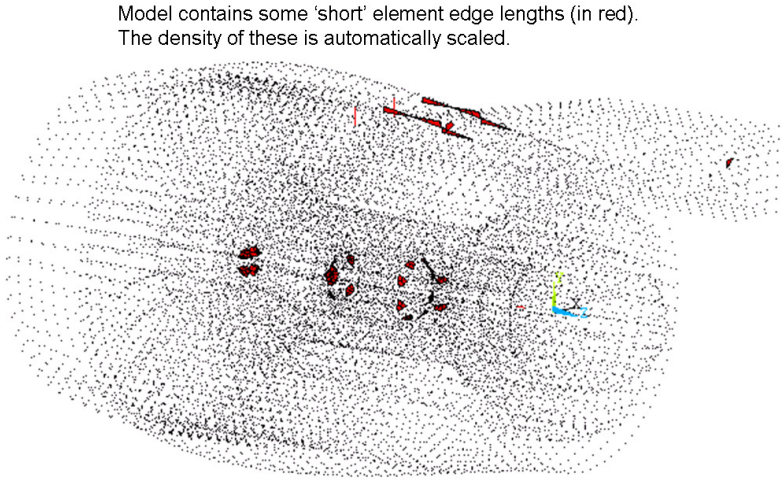

Figure 4.50 Mass scaled elements in baseline model.

In Chapter 7 mass scaling sensitivity trade studies will be addressed to understand the accuracy versus speed tradeoff.

5 Baseline Model: Results & Using Results for Design

Chapters 3&4 focused on developing and debugging the baseline model. This chapter focuses on providing results and interpretations of the results that could be used by part design teams. The next chapter will explore the sensitivity of results to various assumptions and inputs.

5.1 Animations of the Baseline Model FBO

Viewing animations of the baseline engine response to fan blade off loading is essential since there are many simulations interactions occurring during the FBO impact and subsequent rotating imbalance transient. Although animations are somewhat qualitative, they are very insightful and highly recommended for understanding the engine response. Animations can be downloaded from http://www.engr.usask.ca/classes/ME/990/thesis/ with a size of about 30Mb per animation. Right click and 'Save Target As'.

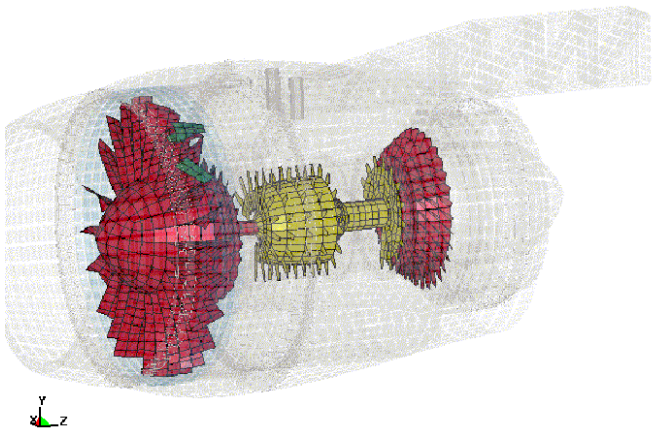

Figure 5.1 Full Engine Animation (full_engine.avi)

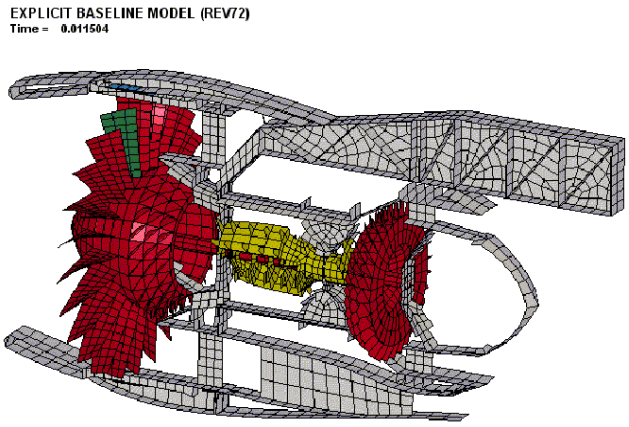

Figure 5.2 Cross Section Animation (section.avi)

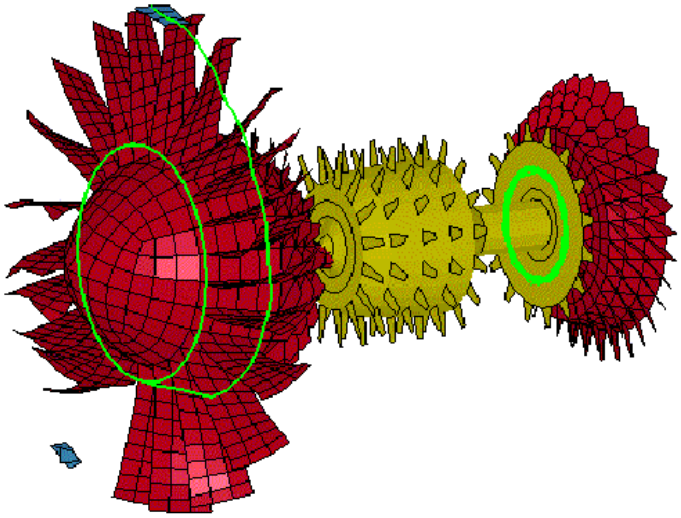

Figure 5.3 Rotor Path Trajectory (rotor_trajectory.avi)

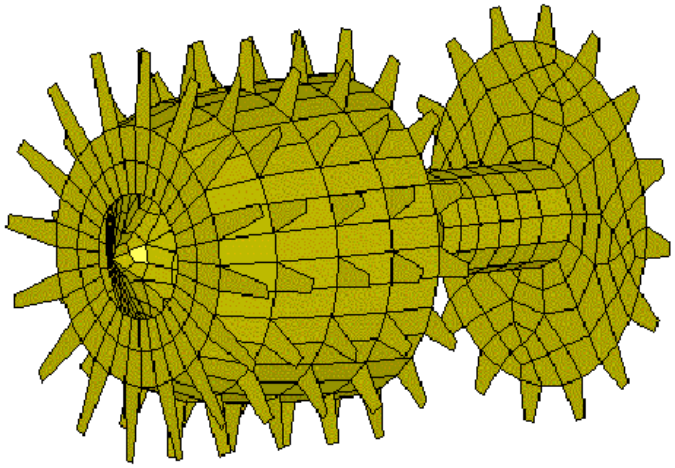

Figure 5.4 High Speed Rotor Animation (high_speed_rotor.avi)

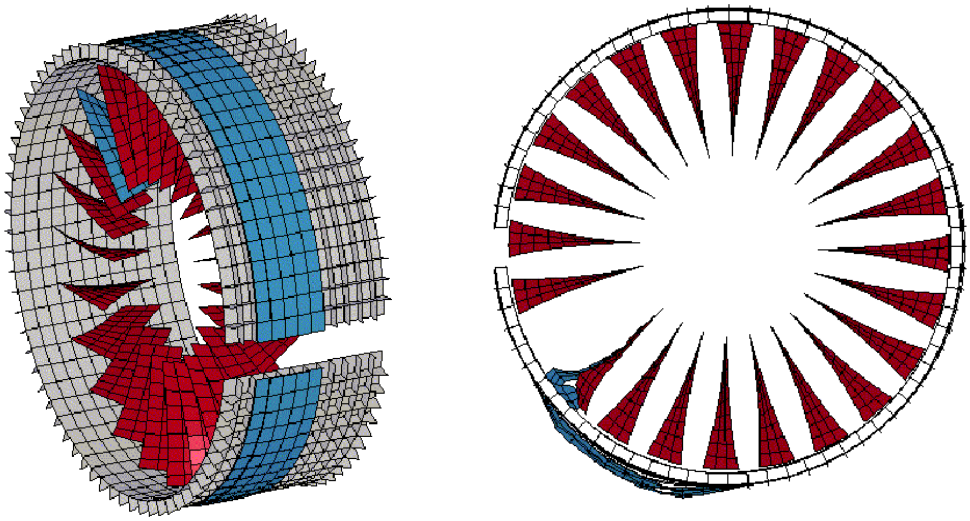

Figure 5.5 Fan Blade, Isogrid and Fabric (side_impact.avi and front_impact.avi)

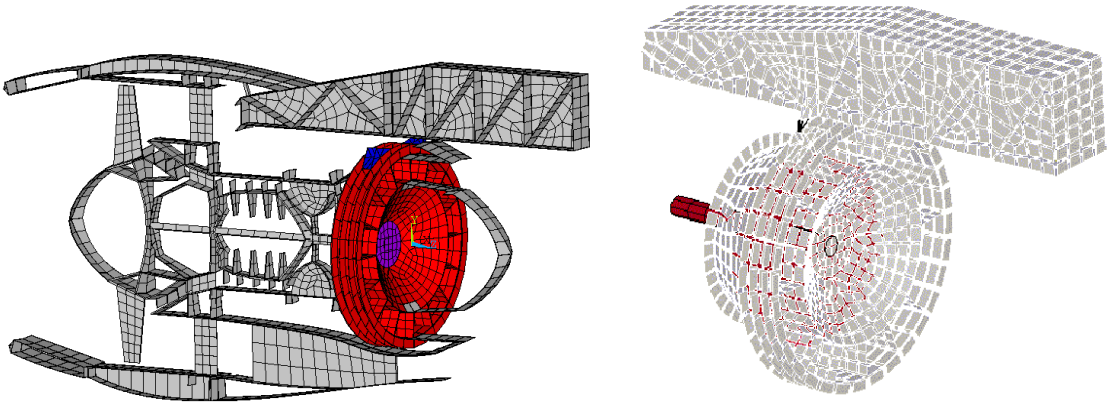

Figure 5.6 Turbine Exhaust Case (turbine_exhaust_case.avi)

Several snapshots in time of the fan blade, fan case, isogrid and fabric interaction are shown in Figure 5.7. The trajectory of a point on the released blade (the green blade) is traced with a green line.

Animations can be downloaded from http://www.engr.usask.ca/classes/ME/990/thesis/ with a size of about 30Mb per animation. Right click and 'Save Target As'.

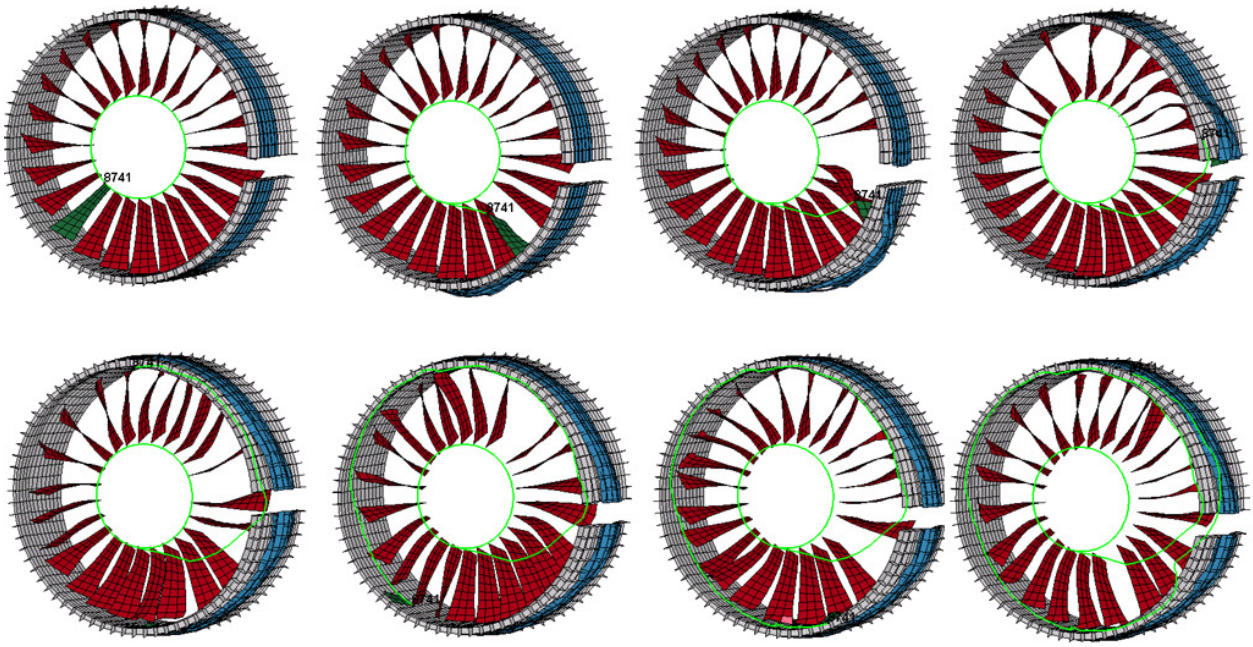

Figure 5.7 Fan Blade/Fan Case/Isogrid/Fabric Interaction

The trajectory of a point on the tip of the released fan blade is shown in Figure 5.8. This static image gives the reader some idea of the blade's path.

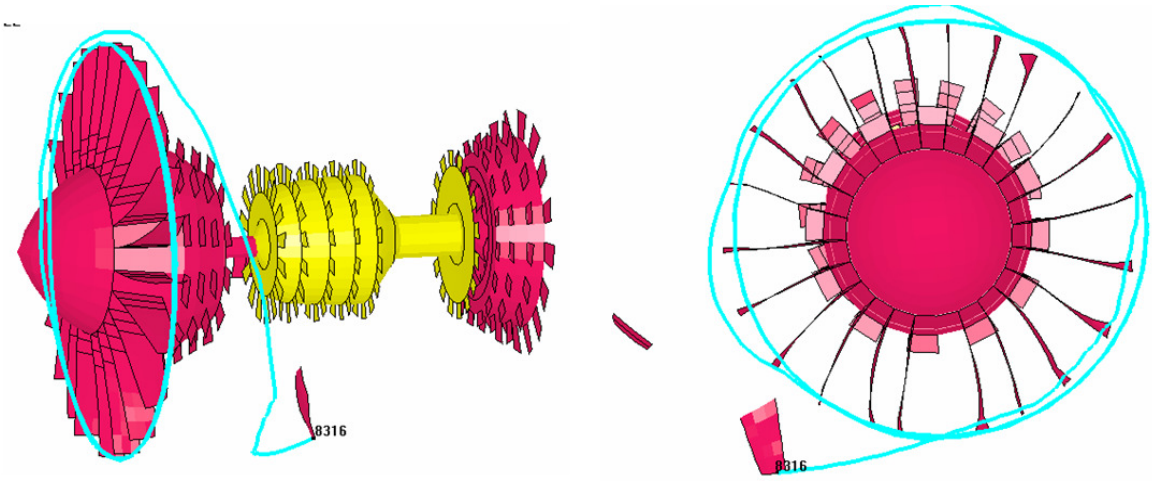

Figure 5.8 Trajectory of tip of released fan blade.

Dramatic deformations in the fan blades and isogrid casings are expected. Figure 5.9 shows the overall engine deformation. The lack of dramatic deformation demonstrates overall model stability. This overall stability is no accident; the reader should note that about 75 geometry, material and engine configuration updates were required to create a stable and realistic (stresses just below yield, realistic energy loss, moderate plastic strain, buckling strength margins, etcetera) baseline model which could be used to for study.

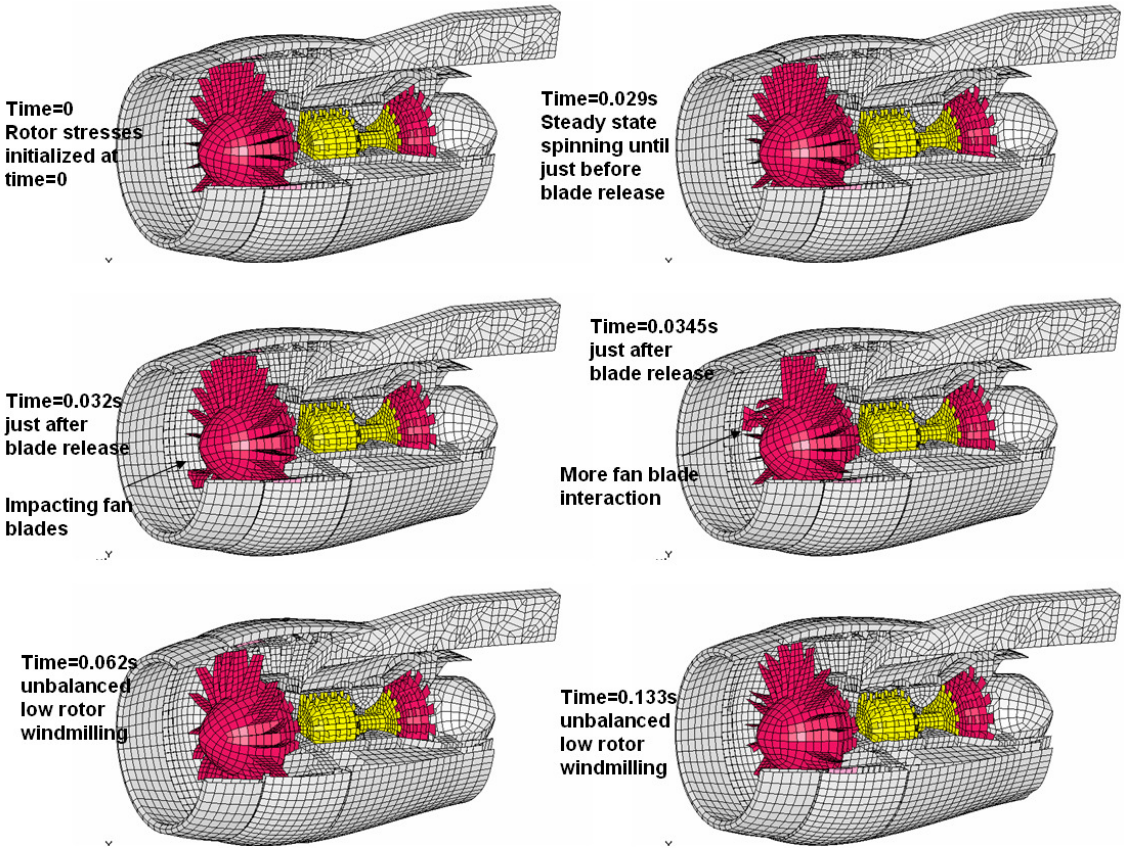

Figure 5.9 Snapshots of the of baseline model structural response.

As mentioned before, the animations provide great insight into the baseline models response but the results are somewhat qualitative. Fortunately, LS-Dyna can provide a host of quantitative results. The following sections will highlight some of the available options.

5.2 Trading Solution Accuracy for Speed

Real world analysis often requires speed versus accuracy trade-offs. Reduced integration elements that exhibit hourglassing, mass scaling due to occasional small element edge length and approximate stress initialization (a numerical tolerance on dynamic relaxation) are examples of techniques that sacrificed accuracy for speed. Their effects on the baseline model will be discussed.

5.2.1 Mass Scaling

A small amount of mass (with units of $lb \cdot s^2 \cdot in^{-1}$) is typically added to the system to increase solution speed (as discussed in Chapter 4). For the baseline model, adding about 0.2% mass was found to increase the run speed by a 2.5 factor (meaning a 1.5 hour run with mass scaling would be expected to take about 3.75 hours if no mass scaling was employed). Extra mass is added to individual elements as their edge lengths change during the simulation. The variation of "percentage mass increase" is shown in Figure 5.10

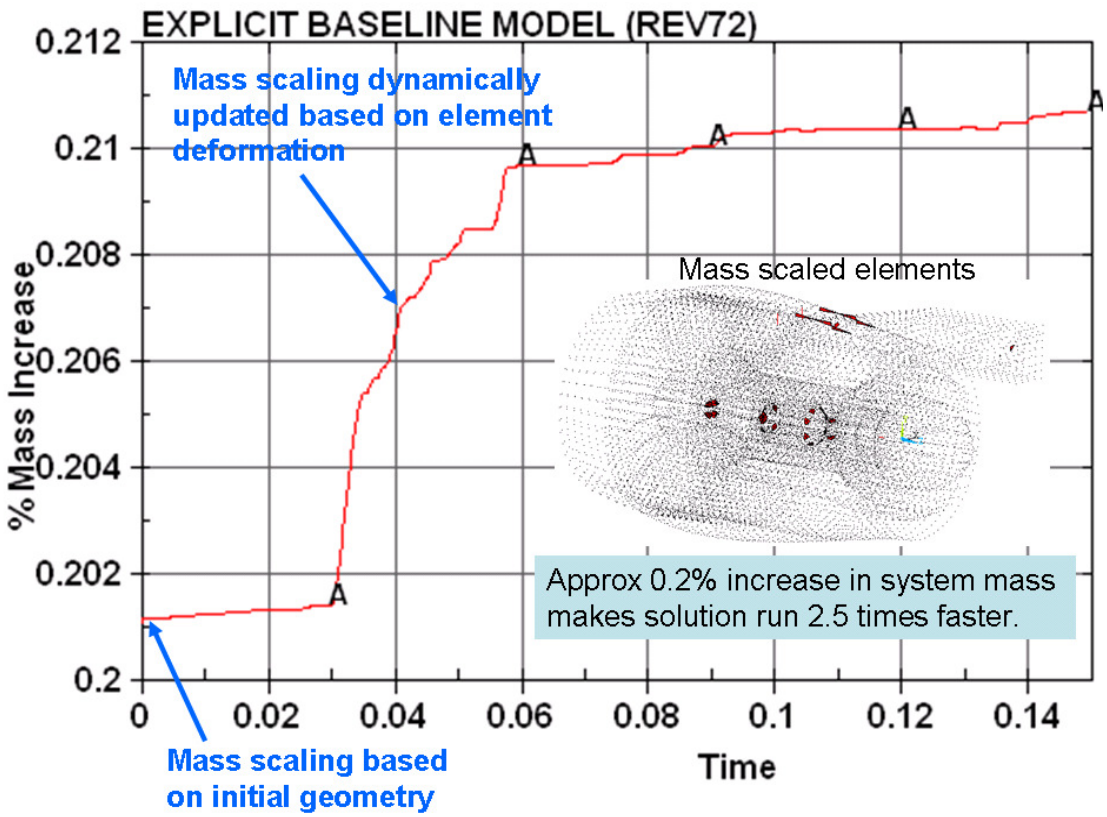

Figure 5.10 Percentage Mass Increase

The total added mass ($lb \cdot s^2 \cdot in^{-1}$) by component is shown in Figure 5.11. The mass added to the low speed rotor (denoted MATSUM along the ordinate) appears alarming; however, this graph shows the added mass which is in the order of ½ percent of the total system mass.

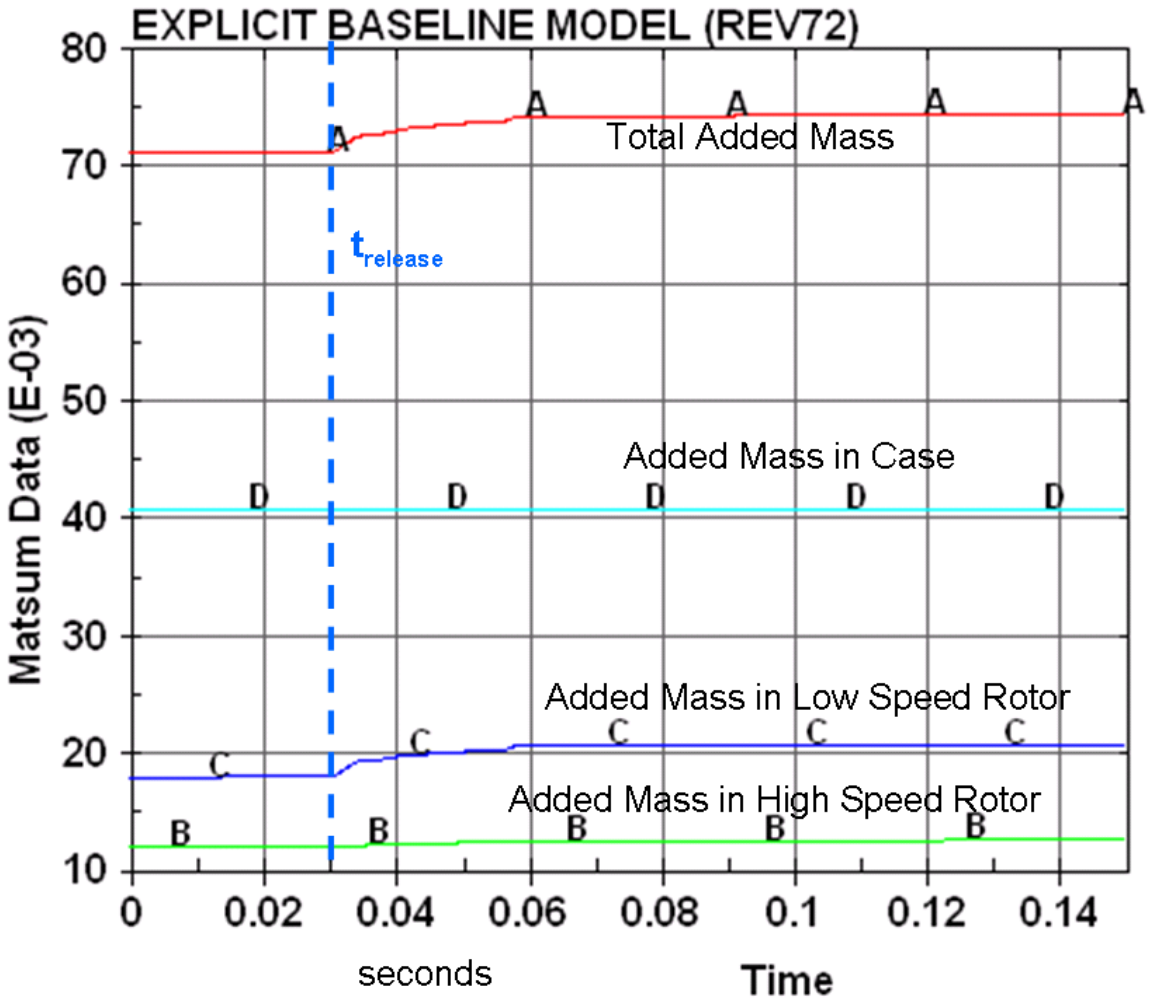

Figure 5.11 Mass added to components during integration

5.2.2 Hourglassing by Component

Single point integration elements were used whenever possible as they are about 4 times faster than fully integrated elements. Unfortunately, as discussed in Chapter 4, these single point integration elements exhibit hourglassing, a form of spurious energy, which reduces solution accuracy.

The component breakdown of hourglassing energy amongst the high rotor, low rotor and cases is:

$$HG_{total} = HG_{low} + HG_{high} + HG_{case} \qquad (5.1)$$

Figure 5.12 compares the hourglassing energy to the total energy and also breaks down the energy by component.

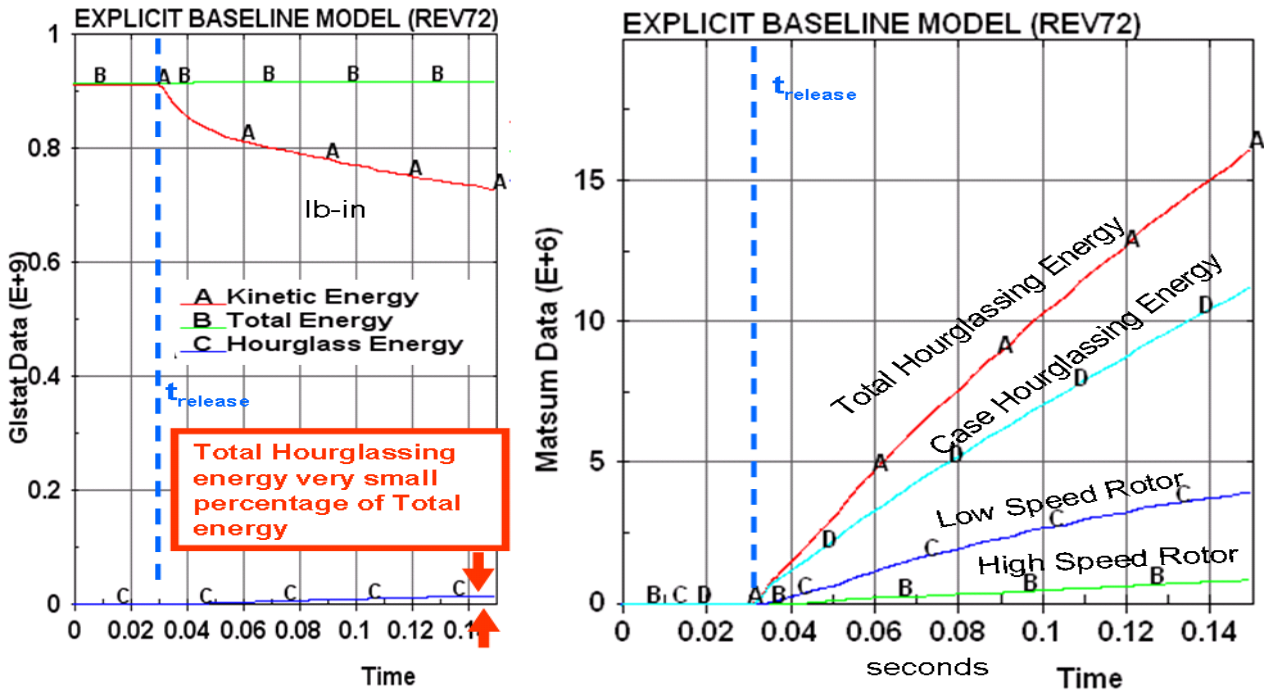

Figure 5.12 Total Hourglassing Energy

Any amount of hourglassing energy is a potential source of error; however, industry routinely sacrifices some accuracy to gain solution speed. Balancing this trade-off requires judgment and experience. But in any case it is always important to monitor the total hourglassing energy and also be able to identify the offending components that exhibit hourglassing (so that some fully integrated elements can be defined to fix the hourglassing problem).

5.2.3 Stress Initialization Approximations

The bearing reaction prior to blade release in Figure 5.13 should be approximately zero. Small non-zero amplitudes were intentionally permitted to save CPU time and offset the high cost of converging dynamic relaxation to a very tight convergence. This will introduce a small error into the results; however, the speed gained is an engineering tradeoff. The ordinate (labeled NODFOR) is the nodal force transmitted through the center node of the case.

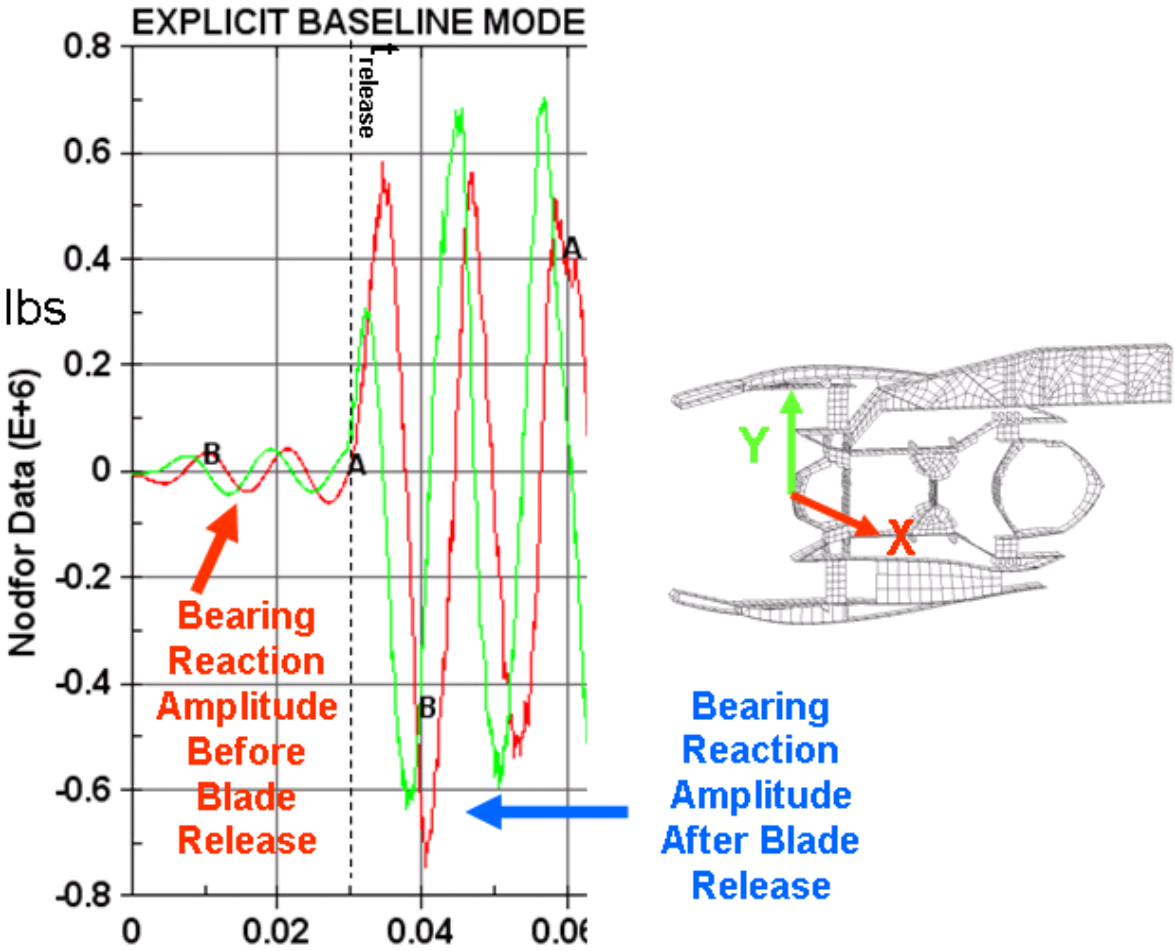

Figure 5.13 Residual Bearing reaction force due to approximate stress initialization

5.3 System Energy

The loss of rotor kinetic energy is balanced by the gain of internal energy (plastic work) and sliding energy (friction). It is important for engine designers to understand and control the mechanisms that absorb kinetic energy. These energies are further broken down by component to gain understanding into energy absorption mechanisms within the engine.

5.3.1 Global Energy Balance of Baseline Model

The global energy balance is shown below. The loss of kinetic energy is balanced by the gains of kinetic and sliding energy. Note that damping and hourglassing energies are minimal.

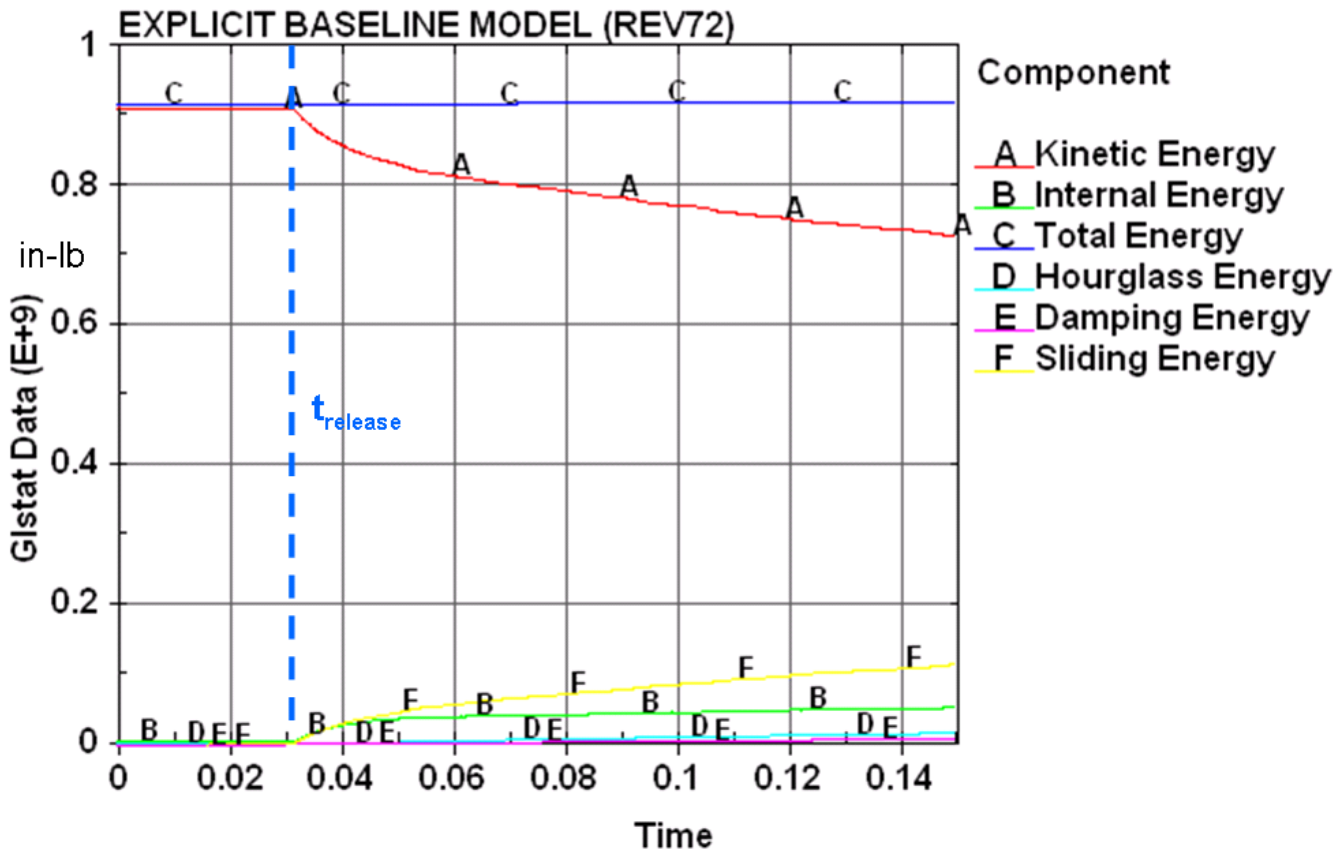

Figure 5.14 Global energy balance of baseline model.

5.3.2 Kinetic Energy Components

The spinning rotors contain huge amount of kinetic energy. The component break down of kinetic energy is.

$$KE_{total} = KE_{low} + KE_{high} + KE_{case} \qquad (5.2)$$

The kinetic energy components of the high and low speed rotor as well as static cases are shown in Figure 5.15.

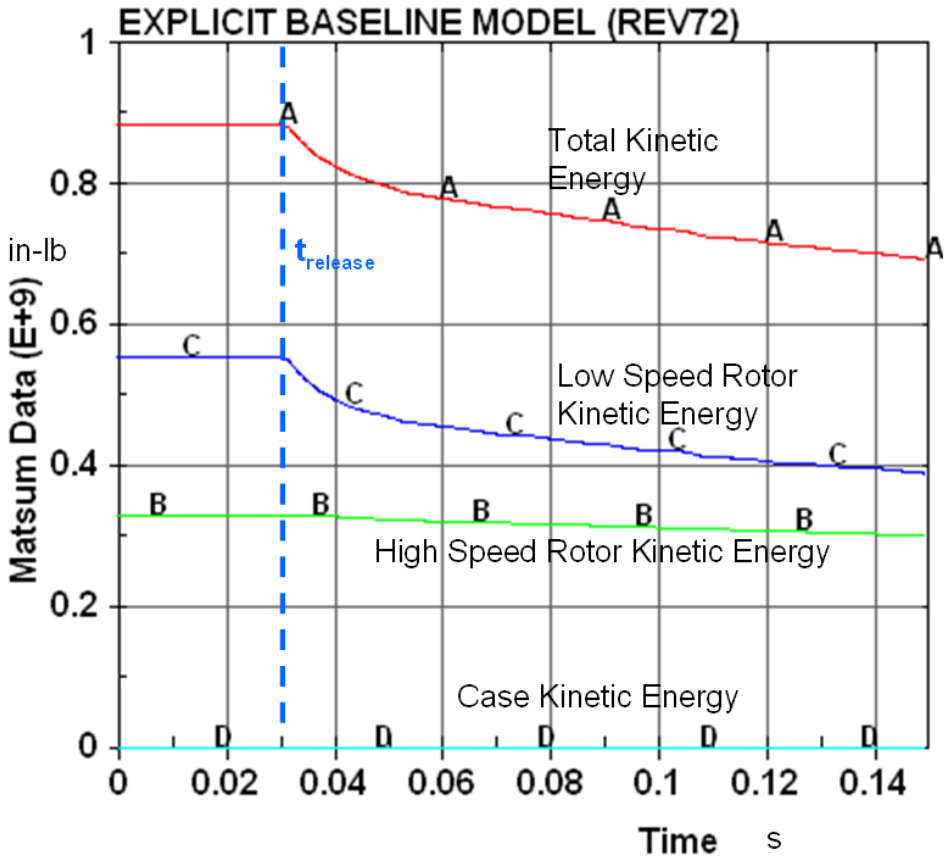

Figure 5.15 Components of Kinetic Energy

This figure shows (for the baseline configuration) that the low rotor (blue) is the primary driver for reducing kinetic energy. This proportion may change for other geometries.

5.3.3 Sliding Energy Dissipated at Contact Interfaces

The total sliding energy, ***SliE***, can be decomposed as:

$$SliE_{total} = \sum_{i} SliE_i \qquad (5.3)$$

where i is the number of defined contact sliding interfaces in the model. Recall that the sliding energy is the product of friction coefficient, normal pressure and tangential sliding. Sliding energy gains at individual contact interfaces are shown below.

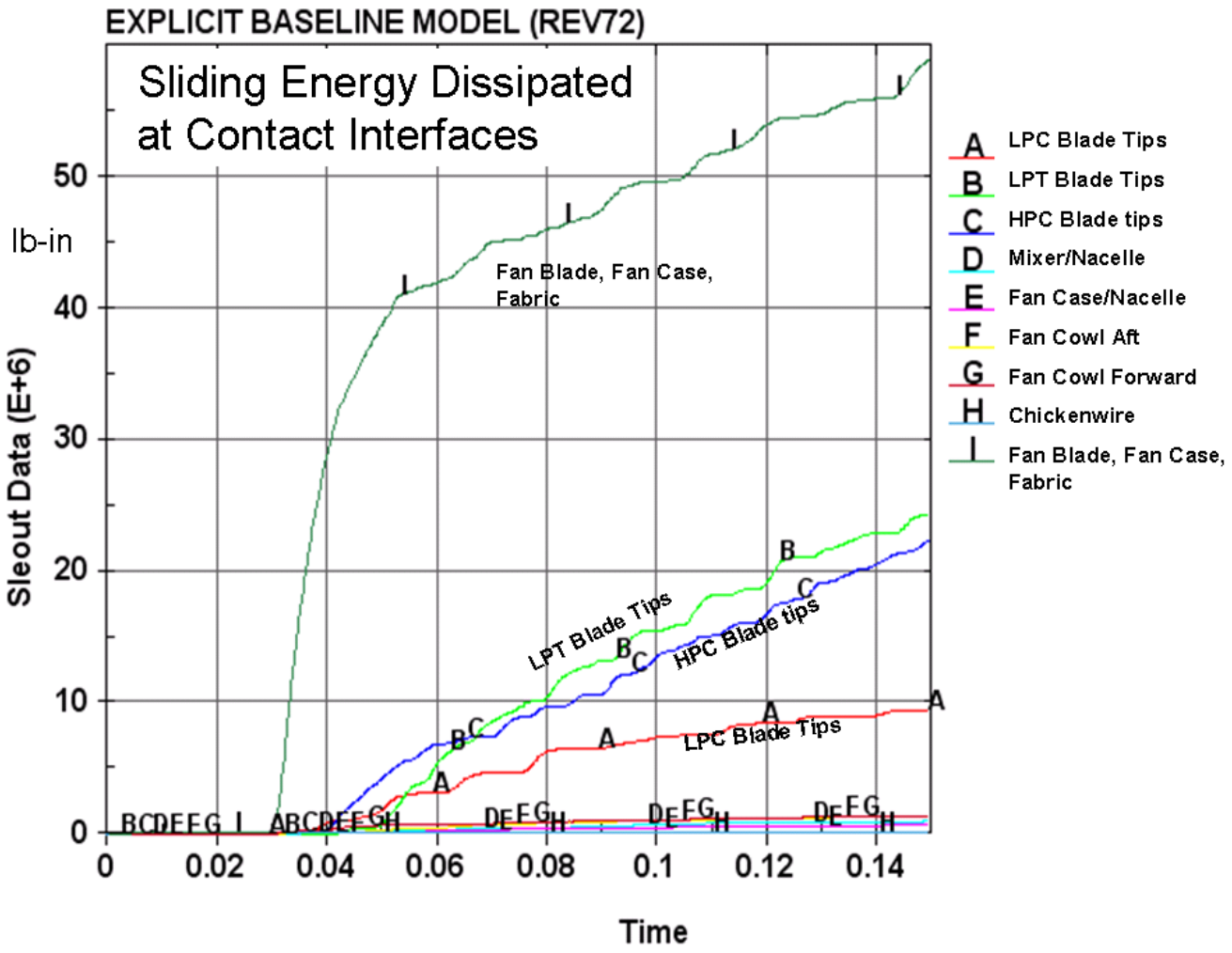

Figure 5.16 Sliding Energy Dissipated at Contact Interfaces

Figure 5.17 shows the sliding interfaces where energy is dissipated.

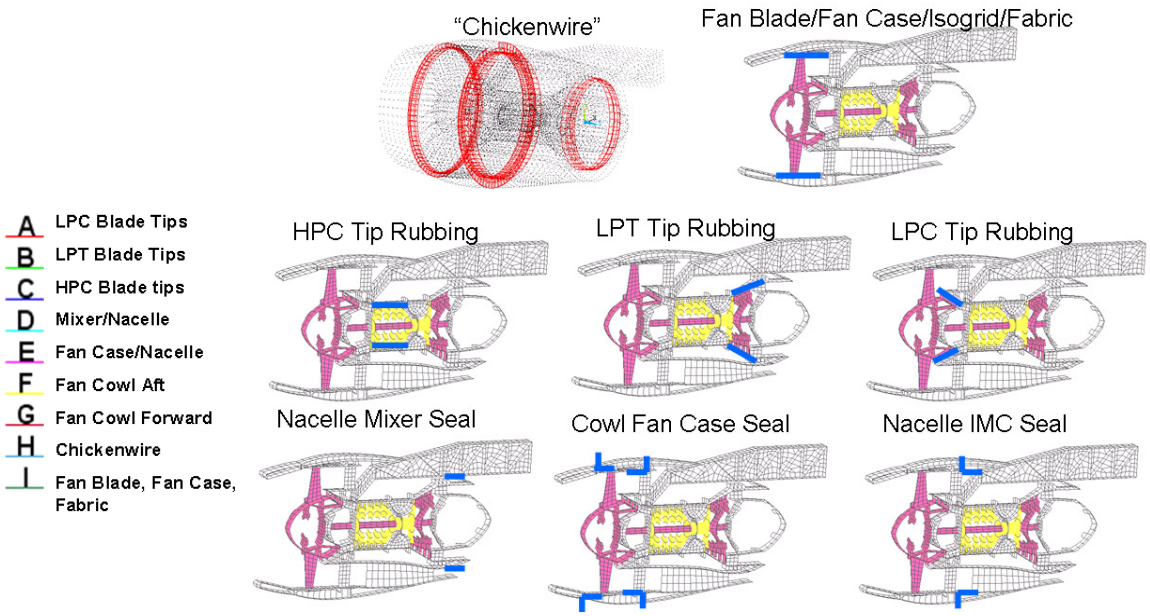

Figure 5.17 Contact Interfaces to Dissipate Sliding Energy

5.3.4 Internal Energy Components

Internal energy is the work done by strains, ***StrE***. This total can be broken down as:

$$StrE_{total} = StrE_{low} + StrE_{high} + StrE_{case} \qquad (5.4)$$

The component break down of strain energy is shown in the plot below. This energy includes both elastic and inelastic strain work done. Time is in seconds and energy in inch·pounds. Note how both the high and low rotor have some strain energy prior to blade release due to the pre-stressing. The internal energy histories of the high and low speed rotors, as well as the static cases, are shown below. Note that the high speed rotor's 'flat' response is due to it being composed of elastic material.

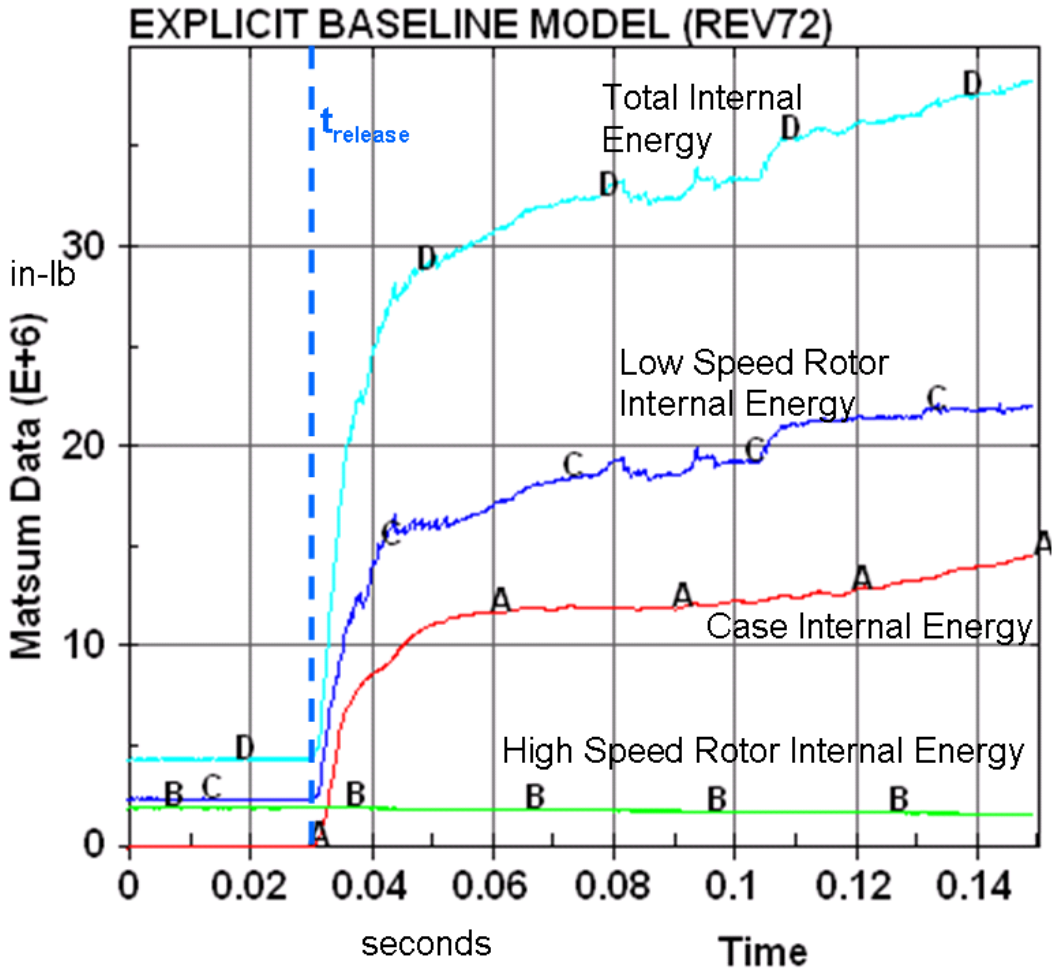

Figure 5.18 Internal Energy History by Component

5.3.5 Damping Energy

The component breakdown of damping energy, ED, dissipated would be:

$$ED_{total} = ED_{low} + ED_{high} + ED_{case} \qquad (5.5)$$

The total energy dissipated by damping on the blades is shown in Figure 5.19. Recall that no blade damping is applied until 'fuel shut off' at the blade release time of 0.03 seconds.

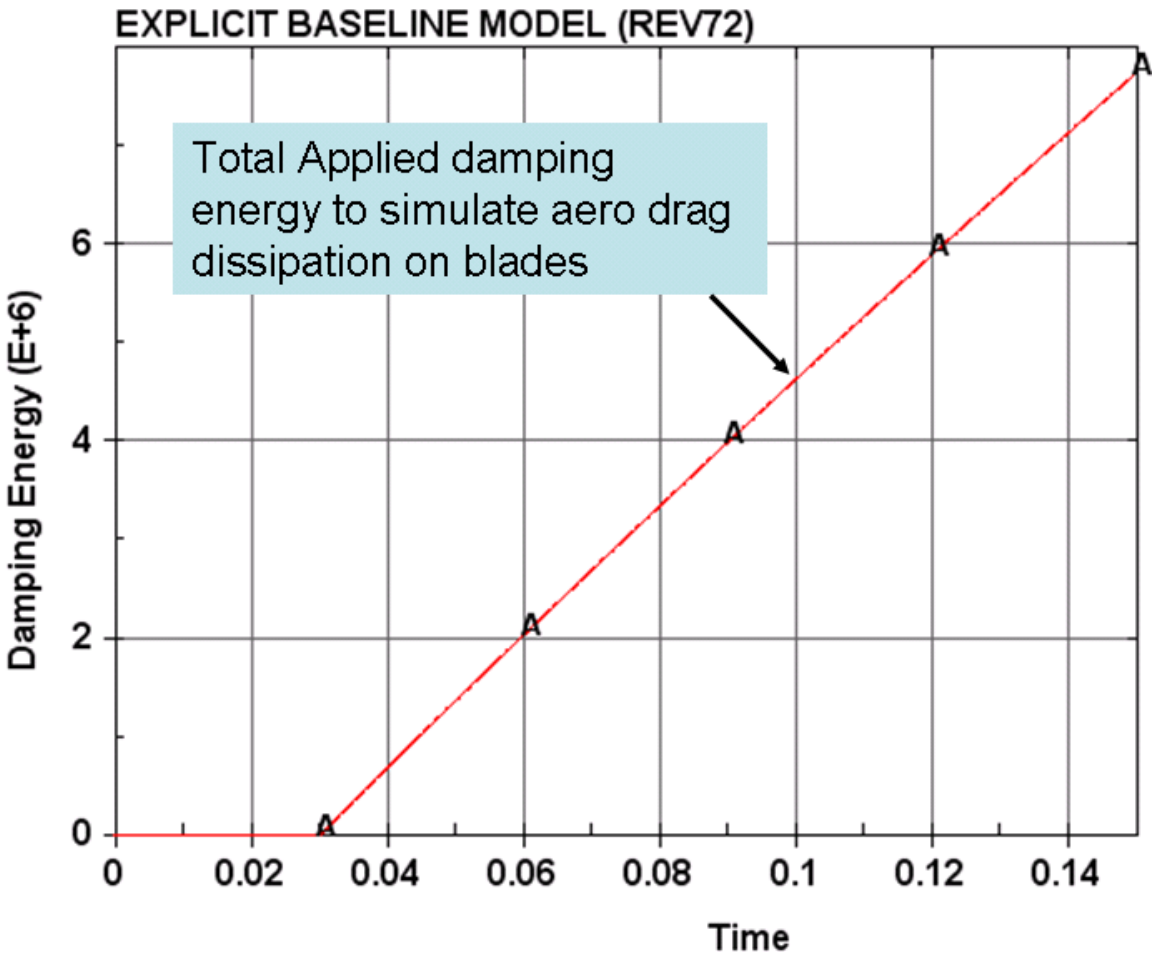

Figure 5.19 Aero Damping Applied to Blades

5.4 System Load Paths

The baseline model provides all types of loading and reaction information useful for component design. Some examples include:

- bearing reactions
- blade tip rubbing forces,
- fixed point boundary reactions
- loading across part connection

Results of these will be presented as well as how they might be used for designing components.

5.4.1 Bearing Reactions

The center nodes of the rotors were coupled (DOF coupling) to the static structure as described in Chapter 3. The rotors transmit load to the static structure and the force reacted out through each individual node (the 'bearing') as shown in the following figures. Note that, for the baseline model, the rotor blades were re-meshed with new blades as shown in Figure 4.35; any analytical estimates of the unbalanced force based on the old meshing should only differ slightly.

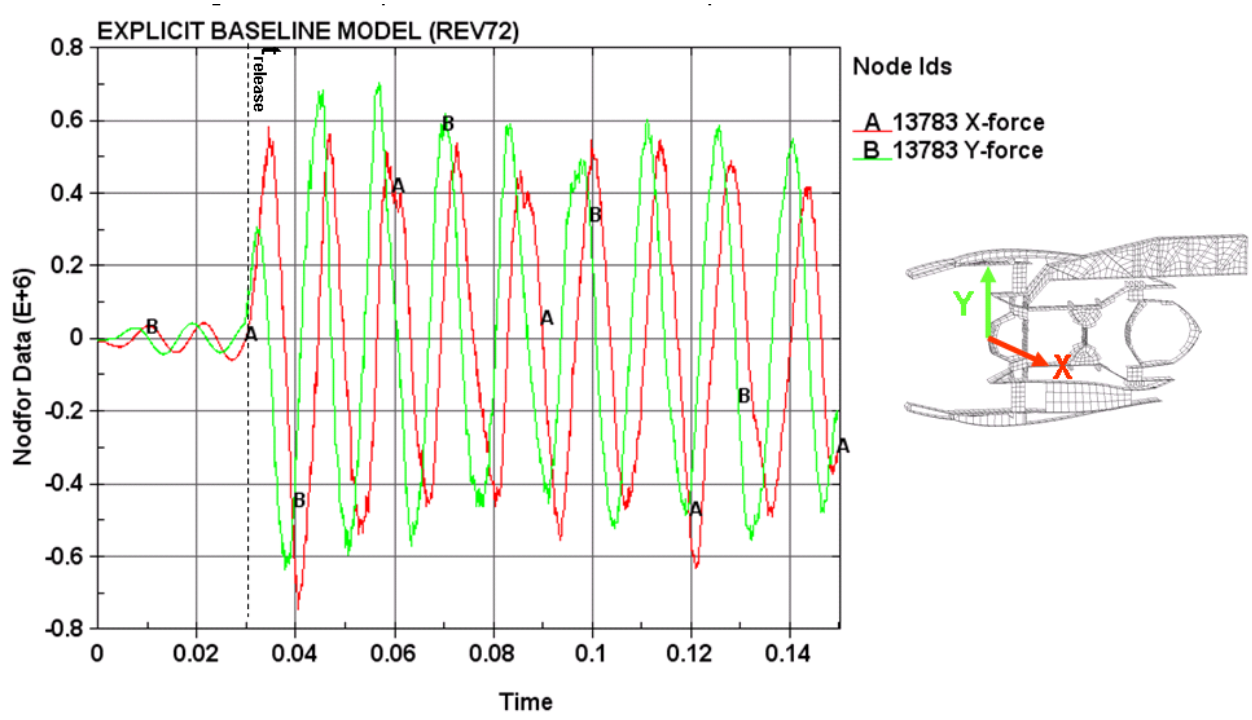

Figure 5.20 Low Rotor Forward Bearing Reactions.

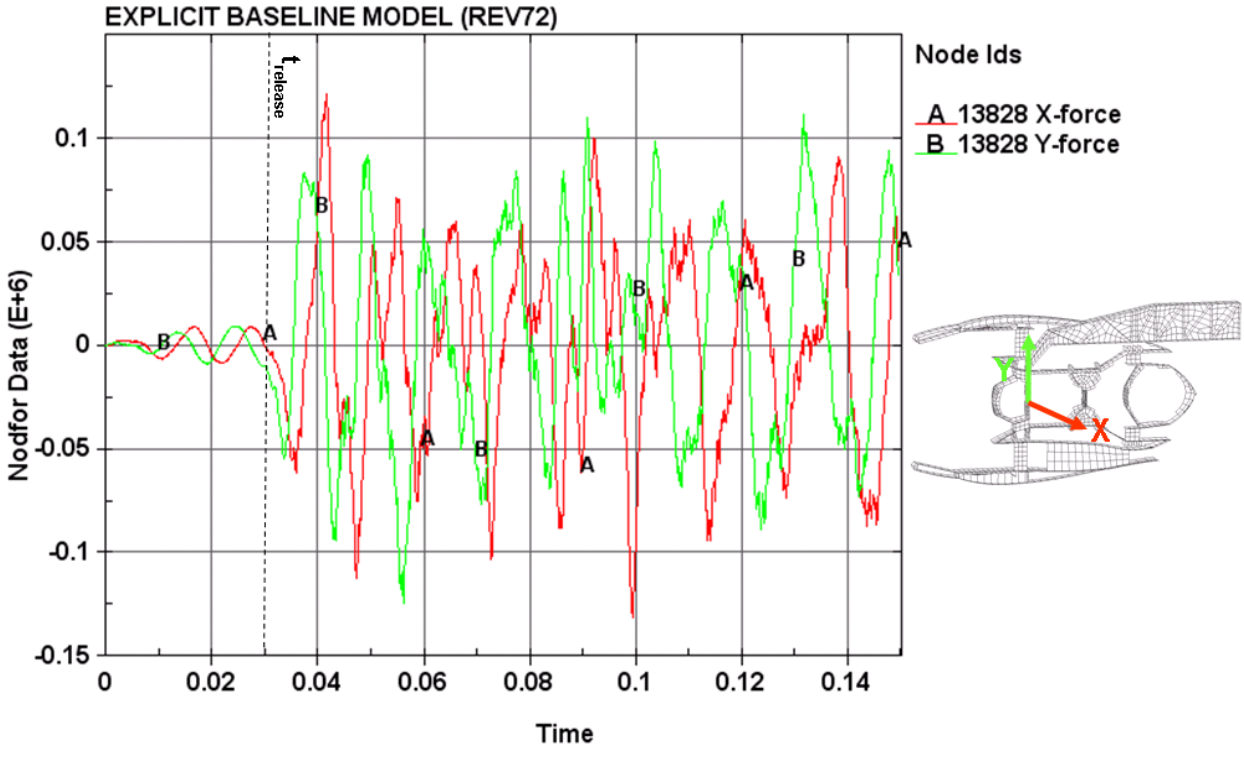

Figure 5.21 High Rotor Forward Bearing Reactions.

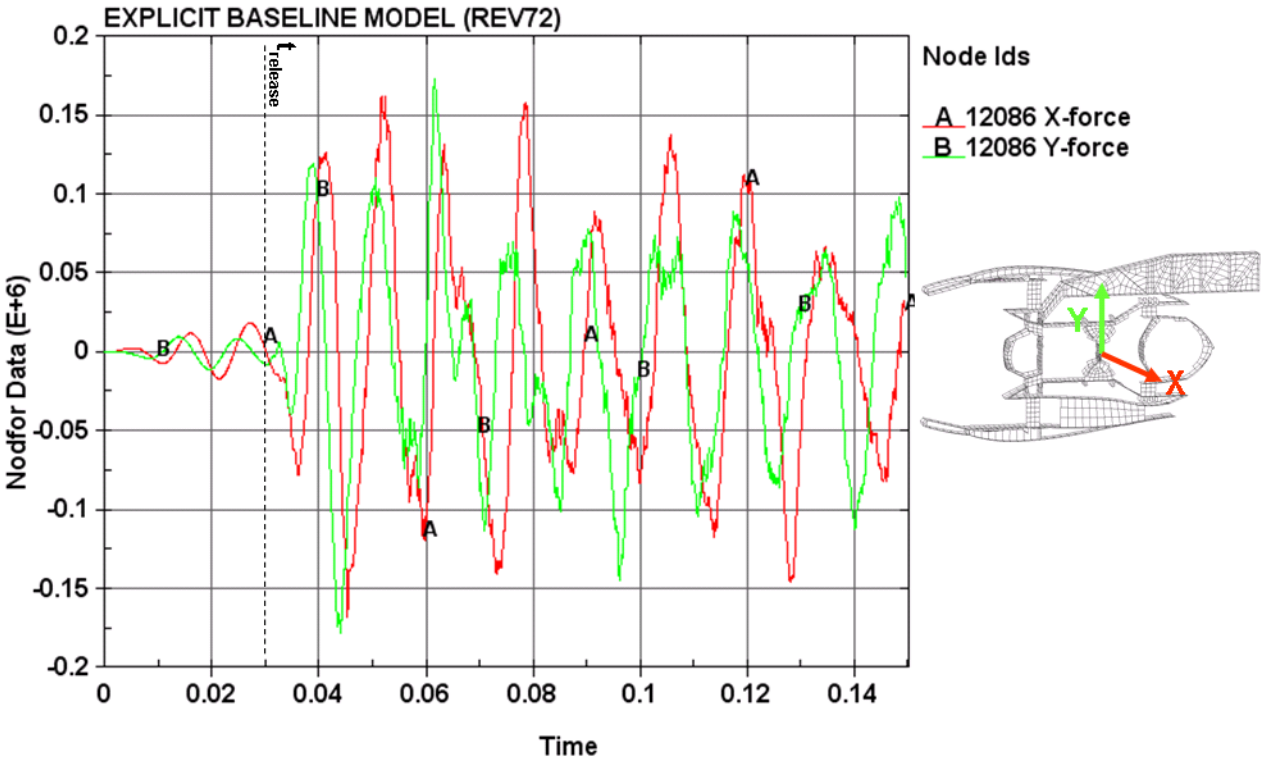

Figure 5.22 High Rotor Aft Bearing Reactions.

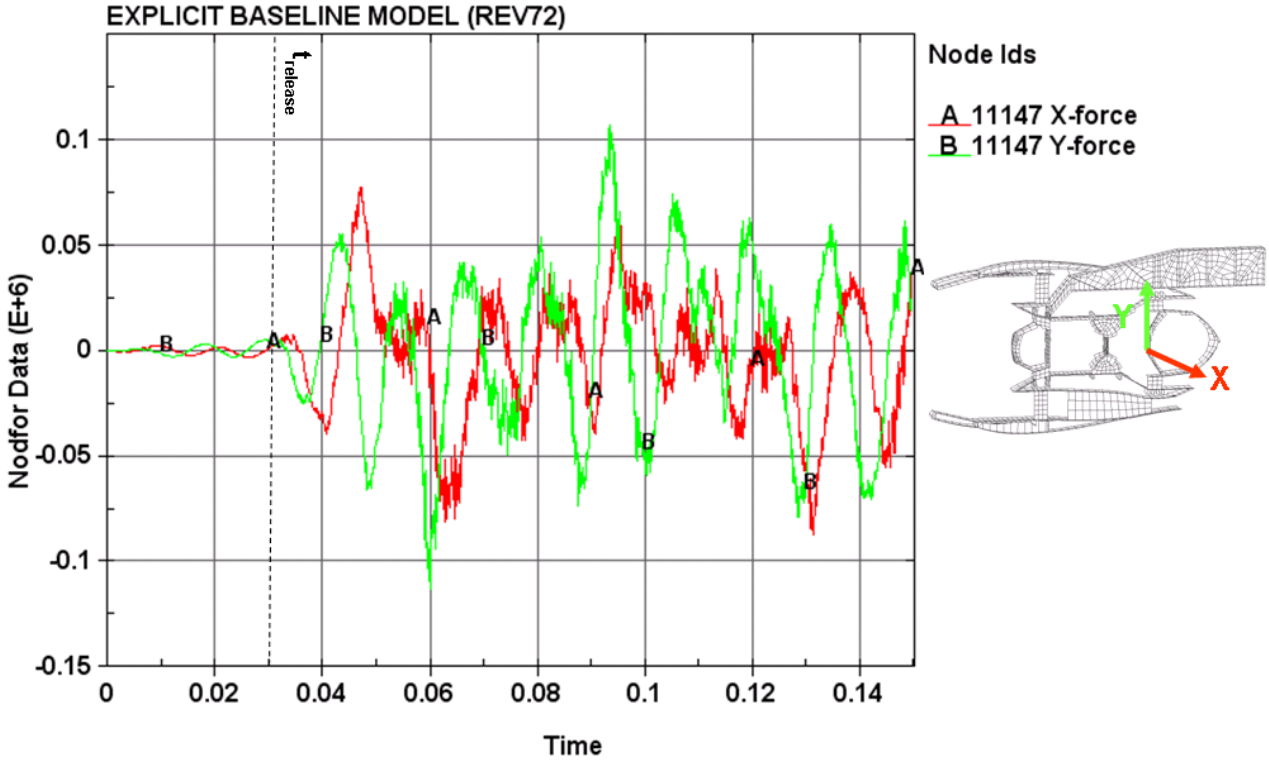

Figure 5.23 Low Rotor Aft Bearing Reactions.

5.4.1.1 Using Bearing Reaction for Design of a Component

The turbine exhaust case (TEC) in the aft end of the engine is used an example to understand how bearing reaction data might be used by a design team to create an engine component. The low rotor bearing reaction is re-plotted in Figure 5.24.

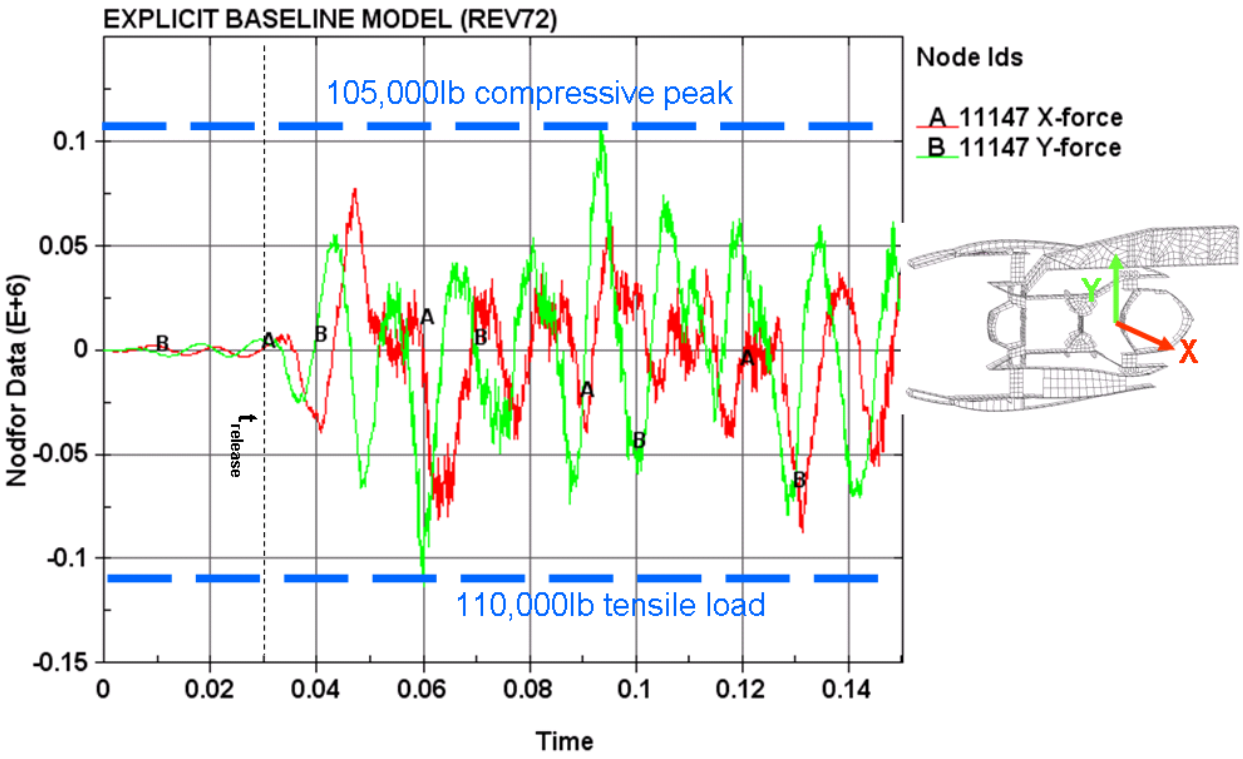

Figure 5.24 Bearing Reaction peak compressive and tensile forces

The peak vertical force range of +105,000 lb to -110,000 lb could be used to develop free body diagrams for various engine components as shown in Figure 5.25. Then the mount lugs, shear pins, cone thickness for buckling strength, airfoil buckling, etcetera, might be sized and developed.

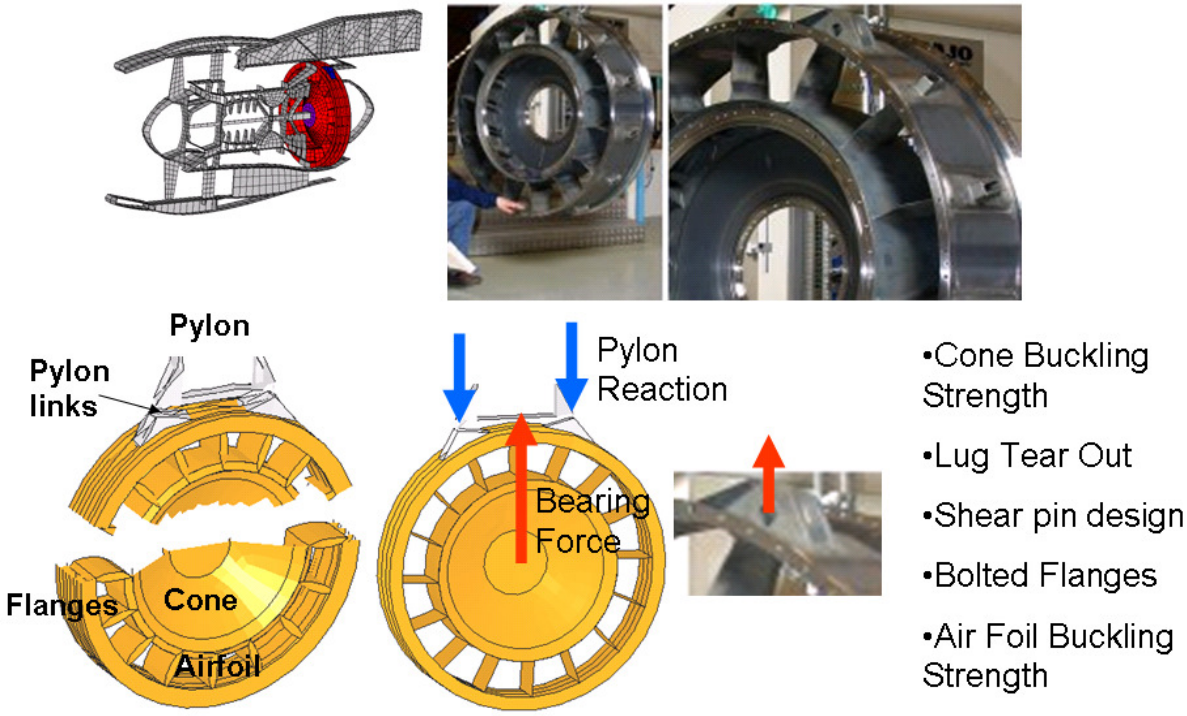

Figure 5.25 Design of TEC to meet FBO loads

Of course, the aerospace industry likely uses more sophisticated analytical methods to optimize component weight but the example demonstrates how FBO system models can assist in determining ultimate loads for a particular component. If the predicted loads are too high, the part may be over-designed i.e. overweight; conversely, if the predicted loads are too low, the part may be under-designed and at risk for failure. In any case, it becomes clear that even the most sophisticated design methods are limited by the accuracy of FBO system model load predictions.

5.4.2 Blade tip rubbing Forces

During routine operation the blades run inside the cases with a small clearance. This gap can close during FBO and the blade tips can hit the cases creating blade tip rubbing force. This is demonstrated with the Figure 5.26.

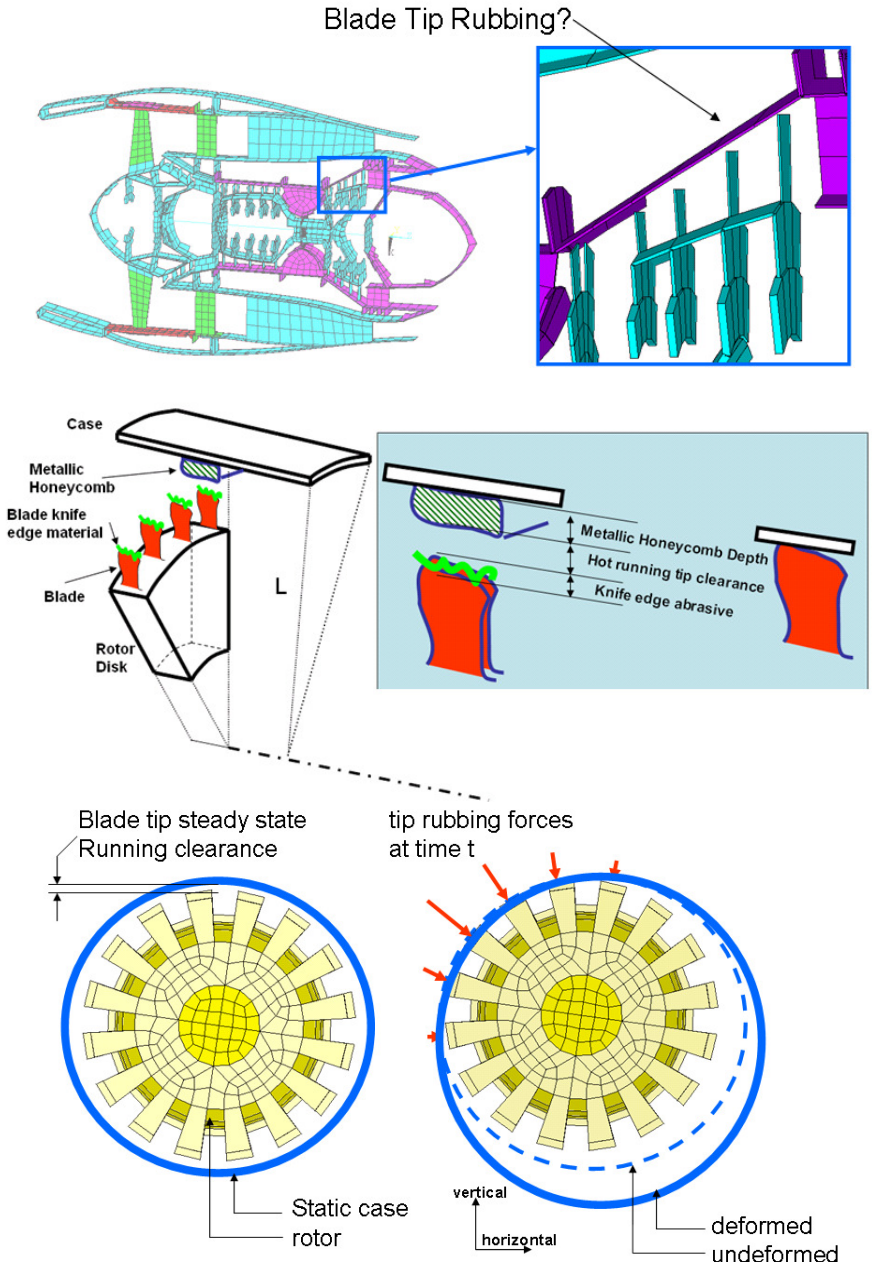

Figure 5.26 Blade tip rubbing forces.

If these forces are too high the blades can fracture, traveling downstream and fracturing the next set of blades, and so on. This total blade annihilation is known [6] as engine de-cobbing and is very undesirable. The total force at each tip rubbing interface is straight forward to extract from LS-Dyna and is shown, for the baseline model, in the figures below.

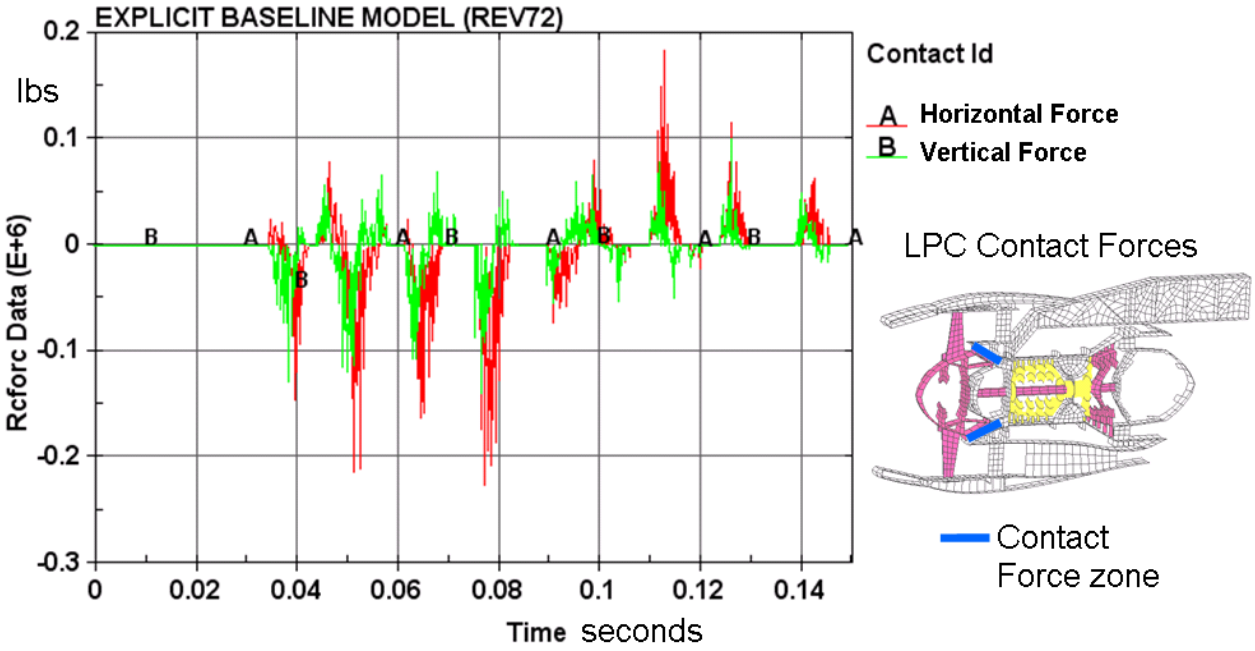

Figure 5.27 Total contact Forces in the Low Pressure compressor

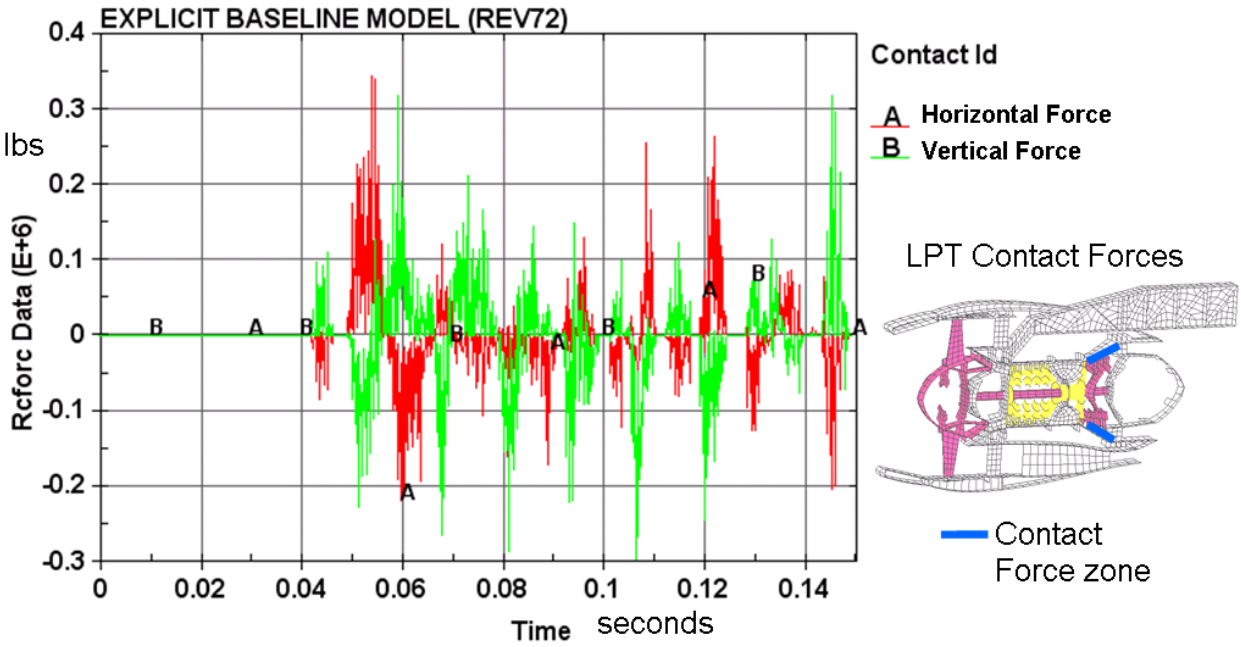

Figure 5.28 Total contact Forces in the Low Pressure turbine

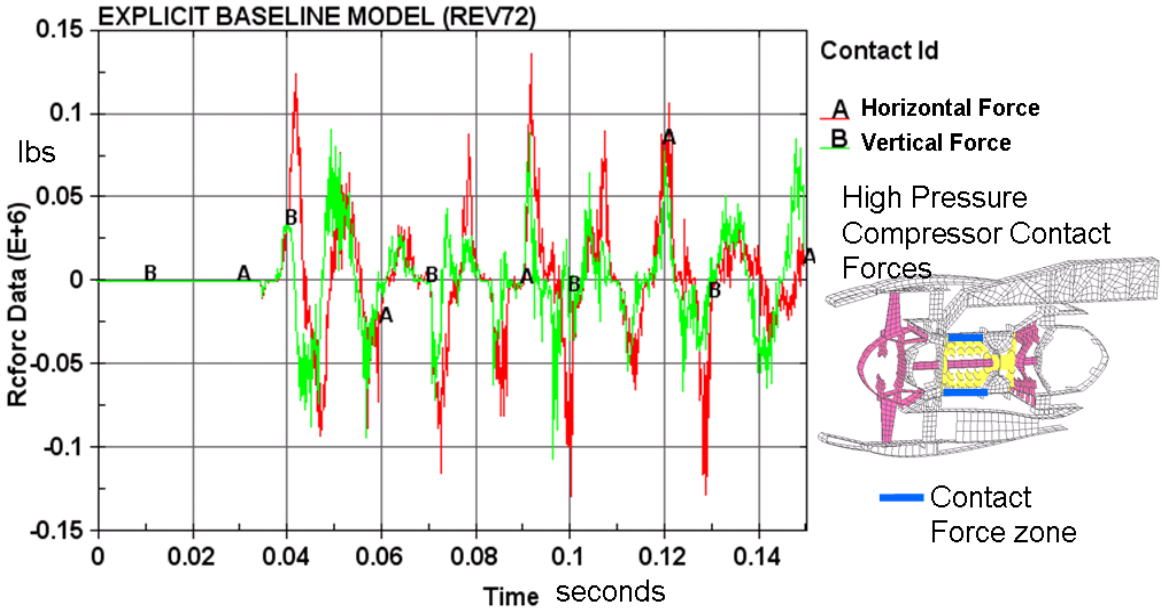

Figure 5.29 Total contact Forces in the High Pressure Compressor.

The LS-Dyna baseline model does not have the mesh resolution to predict individual blade failure; however, global design configurations (a specific combination of material, speed, geometry, and etcetera, comprising the system model) that tend to reduce the tip rubbing force are considered favorable.

5.4.3 Pylon Fixed End Reactions

The horizontal and vertical reactions of the fixed end of the pylon are shown in Figure 5.10 below.

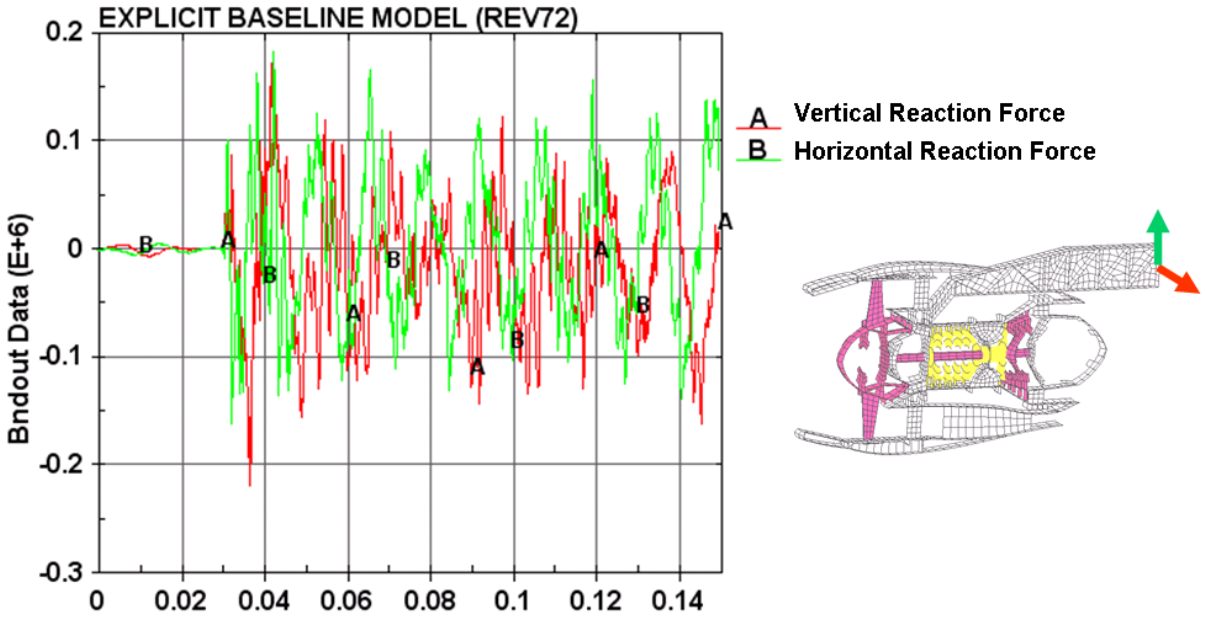

Figure 5.30 Horizontal and vertical reactions at end of fixed pylon

Knowledge of these forces would help in the design of hardware (pins, brackets, etc.) to mount the pylon to the airframe.

5.4.4 Pylon to IMC Reactions

The horizontal and vertical forces transmitted through the pylon/IMC interface are shown in Figure 5.31 below. These forces can be used to size pins, lug mounts, etcetera.

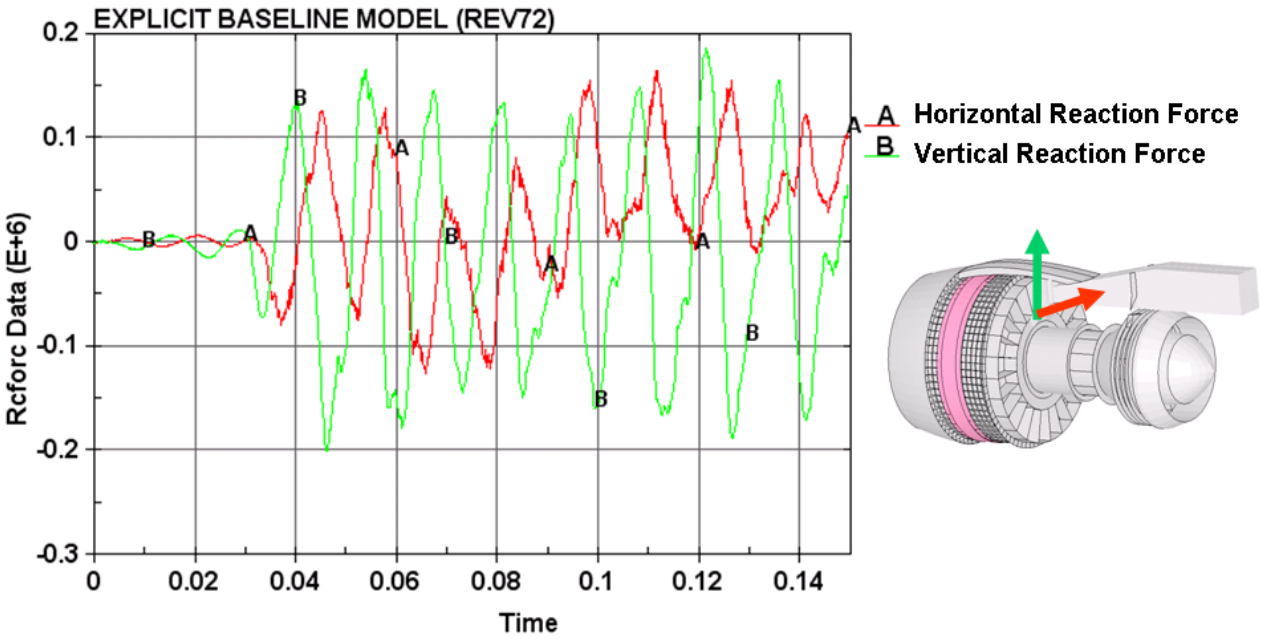

Figure 5.31 Loading transmitted through Pylon to Intermediate Case interface.

5.4.5 TEC Link axial force

The horizontal and vertical reactions of the TEC link are shown in Figure 5.32 below. These forces can be used to size pins, lug mounts, etcetera.

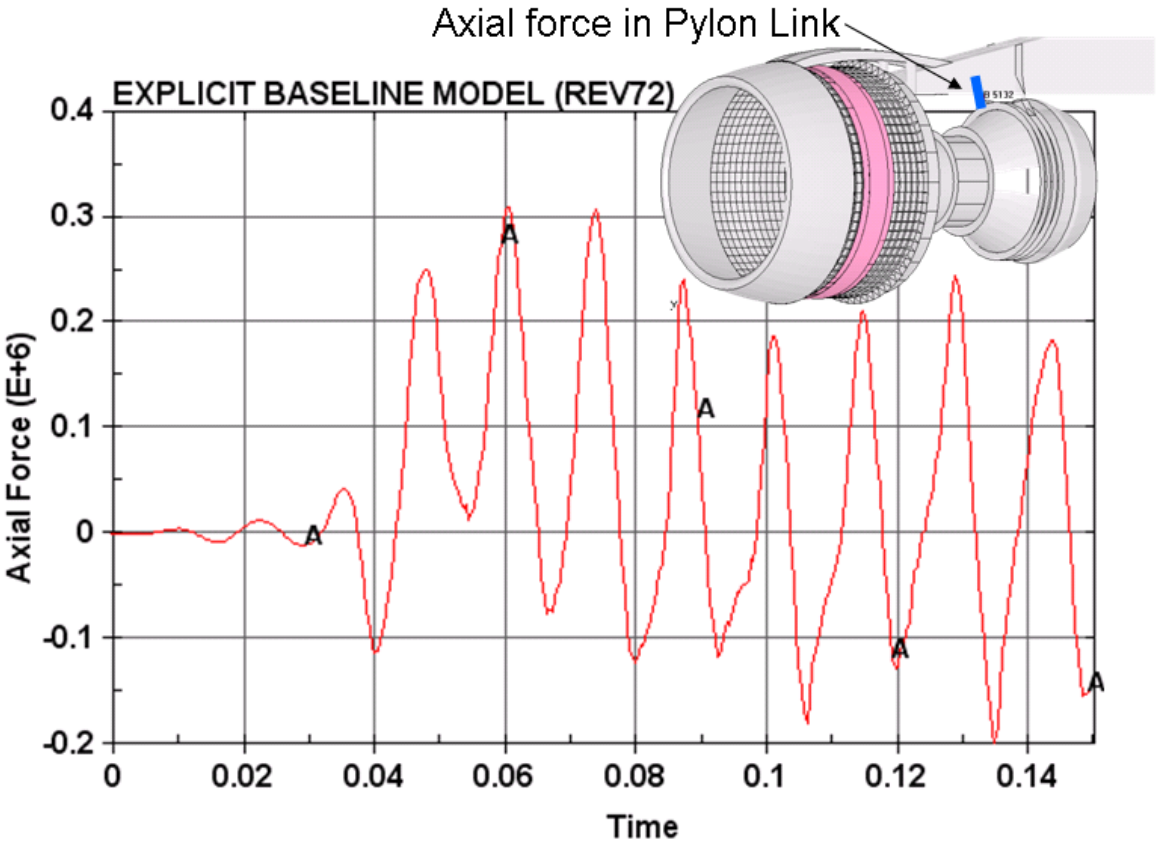

Figure 5.32 Axial Force in TEC to pylon support Link.

5.5 Additional Results

Even though the baseline model is somewhat coarse, the LS-Dyna model readily provides a host of additional information that can be used for designing components. Some examples include plastic strains, displacements due to plastic strain, stresses and nodal accelerations. Some examples are further elaborated upon in the following sections.

5.5.1 Plastic Strains

The plastic strain at a point on the isogrid is shown below. This strain history indicates that blade impact caused almost all the strain.

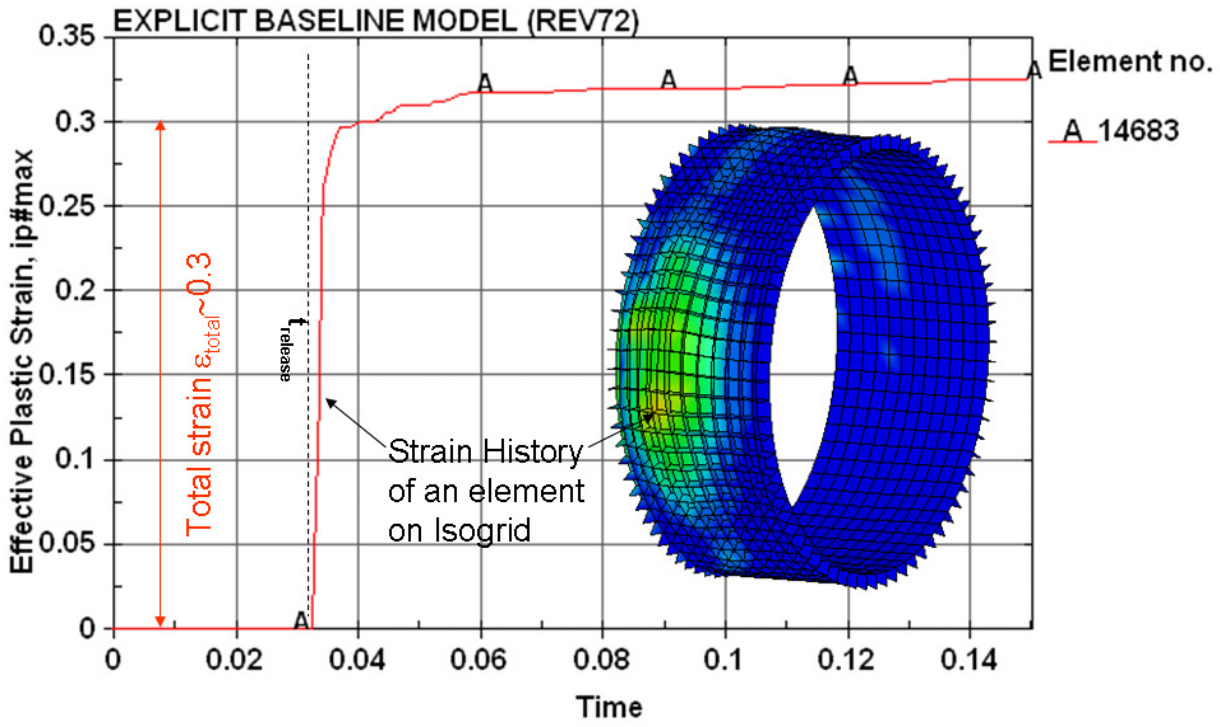

Figure 5.33 Strain (mainly inelastic) at a point in isogrid

5.5.2 Nodal Displacements

The total displacement of a node is shown in Figure 5.34. This node was on the element from Figure 5.33.

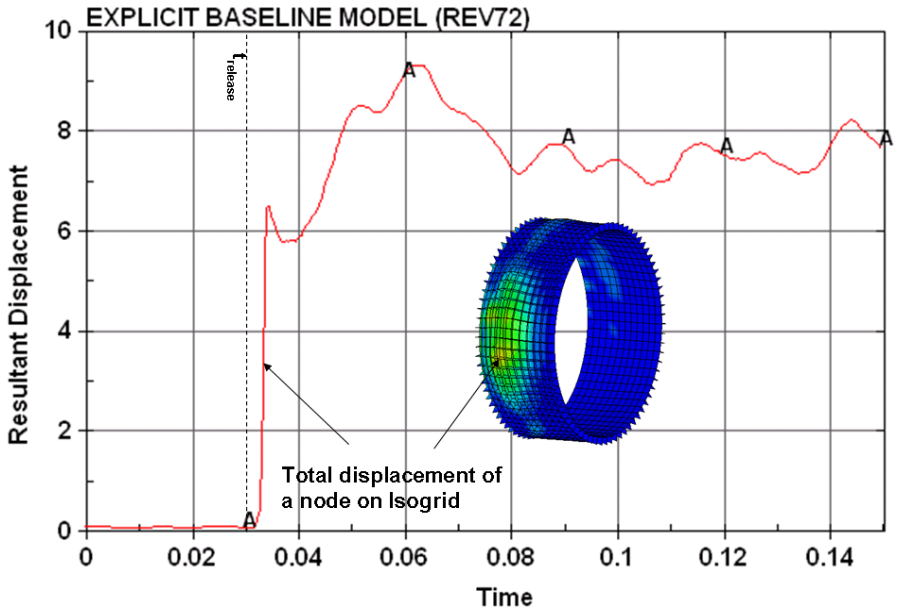

Figure 5.34 Displacement (due to large inelastic strains) at a point on isogrid

Note that the displacement is about 7" which can create secondary interference with engine external components as shown in Figure 5.35.

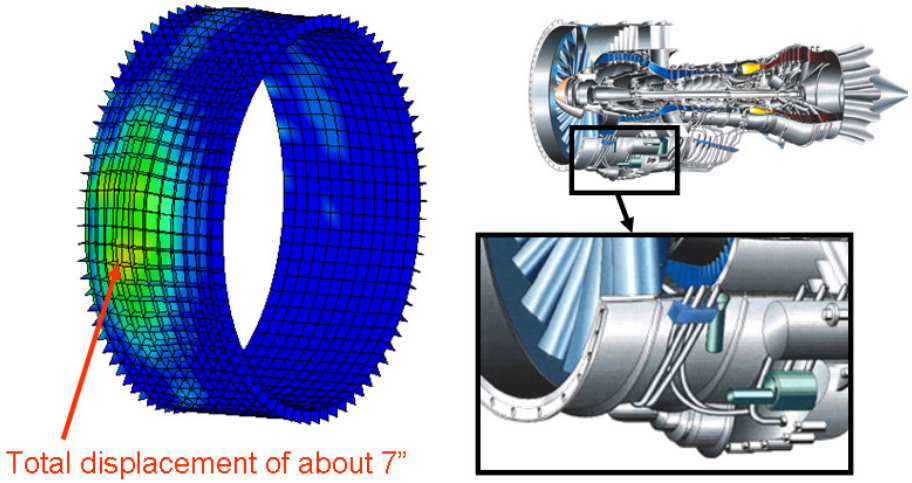

Figure 5.35 Evaluating the acceptability of displacements due to plastic strain.

These displacements can be used by engine designer to determine if the fan blade off event deformation in one part causes interference (such as breaking tubes or piping shown in Figure 5.35) with other equipment mounted on the engine.

5.5.3 Stresses

During FBO bolted large global bending moments are transmitted through the engine cases. This moment is known in the industry as backbone bending [5,6] and can cause bolted joint failure. See Figure 5.33 below. The baseline finite element mesh does not have the resolution to predict or track individual bolt strength since bonded surface to surface contact was used to join this interface.

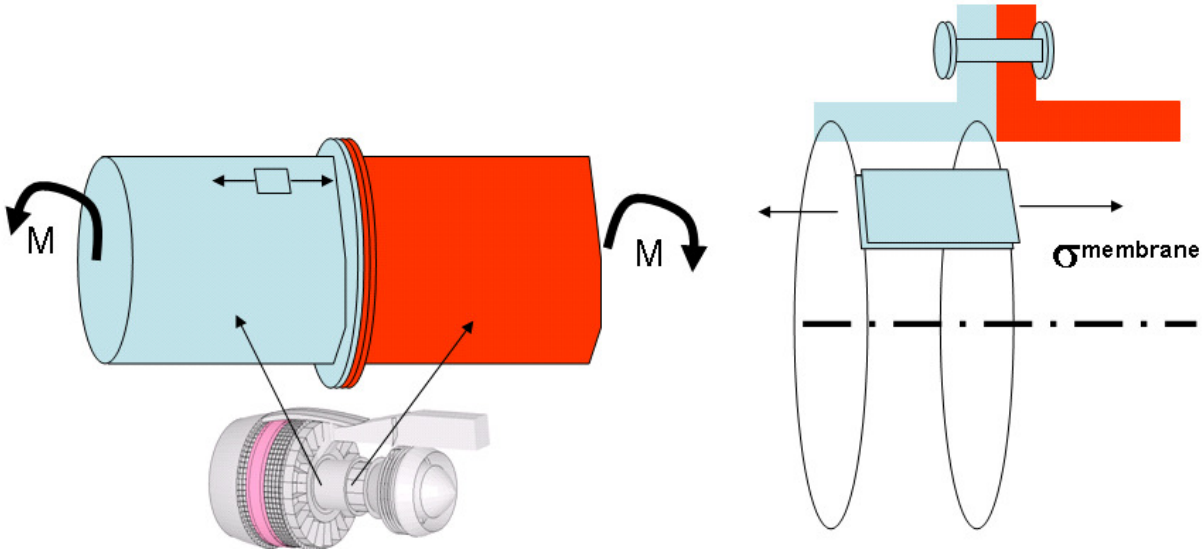

Figure 5.36 Extracting Membrane stress near flange

For design iteration purposes the membrane stress near the flange can be easily extracted and used as a relative better/worse indicator for any particular bolted joint.

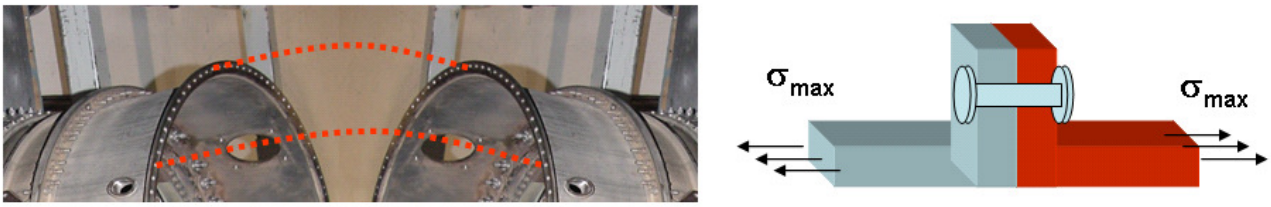

Figure 5.37 Using maximum stress from FBO to design bolted flange joint.

An example of this relative stress is shown in Figure 5.38 for the compressor-to-combustor bolted joint.

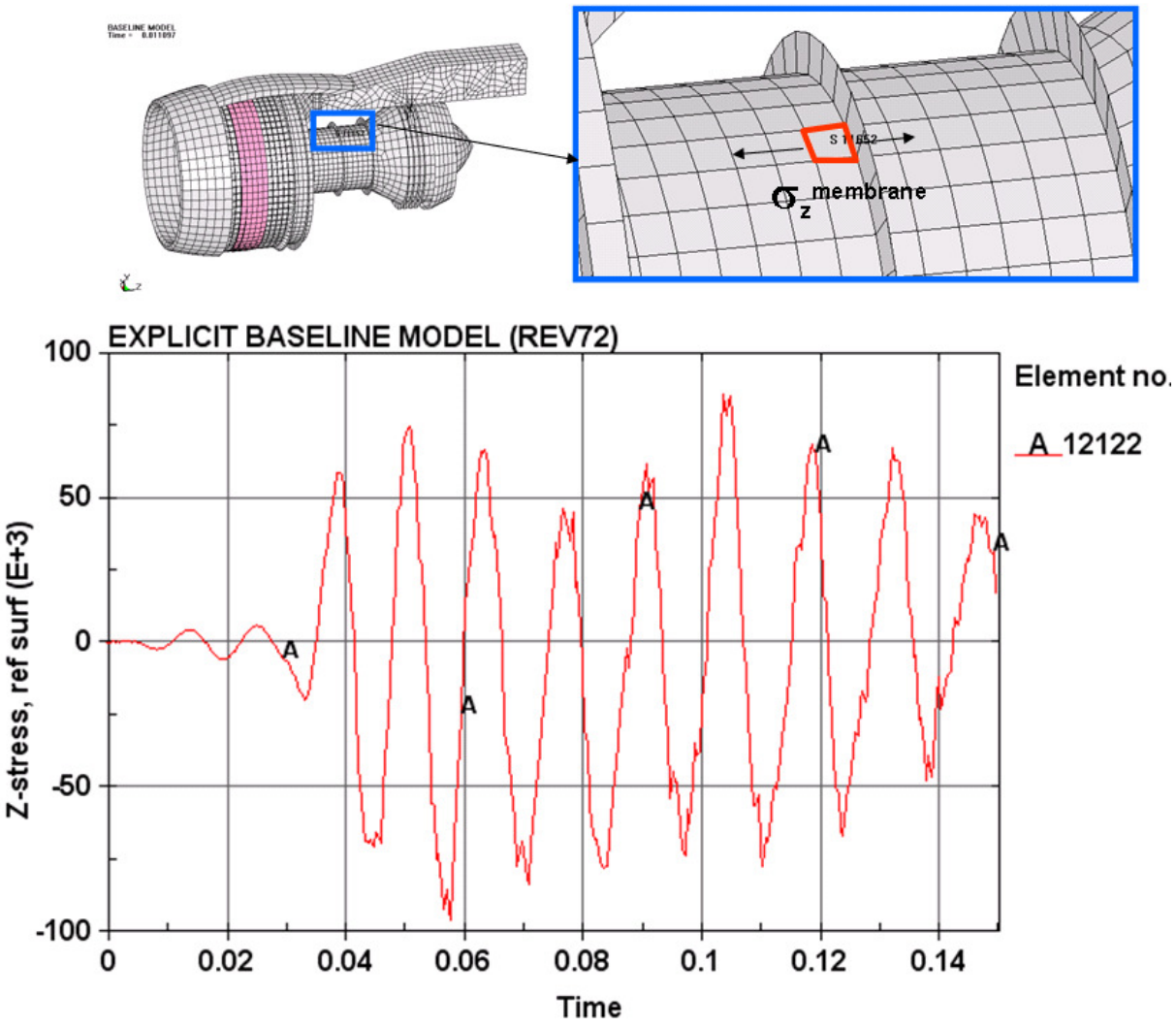

Figure 5.38 Local stresses at compressor-to-combustor joint.

5.5.4 Nodal Acceleration

Other non-engine components (fuel pumps, lubrication, cooling, electrical controls, etc.) are attached to the engine cases as shown in Figure 5.39.

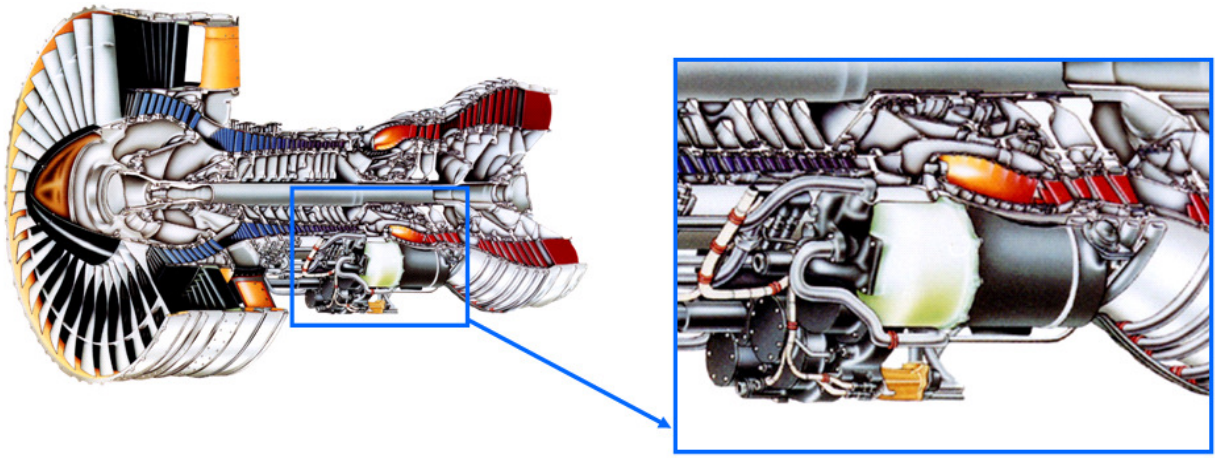

Figure 5.39 External Components attached to engine cases

These components are attached by various methods. Figure 5.40 shows a mounting bracket for a component.

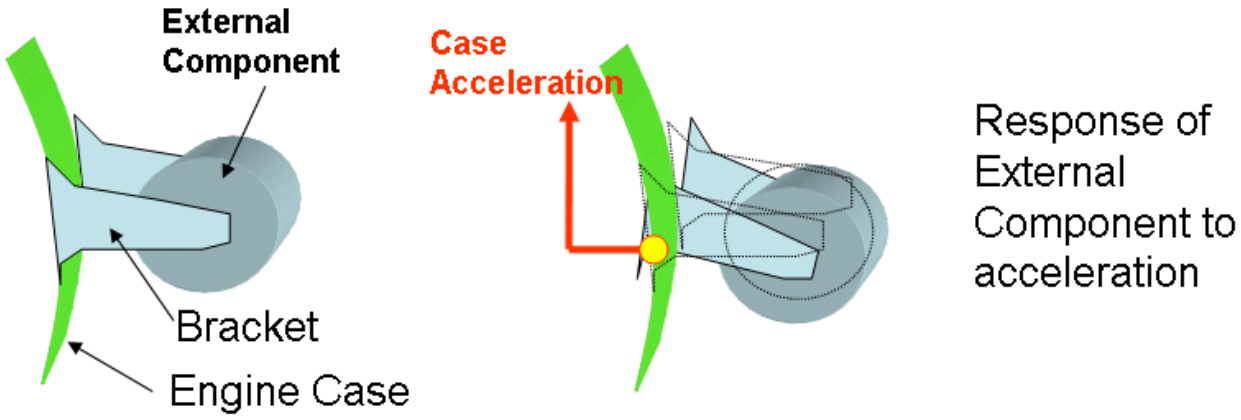

Figure 5.40 External components response to case accelerations

During FBO the mount point on the case may experience acceleration loads as shown in Figure 5.41. The peak acceleration can be used by designers to size the brackets.

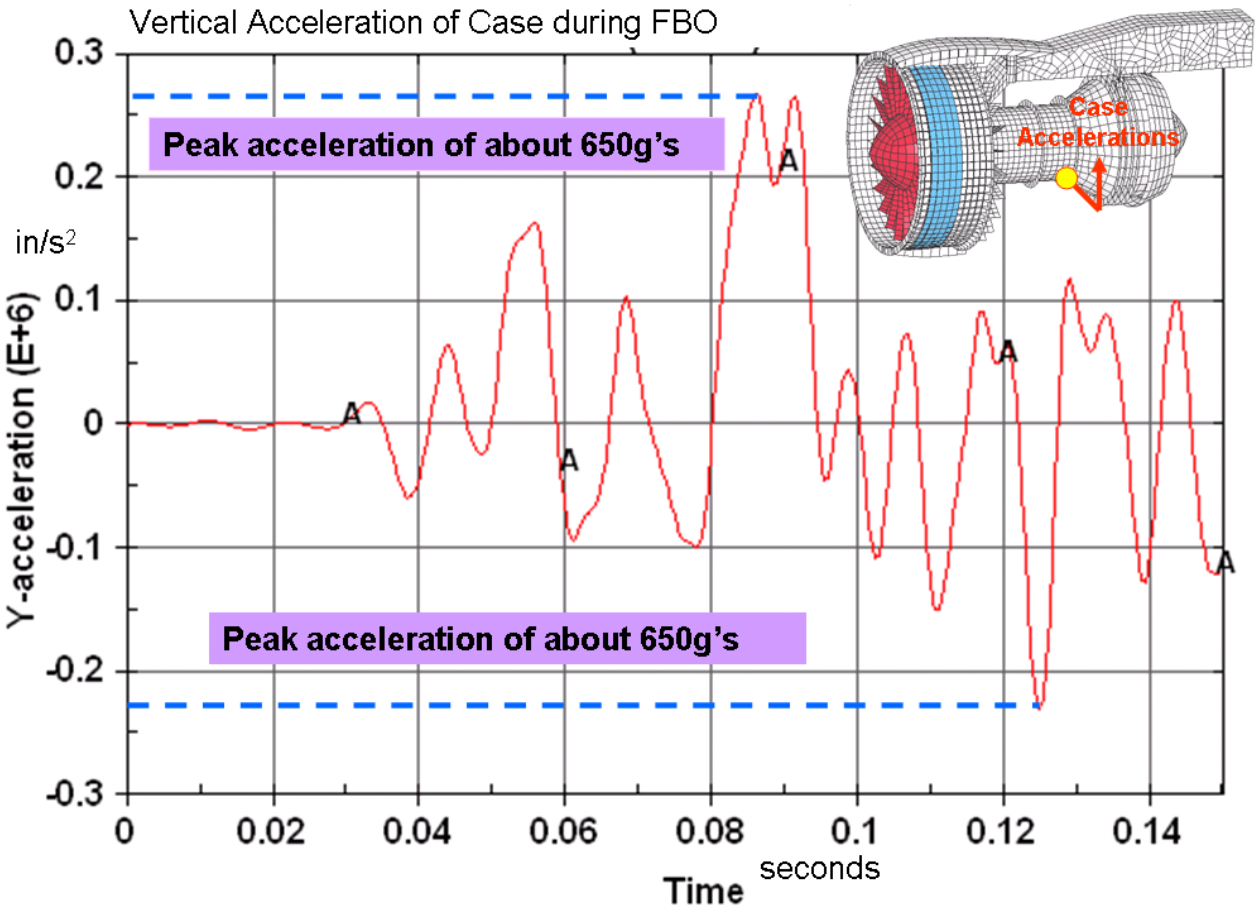

Figure 5.41 Acceleration of Engine Case at component mount location

5.6 Review of Computational Challenges for FEA Modeling

In Chapter 2 some of the computational issues were outlined. This list is repeated below.

Blade impact/energy absorption FEA modeling might consider:

1. steady state pre stresses in rotors
2. transient dynamics
3. finite rotations and translations (versus infinitesimal)
4. impact/contact of fan blades to case
5. impact/contact of fan blade to fan blade
6. elasto-plastic response of metals
7. failure criteria for metals
8. strain rate effects on yield strength for metals
9. fiber wrap/isogrid casing interaction
10. elastic/inelastic orthotropic/anisotropic material response of fabric wrap
11. contact/impact interaction of case with adjacent components
12. friction/rubbing interaction of rotor blade tips with case
13. gyroscopic effects from spinning rotors.

Rotor Imbalance FEA modeling might consider:

1. residual transient shock/vibrations from the blade impact in the fan case
2. transient dynamics of rotors with finite rotations and translations (versus infinitesimal)
3. transient dynamics in cases
4. case/rotor interactions at bearings
5. gyroscopic effects from spinning rotors attached to deformable cases
6. case/rotor interactions through friction/rubbing
7. nonlinear response of rotors/cases to large cyclic loads (buckling, elastic-plastic yielding or large deformations)
8. aerodynamic drag on rotors.

The baseline model results demonstrates that, with the exception more secondary effects such as aerodynamics, acoustics and thermodynamics, of the primary structural behaviors of FBO through the engine was able to be included into the baseline model using LS-Dyna. With some experimental test data (which is not easy to find in the public domain) some of the model variables (friction coefficient, yield strength, material failure, etc) it is expected that the baseline model could be a great predictive tool for the structural performance of the entire engine.

6 Baseline Model Sensitivity

Chapter 5 showed some of the results that could be obtained from the baseline model when all the physical and geometrical nonlinearities were included. However, the question remains whether it is really necessary to include all the material and contact interface nonlinearities? This chapter addresses that question by progressively suppressing model physics toward a more 'linear' baseline model and comparing results. Several apples-to-apples (meaning identical except as noted) variations of the baseline model were constructed and contrasted to understand how the system response changes as the physics of the problem changed.

6.1 Model Definitions for Sensitivity Study

The baseline model and LS-Dyna defaults was described in detail in Chapter 3 and Chapter 4. The results of the baseline model were presented in detail in Chapter 5. Slight variations to the baseline model input data are defined in the following section. The changes to each variant input file were explicitly defined (i.e. unless a change is spelled out the reader should not assume any change). After defining and solving these variations (described later in Chapter 6), the results will then be presented and compared to the baseline results.

The ***bold italic*** is used to emphasize and differentiate the naming of the LS-Dyna input file variations.

6.1.1 No Mass Scaling Variation

The baseline model was also solved with ***no mass scaling***. The only change to the baseline LS-Dyna input files was suppressing the mass scaling input definition.

6.1.2 Strike Position Variation

A released fan blade may strike the fan case at any arbitrary angular position. A 6:00 o'clock strike, as defined in the figure below, was chosen for the baseline model; note the deformed fan blade and the plastic strain contour in the case. Due to the unsymmetrical mounting of the engine to the pylon, the particular strike angle is expected to create an asymmetric response in the cases. By specifying a slightly different release time, $t_{release}$, a specific strike angle can be prescribed and the expected asymmetrical response verified.

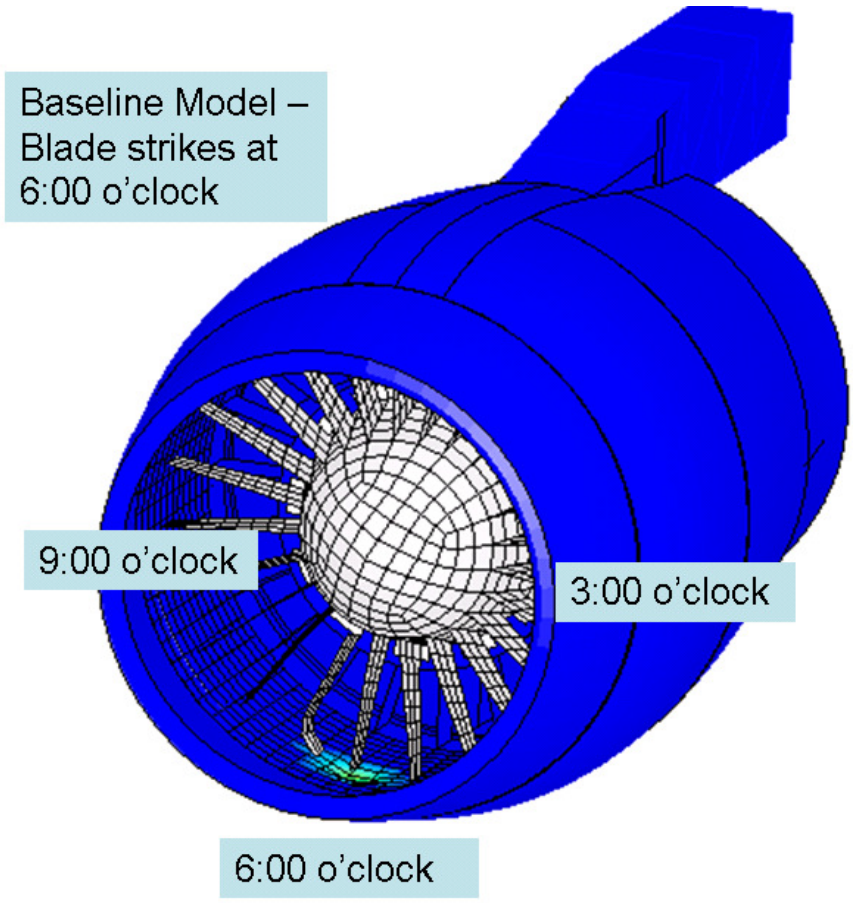

Figure 6.1 A released blade may strike any circumferential position.

Two variations of the baseline model were modified and solved to obtain ***3 o'clock strike*** and ***9 o'clock strike*** positions. The only change to the input files was the blade release time (or the death time of the contact definition holding down the blade).

6.1.3 Contact Sensitivity

The baseline model included the fan/isogrid/fabric sliding contact interface; the baseline results showed this interface to be a primary driver for dissipating kinetic energy. The baseline model also included extensive secondary sliding contact interfaces (blades and nacelle seals) as shown in Figure 6.2.

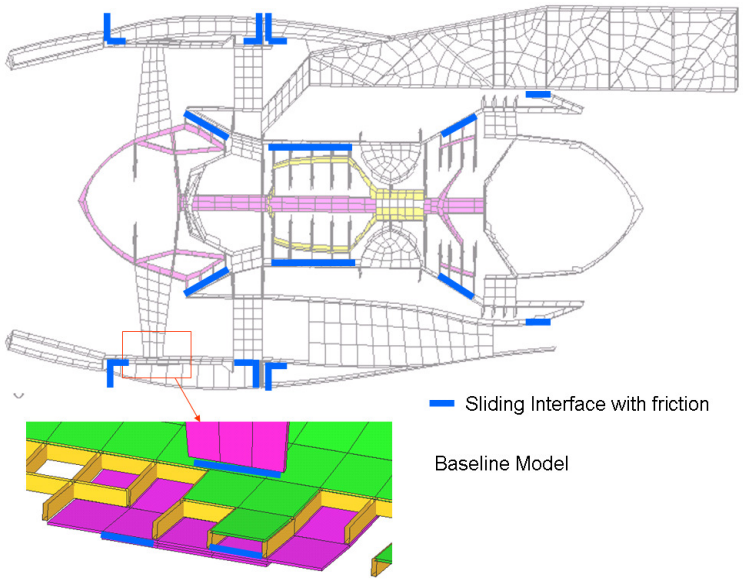

Figure 6.2 Primary (fan blade/isogrid) and secondary contact

A model was solved with the secondary contact definitions suppressed. This model was called the ***single contact*** model and is shown in **Figure 6.3**.

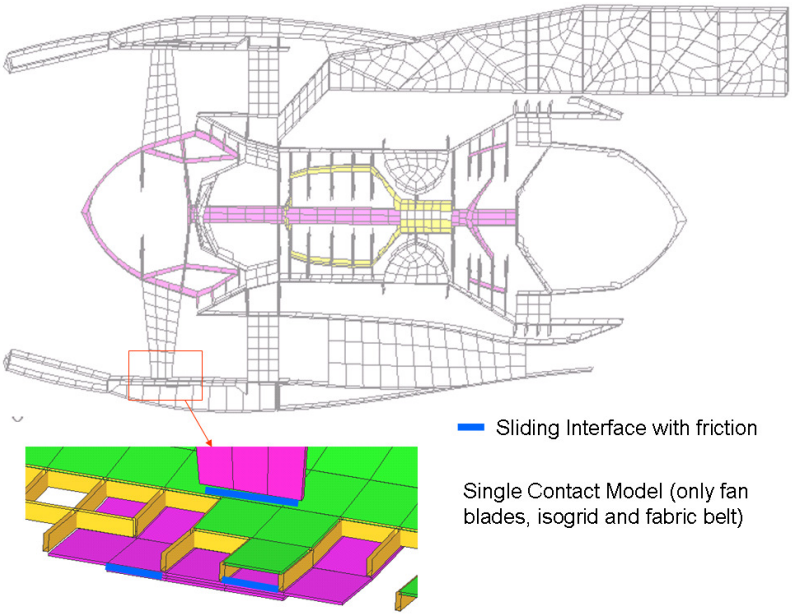

Figure 6.3 Single Contact model has only fan/isogrid/fabric contact.

6.1.4 Sensitivity to Elastic Behavior

Recall that the baseline model was composed of various elastic and elastic plastic material models as shown in Figure 6.4.

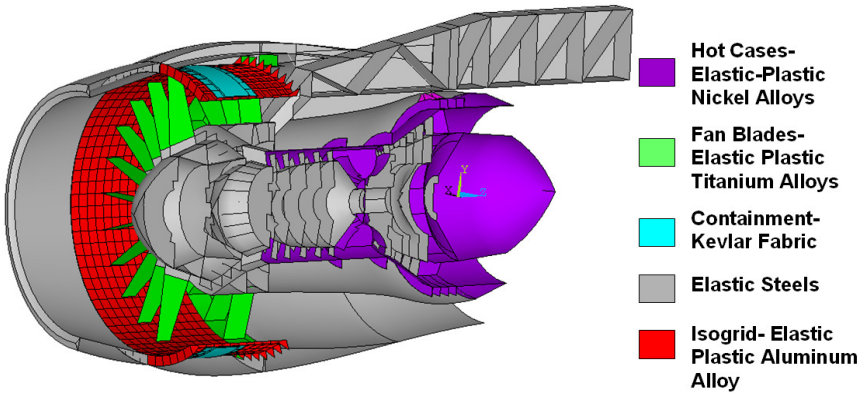

Figure 6.4 Recap of Materials in Baseline Model

To gain an understanding of how inelastic materials might effect baseline model results two derivative input files (no other input was changed) were created with:

- all materials in model were changed to elastic definitions i.e. the elastic-plastic constitutive definitions were deactivated. A consistent Young's moduli, density and Poisson's ratio for each material group was retained i.e. the entire model was not set to a single uniform elastic property. This variation was defined as the ***Elastic Model***.
- The hot cases (nickel alloys) (purple) were made elastic (with consistent elastic properties for a hot nickel alloy). All other materials retained the baseline model properties (including existing inelastic constitutive definitions). This variation was defined as the ***Hot Case Elastic model***.

The hot nickel exhaust cases (purple in Figure 6.4 above) are shown in more detail in Figure 6.5. These cases react out significant but secondary loads during FBO event.

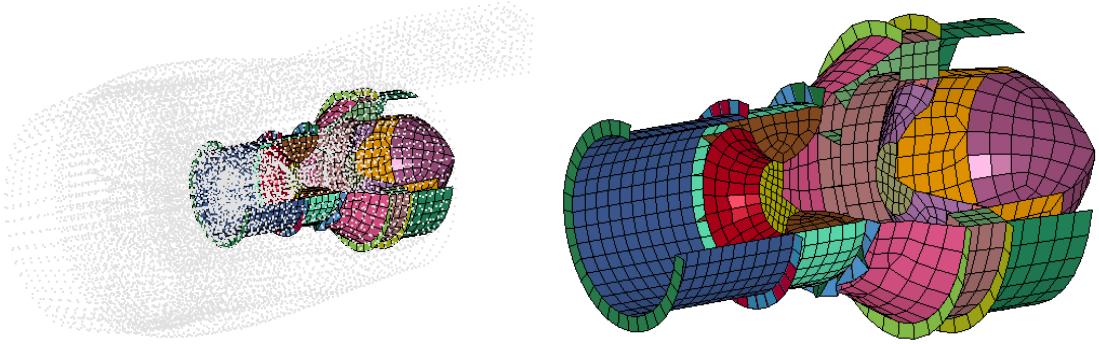

Figure 6.5 Shell Elements in Hot Case

6.1.5 Sensitivity to Both Contact and Elastic Material

To gain an understanding of how both inelastic materials and contact together might effect baseline model results two derivative input files (no other input was changed) were created by combining the effects of:

- Single Contact combined with the Hot Case Elastic model (both previously defined). Specifically, this involves only fan blade/isogrid/fabric contact where the hot nickel exhaust case has been assigned elastic properties; the rest of the material definitions as per the baseline model. This run was entitled ***Hot Case with Single Contact***.
- Single Contact combined with the Elastic Model. Fan blade/isogrid/fabric contact only with all elastic materials. This run was entitled ***Elastic with Single Contact***.

6.2 CPU Execution Times

The sensitivity runs were all performed on a 2.4 GHz Dell 380 Desktop computer; execution times were measured as shown in Table 6.1.

Table 6.1 Execution time of sensitivity studies.

LS-Dyna Input File Variation	CPU Time (seconds)
Baseline	8494
No Mass Scaling	17406
Three o'clock strike	6796
Nine o'clock strike	6485
Single Contact	6488
Hot Case Elastic	7646
Elastic	5744
Hot Case with Single Contact	6567
Elastic with Single Contact	5140

In contrast to implicit methods, the explicit solution has very low RAM requirements. The baseline model required only 4Mb of RAM to solve. Implicit models with contact and friction have huge memory requirements to handle the unsymmetrical sparse matrices that must be formulated each time step.

The ***d3hsp*** output file provide by LS-Dyna also includes a breakdown of the solution processing requirements. A portion of this d3hsp output is shown below.

```
Memory required for explicit solution :     3979990
Additional dynamically allocated memory:       41087
                          Total:     4021077
T i m i n g   i n f o r m a t i o n
                  CPU(seconds)   %CPU  Clock(seconds) %Clock
 ---------------------------------------------------------------------
 Initialization .....  9.0000E+00   0.11    8.6560E+00   0.10
 Element processing ...        3.0020E+03  35.34    2.9650E+03  34.91
 Binary databases .....        1.0000E+02   1.18    1.1050E+02   1.30
 ASCII database .......        1.7000E+01   0.20    1.5808E+01   0.19
 Contact algorithm ....        5.3640E+03  63.15    5.3927E+03  63.49
   Interface ID     1          2.0000E+00   0.02    9.3300E-01   0.01
   Interface ID     2          1.1000E+01   0.13    1.0835E+01   0.13
   Interface ID     3          1.2000E+01   0.14    1.4636E+01   0.17
   Interface ID     4          1.2000E+01   0.14    1.2891E+01   0.15
   Interface ID     5          4.0000E+00   0.05    2.4120E+00   0.03
   Interface ID     6          1.0000E+00   0.01    1.2220E+00   0.01
   Interface ID     7          0.0000E+00   0.00    1.5240E+00   0.02
   Interface ID     8          1.0000E+00   0.01    1.2250E+00   0.01
   Interface ID     9          1.0000E+00   0.01    6.6700E-01   0.01
   Interface ID    10          4.0000E+00   0.05    2.0890E+00   0.02
   Interface ID    11          0.0000E+00   0.00    1.3610E+00   0.02
   Interface ID    12          1.0000E+00   0.01    1.2620E+00   0.01
   Interface ID    13          2.0000E+00   0.02    5.1600E-01   0.01
   Interface ID    14          4.0000E+00   0.05    1.4650E+00   0.02
   Interface ID    15          3.0000E+00   0.04    4.7460E+00   0.06
   Interface ID    16          5.0000E+00   0.06    8.9240E+00   0.11
   Interface ID    17          7.0000E+00   0.08    1.2270E+01   0.14
   Interface ID    18          1.7000E+01   0.20    1.8177E+01   0.21
   Interface ID    19          5.1500E+02   6.06    5.4052E+02   6.36
   Interface ID    20          4.7620E+03  56.06    4.7534E+03  55.96
 Contact entities .....        0.0000E+00   0.00    0.0000E+00   0.00
 Rigid bodies .........        2.0000E+00   0.02    1.3890E+00   0.02
 Implicit Nonlinear ...        0.0000E+00   0.00    0.0000E+00   0.00
 Implicit Lin. Alg. ...        0.0000E+00   0.00    0.0000E+00   0.00
 ---------------------------------------------------------------------
 T o t a l s        8.4940E+03  100.00    8.4940E+03  100.00
Problem time     =    1.5000E-01
Problem cycle    =    30304
Total CPU time   =    8494 seconds (   2 hours 21 minutes 34 seconds)
```

Note how there were two computationally expensive operations (highlighted in red). About 35% percent of the time was spent computing element stresses; the *contact_automatic_general_interior definition took about 56% of the CPU time. This may seem expensive but it is actually remarkably inexpensive if when one considers the combinatorial gamut of contact possibilities computed by this comprehensive contact definition. Based on the author's experience, such a sophisticated definition would not be possible on anything other than an 'academic' model (meaning a large, multi-component mesh) if solved by implicit codes.

6.3 Results Comparison: Global Energy Balance

Baseline, elastic and single contact are compared in Figure 6.6. Note how the energy absorption mechanisms differ. For each variation, note how the kinetic energy lost is approximately equal to the internal and sliding energy gained i.e. conservation of energy is enforced. The differences between these absorption mechanisms create differences in load paths through components during the FBO.

Table 6.2 summarizes the energy balance due to baseline input variations; underlined entities are extracted from Figure 6.6; the remainders are from Appendix A.

Table 6.2 Global Energy Balance ($\cdot 10^9$ in·lbs)

	Final Kinetic Energy	Final Sliding Energy	Final Internal Energy
Baseline	0.72	0.11	0.05
No Mass Scaling	0.72	0.12	0.05
Three o'clock strike	0.76	0.11	0.04
Nine o'clock strike	0.75	0.11	0.04
Single Contact	0.79	0.07	0.04
Hot Case Elastic	0.73	0.12	0.05
Elastic	0.73	0.15	Minimal[14]
Hot Case with Single Contact	0.78	0.07	0.05
Elastic with Single Contact	0.78	0.10	Minimal[1]

[14] Strain energy is minimal because elastic strains are orders of magnitude smaller than plastic strains.

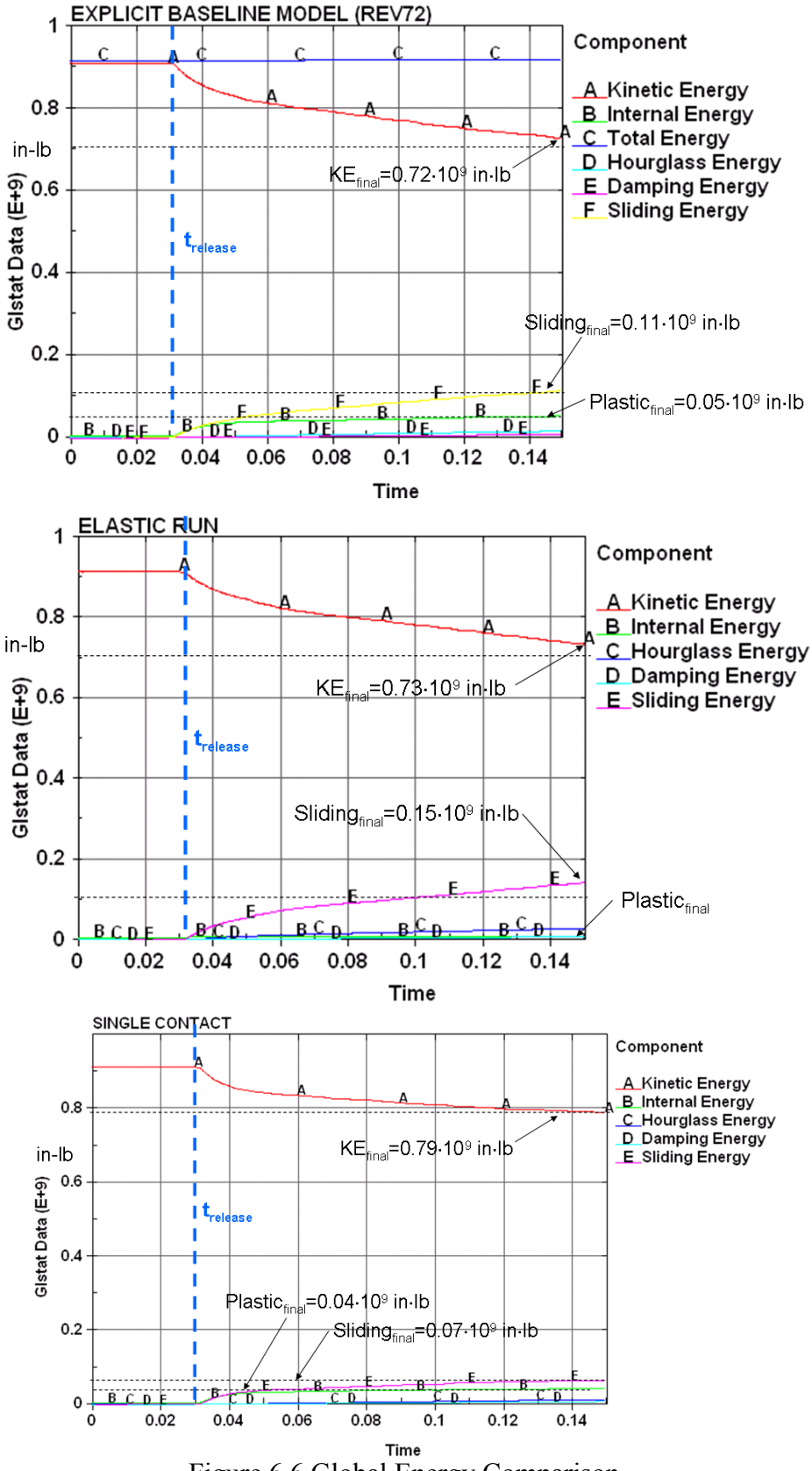

Figure 6.6 Global Energy Comparison

6.4 Results Comparison: Bearing Force Amplitudes

For the readers convenience, the four primary rotor bearings are repeated in Figure 6.7. The peak loading magnitude transmitted through the bearings during FBO is very important for the design of the engine. The reactions vary as the physics of the model (variations to baseline) is changed.

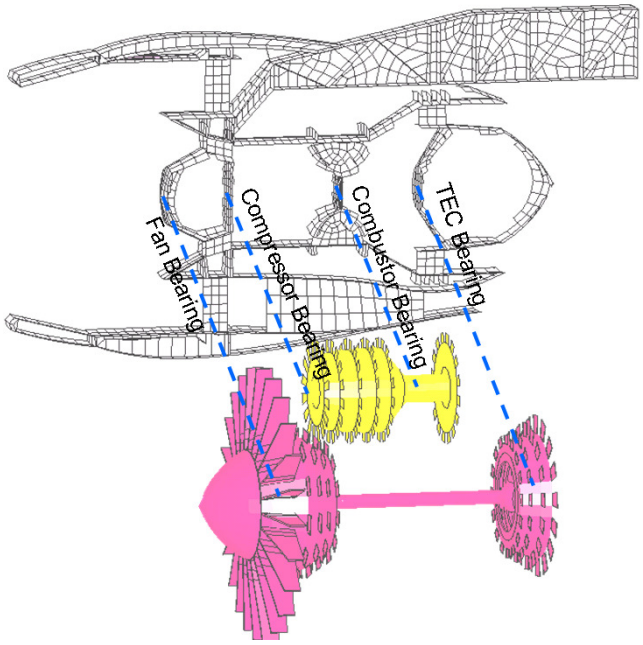

Figure 6.7 Definition of Rotor Bearings Locations

For brevity, three of the four rotor bearing reactions were measured. These were the:

- Fan Bearing
- TEC (Turbine Exhaust Case) Bearing
- Combustor Bearing

6.4.1 Fan Bearing Reaction

The fan bearing reactions are shown in Figure 6.8 and Appendix B. The peak loadings from these are summarized in Table 6.3.

Table 6.3 Fan Bearing Force Amplitudes ($\cdot 10^3$ lbs)

LS-Dyna Input File Variation	Peak + X	Peak - X	Peak + Y	Peak - Y
Baseline	550	-750	700	-625
No Mass Scaling	500	-650	675	-575
Three o'clock strike	650	-850	875	-650
Nine o'clock strike	750	-650	600	-750
Single Contact	750	-750	800	-750
Hot Case Elastic	575	-750	725	-650
Elastic	650	-725	775	-700
Hot Case with Single Contact	875	-1000	1000	-750
Elastic with Single Contact	1250	-1400	1250	-1050

6.4.2 TEC Bearing Reaction

The TEC (turbine exhaust case) bearing reactions are shown in Figure 6.9 and Appendix C. The peak loadings from these are summarized in Table 6.4.

Table 6.4 TEC Bearing Force Amplitudes ($\cdot 10^3$ lbs)

LS-Dyna Input File Variation	Peak + Y	Peak - Y
Baseline	105	-110
No Mass Scaling	102	-100
Three o'clock strike	105	-90
Nine o'clock strike	105	-100
Single Contact	75	-100
Hot Case Elastic	120	-120
Elastic	100	-100
Hot Case with Single Contact	75	-120
Elastic with Single Contact	65	-95

6.4.3 Combustor Bearing Reaction

The combustor bearing reactions are shown in Figure 6.10 and Appendix D. The peak loadings from these are summarized in Table 6.5.

Table 6.5 Combustor Bearing Force Amplitudes ($\cdot 10^3$ lbs)

LS-Dyna Input File Variation	Peak +	Peak -
Baseline	175	-175
No Mass Scaling	140	-160
Three o'clock strike	160	-150
Nine o'clock strike	150	-170
Single Contact	190	-200
Hot Case Elastic	175	-180
Elastic	150	-200
Hot Case with Single Contact	190	-250
Elastic with Single Contact	210	-240

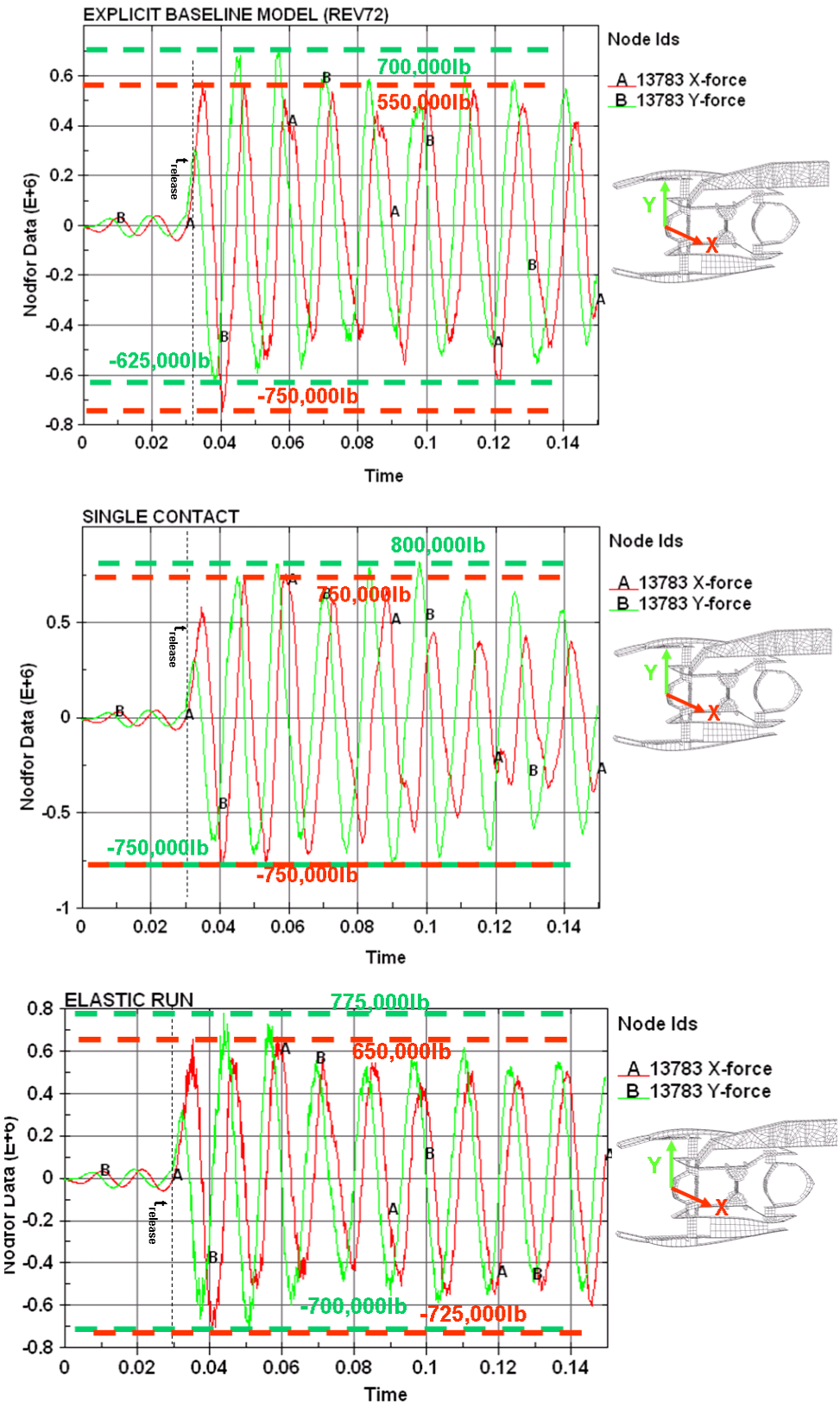

Figure 6.8 Fan Bearing Reactions

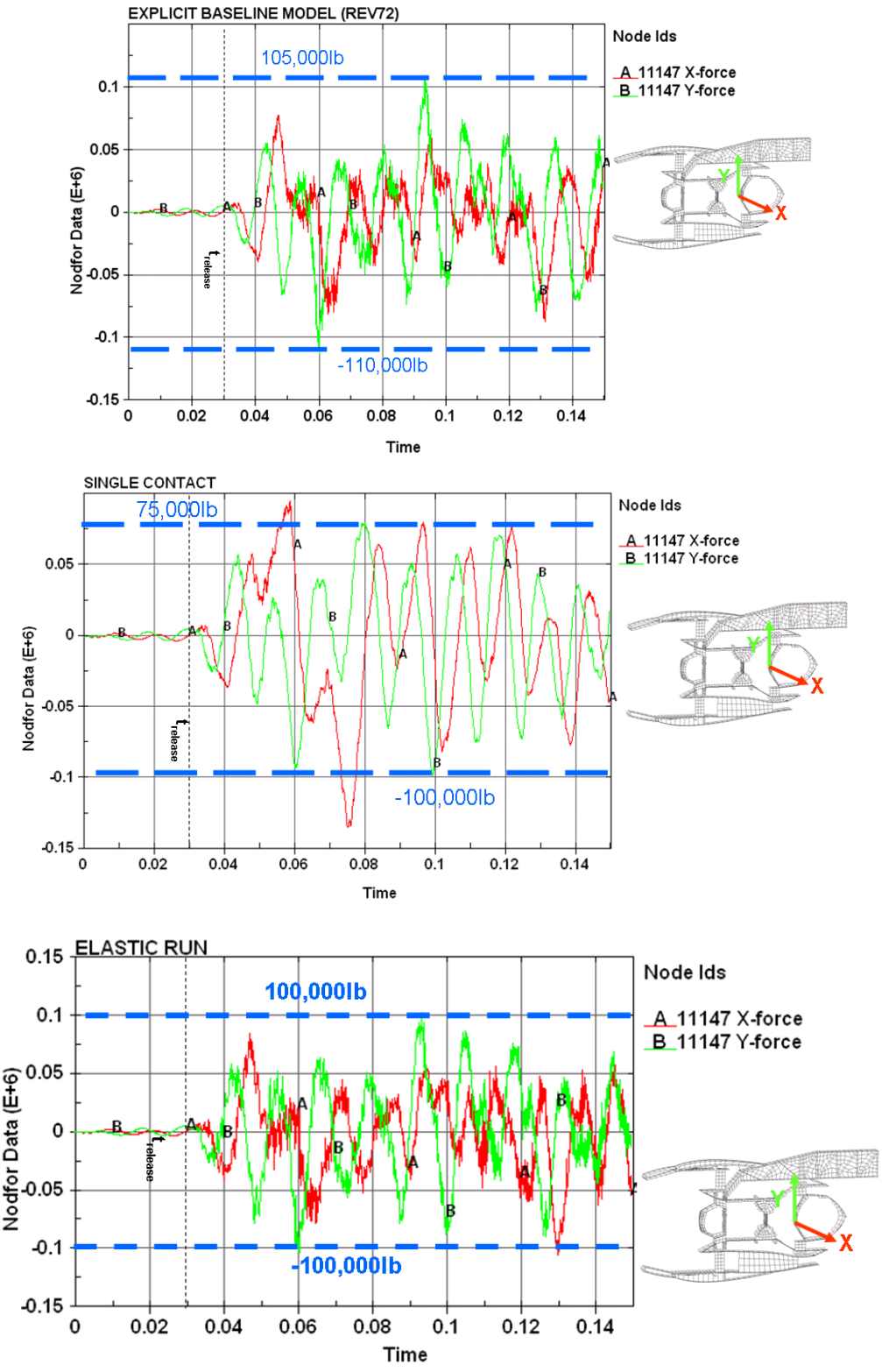

Figure 6.9 TEC Bearing Reaction

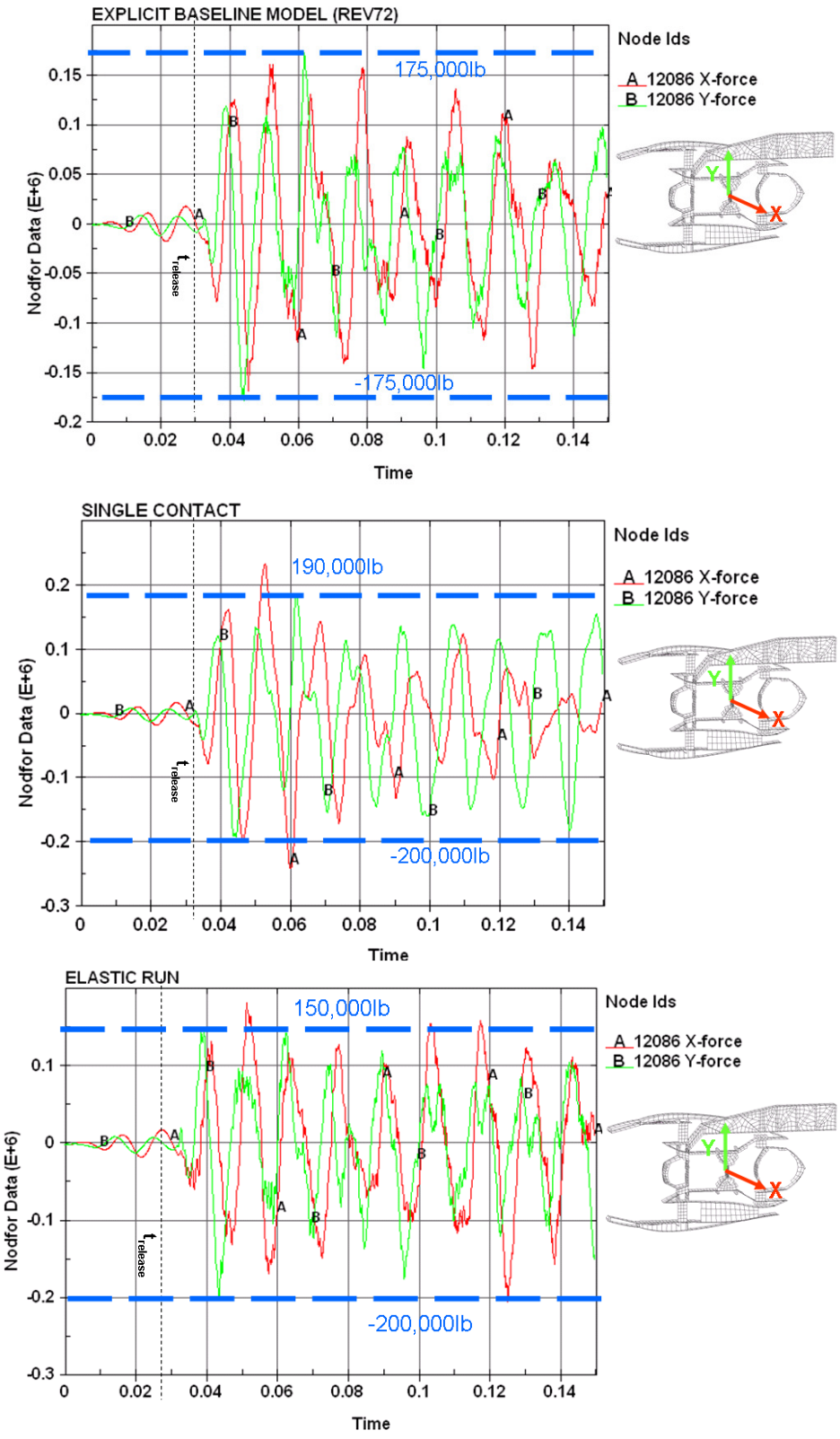

Figure 6.10 Combustor Bearing Reaction

6.5 Results Comparison: Engine Mounting Loads

For convenience, the two primary engine-to-pylon mounting points are repeated in Figure 6.11. The magnitude of the transient reaction during FBO is very important for the design of the engine. The reactions vary as the physics of the model is changed.

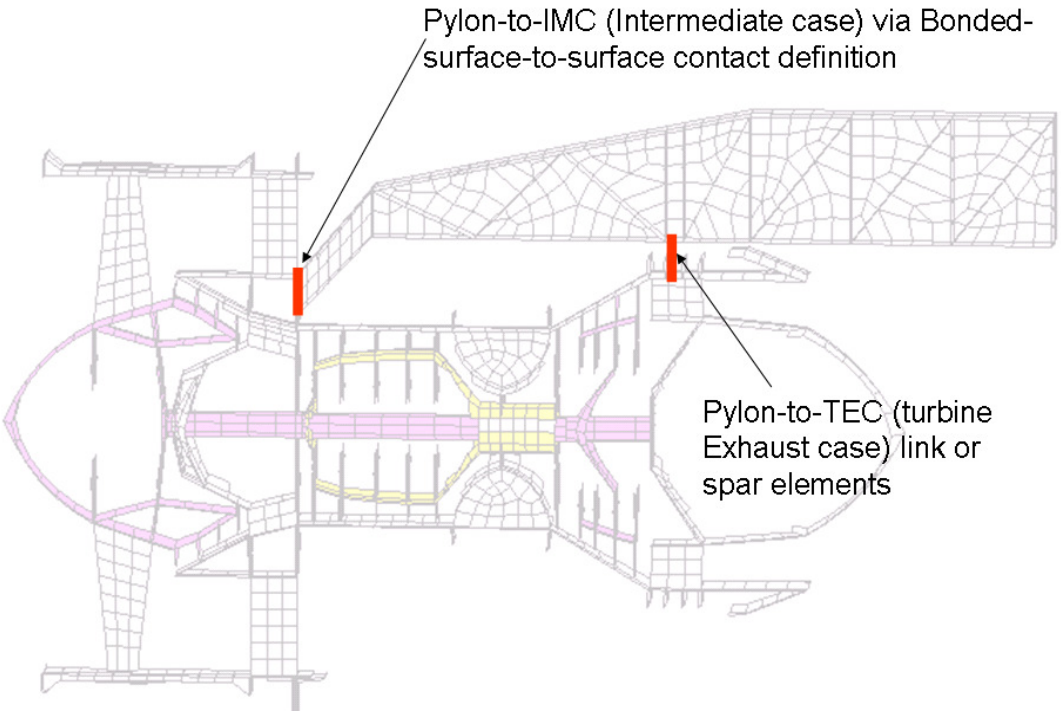

Figure 6.11 Location of primary engine mounts

The loads transmitted by FBO were measured through:

- Pylon-to-IMC bonded contact interface
- Pylon-t-TEC axial link force

6.5.1 Pylon-to-IMC Loads

The IMC-to-Pylon transmitted forces are shown in Figure 6.12 and Appendix F. The peak loadings from these are summarized in Table 6.6.

Table 6.6 Pylon-to-IMC Force Amplitudes ($\cdot 10^3$ lbs)

LS-Dyna Input File Variation	Peak +Vertical	Peak Vertical (-)
Baseline	185	-200
No Mass Scaling	190	-190
Three o'clock strike	240	-210
Nine o'clock strike	225	-210
Single Contact	265	-225
Hot Case Elastic	225	-210
Elastic	215	-225
Hot Case with Single Contact	275	-225
Elastic with Single Contact	275	-200

6.5.2 TEC-to-Pylon Link Reaction

The TEC-to-Pylon link force is shown in Figure 6.13 and Appendix G. The peak loadings from these are summarized in Table 6.7.

Table 6.7 Tec-to-Pylon Link Force Amplitudes ($\cdot 10^3$ lbs)

LS-Dyna Input File	Peak +Axial	Peak - Axial
Baseline	300	-200
No Mass Scaling	310	-160
Three o'clock strike	325	-175
Nine o'clock strike	350	-200
Single Contact	340	-100
Hot Case Elastic	360	-190
Elastic	375	-150
Hot Case with Single Contact	400	-150
Elastic with Single Contact	420	-175

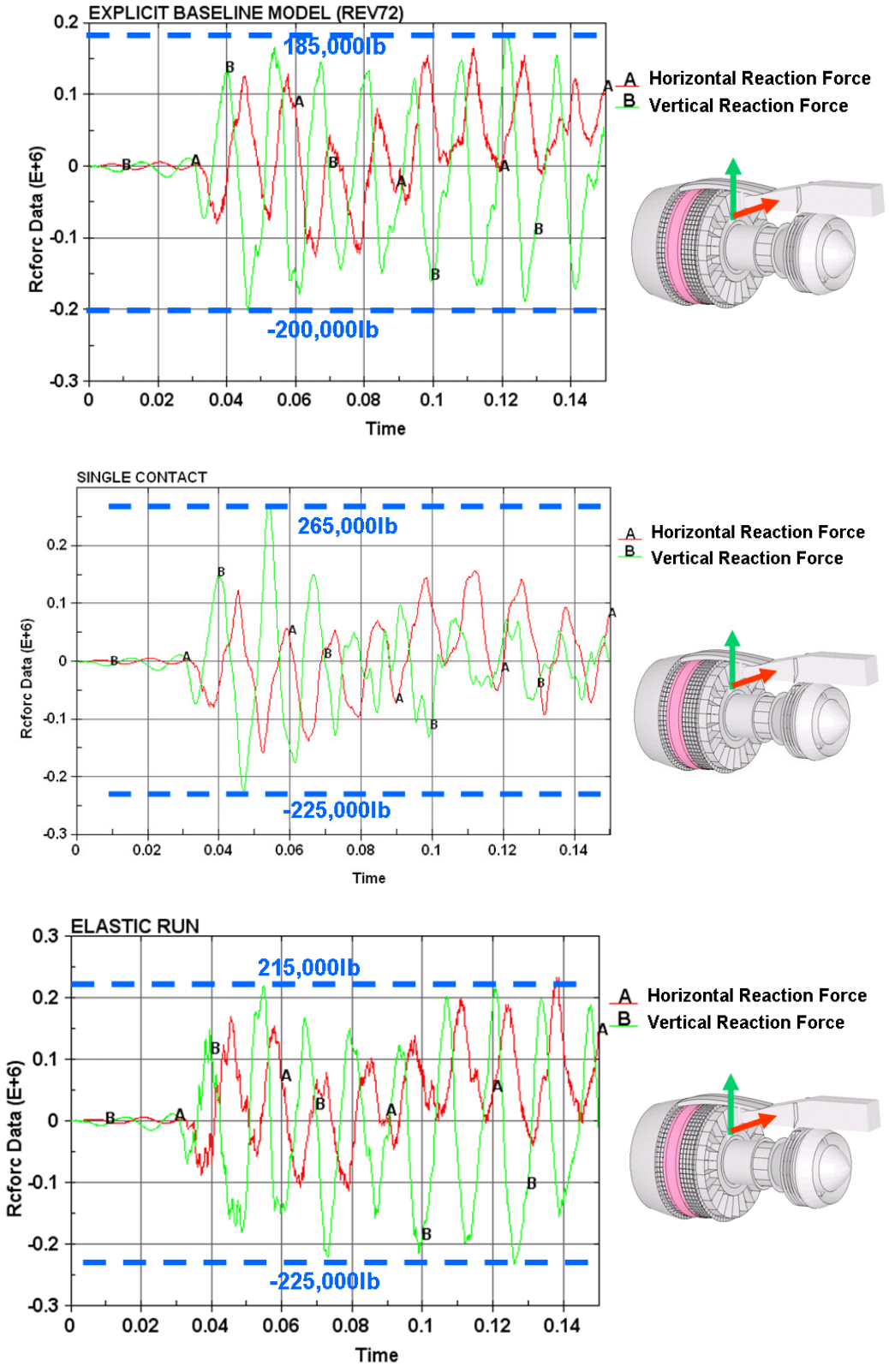

Figure 6.12 IMC-to-Pylon Force

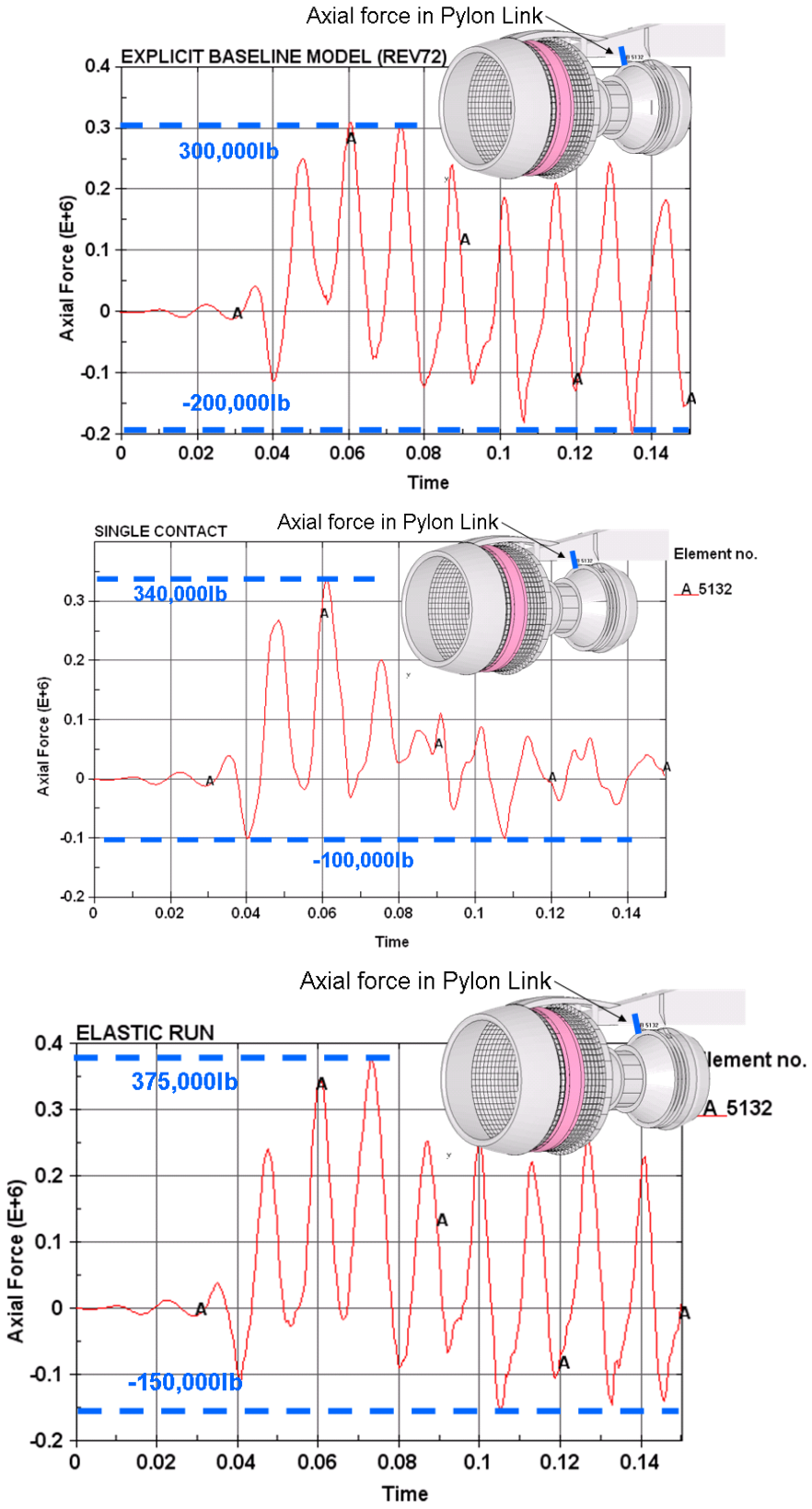

Figure 6.13 TEC-to-Pylon Link Force

6.6 Results Comparison: Blade Tip Rubbing Force

A schematic of the LPT (low pressure turbine) blade tip rubbing is repeated in Figure 6.14. The blade tip force is the total force exerted by all blades on the surface of the case.

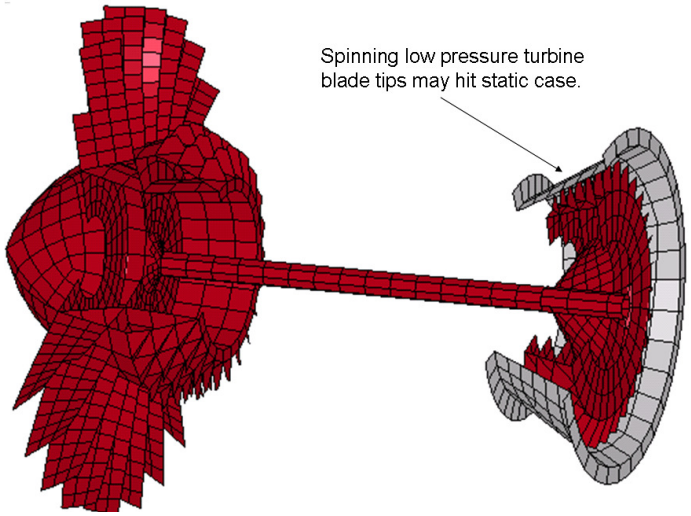

Figure 6.14 Low pressure turbine blade tip rubbing

6.6.1 LPT Blade tip Forces

The LPT (low pressure turbine) blade tip rubbing force is shown in Figure 6.15 and Appendix E. The peak loadings from these are summarized in Table 6.8.

Table 6.8 LPT Blade Tip Force (absolute value) ($\cdot 10^3$ lbs)

LS-Dyna Input File	|Peak|
Baseline	350
No Mass Scaling	375
Three o'clock strike	325
Nine o'clock strike	390
Single Contact	0 [15]
Hot Case Elastic	450
Elastic	475
Hot Case with Single Contact	0
Elastic with Single Contact	0

[15] The LPT contact definition was suppressed for the Single Contact load case.

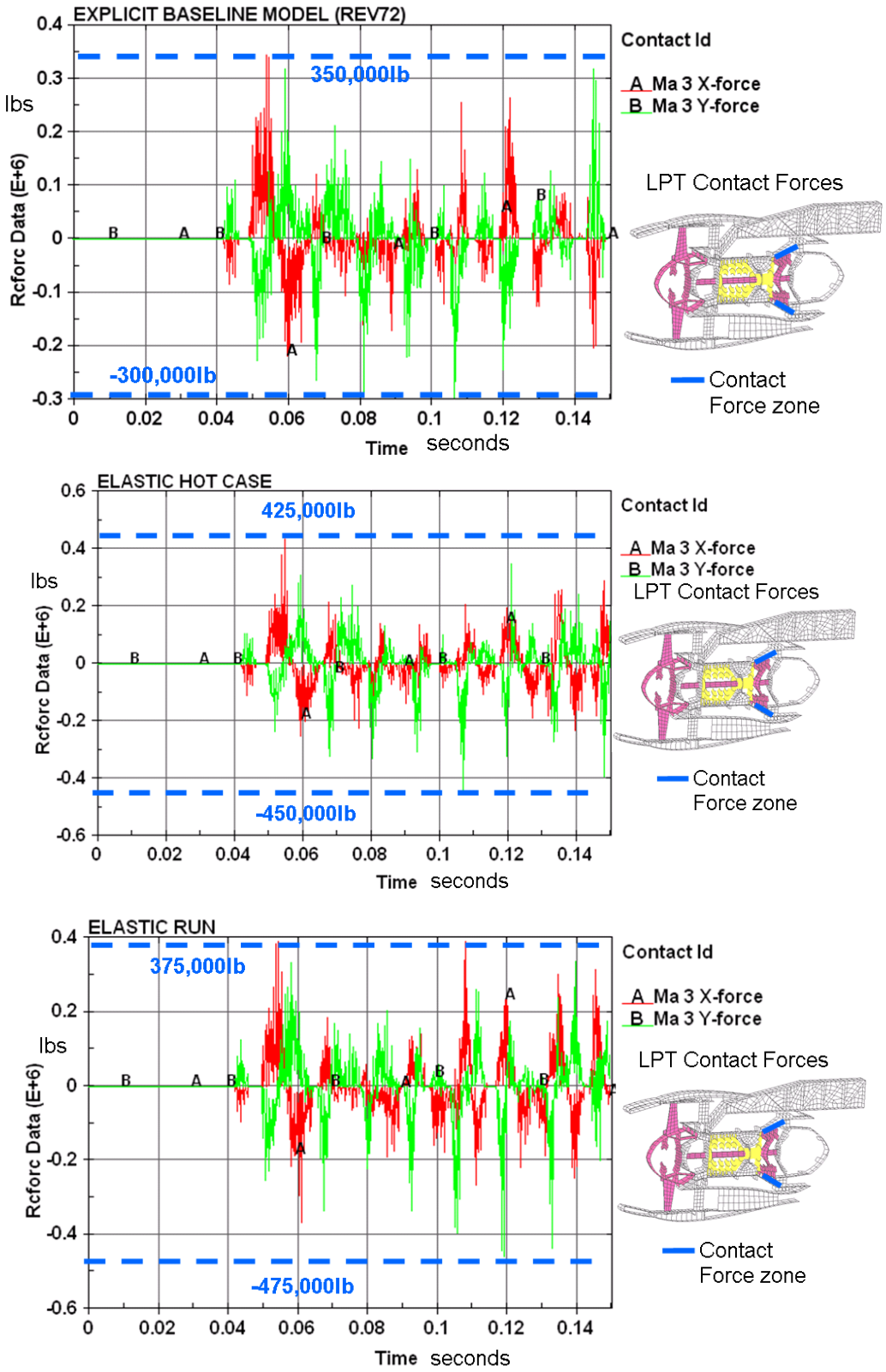

Figure 6.15 LPT Blade Tip Rubbing Forces

6.7 Results Discussion

6.7.1 Results Discussion: Mass Scaling

Comparing ***Baseline*** to ***No Mass Scaling*** results in Table 6.2 through Table 6.8 shows about 10% error in the model. This error can be further improved by decreasing the amount of mass scaling; however, Table 6.1 shows that the Baseline model runs twice as fast. This trade-off between speed and accuracy requires engineering judgment- to the author a 2x speed increase with a 10% accuracy decrease was a fair balance.

6.7.2 Results Discussion: Blade Strike Position

Comparing the peaks results in Table 6.2 through Table 6.8 for ***Baseline*** (a six o'clock strike) to ***Three O'Clock Strike*** and ***Nine O'Clock Strike*** shows about a 5-20% variation in model results. The only difference between the three runs is blade strike position. Observing the asymmetry of the engine-to-pylon mounting indicates that the FBO loading magnitudes are likely sensitive to strike position - and the results validate this idea. Clearly, any baseline model should be run with a series of strike positions to determine an upper and lower bound to the output.

6.7.3 Results Discussion: Suppressing Physics (nonlinearities)

For the baseline model the two primary energy dissipation mechanisms were elastic plastic deformation and sliding interfaces. The global energy balance showed sliding energy to be slightly more significant than plastic work. These dissipation mechanisms are created by highly nonlinear phenomena of contact and inelastic behavior. To understand the effects of the nonlinearities the baseline model was progressively 'linearized' to behave more like the implicit full engine models described in [9,16,17]. The ***elastic with single contact*** was intended to mimic the nonlinearities in the implicit full engine model (even though it was solved using explicit integration).

Figure 6.16 below orders the runs sequentially from most nonlinear model (***baseline***) to the least nonlinear model (***elastic with Single Contact***).

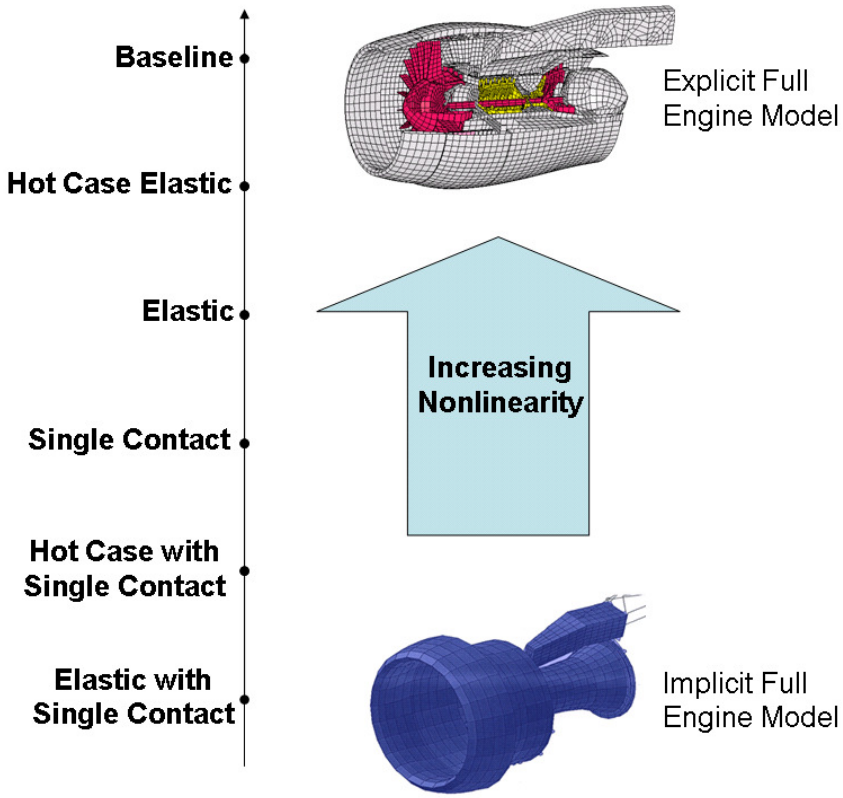

Figure 6.16 Nonlinearities in Full Engine Model

Progressively reducing the nonlinearities and looking at detailed result trends allows one to identify the most dominant nonlinear effects. The ***No Mass Scaling***, ***Three O'Clock Strike*** and ***Nine O'Clock Strike*** cases were not so-called apples-to-apple comparisons thus their results not used in this section. With this in mind the results of Table 6.2 through Table 6.8 were plotted on Figure 6.17 and Figure 6.18. Note that since FBO is well known to be inherently highly nonlinear, the wording 'more physics' means including more nonlinear behavior and 'less physics' means including less nonlinear behavior.

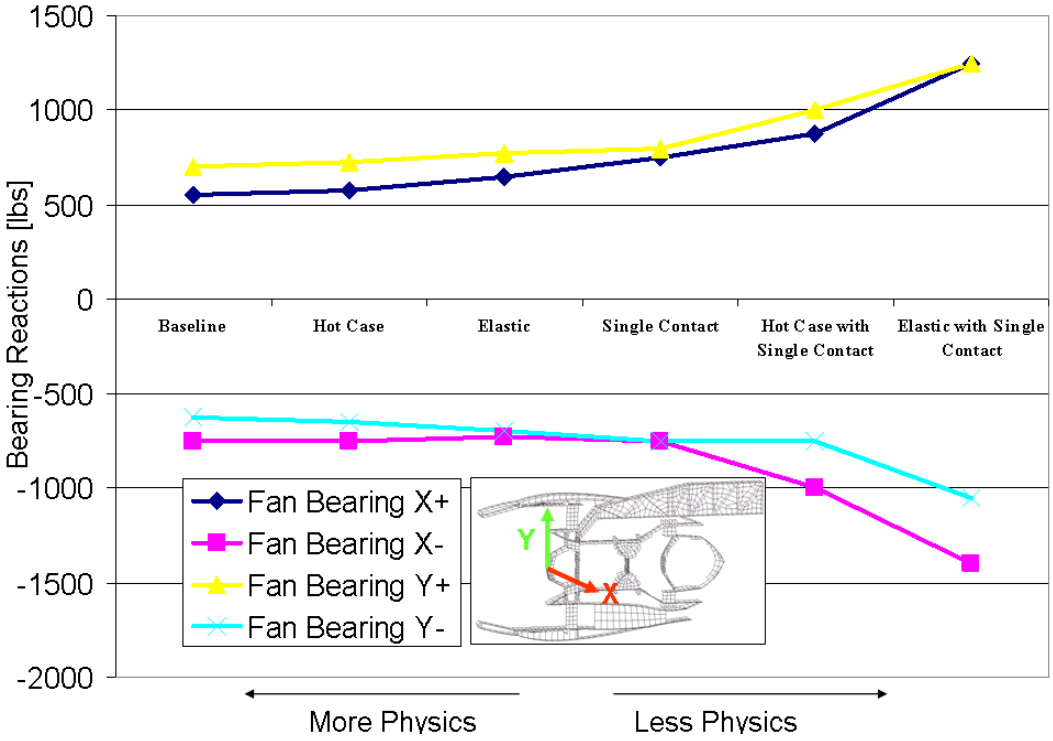

Figure 6.17 Sensitivity to Model Physics: Fan Bearing

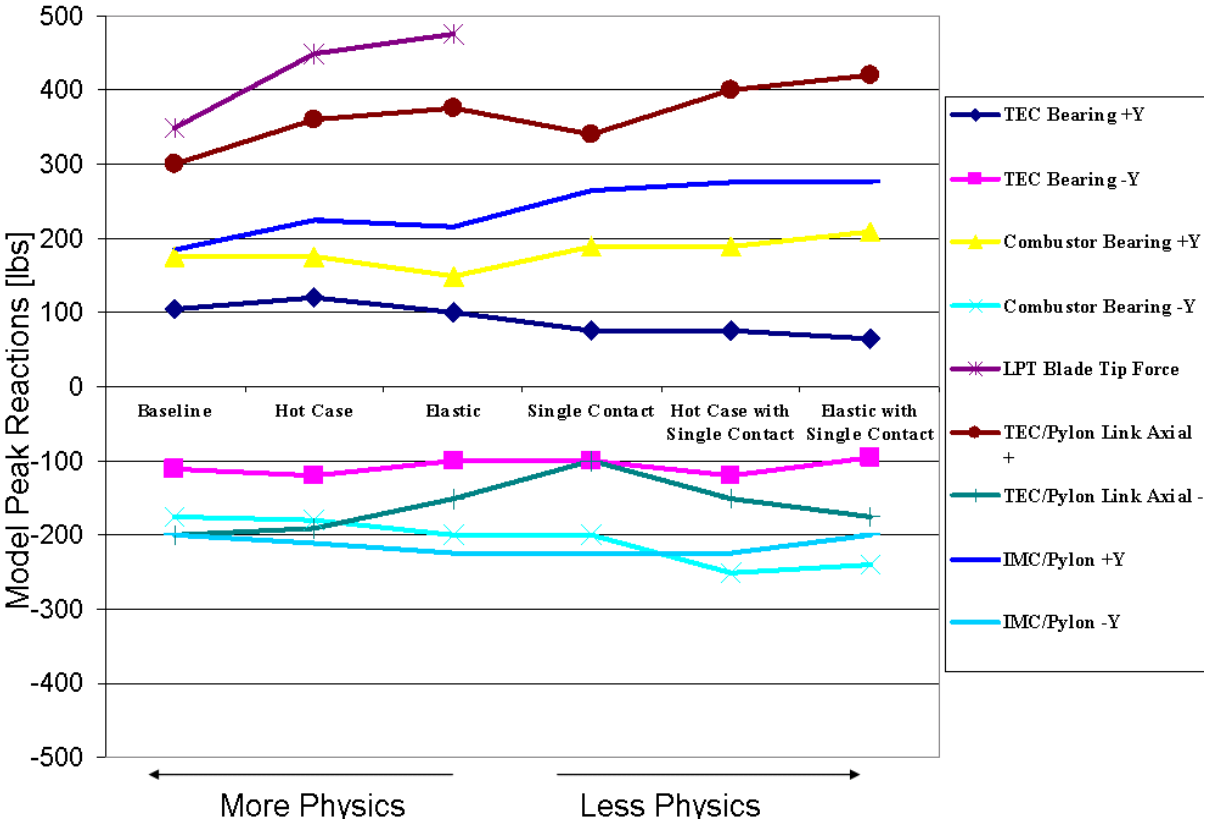

Figure 6.18 Sensitivity to Model Physics: System Loading

The observation that each predicted response curve is reasonably flat (the loads are relatively constant) is no coincidence. As mentioned before, great care (about 75 revisions worth of care) was taken to build a 'realistic' baseline model i.e. one that had reasonable thicknesses, stresses near yield, small plastic strains, elastically stable, avoid resonant frequencies, etc. In an aircraft engine, most components are neither grossly over designed nor under-designed. Using this 'realistic' reasonable starting point the effect of decreasing the model complexity (the so-called model 'physics') can be more reliably and realistically studied.

For example, in the baseline model, the plastic strain distribution (at final simulation time) in this elastic-plastic exhaust system is shown in Figure 6.19. Note that some small localized inelastic strains (with strain magnitudes in the order of 10%) have formed. According to industry sources [5,6] these types of strain levels, along with minor but noticeable yielding can be expected in many components after a successful FBO test.

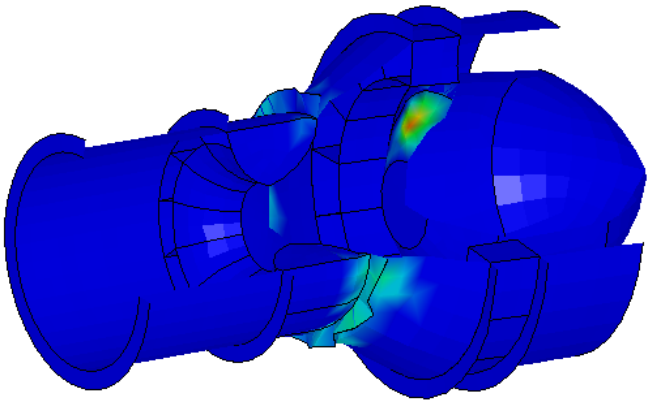

Figure 6.19 Localized Final Plastic Strains in Hot Case for Baseline Model

The ***hot case*** model variation (where the exhaust case in Figure 6.19 was replaced with elastic materials) shows a relatively significant change to the overall response. Figure 6.17 and Figure 6.18 clearly show how uncertainty in FBO force results increases as the physics of the model are progressively suppressed.

The IMC-to-Pylon (+Y) and TEC Bearing force (+Y) from Figure 6.18 are re-plotted on Figure 6.20 for further discussion on their importance. The ***baseline*** model predicts the IMC-to-Pylon Mount load as about $180 \cdot 10^3$ lbs; the ***elastic with single contact*** model predicts about $275 \cdot 10^3$

lbs. Similarly, the ***baseline*** model predicts the TEC Bearing load as about $105 \cdot 10^3$ lbs; the ***elastic with single contact*** model predicts about $65 \cdot 10^3$ lbs. As mentioned before, a teams of engineers design and size individual components to these loads. A full engine FEA model provides FBO loads transmitted through each component. These FBO loads often dictate the size or wall thicknesses of the large diameter case components and are important for total engine weight.

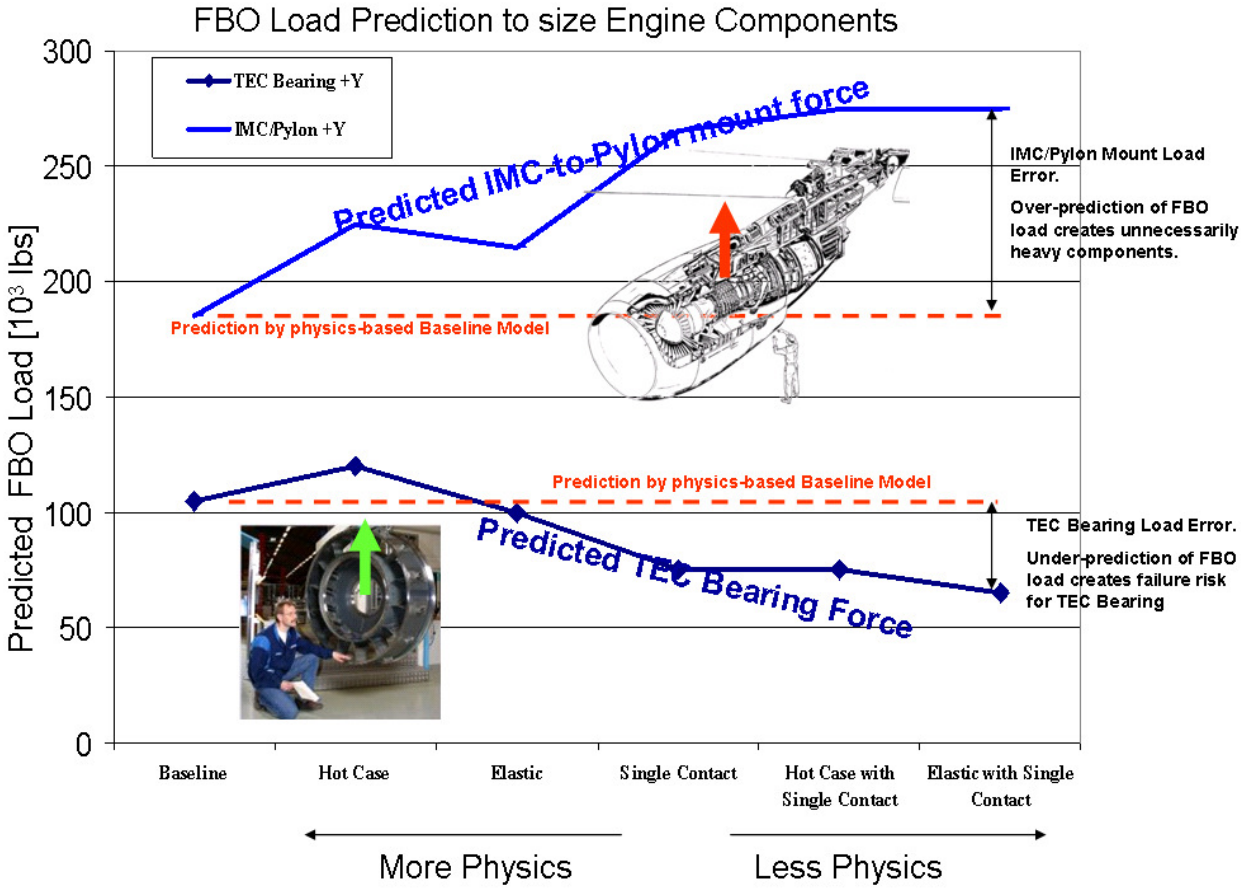

Figure 6.20 Modeling less physics increases loading uncertainty.

Note how the ***elastic with single contact*** model simultaneously over-predicts and under-predicts loads-depending of the component. This introduces uncertainty into the predicted loads which must be countered with design conservatism (adding extra thickness) to ensure a successful FBO test. The push-pull conflict in the aircraft engine industry between reducing weight and passing the FBO test indicates how important it is to ensure that the relevant physics are included in the finite element model.

6.7.4 Discussion of Modeling FBO Physics

As physics are removed from the model there were fewer mechanisms to absorb the kinetic energy. The fan bearing reactions comparison for the ***baseline*** versus ***elastic with single contact*** is shown in Figure 6.21. Note how the amplitude converges for the ***baseline*** case as might be expected when one carefully considers the mechanical response of the FBO event. Conversely, for the ***elastic with single contact*** case, the amplitude increases. This diverging behavior is not expected and the typical user would be tempted to apply 'damping' to the model to eliminate energy from the system.

The conversion of kinetic energy into plastic work and sliding energy are the primary physics of the problem. Historically, these effects were very difficult to include in finite element simulations and simple 'smeared' approximations such as damping were tolerated to obtain a solution to a computationally challenging problem; however, today this is a different story. Ignoring these effects and prescribing an artificial 'damping' effect in their place is not a good strategy for accurate simulation of the FBO event.

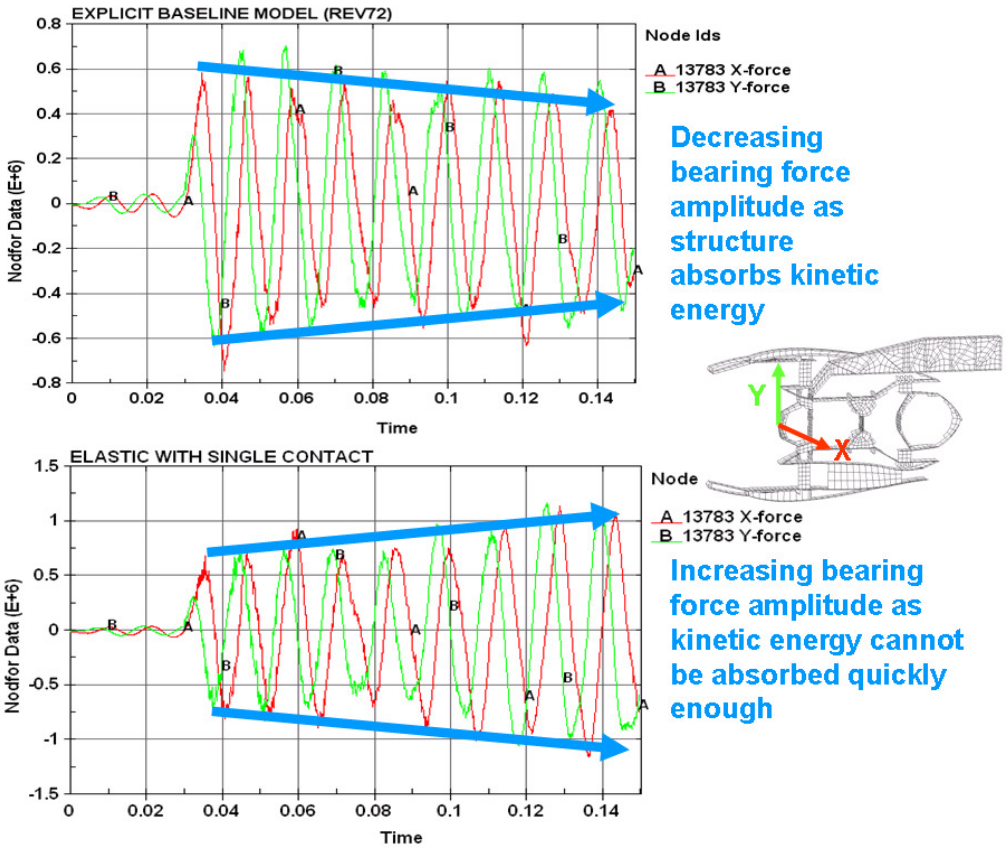

Figure 6.21 Fan Bearing Reactions: Baseline versus Elastic Single Contact

Table 2.1 highlighted some of the research efforts used in an implicit based FBO full engine model. This table is revisited in Table 6.9 with added comments on the explicit modeling effort based on having developed the full engine FBO model with an explicit tool.

Table 6.9 Comparison of Implicit and Explicit Modeling Effort

	Implicit Modeling Effort	**Explicit Modeling Effort**
1	5% damping at 60 Hz.	Not required. Physically based sliding friction and plasticity independently remove system energy.
2	the rotor speed is prescribed i.e. rotor speed is a problem input	Rotor speed is a natural FBO simulation output.
3	4 μs integration timestep size	Similar order size timestep size to implicit. Much smaller CPU time per timestep. Always robust.
4	Reported radial displacement amplitudes (due to resonance) in the order of 35" (~1000mm)	A 35" displacement is not reality. All kinematic/constitutive/kinetic measures in LS-Dyna are, by default, nonlinear.
6	Derivation of skew symmetric 'plowing' forces (applied to the end of a beam element) to artificially induce an axial force component during tip rubbing.	3D shell models of blades will automatically capture this plowing effect.
7	case flexibility ignored or difficult to include	Automatically included in LS-Dyna. Little, if any, CPU penalty.
8	tip rubbing study highly influenced by damping coefficient as well as large displacement	Large displacements automatically handled correctly. No 'damping' is required in LS-Dyna as energy dissipation mechanisms naturally included
9	Complicated gyroscopic derivations with a host of assumptions.	Automatically included. Better physics including higher order terms, contact and coupling to flexible structure

Further examples could be included but the point has been made- explicit solution has some compelling technical advantages for full engine modeling of FBO.

7 Conclusions and Further Work

Chapters 3, 4 and 5 developed an explicit integration full engine model for computing FBO loading for use in engine component design. Chapter 6 validated that including the primary nonlinear behavior that was considered is necessary to accurately simulate the FBO event. This chapter will discuss how to move forward with this idea and where it may go in the future.

7.1 Concluding Comments on Chapter 1

An important point for industry is that the FAA certification requirement for passing FBO includes allowing for simulation of the FBO event. One major stumbling block is that no manufacturer (published at least) has been able to demonstrate and convince the FAA that their full engine modeling methodology is accurate enough to replace the physical test. It is hoped that the proposed methodology in this work, with potential improvements over existing methods, can be used to make rig testing less prevalent. If its predictive capability is proven it is hoped the FBO rig test could eventually be waived.

7.2 Concluding Comments on Chapter 2

Computer hardware and software have made explicit integration technology viable for full engine modeling of the FBO event. A tool such as LS-Dyna is more robust and faster for solving this class of problem.

7.3 Concluding Comments on Chapter 3

This chapter outlined a very general, modular, systematic approach to full engine FBO modeling. At first glance, this modular approach seems uninteresting, at least from an academic point of view; however, when large teams tackle a large multi-component structure (such as an aircraft engine) a fast, general, robust approach to modeling is essential for securing confident results in a timely fashion.

The materials section showed a fairly simple bilinear elastic plastic behavior; just the basic behavior was implemented for this proof-of-concept work. However, appropriate constitutive model selection and establishing accurate material constants is very important for the FBO simulation. A large engine manufacturer would be able to dedicate more time, experimental testing and trade studies to this important facet of simulation.

The mesh size was purposely made coarse for this study and took about 1.5 hours on a simple 2.4 GHz PC; however the mesh could be significantly refined and still be feasible. For example if the mesh edge length in Figure 7.1 was refined by a factor of three (meaning each shell edge was divided into three) the resulting mesh would be about 9 times larger. This new mesh would also have a critical timestep size of about 1/3 which would slow down the total simulation time to solve the event by a factor of about 27. A four CPU cluster could be used to reduce the total run time of a fine mesh to about ¼ x 1.5 hours x 27 = 10 hours. Ten hours runs can be made overnight making full engine FBO simulation possible.

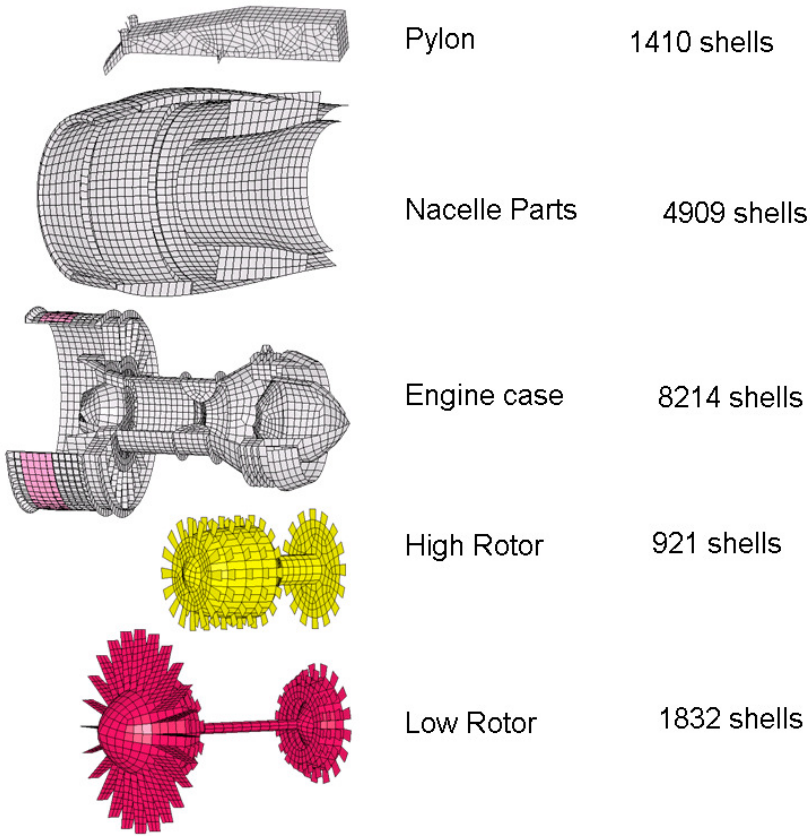

Figure 7.1 Expanding the baseline model mesh

7.4 Concluding Comments on Chapter 4

Any new modeling techniques must have accuracy validations and checks. This work checked some quantifiable 'basics' such as released blade energy, unbalanced force, etc. Engine designers may be able to provide more insight and ideas for further validation.

Some software related accuracy validations could be optimized further. For example, the rotor pre-stress loading was solved using dynamic relaxation (a technique employing damping of dynamic motion). Clearly this problem is a static one and could be solved more efficiently using implicit methods (ANSYS, NASTRAN, etc.) and then these results mapped into an explicitly solved transient. Debugging this implicit-to-explicit process was deemed unfeasible for this work but becomes efficient when the model size and run times become large.

7.5 Concluding Comments on Chapter 5

The author used some limited industry experience with individual component design to extrapolate the type of results that a full engine FBO model might be expected to provide; the results herein are admittedly very limited. Engine manufacturers are likely to have much more comprehensive results extraction. How the results might be used for individual component design was similarly extrapolated.

In addition to use in design studies, results from a similar baseline model could also be 'calibrated' to manufacturer experimental data. This calibration would be done by building a LS-Dyna 'baseline' model to manufacturer's already existing engine. The results from this simulation would be compared to the manufacturers FBO test data. The simulation variables (friction coefficient, etc) could then be adjusted until simulation results match test data. This approach would improve the overall modeling accuracy.

7.6 Concluding Comments on Chapter 6

Figure 6.20 showed how the FBO load prediction becomes more uncertain as the nonlinearity in the model is reduced. As the FBO load predictions becomes more uncertain engine manufacturers must adopt a more conservative design approach which, in general, increases

component weight. These results clearly indicate the nonlinearities must be included when modeling FBO.

7.7 List of Potential Baseline Model Improvements

Some model improvements could be including or incorporating:

1. Implicit pre-stressing of rotors to initial stresses and displacement state. This would involve mapping the steady state stress and displacement field into the transient FBO run.
2. Include ablative/erosive capable materials at tip rubs. This would encompass variable friction coefficients. This would require methodology implementation as well as calibration to test data.
3. Use birth-death in contact definitions to optimize run times. For example, the computationally expensive fan blade/isogrid/fabric contact definition could be active for two revolutions and then killed. After two revolutions a blade-tip-to-isogrid and isogrid-to-fabric definitions could be invoked; this could likely handle the longer duration rotating imbalance phenomena.
4. Flexible bodies with primarily elastic behavior could be switched to rigid bodies after a prescribed number of revolutions. LS-Dyna does not compute stresses in rigid bodies and this flexible-to-rigid switching capability could be exploited to save significant time.
5. Develop the implicit-explicit switching capabilities in LS-Dyna to solve a full suite of FBO related analyses such as implicit preload, explicit blade impact and transient, followed by implicit modeling of the engine rundown. After the FBO event the engine may run down (slow down) and pass through several systems resonance points; this event is a lower frequency than FBO impact and may be more efficiently handled by implicit methods.
6. Create result interfaces to track the transmitted load/displacement history passing though a simplified representation of critical components (a rotor bearing, for example, which was grossly simplified in the baseline model). Then the transmitted load/displacement history can be easily applied to a more detailed model of a critical component.

7.8 FBO Modeling for the future

This work showed that a LS-Dyna based full engine FBO model is both practical and feasible with today's hardware and software. Preliminary discussions with NASA and FAA technical experts on FBO [21,22] indicate that the baseline model described herein may be very useful to engine manufacturers. This is encouraging and hopefully some of the ideas can be implemented.

8 References

[1] LS-Dyna Users Manual, Version 970, Livermore Software Technology Corporation, Livermore, CA 94551 USA 2004

[2] LS-Dyna Theoretical Manual 2006, Version 970, Livermore Software Technology Corporation, Livermore, CA 94551 USA

[3] Javier Bonet, Richard Wood, **Nonlinear Continuum Mechanics for Finite Element Analysis** October 2000, Cambridge University Press, Cambridge UK.

[4] Ted Belytschko, Wing Kam Liu, Brian Moran, **Nonlinear Finite Elements for Continua and Structures** 1997, John Wiley and Sons, Ltd

[5] Mr. Bob Phoenix, Stratford, CT, retired analysis engineer, Lycoming. Private conversation. 2006

[6] Mr. Charles Luchin, Stratford, CT, retired design engineer, Lycoming. Private conversation. 2006

[7] Federal Aviation Administration (1984) Federal Aviation Regulation Part 33, Section 33.94.

[8] NASA website: http://www.nasa.gov/centers/glenn/news/AF/2007/Jan07_BladeOut.html

[9] NASA website. http://structures.grc.nasa.gov/competencies/computational.html 2007

[10] Brian Rice, Stephen Mitchell “Smart Fan Containment System”, 2005 NASA/CR—2005-213969

[11] J. Sharda, C. Deenadayalu, B. Mobasher and S. D. Rajan, “Modeling of Multi-Layer Composite Fabrics for Gas Turbine Engine Containment Systems”, *ASCE J of Aerospace Engineering*, 19:1, 38-45, 2006.

[12] Xiahua Zheng, Robert K. Goldberg, Wieslaw K. Binienda, Gary D. Roberts “LS-DYNA Implementation of Polymer Matrix Composite Model Under High Strain Rate Impact” Society for the Advancement of Materials and Process Engineering, NASA/TM—2003-212583

[13] Lawrence, Charles; Carney, Kelly; Gallardo, Vicente, Aircraft Engine Blade Off Dynamics 7th International LS-Dyna Users Conference, 2002

[14] Gary Roberts, Duane Revilock, Wieslaw Binienda, Walter Nie, Ben Mackenzie and Kevin Todd “Impact Testing and Analysis of Composites for Aircraft Engine Fan Cases” Glenn Research Center, April 2002, NASA/TM—2002-211493

[15] S-Y. Chen, May 2000, "Using Explicit FE Analysis for Structural Analysis of Impact: From simple Calibrations to Very Complicated Models", Fourth FAA Uncontained Engine Debris Characterization Modeling and Mitigation Workshop, Stanford Research Institute (SRI) International, California, USA.

[16] Lawrence, Charles; Carney, Kelly; Gallardo, Vicente, Simulation of Aircraft Engine Blade Out Structural Dynamics, NASA/TM-2001-210957/Rev1, 2002 (5 element Asymmetric Matrices study)

[17] Lawrence, Charles; Carney, Kelly; Gallardo, Vicente, A study of Fan Stage/Casing Interaction Models, NASA/TM-2003-212215 (5 element gap study)

[18] http://www.sri.com/psd/fracture/material_properties.html
http://www.sri.com/psd/fracture/detailed_model.html 2007

[19] Klaus-Jurgen Bathe, **Finite Element Procedures** 1996, Prentice Hall, New Jersey

[20] Stouffer, Donald; Dame, Thomas; **Inelastic Deformation of Metals** 1996, Wiley Inter-Science

[21] Chuck Lawrence, Kelley Carney, Private communication, NASA Glen, Ohio 2007

[22] Chuck Lawrence, Private communication, NASA Glen, Ohio 2007

[23] Figure made from images taken from Pratt and Whitney website. 2007

[24] Figure made from images taken from GE website. 2007

[25] Figure made from images taken from Rolls Royce website. 2007

[26] Figure made from images taken from FAA website. 2007

[27] Figure made from images taken from NASA website. 2007

[28] Figure made from images taken from Goodrich website. 2007

[29] Figure made from images taken from Boeing website. 2007

[30] Figure made from images taken from Airbus website. 2007

[31] Figure made from images taken from USAF website. 2007

[32] Figure made from images taken from Volvo website. 2007

Appendix A: Global Energy Histories

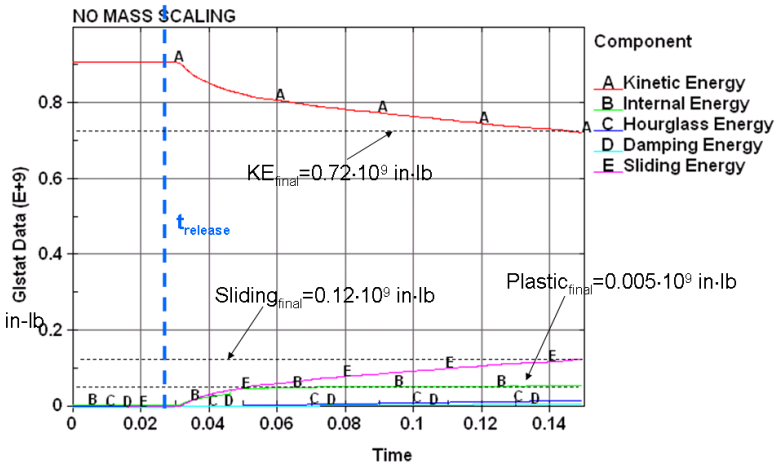

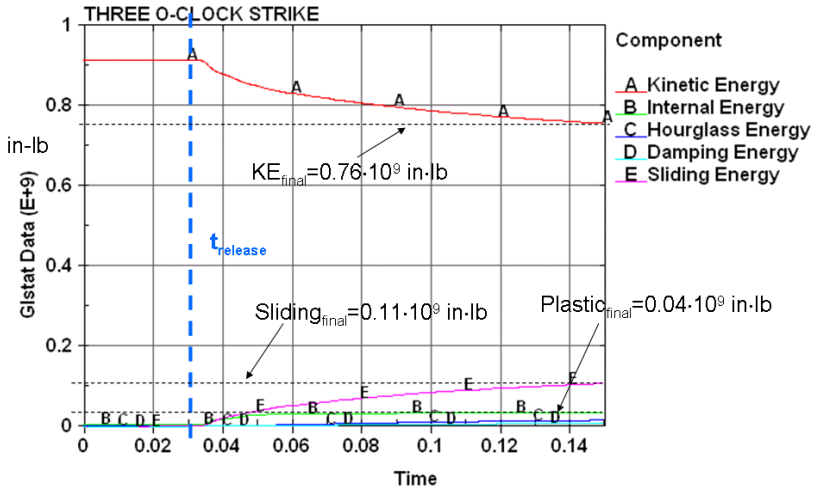

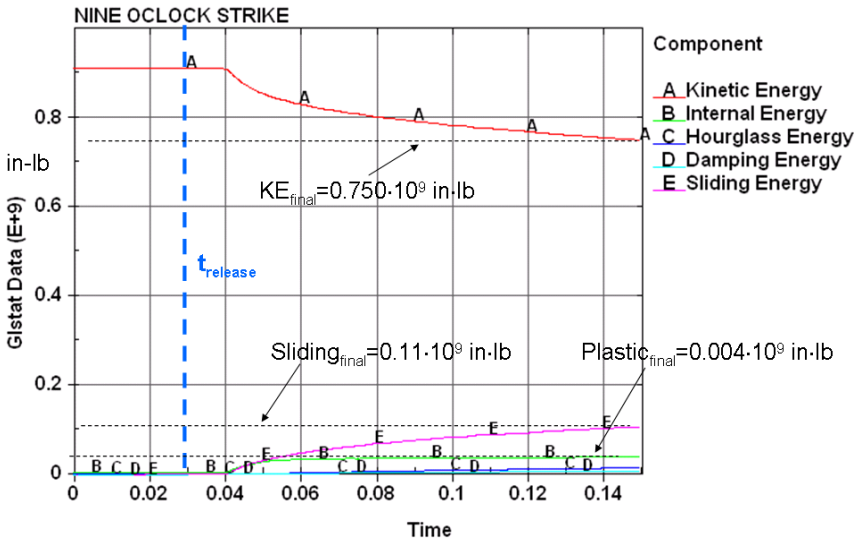

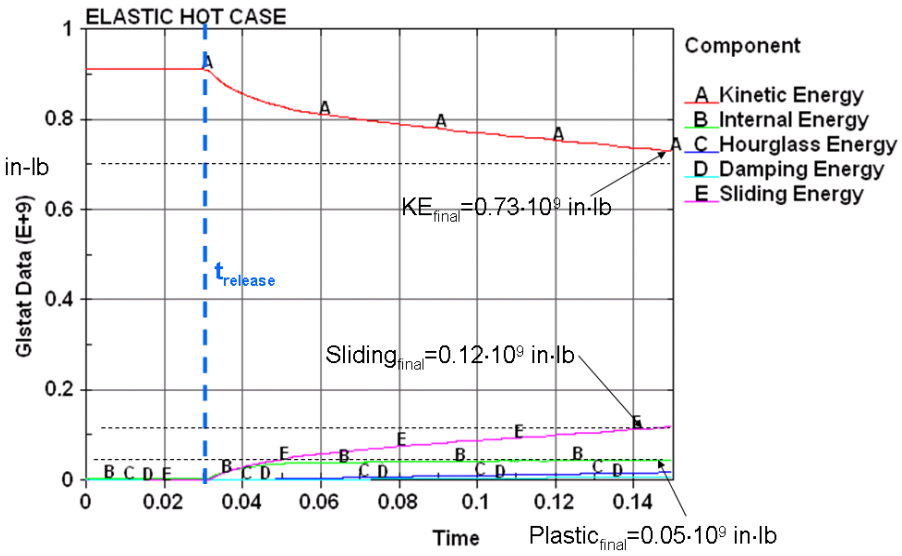
ELASTIC HOT CASE
Component
A Kinetic Energy
B Internal Energy
C Hourglass Energy
D Damping Energy
E Sliding Energy
in-lb
Glstat Data (E+9)
Time
KE_final=0.73·10^9 in·lb
t_release
Sliding_final=0.12·10^9 in·lb
Plastic_final=0.05·10^9 in·lb

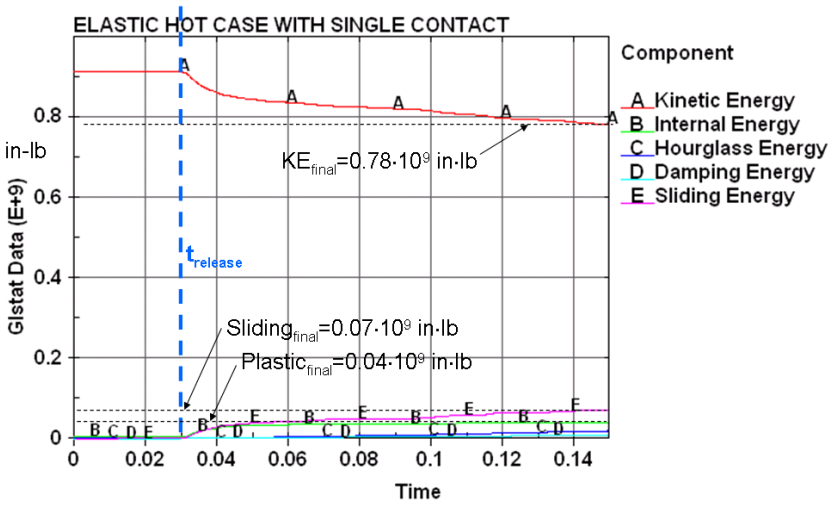
ELASTIC HOT CASE WITH SINGLE CONTACT
Component
A Kinetic Energy
B Internal Energy
C Hourglass Energy
D Damping Energy
E Sliding Energy
in-lb
Glstat Data (E+9)
Time
KE_final=0.78·10^9 in·lb
t_release
Sliding_final=0.07·10^9 in·lb
Plastic_final=0.04·10^9 in·lb

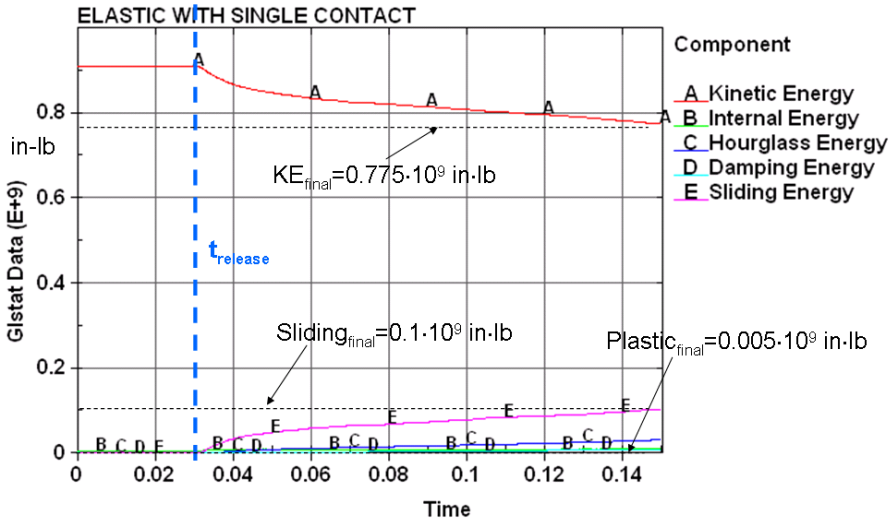
ELASTIC WITH SINGLE CONTACT
Component
A Kinetic Energy
B Internal Energy
C Hourglass Energy
D Damping Energy
E Sliding Energy
in-lb
Glstat Data (E+9)
Time
KE_final=0.775·10^9 in·lb
t_release
Sliding_final=0.1·10^9 in·lb
Plastic_final=0.005·10^9 in·lb

Appendix B: Fan Bearing Reactions

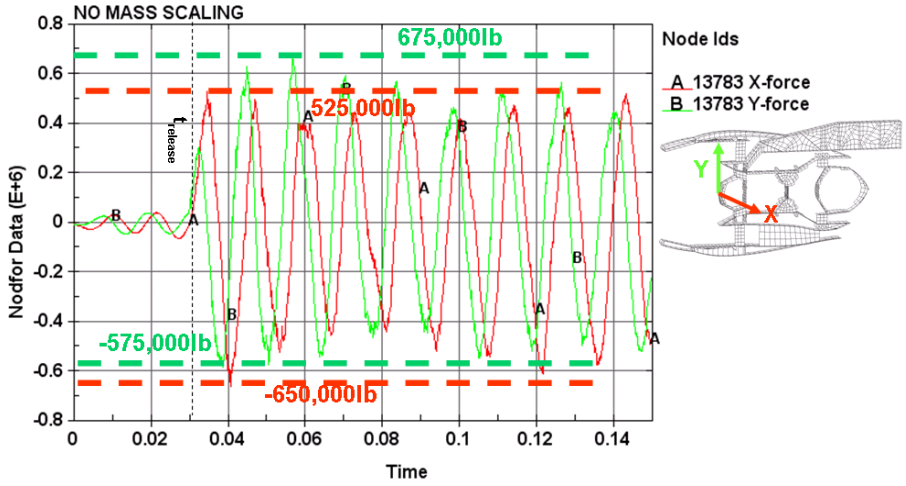

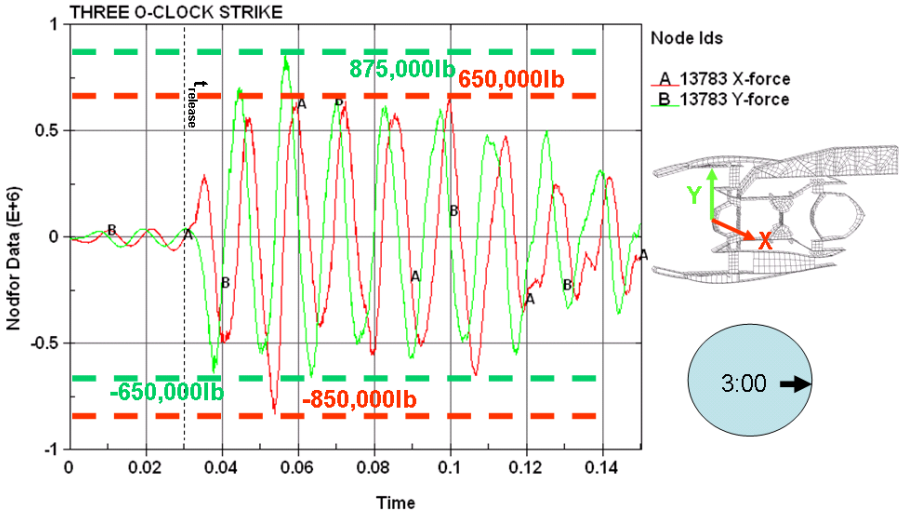

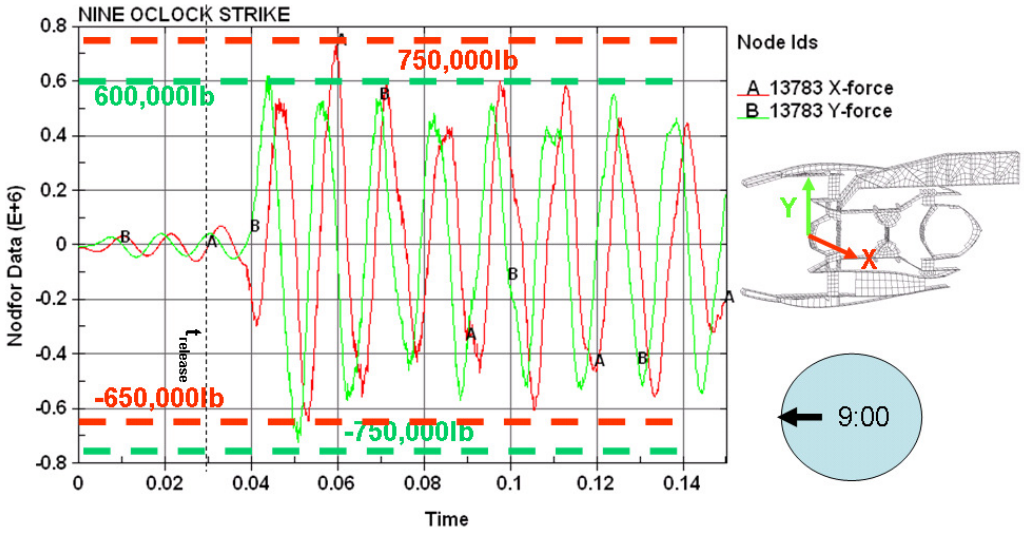

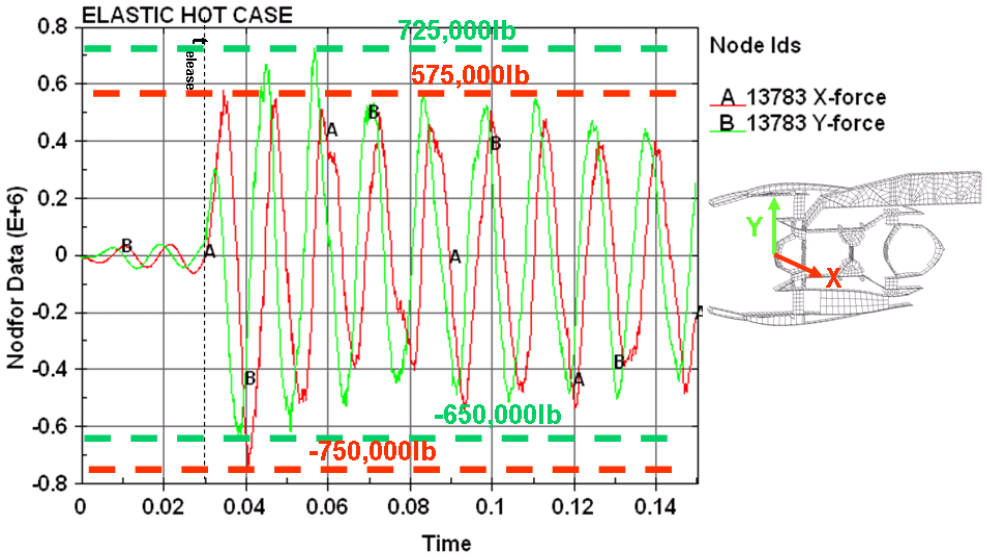
ELASTIC HOT CASE
725,000lb
575,000lb
-650,000lb
-750,000lb
t release
Node Ids
A 13783 X-force
B 13783 Y-force
Nodfor Data (E+6)
Time
Y
X

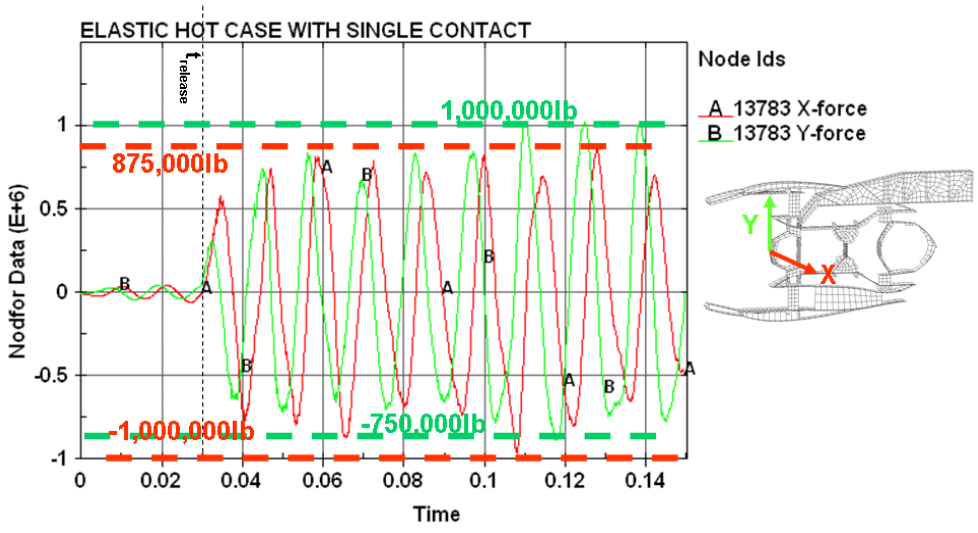
ELASTIC HOT CASE WITH SINGLE CONTACT
1,000,000lb
875,000lb
-1,000,000lb
-750,000lb
t release
Node Ids
A 13783 X-force
B 13783 Y-force
Nodfor Data (E+6)
Time
Y
X

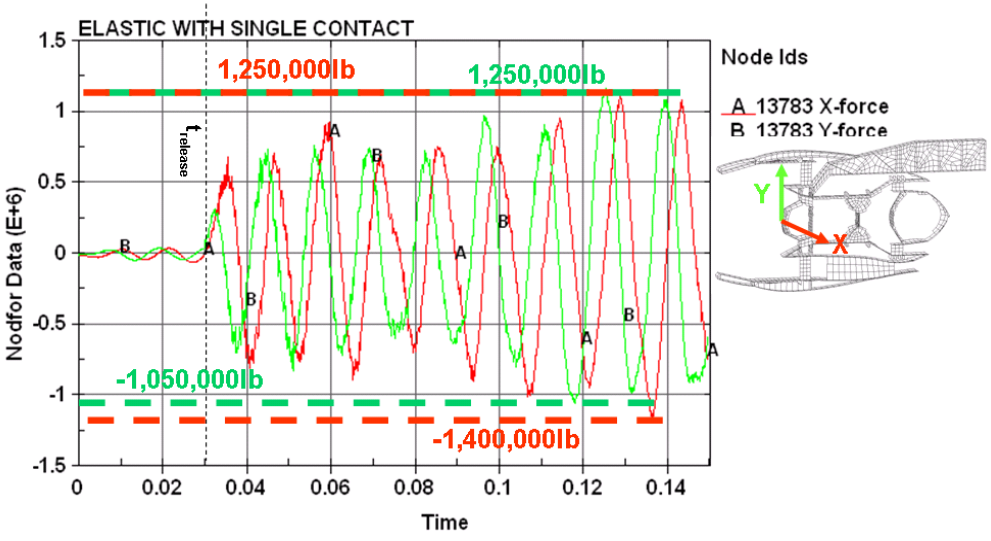
ELASTIC WITH SINGLE CONTACT
1,250,000lb
1,250,000lb
-1,050,000lb
-1,400,000lb
t release
Node Ids
A 13783 X-force
B 13783 Y-force
Nodfor Data (E+6)
Time
Y
X

Appendix C: TEC Bearing Reactions

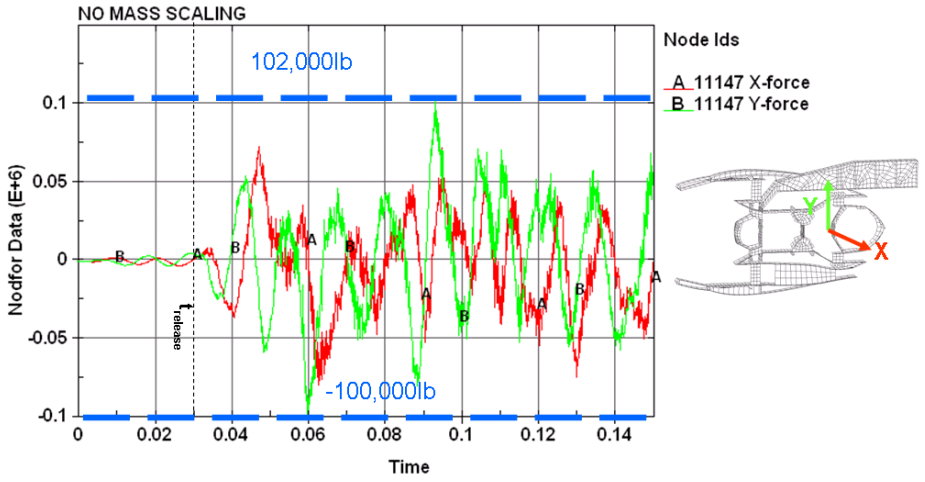

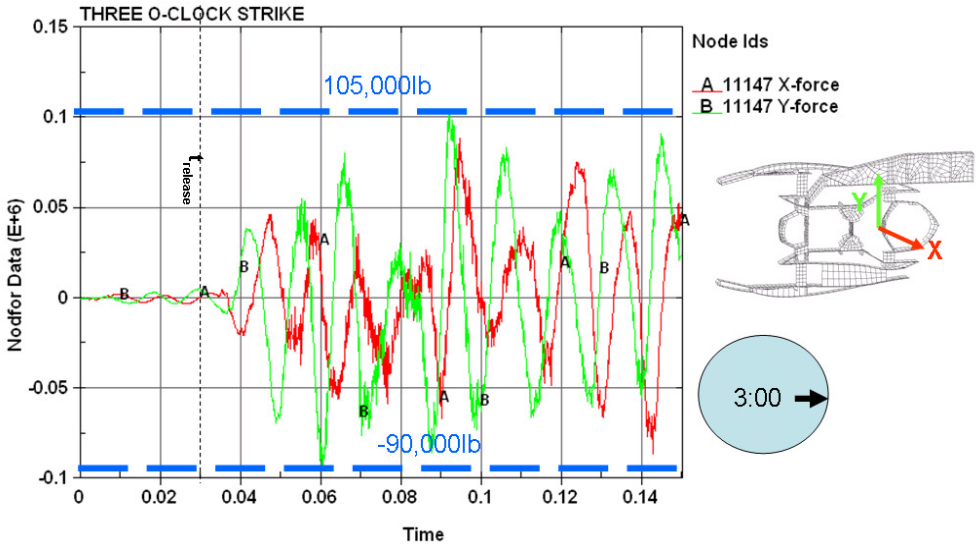

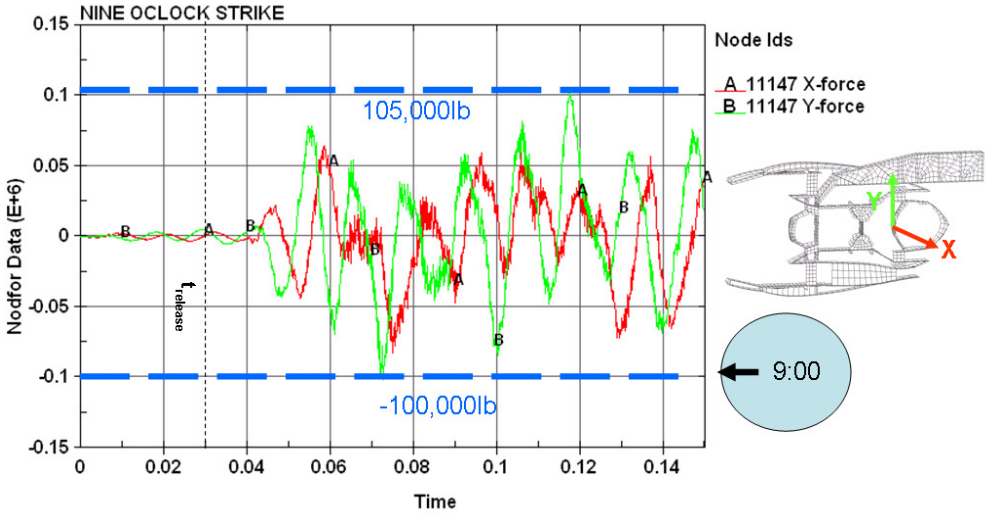

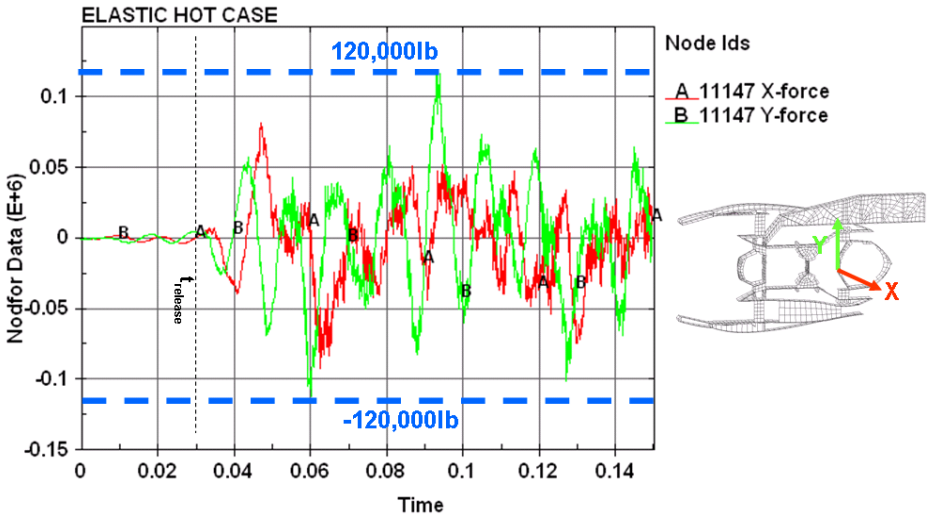
ELASTIC HOT CASE
120,000lb
-120,000lb
Node Ids
A 11147 X-force
B 11147 Y-force
Nodfor Data (E+6)
Time
0.1
0.05
0
-0.05
-0.1
-0.15
0
0.02
0.04
0.06
0.08
0.1
0.12
0.14
Y
X

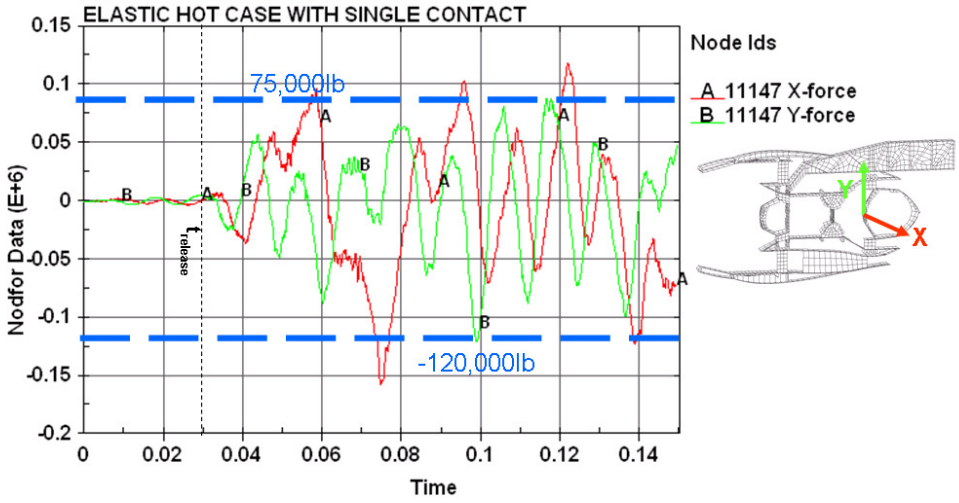
ELASTIC HOT CASE WITH SINGLE CONTACT
75,000lb
-120,000lb
Node Ids
A 11147 X-force
B 11147 Y-force
Nodfor Data (E+6)
Time
0.15
0.1
0.05
0
-0.05
-0.1
-0.15
-0.2
0
0.02
0.04
0.06
0.08
0.1
0.12
0.14
Y
X

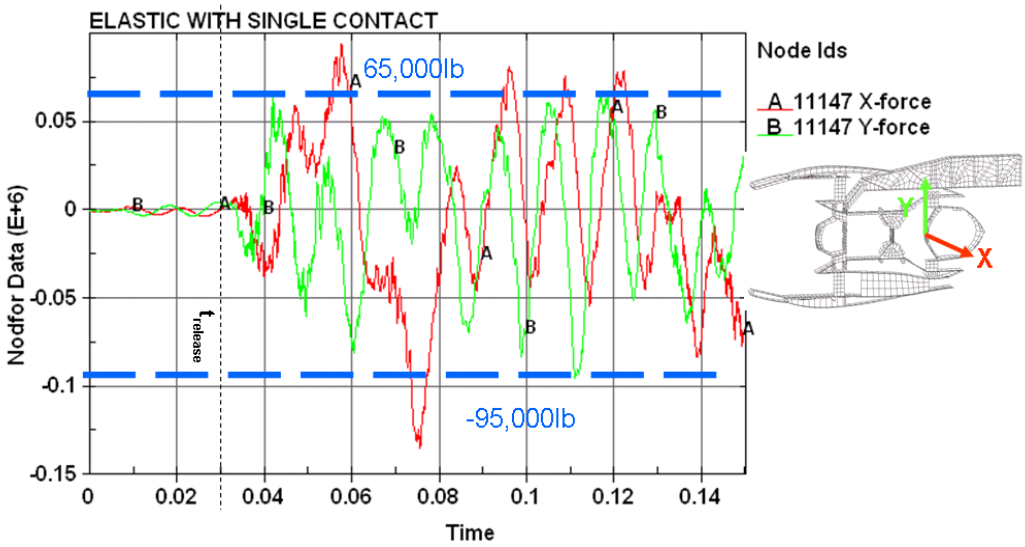
ELASTIC WITH SINGLE CONTACT
65,000lb
-95,000lb
Node Ids
A 11147 X-force
B 11147 Y-force
Nodfor Data (E+6)
Time
0.05
0
-0.05
-0.1
-0.15
0
0.02
0.04
0.06
0.08
0.1
0.12
0.14
Y
X

Appendix D: Combustor Bearing Reactions

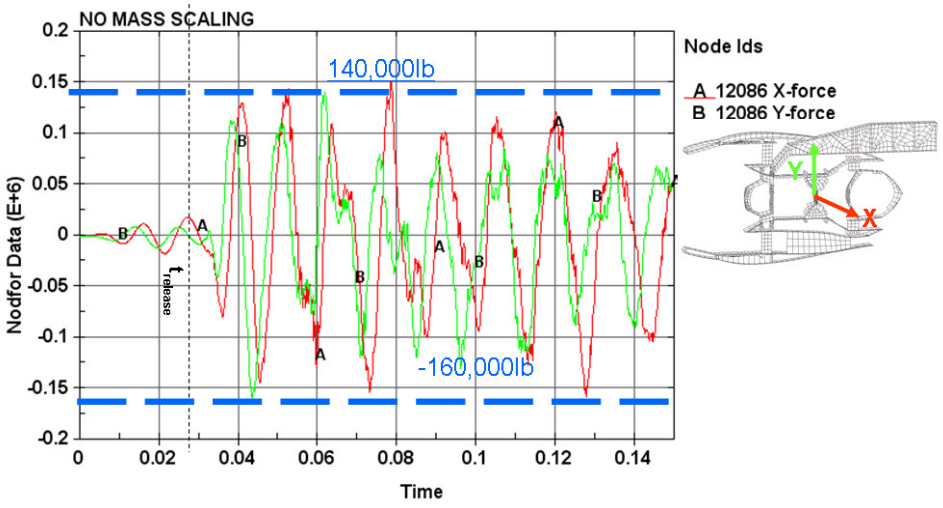

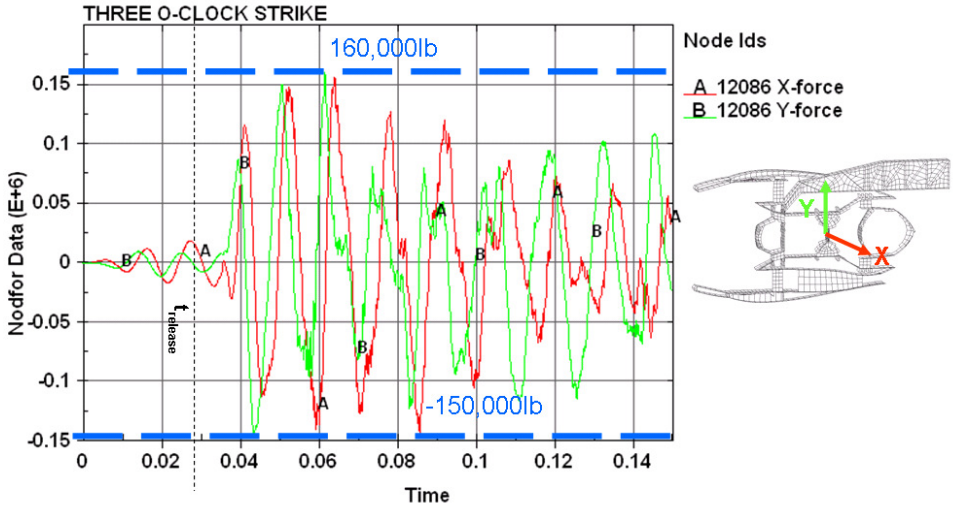

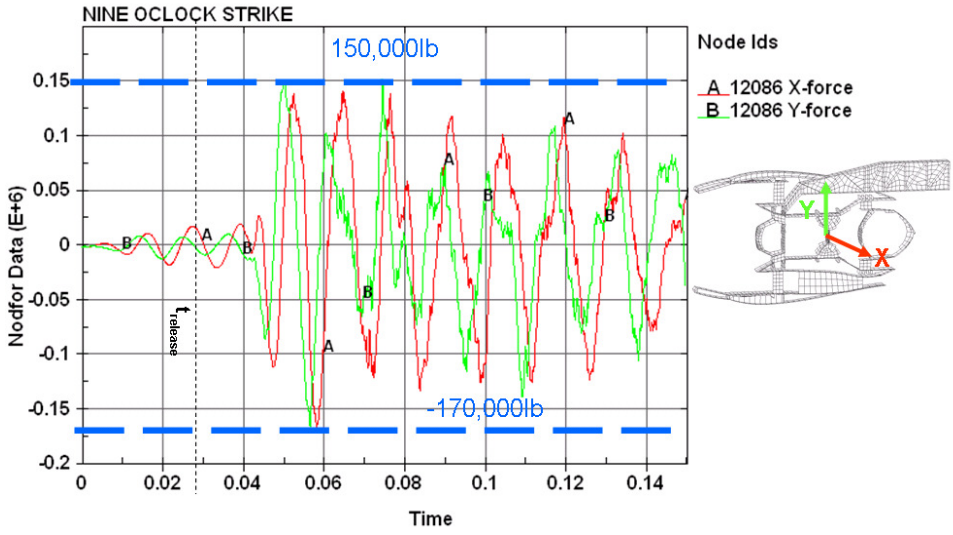

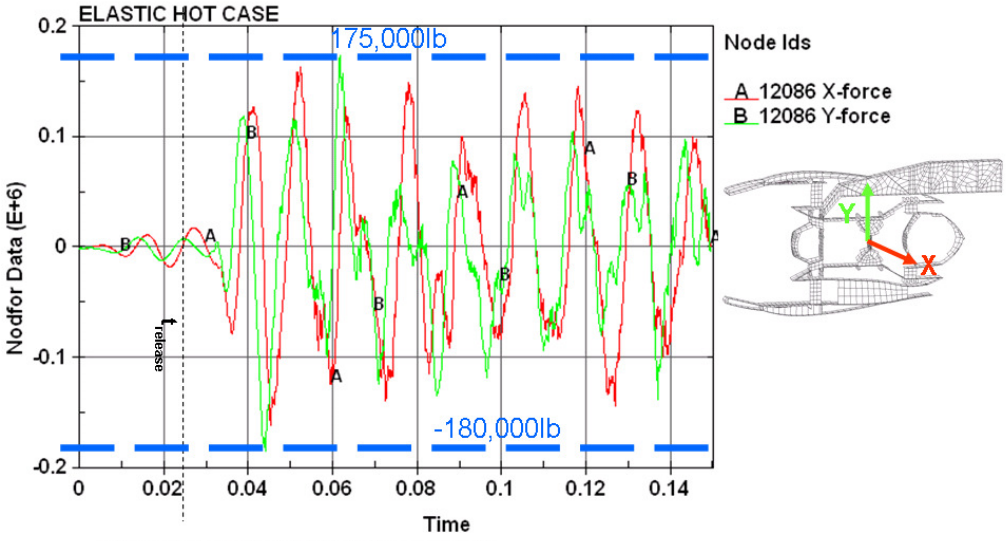
ELASTIC HOT CASE
175,000lb
-180,000lb
Node Ids
A 12086 X-force
B 12086 Y-force
Nodfor Data (E+6)
Time
t release
Y
X

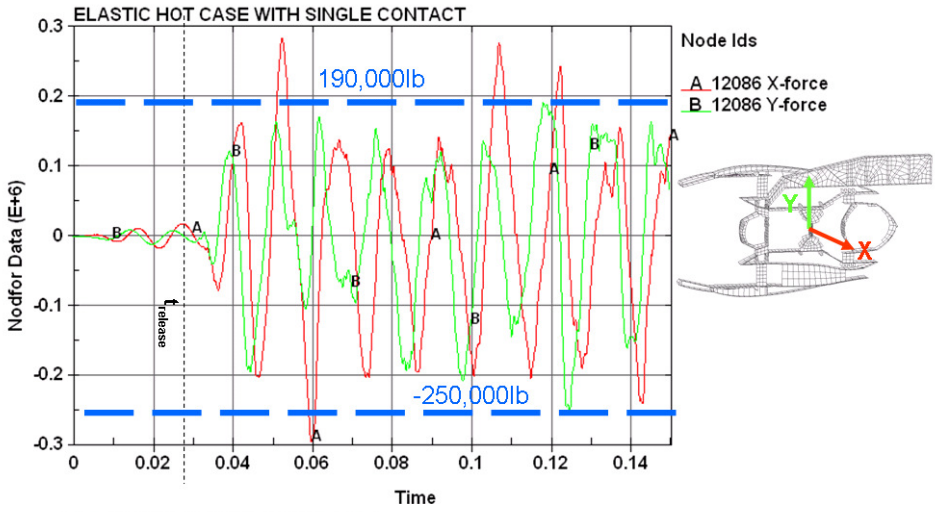
ELASTIC HOT CASE WITH SINGLE CONTACT
190,000lb
-250,000lb
Node Ids
A 12086 X-force
B 12086 Y-force
Nodfor Data (E+6)
Time
t release
Y
X

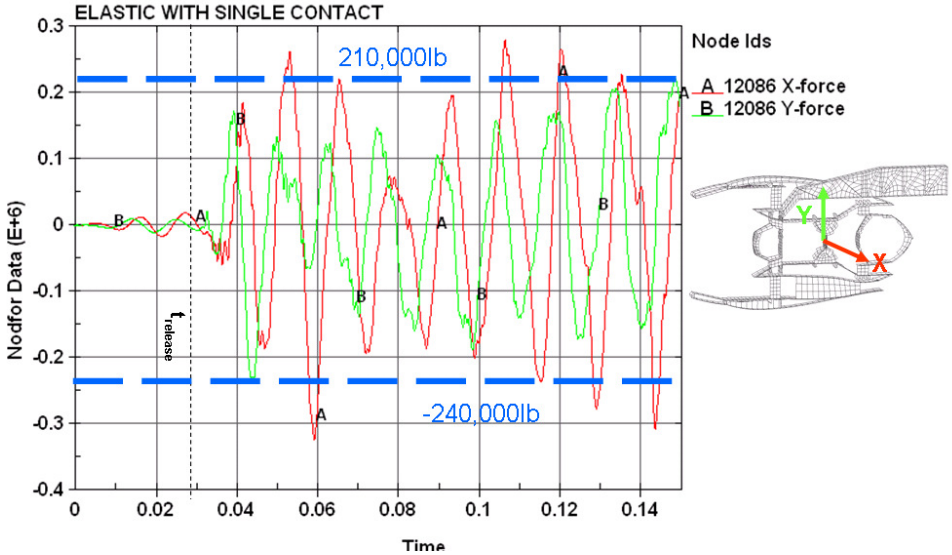
ELASTIC WITH SINGLE CONTACT
210,000lb
-240,000lb
Node Ids
A 12086 X-force
B 12086 Y-force
Nodfor Data (E+6)
Time
t release
Y
X

Appendix E: LPT Blade Tip Rubbing Forces

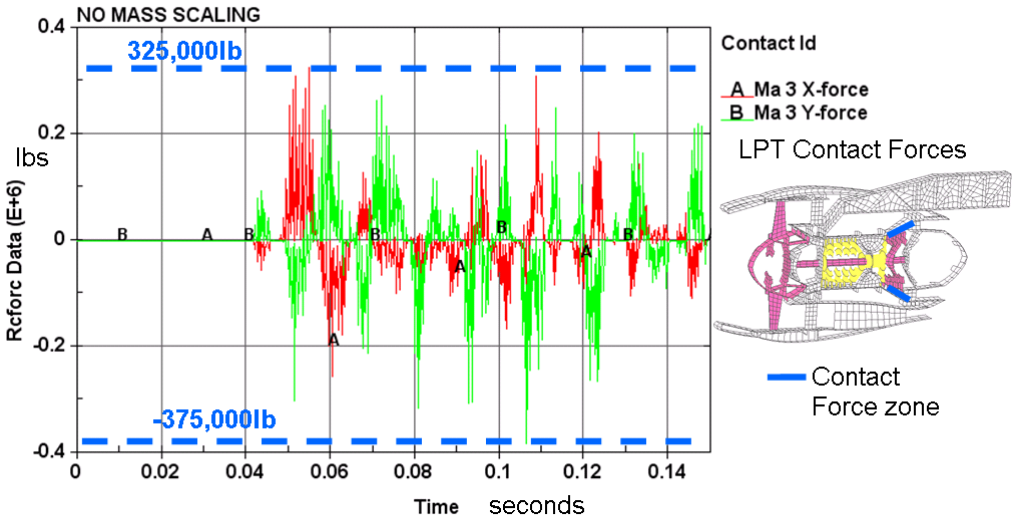

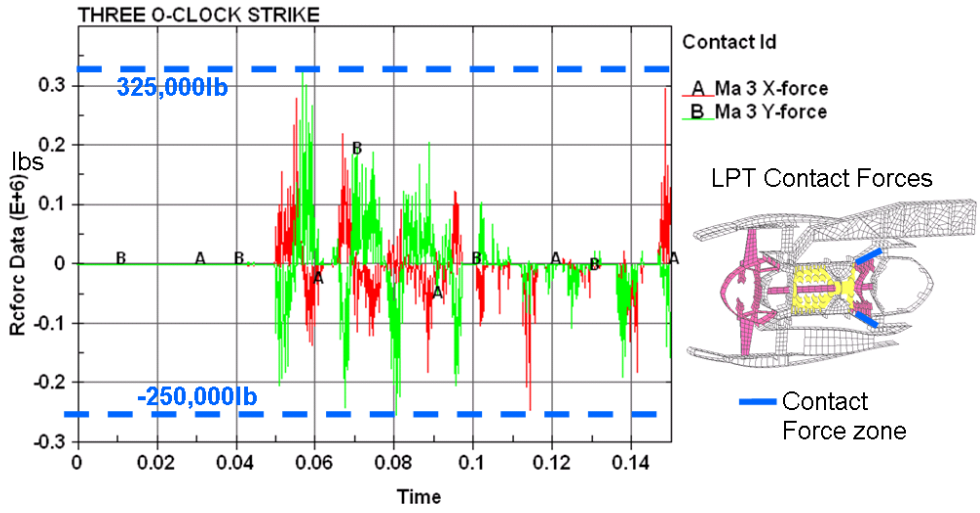

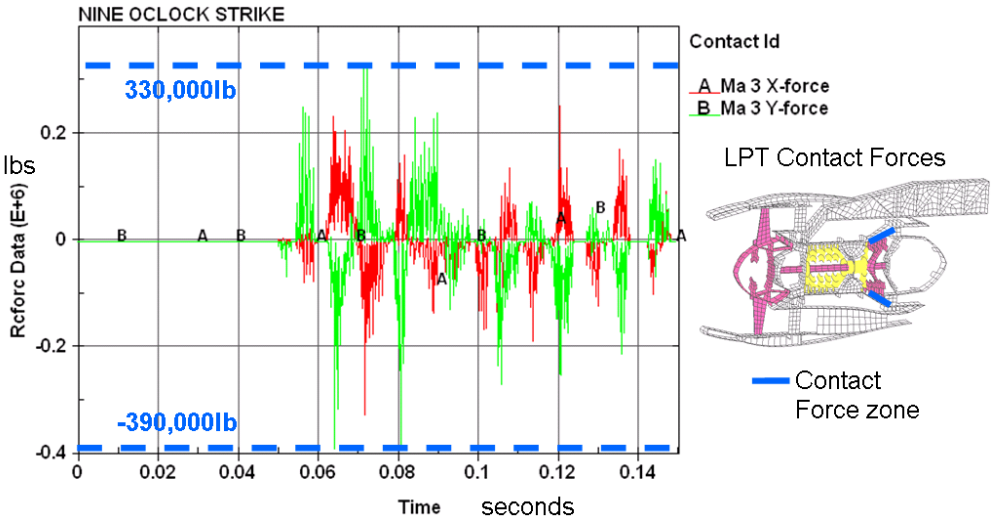

Appendix F: IMC-to-Pylon Forces

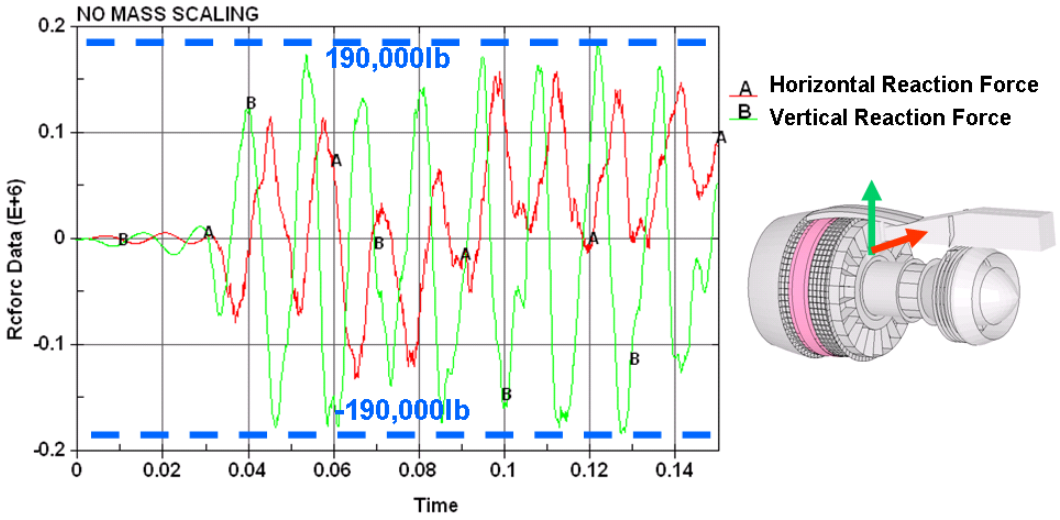

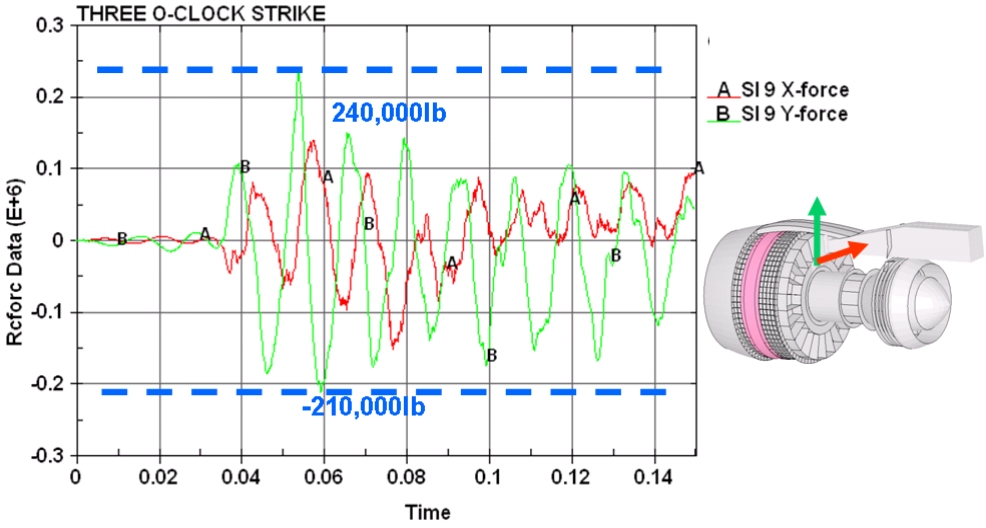

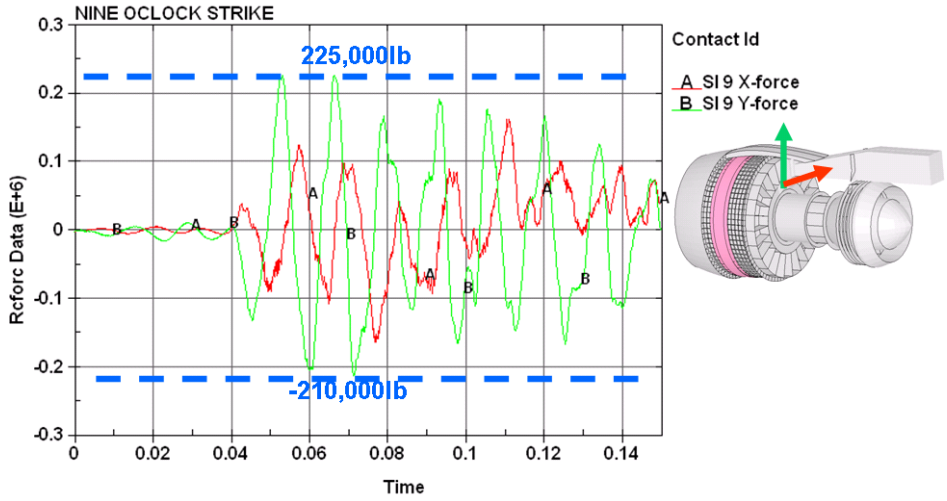

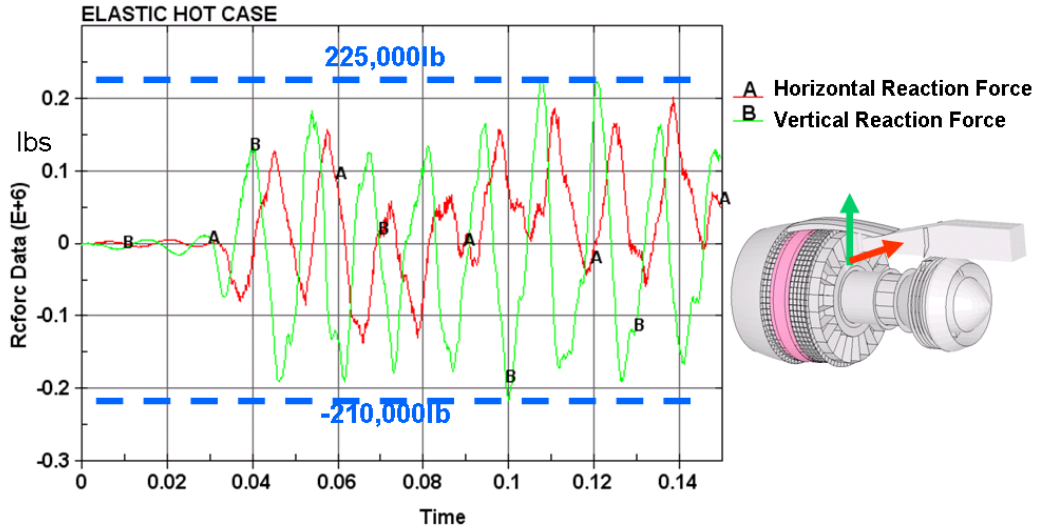
ELASTIC HOT CASE
225,000lb
-210,000lb
lbs
Rcforc Data (E+6)
Time
A Horizontal Reaction Force
B Vertical Reaction Force

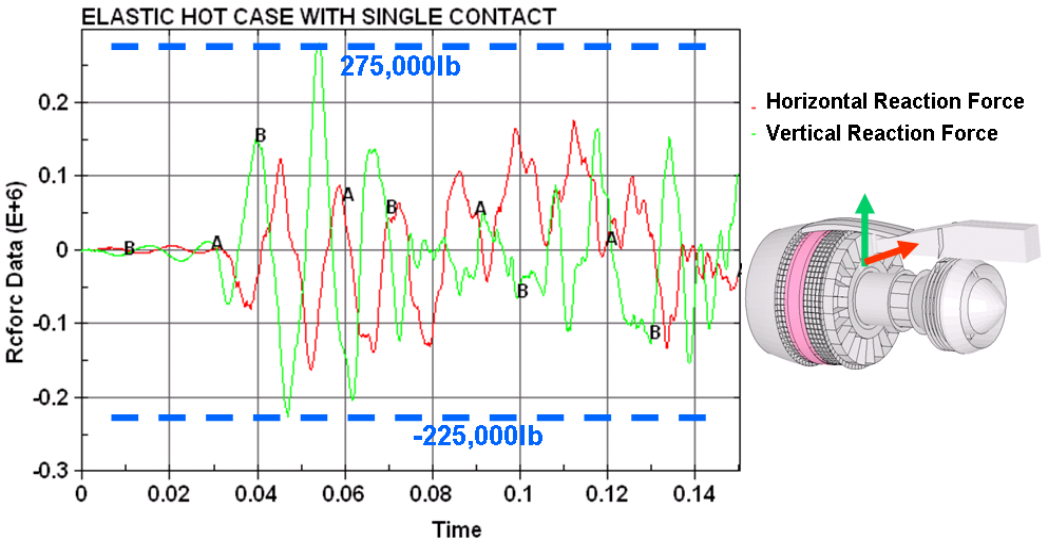
ELASTIC HOT CASE WITH SINGLE CONTACT
275,000lb
-225,000lb
Rcforc Data (E+6)
Time
Horizontal Reaction Force
Vertical Reaction Force

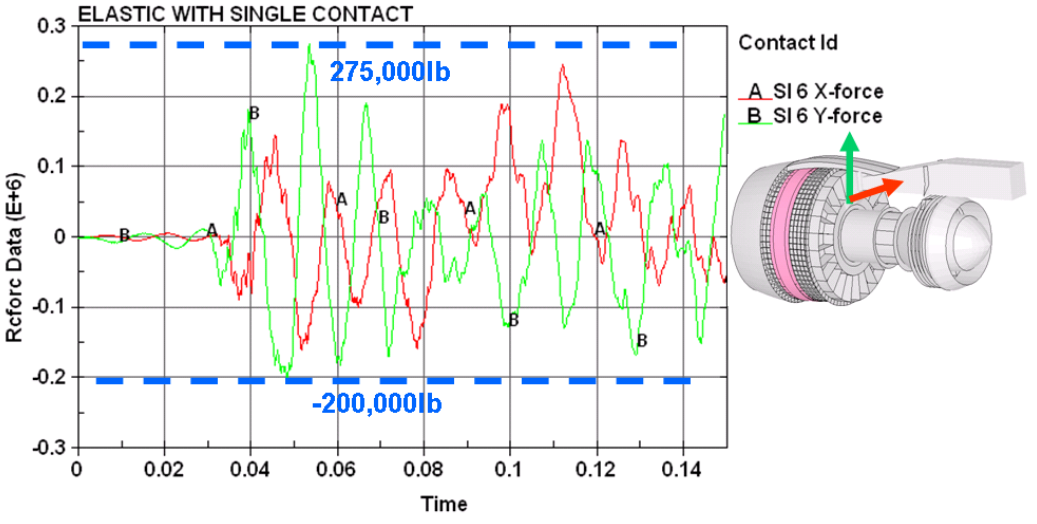
ELASTIC WITH SINGLE CONTACT
275,000lb
-200,000lb
Rcforc Data (E+6)
Time
Contact Id
A SI 6 X-force
B SI 6 Y-force

Appendix G: TEC-to-Pylon Forces

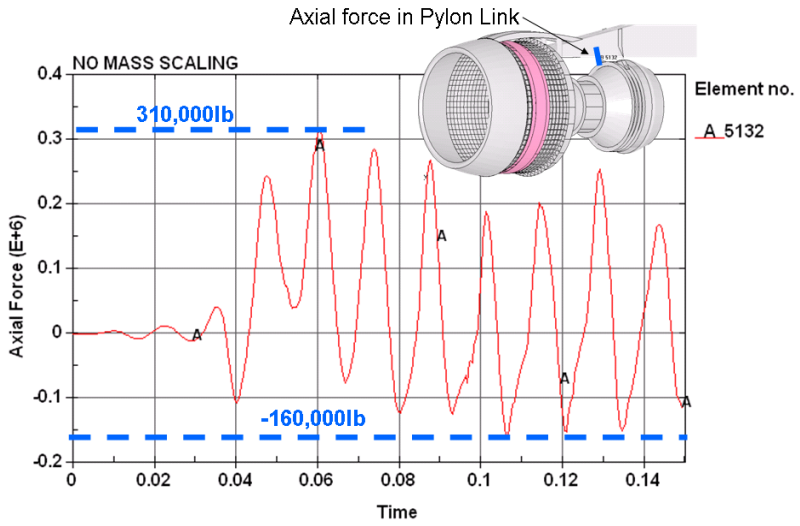

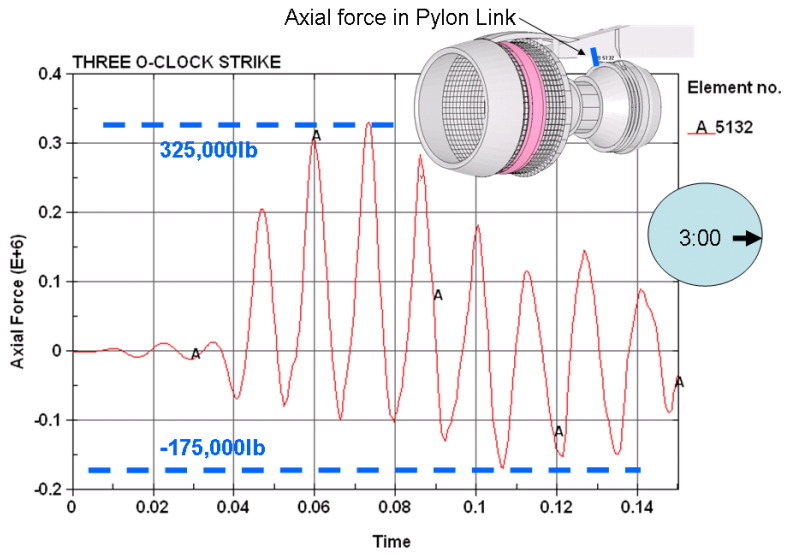

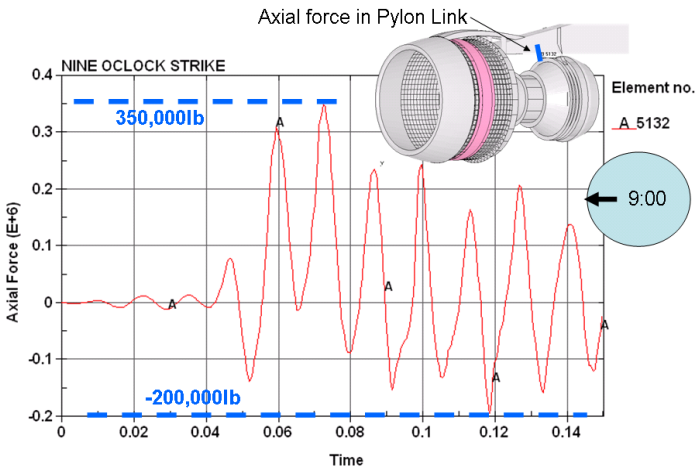

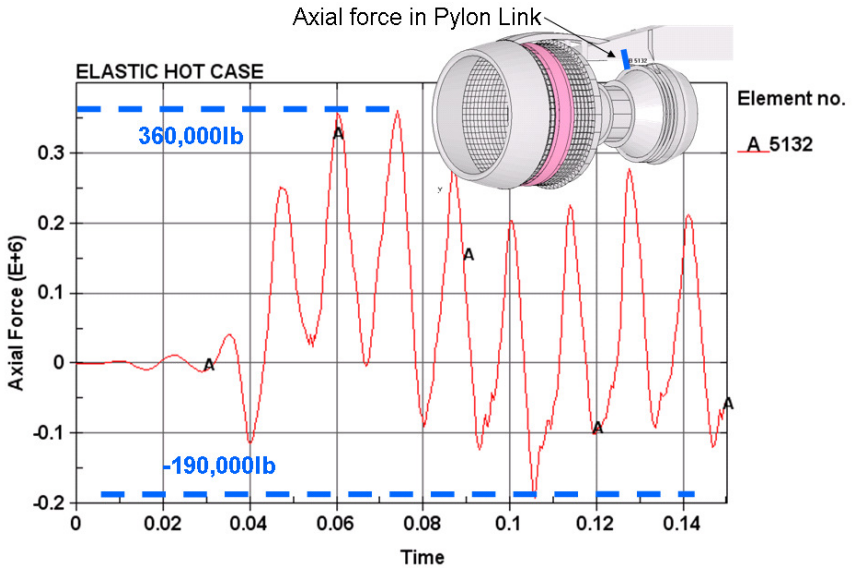
Axial force in Pylon Link
ELASTIC HOT CASE
360,000lb
-190,000lb
Element no.
A 5132
Axial Force (E+6)
Time

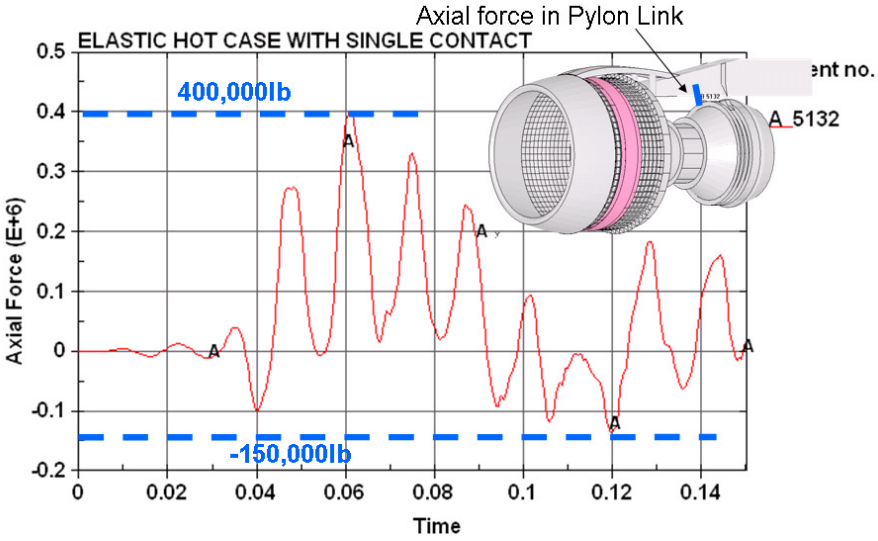
Axial force in Pylon Link
ELASTIC HOT CASE WITH SINGLE CONTACT
400,000lb
-150,000lb
A 5132
Axial Force (E+6)
Time

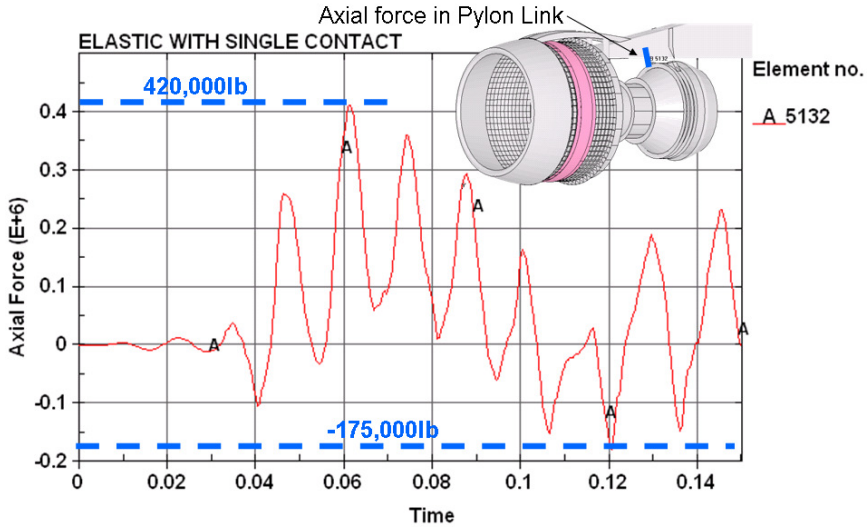
Axial force in Pylon Link
ELASTIC WITH SINGLE CONTACT
420,000lb
-175,000lb
Element no.
A 5132
Axial Force (E+6)
Time